Tomasz Piotr Baraniecki

Praseodymium Doped Fluoride Fiber Lasers

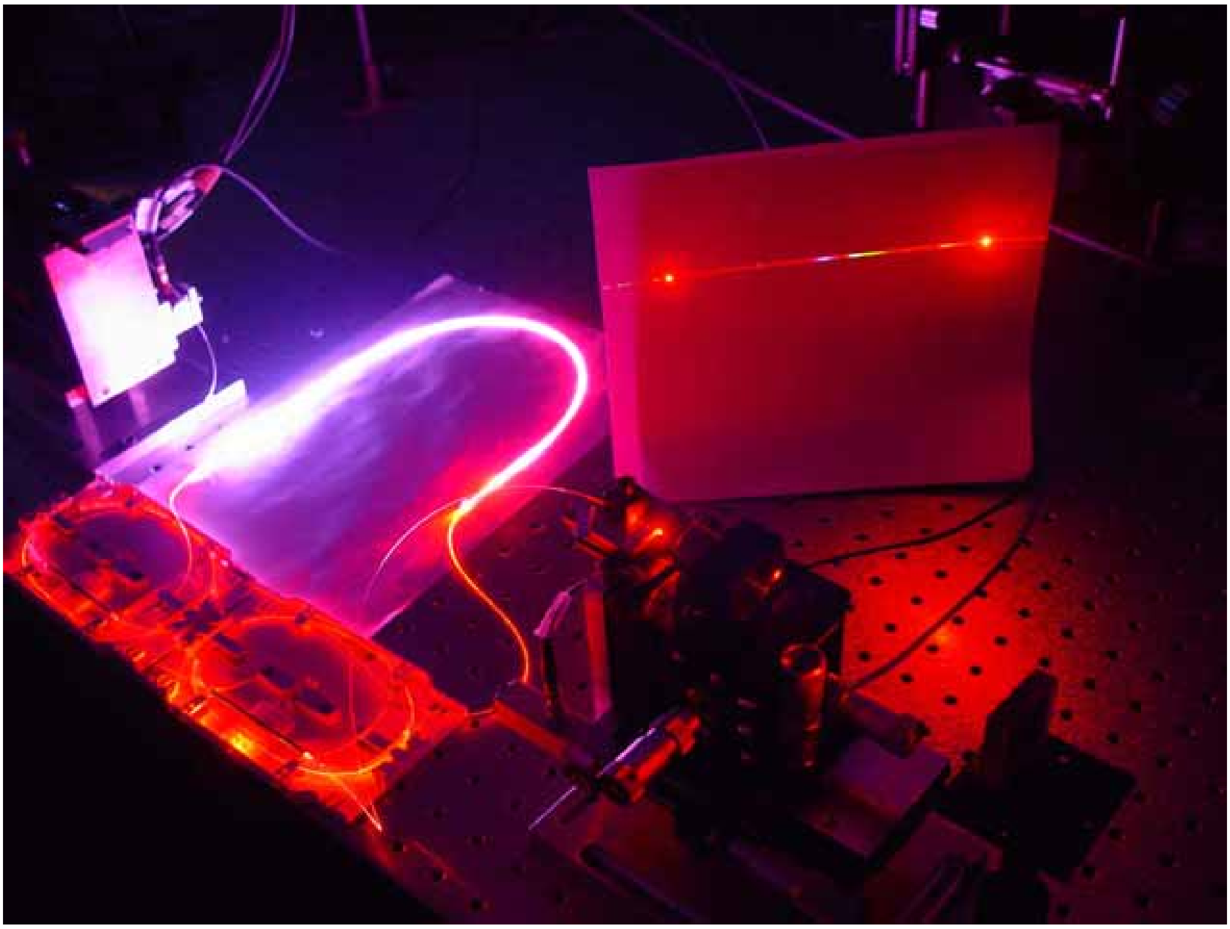

Cuvillier Verlag Göttingen

Praseodymium Doped Fluoride Fiber Lasers

Von der Fakultät für Elektrotechnik und Informationstechnik
der Technische Universität Carolo-Wilhelmina zu Braunschweig

zur Erlangung der Würde

eines Doktor-Ingenieurs (Dr.-Ing.)

genehmigte Dissertation

von: Dipl.-Ing. Tomasz Piotr Baraniecki

aus: Wrocław (Polen)

eingereicht am: 08.06.2006

mündliche Prüfung am: 19.07.2006

Referenten: Prof. Dr.-Ing. Wolfgang Kowalsky
Prof. Dr. Andreas Waag

2006

Bibliografische Information Der Deutschen Bibliothek
Die Deutsche Bibliothek verzeichnet diese Publikation in der Deutschen Nationalbibliografie; detaillierte bibliografische Daten sind im Internet über http://dnb.ddb.de abrufbar.
1. Aufl. - Göttingen : Cuvillier, 2006
Zugl.: (TU) Braunschweig, Univ., Diss., 2006
ISBN 3-86537-957-5

Nonnenstieg 8, 37075 Göttingen
Telefon: 0551-54724-0
Telefax: 0551-54724-21
www.cuvillier.de

1. Auflage, 2006
Gedruckt auf säurefreiem Papier

ISBN 3-86537-957-5

Acknowledgements

This thesis is the results of my research work as scientist at the *Institut für Hochfrequenztechnik* (IHF) of the Technical University at Braunschweig in the years 2000-2006. Completing a PhD was truly a marathon event, and I would not have been able to complete this journey without the aid and support of the staff at IHF and other people.

First of all, I want to thank Prof. Dr. Achim Enders, the chairman of the Examination committee as well as the co-examinators Prof. Dr.-Ing. Wolfgang Kowalsky, the director of the IHF, and Prof. Dr. Andreas Waag, the director of the Institute for Semiconductor Technology at the Technical University of Braunschweig and Dr.-Ing. Reinhard Caspary the coordinator of my research activities and Heads of the Research Group. Prof. Kowalsky and Dr. Caspary were my supervisors and they were able to provide an excellent working atmosphere in the institute and inside the research group. I would like to express my special thanks to Dr. Reinhard Caspary. His extensive knowledge and still new ideas helped me to find out the best solutions of scientific problems. It was a real pleasure to work with him and I am very thankful for his great support.

A warm thanks goes out to Dr.-Ing. Udo Unrau, the former Head of the Research Group. He was the person, who invited me to Braunschweig and made it possible for me to do my research in the field of the fiber laser. I am very thankful for his support in scientific problems and a great help by correction of this thesis. He spent several days correcting my manuscript and making it smoother and easier to understand. Without his work this thesis will not have the present form.

I would like to thanks my colleagues from the research group for the cooperation and many fruitful discussions. I wish to thank Dr.-Ing. Marcin Kożak, Dr. Dirk Geobel, Kathleen Möhring, Siew Kien Mah, Dr.-Ing. Thorsten Buschmann, Hotan Shalibeik, Elke Seiler, Dr. Ranjan Sen. I would like to specially thank Dr. Dirk Goebel and Kathleen Möhring, who produced fibers and glass samples used in my investigations.

As English is not my native language, I needed additional help to eliminate linguistic mistakes in my manuscript. Several people were involved in correcting this work and I am very grateful to Philip Bower for many appropriate suggestions, he helped me to avoid a number of mistakes.

Chciałbym serdeczne podziękować moich rodzicom Zuzannie i Zdzisławowi Baranieckim, a także rodzeństwu Marcie, Piotrkowi i Bartkowi, oraz moim dziadkom. Dziękuję wam za okazywaną mi pomoc i wsparcie podczas mojego pobytu w Braunschweigu. Tą pracę chciałbym dedykować mojemu tacie, który niestety nie doczekał jej zakończenia. Chciałbym także wyrazić wdzięczność moje przyszłej żonie Dagmarze, która nieustannie motywowała i pomagała mi przy pisaniu tego doktoratu.

Tomasz Baraniecki

Kurzzusammenfassung

Ziel dieser Arbeit ist die Entwicklung und die Optimierung von Faserlasern, die im sichtbaren Spektralbereich emittieren und auf Pr^{3+}/Yb^{3+} dotierten Fluoridglasfasern basieren. Blaue, grüne, orange und rote Faserlaser werden in verschiedenen Aufbauten präsentiert.

Es werden grundlegende physikalische und technische Ansichten von Lasern dargestellt, mit besonderem Augenmerk auf Aufkonversions-Faserlaser. Zudem werden spektroskopische Messungen dargestellt, wo Pr^{3+} dotierte ZBLAN und IBZP Glassproben untersucht werden. Kein bedeutender Unterschied der Absorptionsspitzen beider Gläser wurde beobachtet. Aber die Emissionsstärken von Pr^{3+} dotierten Fluoridgläser sind abhängig von der Glas-Zusammensetzung, besonders im Fall des roten und orangen Überganges.

Die Kenntnisse, die aus den Spektroskopiemessungen gesammelt wurden, sind wertvoll für den Aufbau von Faserlasern in Fabry-Perot Konfiguration. Dieser Aufbau ermöglicht es Laser, die bei 490 nm, 520 nm und 635 nm emittieren, zu realisieren. Der größte Wirkungsgrad wurde beim roten Laser gemessen, mit 20 mW Ausgangsleistung bei 500 mW Pumpleistung. Bei der gleichen Pumpleistung weisen grüne und blaue Laser entsprechend 9.3 mW und 4.8 mW Ausgangsleistung auf. Während dieser Arbeit wurde die Optimierung des roten Lasers durchgeführt. Die optimale Pumpwellenlänge liegt bei ca. 840 nm und die Pumpwellenlängenänderungen um ± 10 nm haben nur kleine Intensitätsabweichungen verursacht. Die Auswirkung der Spiegelreflexion und die Faserlänge sind somit untersucht worden. Der rote Laser zeigt ein geringes Rauschen, aber die Ausgangsleistung von dem blauen Laser ist instabil. Für den roten und grünen Laser wurde auch eine Rauschregelung mit einer Rückkopplungsschleife verwendet und eine kleine Verbesserung des Signal-zu-Rausch-Abstandes festgestellt. Die Langzeitstabilität der Laser wurde also getestet und es wurde kein bedeutsamer Abfall der Ausgangsleistung während einer Stunde beobachtet.

Es gibt eine Anzahl von Nachteilen des Fabry-Perot Aufbaus, weswegen auch ein alternativer Ansatz von vollständig aus Fasern aufgebauten Lasern verwendet wurde. Es wurde ein roter Ringlaser aufgebaut, das keine Festkörperspiegel erfordert. Dieser Aufbau verwendet Faserschmelzkoppler, weshalb sich ein Teil dieser Arbeit mit der Herstellung dieser Bauelemente befasst. Ein anderes wichtiges Element des Ringlasers sind Klebespleisse, die eine Verbindung zwischen Quarz- und Fluoridglasfasern ermöglichen. Die optimale Effizienz des roten Ringlasers wurde bei einer Auskopplung von 52 % gemessen, dabei erreicht man 8 mW Ausgangsleistung bei 500 mW Pumpleistung. Faserschleifenspiegel werden als weitere Methode einen vollständig aus Fasern aufgebauten Laser zu realisieren untersucht.

Faserlaser weisen viele Longitudinalmoden aus und man kann Faser-Bragg-Gitter nutzen, um die Linienbreite des Lasers einzuengen. Wenn ein Fasergitter eingesetzt wird, wurde eine Longitudinalmode mit einer Bandbreite von nur etwa 0.2 nm beobachtet. Wenn man das breite Fluoreszenzspektrum von Pr^{3+} ausnutzt, bekommt man ein orange-roten durchstimmbaren Faserlaser, der in Littrow Anordnung realisiert wurde. Damit wurde eine Superfluoreszenzquelle aufgebaut, was 33 mW Ausgangsleistung bei 500 mW Pumpleistung emittiert und eine Linienbreite von etwa 1.7 nm aufweist.

Contents

Introduction

The subject of rare earth doped fiber lasers and amplifiers is an interesting and promising research field because it provides low-cost laser sources and amplifiers at wavelengths that are important for telecommunication, medicine, sensors, metrology and spectroscopy.

Laser action is produced by introduction of suitable rare earth ions into the core of a single mode fiber. The considerable advantages of the fiber configuration arise from the fact that the pump radiation travels along the axis of the fiber and is guided by the core, as is the lasing radiation. Therefore, the coupling between the pump radiation and the ions is very effective, while the pump intensity is very high because of the small core diameter. These factors enable successful lasing of transitions that have no conventional solid-state analogue, via pumping of very weak absorptions using long lengths of fiber. In conventional crystal lasers, on the other hand, high power density is achieved by tight focusing which then limits the effective pumping length through divergence. Fiber lasers are small, robust, flexible, and give easy access to the laser cavity, thus enabling the operations of Q-switching, mode-locking and line-narrowing to be carried out. The inherent high beam quality of single mode fiber lasers is more or less independent of the output power in contrast to laser diodes. Because of the large fluorescence linewidth, large tuning ranges can also be obtained. Fiber lasers are also no longer restricted to low power operation. Cladding pumping enables light from high power pump sources to be used efficiently and converted to multiwatt output powers with a brightness enhanced by more than two orders of magnitude.

Rare earth doped fluoride glass fibers have been shown to be excellent laser materials. Besides their unique properties for fiber lasers, they offer more metastable levels than silica fibers, thus improving performance, adding new wavelengths and allowing easier upconversion lasing. Typical upconversion fiber lasers are pumped in the near infrared but emit laser radiation in the visible range by subsequent absorption of two or more pump photons. For this multi-stage process to be efficient, besides the large interaction length inherent to fiber lasers, long lifetimes of the respective energy levels are necessary, and therefore low phonon energy glasses are needed. In silica, the higher energy levels of dopant ions relax very fast by excitation of vibrations of the glass matrix since it has high phonon energies. In practice, the most important low phonon energy glasses are heavy metal fluoride glasses of which the ZBLAN glass is the most famous type. Rare earth ions are particularly appropriate for upconversion lasers because they have numerous long-living metastable levels which store population during the upconversion process. Upconversion lasers may provide a useful route to the development of visible lasers pumped by cheap semiconductor lasers operating in the near infrared region of the spectrum.

Upconversion fiber lasers operating in the red, green, and blue spectral range offer a good alternative to air-cooled ion lasers and frequency-doubled solid-state lasers. The laser transitions of the Pr^{3+} ion are attractive, because laser operation at blue, green, orange and red wavelengths can all be obtained. Additional doping with Yb^{3+} ions enables to obtaining these laser transitions using only one pump wavelength.

In this work, we will describe different aspects of laser operation. Special attention is paid to the Pr^{3+}/Yb^{3+} doped fiber lasers emitting in the visible spectral range. The study presented in this work consists of seven chapters, and a short description of their contents will be given below.

Chapter 1. This chapter provides fundamental information about lasers and basic principles of laser operation. Absorption, spontaneous and stimulated emission are described as well as the creation of the population inversion.

Chapter 2. In this chapter, properties of laser materials are discussed with special attention to rare earth ions in a glass host. The next object of discussion is interactions between the ions. The upconversion pumping process in praseodymium ions is described in detail. Nonradiative relaxation plays an important role in the upconversion process, and therefore, it is also reviewed.

Chapter 3. The spectroscopic investigations of praseodymium in the glass matrix and their analysis are explained in this chapter. A number of absorption as well as emission lines are investigated in ZBLAN and IBZP glass systems. The fluorescence lifetime of the upper laser level is a very important parameter; therefore, lifetime measurements are performed for both glass types.

Chapter 4. After an introduction of the structure of an optical fiber in general and loss mechanisms, fiber lasers emitting in the visible spectral range are described with a focus on fiber lasers doped with Pr^{3+}. This chapter also contains a comparison of bulk and fiber lasers as well as fiber laser applications. Semiconductor diode lasers and second harmonic generation are presented as another method to generate light in the visible spectrum range.

Chapter 5. Results of measurements on visible fiber lasers in Fabry-Perot configuration are reported in this chapter. We begin with a description of the setup, and then performances of fiber lasers emitting at red, green and blue wavelengths are presented. In addition, investigations of the optimal pump wavelength, mirror reflectivity and fiber length are shown. We also concentrate on short- and long-term stability of fiber lasers. Finally, relaxation oscillations and noise suppression are discussed.

Chapter 6. Here the results of red, all-fiber fiber laser measurements are presented with a focus on the ring laser. This laser makes use of directional couplers; therefore, this chapter begins with a describtion of the fabrication of these components. Next, the glue-splice technique is presented as a solution to the connection problems between fluoride and silica fibers. Fiber Bragg gratings and loop mirrors are presented as other ways to construct an all-fiber laser setup.

Chapter 7. In the last chapter, we the concentrate on tunability of the praseodymium doped fiber lasers. After presentating the configuration used to construction tunable lasers, the orange-red tunable fiber laser is described. Furthermore, a superfluorescence source based on a similar setup is presented.

1 Laser theory

This chapter will provide fundamental information about lasers. It describes the basic principles of laser operation. In 1917, Albert Einstein showed that the process of stimulated emission must exist, but it was not before 1960 that T. H. Maiman was able to demonstrate laser action for the first time [1]. Basic principles and the construction of lasers are relatively simple but on the other hand, a rigorous analysis of the physics of lasers is quite difficult. Therefore, the following approach is very much simplified.

1.1 Interaction of radiation with matter

In order to understand the operation of a laser we have to know some of the principles which govern the interaction of radiation and matter. Atomic systems such as atoms, ions, and molecules can exist only in discrete energy states. A change from one energy state to another is called a transition. To simplify the discussion, let us consider an idealized material with just two energy levels, 1 and 2, having populations of N_1 and N_2, respectively (Figure 1.1). The total number of atoms in these two levels N_0 is assumed to be constant [2]:

$$N_1 + N_2 = N_0 . \tag{1.1}$$

If the system is in the lower level E_1 then, in the presence of photons, it may be excited to the upper level E_2 by absorbing a photon. Alternatively, if the system is in the level E_2 it may return to the ground state with the emission of a photon. The energy difference between the levels must be compensated by the emission or absorption of radiant energy. It is given by the relation [3]:

$$\mathrm{h}\nu_{21} = \frac{hc}{\lambda} = E_2 - E_1 , \tag{1.2}$$

where h is Planck's constant, c the velocity of light in a vacuum, ν_{21} the frequency, and λ the wavelength of the photon. E_2 and E_1 are two discrete energy levels. The emission process may occur in two ways. The first is the *spontaneous emission* process in which the system drops to the lower level in a completely random way. The second is the *stimulated emission* process in which the system is 'triggered' by the presence of another photon to make the transition. The photon must have the proper energy corresponding to the energy difference between the original state and a lower energy level. The stimulated photon has the same frequency, same state of polarization, same phase, and it propagates in the same direction as the stimulating photon. The original radiation is still present, and so the radiation intensity has been amplified. This is the origin of the acronym LASER: '**L**ight **A**mplification by **S**timulated **E**mission of **R**adiation'. The three processes are shown in Figure 1.1. The horizontal straight lines represent the level; the wavy arrows represent photons; and the vertical arrows represent the transitions of electrons from one level to another. The black dot indicates the state of the atom before and after the transition.

1.1.1 Absorption

If a quasi monochromatic electromagnetic wave of frequency ν_{21} passes through an atomic system with energy gap $h\nu_{21}$, then the population of the lower level will be depleted at a rate proportional both to the radiation density $\rho(\nu)$ and to the population N_1 of that level [2]:

$$\frac{\partial N_1}{\partial t} = -B_{12}\rho(\nu)N_1, \tag{1.3}$$

where B_{12} is the coupling constant of radiation and matter for the absorption process (Einstein coefficient). The product $B_{12}\rho(\nu)$ can be interpreted as the probability per unit frequency that transitions are induced by the electromagnetic field.

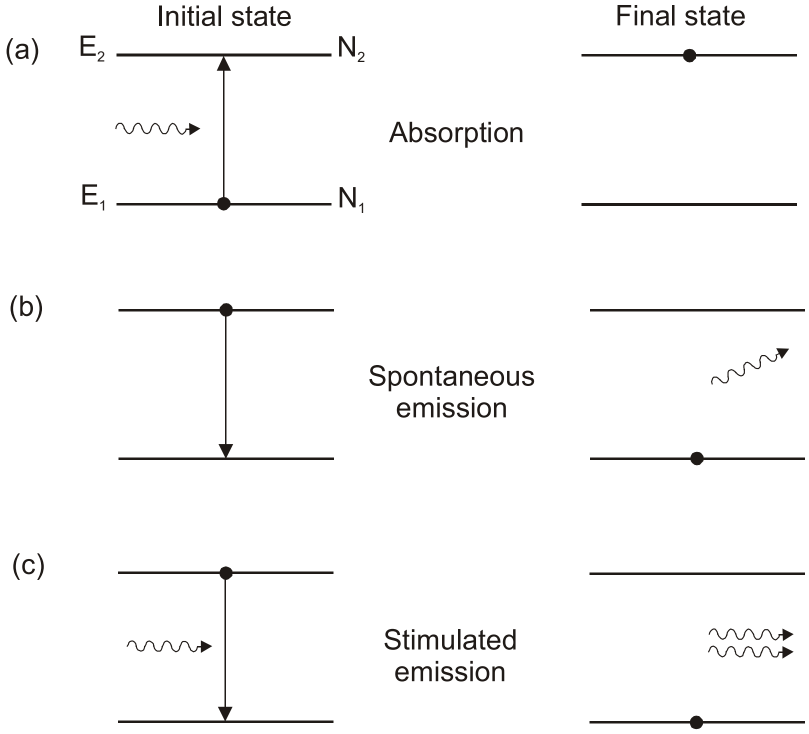

Figure 1.1: Schematic diagram illustrating (a) absorption, (b) spontaneous emission and (c) stimulated emission [1]

1.1.2 Spontaneous emission

After a couple of atoms have been excited to the upper level, the population of the upper level decays spontaneously to the lower level at a rate proportional to the upper level population [2]:

$$\frac{\partial N_2}{\partial t} = -A_{21}N_2, \tag{1.4}$$

where A_{21} is the coupling constant for the spontaneous emission process. This coefficient gives the probability for an atom in level 2 to decay spontaneously to the lower level 1 within a unit of time. Spontaneous emission is characterized by the lifetime of the electron in the excited state in which it will spontaneously return to the lower state and radiate away the energy difference. This radiation lifetime is connected with A_{21} by the relation:

$$\tau_{21} = A_{21}^{-1}. \tag{1.5}$$

In general, the reciprocal transition probability of a process is called its lifetime.

1.1.3 Stimulated emission

As already mentioned, emission takes places not only spontaneously but also under stimulation. The atom gives a quantum to the radiation field by induced emission [2]:

$$\frac{\partial N_2}{\partial t} = -B_{21}\rho(v)N_2, \tag{1.6}$$

where B_{21} is the coupling constant for the stimulated emission process.

If we combine absorption, spontaneous and stimulated emission, as presented in (1.3), (1.4) and (1.6) we can write for the change of the upper and lower level populations in our two-level model:

$$\frac{\partial N_1}{\partial t} = -\frac{\partial N_2}{\partial t} = B_{21}\rho(v)N_2 - B_{12}\rho(v)N_1 + A_{21}N_2. \tag{1.7}$$

For a system in thermal equilibrium, the number of transitions per unit time from E_1 to E_2 must be equal to the number of transitions from E_2 to E_1. Hence we have

$$\underset{\substack{\text{Spontaneous}\\\text{emission}}}{N_2 A_{21}} \quad + \quad \underset{\substack{\text{Stimulated}\\\text{emission}}}{N_2\rho(v)B_{21}} \quad = \quad \underset{\text{Absorption}}{N_1\rho(v)B_{12}}. \tag{1.8}$$

Thus,

$$\rho(v) = \frac{A_{21}/B_{21}}{\frac{B_{12}}{B_{21}}\frac{N_1}{N_2} - 1}. \tag{1.9}$$

The populations of the energy levels 1 and 2 in thermal equilibrium are given by Boltzmann statistics to [1]:

$$\frac{N_1}{N_2} = \frac{g_1}{g_2}\exp\left(\frac{E_2 - E_1}{kT}\right) = \frac{g_1}{g_2}\exp\left(\frac{hv_{21}}{kT}\right), \tag{1.10}$$

where k is Boltzmann's constant and T is the absolute temperature of the material. In general, the probability for occupation of all energy levels is not the same, and g_j is the degeneracy of the jth level. Hence, substituting eq. (1.10) into eq. (1.9) yields:

$$\rho(v) = \frac{A_{21}/B_{21}}{\left[\frac{g_1}{g_1}\frac{B_{12}}{B_{21}}\exp\left(\frac{hv_{21}}{kT}\right)\right] - 1}. \tag{1.11}$$

As we consider the atom system to be in thermal equilibrium, it must give rise to radiation which is identical with blackbody radiation, the density of which can be described by [1]:

$$\rho(v) = \frac{8\pi hv^3}{c^3}\left(\frac{1}{\exp(hv/kT) - 1)}\right). \tag{1.12}$$

Comparing eqs. (1.11) and (1.12) , we can write [2]:

$$\frac{A_{21}}{B_{21}} = \frac{8\pi hv}{c^3} \qquad \text{and} \qquad B_{21} = \frac{g_1 B_{12}}{g_2}. \tag{1.13}$$

The relation between the A's and B's are known as Einstein's relations, and A_{21}, B_{12} and B_{21} are Einstein's constants. Equations (1.13) are very important because they show a connection among three different radiation processes: spontaneous emission, absorption, and stimulated emission. A particular experiment may emphasize one or another coefficient, the results may be applied to a completely different one, e.g. an absorption experiment yields information on the stimulated emission coefficient.

1.2 Creation of population inversion

At absolute zero temperature, Boltzmann's statistic in equation (1.10) predicts that all atoms will be in the ground state. Thermal equilibrium at any temperature requires that a state with a lower energy is more densely populated than a state with a higher energy. Absorption and emission probabilities are always independent of the population distribution among the levels. As long as the population of the higher energy levels is smaller than that of the lower one, the number of absorption transitions is larger than that of emission transitions; there is an overall attenuation of radiation. If the numbers of atoms in both states are equal to g_2:g_1, the number of emissions becomes equal to the number of absorptions, and the material is transparent for the incident radiation. As soon as the population of the higher level becomes larger than that of the lower level, emission processes dominate and the radiation is amplified during its passage through the material. Therefore, for achieving laser amplification, we must create the following condition:

$$N_2 g_2 > N_1 g_1\,; \tag{1.14}$$

i.e., we must create a so-called *population inversion*. Population inversion is clearly an abnormal situation, it is never observed at thermal equilibrium. In order to obtain population inversion, we must have a source of energy to populate the upper level; this process is commonly referred to as *pumping*. The point at which the population of both states is equal to g_2:g_1, is called the inversion threshold.

It is impossible to achieve a population inversion by optical pumping in an electronic system with only two energy levels. For a simple system with no degeneracy, e.g. one with $g_1 = g_2$, we see from eq. (1.13) that $B_{21} = B_{12}$. Hence, if atoms are excited into the upper level the probabilities of further absorption or stimulated emission are equal even with very intensive pumping. The best that can be achieved with a two-level system is equality of population of the two levels; the material becomes transparent. This situation is often referred to as two-level saturation.

As a consequence we must look for materials with more than two levels. Laser materials generally have a large number of energy levels, but only three or four of them will be directly involved in laser operation. The three-level system is illustrated by Figure 1.2a.

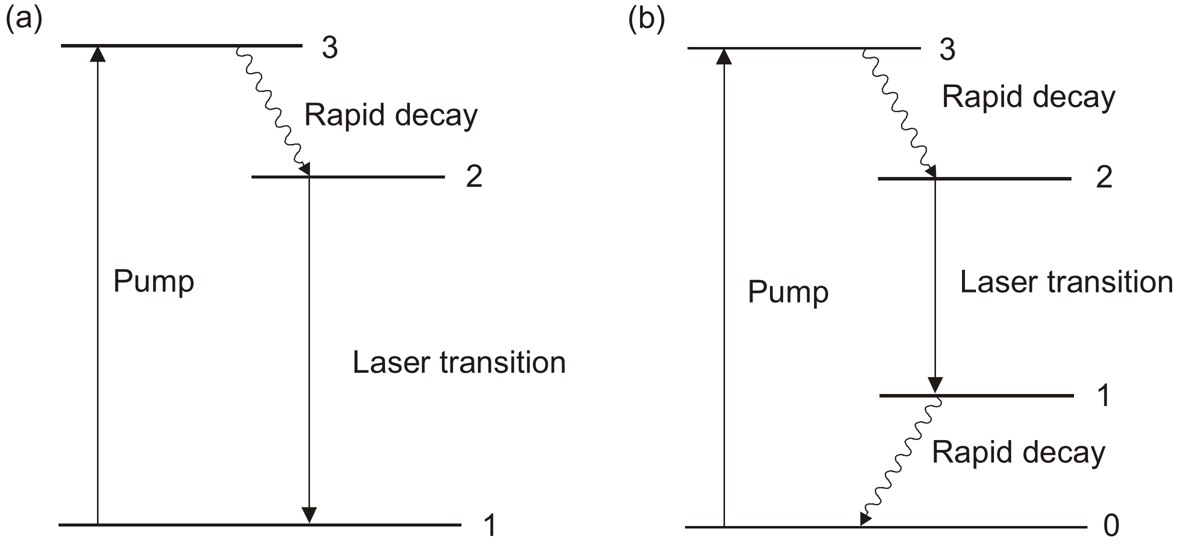

Figure 1.2: Simplified energy level diagram of (a) three-level and (b) four-level laser

Initially, all atoms of the laser material are in the lowest level 1. An auxiliary radiation pump source excites the atoms. The pump radiation raises an atom from the ground state to the pump band, level 3. Most of the excited atoms are transferred by fast radiationless transition into the intermediate level 2. In this process the energy lost by the atom is transferred to the lattice and converts to heat. With higher pump power population inversion between level 2 and 1 is achieved. Finally, the atoms return to the ground level by the emission of a photon. This transition is responsible for a laser's action [2]. It is necessary that the rate of radiationless transfers from level 3 to level 2 is fast compared to the other spontaneous transition rates. Therefore, the lifetime of level 2 should be large; it should be a metastable level. This allows for a large build-up in the number of atoms in level 2. The relatively long lifetime of the metastable level provides a mechanism by which inverted population can be achieved. The main advantage of the three-level system is that the atoms are in effect pumped directly from level 1 into the metastable level 2 with only a pause as they pass through level 3. But the three-level system has the drawback that level 1 is the ground level which normally hosts almost all the atoms. To achieve a population inversion between levels 2 and 1 in a non-degenerated system, half of all the atoms must be moved to level 2, and so intensive pumping is needed. In a degenerated system, the population ratio g_2:g_1 has to be reached.

Figure 1.2b shows a four-level laser system. The pump transition raises atoms again from the ground state (now level 0) to level 3. As in the case of the three-level system, the atoms so excited will decay fast to level 2. The laser transition proceeds now to the fourth, terminal level 1, which is situated above the ground state. From here the atoms undergo a rapid nonradiative transition to the ground level [2]. In a true four-level system, the terminal laser level 1 will always be empty, hence a population inversion of the 2→1 transition can occur even with a small pump power; the high pump rate necessary in a three-level system is no longer needed. Therefore, three-level lasers have higher threshold powers than four-level laser systems, and four-level schemes are to be preferred for this reason. However, by a combination of favourable circumstances, it is possible to overcome the disadvantage of the three-level scheme.

1.3 The laser idea

The laser, despite its name, is more an analogue to an oscillator than to an amplifier. In an electronic oscillator, an amplifier tuned to a particular frequency is provided with positive feedback and, when switched on, any electrical noise signal of the appropriate frequency appearing at the input will be amplified. The input is amplified and the output is fed back to the input, where it undergoes further amplification. The process continues indefinitely until a large output is produced. The amplifier saturates at high input voltages, as it cannot produce a larger output than the supply voltage. The system reaches a steady state in which an output signal is created at the frequency of the resonant amplifier.

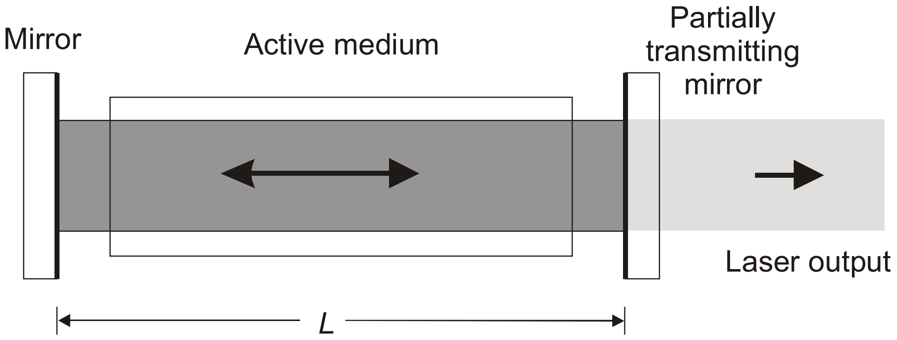

Figure 1.3: A laser consists of an active medium placed within an optical resonator.

In the laser, positive feedback may be obtained by placing the gain medium in an optical resonator, which reflects the light back and forth between its mirrors, e.g. in a Fabry-Perot resonator which is schematically shown in Figure 1.3. The initial stimulus is provided by any spontaneous transition between appropriate energy levels in which the emitted photon travels along the axis of the system. The signal is amplified as it passes through the medium and fed back by the mirrors. As the oscillation power grows the amplifier saturates and the gain decreases below its initial value. A stable condition is reached when the reduced gain is equal to the loss. The gain then just compensates the loss so that the cycle of amplification and feedback is repeated without change, and a steady-state oscillation occurs. Output coupling is achieved by making one of the resonator mirrors partially transparent.

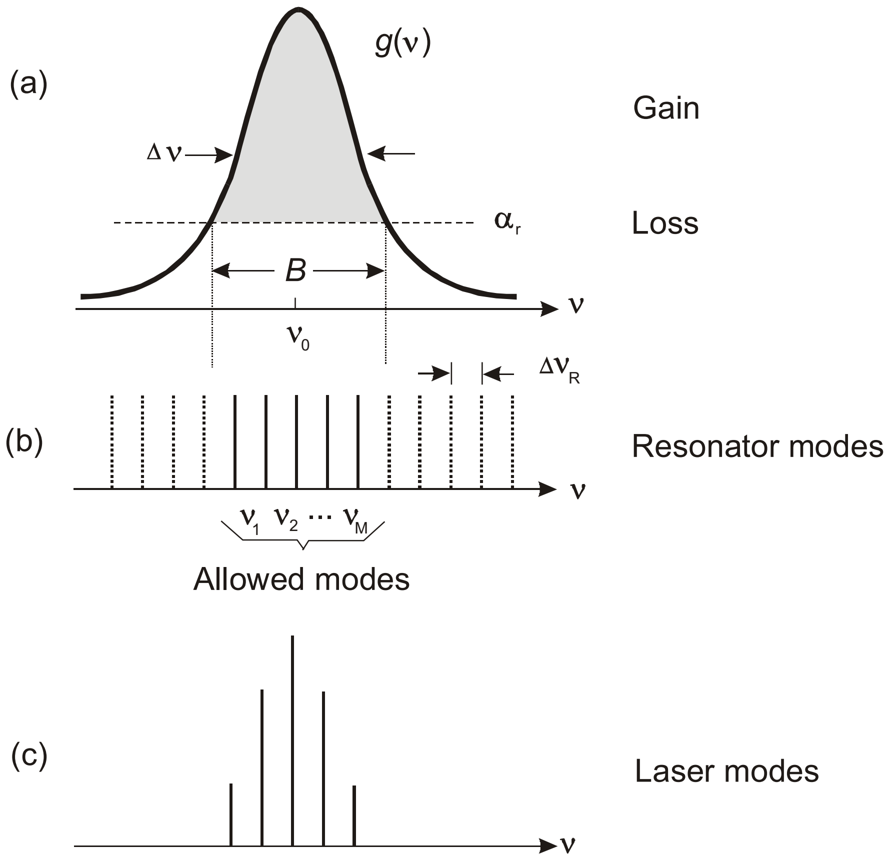

Figure 1.4: (a) Gain coefficient of a laser amplifier and the loss coefficient (dotted region), (b) resonator modes, (c) possible laser modes

As already mentioned, optical feedback is achieved by placing the active medium in an optical resonator. A Fabry-Perot resonator, comprising two mirrors separated by a distance L, contains the active medium. The resonator sustains only frequencies that correspond to a round-trip phase shift of 2π. Resonator modes are separated by the frequency:

$$\nu_R = \frac{c}{2L}. \tag{1.15}$$

The spectral distribution of the laser radiation generated is determined both by the atomic lineshape of the active medium and by the resonator modes. This is illustrated by two conditions for a laser [4]:

- The gain conditions requiring that the initial gain coefficient of the amplifier be greater that the loss coefficient [$g(\nu)>\alpha_r$] is satisfied for all oscillation frequencies lying within a continuous spectral band of width *B* centered about the atomic resonance frequency ν_0, as illustrated Figure 1.4(a). The width *B* increases with the atomic linewidth $\Delta\nu$, and the ratio $g(\nu)/\alpha_r$; the precise relation, depends on the shape of function $g(\nu)$.
- The phase condition requires that the oscillation frequency be one of the resonant modal frequencies:

  $$\nu_q = q\nu_R, \quad q = 1, 2, ... \tag{1.16}$$

  It follows that only a finite number of oscillation frequencies ($\nu_1, \nu_2, \ldots, \nu_M$) are possible.

2 Properties of laser materials

In the previous chapter basic conditions necessary to obtain laser oscillations were discussed. The presence of an idealized active medium was assumed which does not exist in reality. A huge number of real laser materials is in use, but in this chapter we will discuss only the properties of solid-state host materials, especially fluoride glass doped with rare earth ions.

2.1 Rare earth ions

The rare earths or lanthanides are a series of 15 elements beginning with lanthanum (atomic number $Z = 57$) and ending with lutetium ($Z = 71$). Despite their name, such elements are not really rare. E.g. cerium, the second of the lanthanide elements, is present in the crust of the earth at a level of 46 ppm [5]. In condensed matter the rare earths display the oxidation state +3 in which the atom has lost three electrons to form a trivalent ion: two of the 6s electrons and one of the 4f electrons, but the outer 5s and 5p shells remain intact [6]. In order to understand the optical properties of these ions it is necessary to know their energy states. The outermost electrons of these ions form a complete rare gas shell, which is the xenon shell with two 5s and six 5p electrons. This shell is optically inactive. The next inner shell is the 4f shell, which is filled successively with heavier elements. Trivalent cerium, Ce^{3+}, has one 4f electron, and trivalent ytterbium, Yb^{3+}, has 13, as illustrated in Table 2.1.

Table 2.1: Electronic configurations of the lanthanides as elements and triply ionised

Z	Element	Symbol	Element	Ion
54	Xenon	Xe	$1s^2\ 2s^2\ 2p^6\ 3s^2\ 3p^6\ 3d^{10}\ 4p^6\ 5s^2\ 4d^{10}\ 5p^6$	
57	Lanthanum	La	[Xe] $4f^0\ 5d\ 6s^2$	$4f^0$
58	Cerium	Ce	[Xe] $4f^2\ 6s^2$	$4f^1$
59	Praseodymium	Pr	[Xe] $4f^3\ 6s^2$	$4f^2$
60	Neodymium	Nd	[Xe] $4f^4\ 6s^2$	$4f^3$
61	Promethium	Pm	[Xe] $4f^5\ 6s^2$	$4f^4$
62	Samarium	Sm	[Xe] $4f^6\ 6s^2$	$4f^5$
63	Europium	Eu	[Xe] $4f^7\ 6s^2$	$4f^6$
64	Gadolinium	Gd	[Xe] $4f^7\ 5d\ 6s^2$	$4f^7$
65	Terbium	Tb	[Xe] $4f^9\ 6s^2$	$4f^8$
66	Dysprosium	Dy	[Xe] $4f^{10}\ 6s^2$	$4f^9$
67	Holmium	Ho	[Xe] $4f^{11}\ 6s^2$	$4f^{10}$
68	Erbium	Er	[Xe] $4f^{12}\ 6s^2$	$4f^{11}$
69	Thulium	Tm	[Xe] $4f^{13}\ 6s^2$	$4f^{12}$
70	Ytterbium	Yb	[Xe] $4f^{14}\ 6s^2$	$4f^{13}$
71	Lutetium	Lu	[Xe] $4f^{14}\ 5d\ 6s^2$	$4f^{14}$

As long as the 4f shell is not completely filled with 14 electrons, a number of 4f levels are unoccupied, and electrons already present in the 4f shell can be raised by light absorption into these empty levels. The observed IR and visible optical spectra of trivalent rare earth ions are a consequence of transitions among 4f states. However, since the electrons of $5s^2$ and $5p^6$ shield the 4f electrons, the effects of the environment on 4f electrons are reduced [7]. Therefore, the fluorescence and absorption wavelengths are therefore less dependent on external electric fields. In contrast, the ions of the transition elements (for example Cu, Cr) show very broad absorption and fluorescence features due to the fact that their optically active d-electrons interact strongly with the crystal field [8, 9]. Rare earth ions are good candidates for active ions in laser materials because they show many absorption and fluorescence transitions in almost every region of the visible and the near-infrared range. Rare earths also have other important characteristics in comparison to other optically active ions: the wavelengths of their emission and absorption transitions are relatively insensitive to host materials, the lifetimes of metastable states are long and the quantum efficiency tends to be high [10]. These properties lead to an excellent performance of rare earth ions in many optical applications.

As already mentioned, the electronic configuration and the effects of the environment determine the electronic energy levels of rare earth ions. The Hamiltonian for an individual rare earth ion can be written and decomposed as [7]:

$$H = H_{\text{free ion}} + V_{\text{ion-static lattice}} + V_{\text{ion-dynamic lattice}} + V_{\text{EM}} + V_{\text{ion-ion}} \tag{2.1}$$

Here, $H_{\text{free ion}}$ describes the ion in complete isolation, $V_{\text{ion-static lattice}}$ and $V_{\text{ion-dynamic lattice}}$ contain the static and dynamic interaction of the ion with the host, V_{EM} indicates the interaction of the ion with the electromagnetic field, and $V_{\text{ion-ion}}$ treats the interaction between rare earth ions. Taking these interactions among atoms into account, we can describe the energy levels for rare earth ions. Figure 2.1 shows a portion of the energy levels for praseodymium.

The two 4f-electrons of praseodymium ions in the central field interact electrostatically (coulombic interaction between electrons), and as a result their energy level splits into seven levels with different energies such as ^1S, ^3P, ^1D, ^3F, ^1G, ^3H, and ^1I. Then, due to spin-orbit coupling, the triplett levels ^3H and ^3F which have S=1 split into three levels such as $^3H_6$, $^3H_5$, $^3H_4$, and $^3F_4$, $^3F_3$, $^3F_2$, whereas the singulett level ^1G does not split.

Expressions such as $^3H_6$, $^3H_5$, $^3H_4$ are called term symbols which provide three pieces of information [7]:

1) The letter indicates the total orbital angular momentum L defined by the letters S, P, D, F, G, H, I,… which correspond to $L = 0, 1, 2, 3, 4, 5, 6,\ldots$ respectively.
2) The left superscript in the term symbol shows the multiplicity of the terms. This is given by the total spin S, and the multiplicity is $2S + 1$.
3) The right subscript in the term symbol is the value of the total angular momentum quantum number J and is given by:

$$J = L + S, L + S - 1, \ldots ,|L - S|. \tag{2.2}$$

Russell-Saunders coupling (*LS* coupling) is most often used for the states of lanthanides, and the states are expressed as ${}^{2S+1}L_J$. In the case of ^{3}H, L = 5 and S = 1 holds, so that J = 6, 5, and 4 is possible. Therefore, ^{3}H splits into ${}^3H_6$, ${}^3H_5$, ${}^3H_4$. The effect of the structural environment in condensed matter is another important issue. When a many-electron atom is placed in an external field such as a magnetic field or an electric field, the energy levels are split. In general, when a magnetic field is applied to ions, the energy levels split into levels whose number depends on the value of the total angular momentum quantum number *J*. This splitting is called the Zeeman effect. On the other hand, if an electric field is applied to ions, the splitting is called the Stark effect.

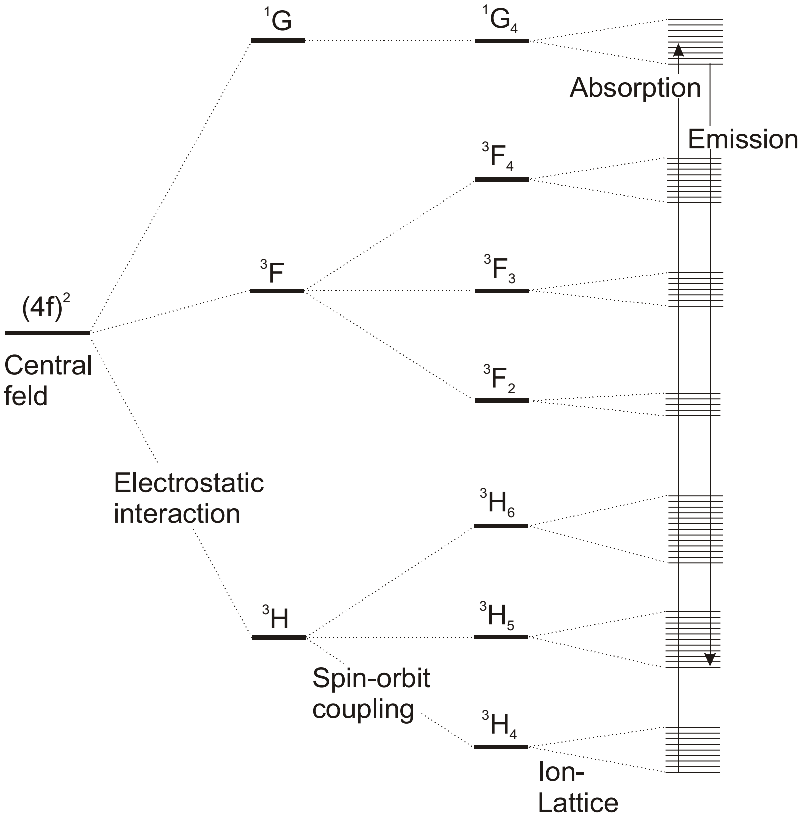

Figure 2.1: Energy diagram for praseodymium ions with two 4f-electrons [7]

In glass materials, the electrostatic interaction between the ions and lattice is dominant, so the energy level splitting is the Stark effect, as shown in Figure 2.1.The number of Stark levels is 2*J*+1. As a result of the shielding of the 4f electrons, these Stark shifts are quite small, only around a few hundred inverse centimetres. Additionally, the magnitude of the energy split depends on the magnitude of local electrical fields, which varies depending on their location in the host material. The magnitude of the Stark splitting is slightly different for each individual ion because of the differences in the crystal field surrounding the rare earth ions. Therefore, the Stark level has a noticeable broadening originating from the site-to-site difference in the Stark level of the individual ions, which is schematically shown in Figure 2.2.

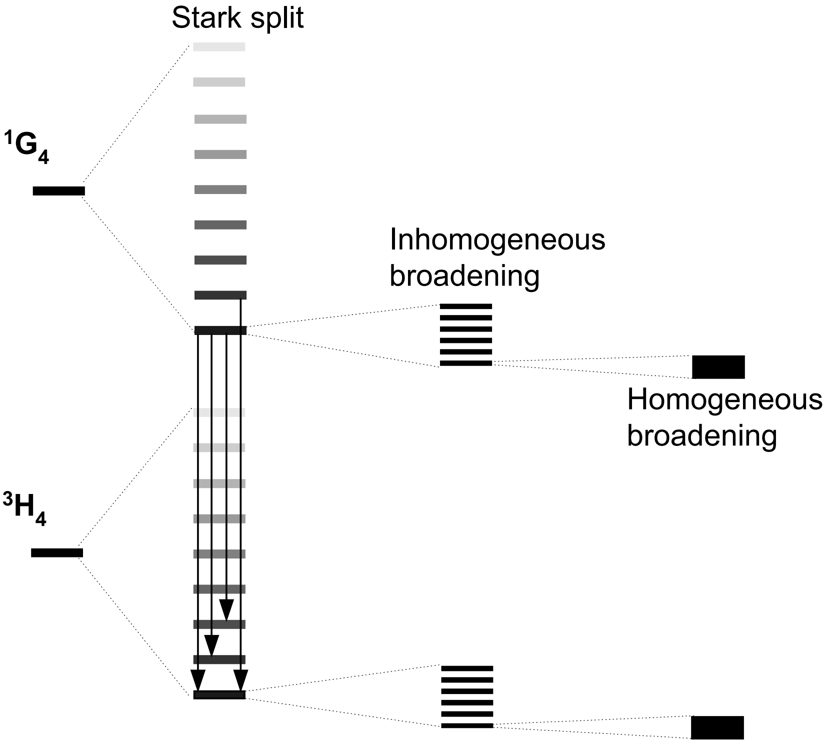

Figure 2.2: Schematic diagram showing details of the structure of Pr^{3+} ion energy levels

This broadening is an inhomogeneous broadening and originates from the material structure. In addition, the individual Stark levels fluctuate and broaden as a result of the fluctuation of the crystal fields caused by thermal atomic motions. This broadening due to thermal fluctuation is called homogeneous broadening. A transition between two Stark levels takes place by the creation or annihilation of a phonon. Lowering the temperature reduces the phonon population and thus causes spectral narrowing. Phonon broadening acts on all of the rare earth ions to a similar degree and is thus homogeneous. In thermal equilibrium, the energy population of ions has a Boltzmann distribution, and there is a large difference in the population of the sublevels. In Figure 2.2, the colour intensity of Stark sublevels indicates such a population difference in the sublevels. The sublevels with lower energy have a higher population of ions. Hence, the absorption spectra shift towards shorter wavelengths and the fluorescence spectra towards longer wavelengths. The absorption and emission of photons in rare earth ions take place between different energy levels, specifically between different Stark levels. The resulting asymmetry of the fluorescence and absorption bands would not occur if all the Stark levels were equally populated.

The Stark split in glass materials varies depending on location of the ions and the field magnitude. This variation in Stark split energy provides for the spectral band in the absorption and fluorescence characteristics of rare earth ions. As a result, different condensed materials such as silica glass, fluoride glass and crystals show different spectral characteristics of absorption and emission of rare earth ions because of their different Stark split energy levels. In the next part of this chapter we will inspect features of different host materials.

2.2 Host materials

Materials for laser operation should have strong absorption bands and a reasonably high quantum efficiency for the fluorescent transition of interest. Such characteristics are generally shown by solids which contain a small amount of elements in which optical transitions can take place between states of inner, incomplete electron shells. Roughly, solid-state host materials may be grouped in crystalline solids and glasses. The host must have good optical, mechanical and thermal properties in order to resist the operating conditions of practical lasers. Desirable properties include hardness, chemical inertness, absence of internal strain and refractive index variation, and ease of fabrication. Several interactions between the host materials and the additive ions restrict the number of useful material combinations [2]. For rare earth doped crystals, the absorption and emission between Stark components of different levels usually can be observed at room temperature as discrete lines. In contrast, individual Stark transitions for glass hosts cannot be resolved. This difference is shown in Figure 2.3.

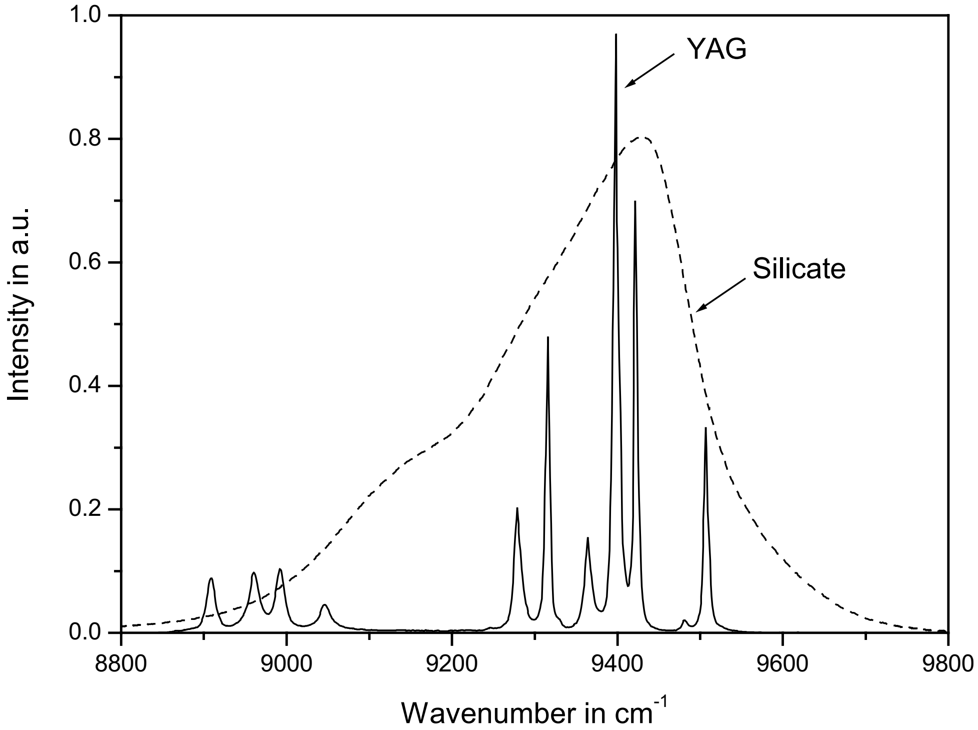

Figure 2.3: Comparison of the emission spectra for Nd^{3+}-doped YAG and silicate glass [10]

The spectra have been adjusted to fit the same scale in order to facilitate comparison. Crystalline hosts provide high intensity at nearly discrete wavelengths while glass hosts have lower intensities over a broad, continuous range of wavelengths. This is possible because of the disordered structure of glass; there are site-to-site variations in the local field acting on the laser ions in glasses which cause a range of Stark energy level splitting of ~50-10 cm^{-1}. It is in the same order of magnitude as the spacing between individual Stark levels; hence, optical transitions between Stark levels are poorly resolved for glasses at room temperature. The resultant inhomogeneously broadened optical transitions between the *J* states of rare earths may have total effective line widths of several hundred cm^{-1} and lasing can usually be obtained throughout this inhomogeneously broadened emission band. Therefore rare earth glass lasers offer some features not readily available in crystalline materials [11].

Both homogeneous and inhomogeneous processes are responsible for broadening the sharp line structure of the crystal into the broad spectrum seen for the glass. For a homogeneously broadened transition, radiation of a given wavelength will interact with all ions with equal probability. Thus, photons of any suitable pump wavelength will produce the same gain spectrum, and photons of any signal wavelength in the band can saturate it completely. If inhomogeneous broadening dominates, individual sections of the gain spectrum act independently and can be individually addressed by photons of different wavelengths. In a homogeneously broadened system, all the power can be extracted by a signal at any wavelength within the gain spectrum, and signals at different wavelengths can interact with each other by perturbing the gain spectrum. This leads to high efficiency for lasers and power amplifiers. Homogeneous line widths are more than an order of magnitude larger in glasses than in crystals, and inhomogeneous line widths are essentially independent of temperature [10]. Because of the obvious advantages of glasses we will describe these host materials in more detail.

Glasses are an important class of host materials for some of the rare earths. The practical advantages compared to crystalline materials are a comparatively easy fabrication and good optical quality. As already mentioned, laser ions placed in glass show a larger fluorescent linewidth than in crystals. On the other hand, glass has a much lower thermal conductivity than most crystalline hosts [2]. In general, if a liquid material is cooled down gradually, it crystallizes, expelling the specific latent heat at a characteristic temperature, that is, the melting temperature. However, some special materials do not crystallize below the melting temperature and their viscosity increases to such a high value that they become solid with a disordered arrangement of atoms, quite like that in the liquid state. Such a super cooled liquid is called glass. Therefore, glasses have only a short-range order and form a 3-dimensional matrix, but lack the uniformity, symmetry, and structure of a crystalline material, and they have no long-range periodicity. Glasses are in a state somewhere between a crystalline solid and a liquid.

Some oxides have the ability to form glasses by themselves. They are called glass network formers, e.g. SiO_2, GeO_2, B_2O_3 or P_2O_5. Network formers can form glasses not only by themselves but also in mixture with other network formers in many mixing ratios. They are all capable of forming a 3-dimensional network with oxygen, thus providing the very strong covalent bonds. On the other hand, some oxides, which are commonly called network modifiers, cannot form a glass by themselves but can form glasses in mixtures with network formers to a certain content. Oxides of alkali metals and alkali-earth metals such as Li_2O, Na_2O, K_2O are typical network modifiers. The structure of Na_2O-SiO_2 glass is shown in Figure 2.4a. Another group of oxides, e.g. TiO_2, Al_2O_3, ZrO_2 and BeO, have characteristics that fall between those of network formers and network modifiers. They are called intermediate oxides [7].

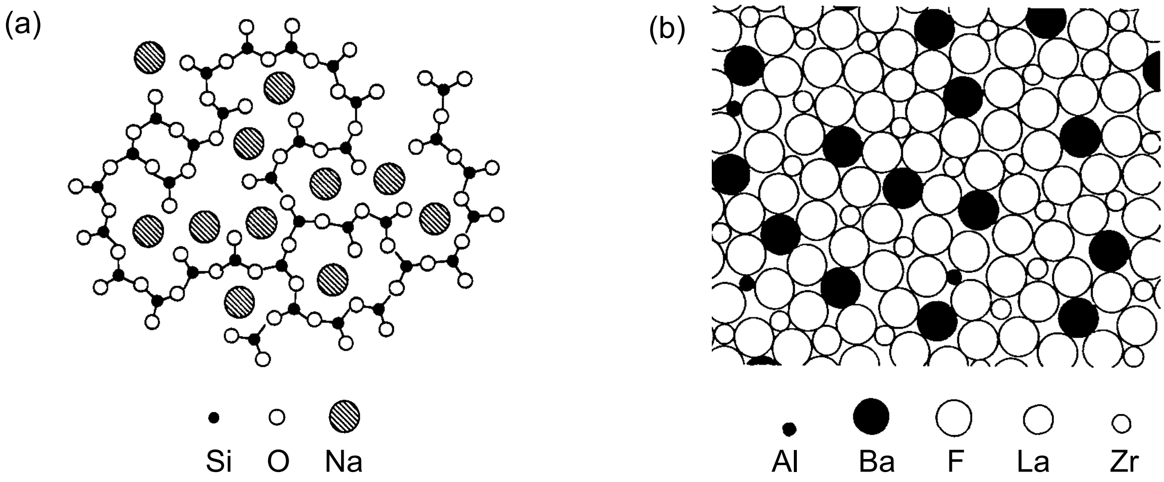

Figure 2.4: Schematic representation of the structure of: (a) Na_2O-SiO_2, (b) ZBLAN [7]

Heavy metal fluoride glasses (HMFG), based on zirconium fluoride (ZrF_4) and indium fluoride (InF_3), provide an interesting alternative to oxide glasses as rare earth hosts. The most stable HMFG is ZBLAN, made from the fluorides of zirconium, barium, lanthanum, aluminium, and sodium (Zr, Ba, La, Al, and Na) in the stochiometry 53:20:4:3:20 mol%, respectively. Here Zr and Al are network formers, La, usually an intermediate, plays here the role of a former, and Ba as well as Na are network modifiers. Figure 2.4b shows the structure model of ZBLAN glass. This glass is called a fluorozirconate glass because its major component is Zr. In contrast to oxide glasses, the bonding of HMFG is not covalent but ionic, and much weaker. This is the reason for a better infrared transparency.

At long wavelengths, the transparency of an optical material is limited by the existence of an infrared vibration or 'multiphonon' edge. Location and steepness of this edge in a multicomponent material, such as ZBLAN, are a complicated function of the effective charges, masses and interatomic bonding forces [12]. For sake of simplicity, a crude model for the stretching vibrations of individual cation-anion pairs in a substance will be given. Any such linear diatomic pair has a fundamental vibrational frequency v_0 which can be approximated by the relation:

$$v_o = (1/2\pi)(f/\mu)^{1/2}, \tag{2.3}$$

where f is the restoring force or force constant between the two ions of mass m_1 and m_2, and μ is the reduced mass defined by $m_1 m_2/(m_1+m_2)$. Photons, the frequency of which matches the fundamental vibration frequency, are strongly absorbed; the energy of absorbed photons increases the amplitude of the interatomic vibrations. At frequencies far away from the fundamental, there is little absorption and the material is highly transparent. From eq. (2.3) it is clear that the fundamental vibration frequency decreases (or alternatively, the corresponding wavelength increases; Table 2.2) with increasing reduced mass and with decreasing strength of the interatomic bond given by the force constant f. This constant is two times larger for silica glass than ZBLAN glass.

Table 2.2: Fundamental vibration frequencies (or wavelengths) for silica and ZBLAN [12]

Material	**Pair**	**Atomic mass**		**Fundamental vibrations**		***f***
		m_1	**m_2**	**cm^{-1}**	**µm**	**kg/s^2**
SiO_2	Si-O	28	16	1250 - 650	8 - 15	550
ZrF_4	Zr-F	91	19	600 - 400	17 - 25	230

In ZBLAN containing weakly bonded, heavy cations and anions, relatively low fundamental vibration frequencies are found. Consequently, materials such as ZBLAN have a high degree of transparency at wavelengths in the 2-5 µm infrared range. By contrast, the strongly bounded silicon-oxygen pair has higher frequency fundamental vibrations in the 8-15 µm range. As result, silica glass is transparent only up to ~3 µm, beyond which strong absorption occurs as shown on Figure 2.5.

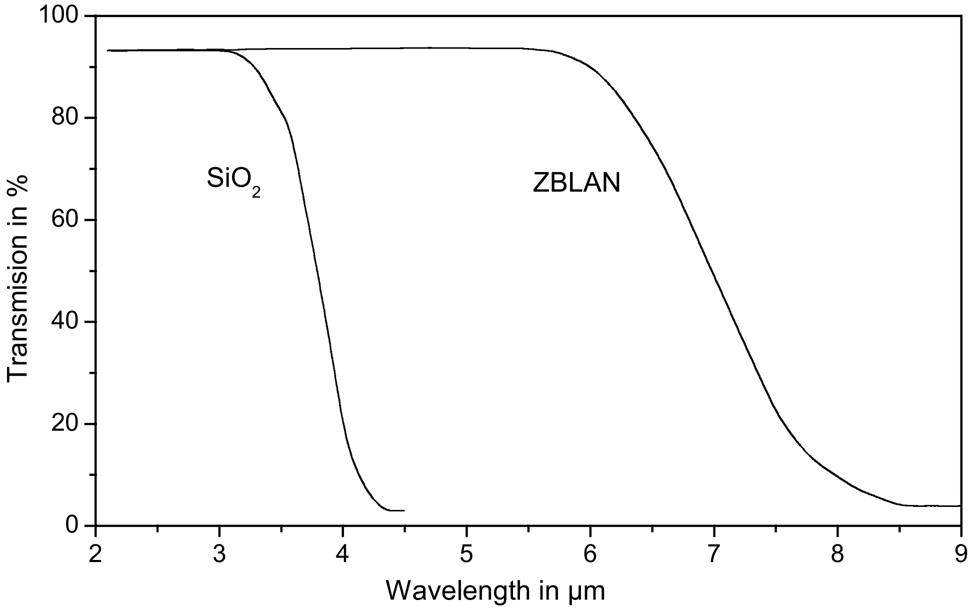

Figure 2.5: Infrared transmission spectra of silica and ZBLAN (thickness = 5 mm) [13]

In the disordered atomic arrangement characteristic of glass a large number of vibrational modes in addition to the fundamental can occur. The atoms in the structure have many degrees of freedom, and the bending or twisting motions of ionic pairs or other atomic structural groupings all absorb energy at wavelengths longer than that of the fundamental. Combinations of these modes with the fundamental vibration give rise to a continuous absorption spectrum. This causes high attenuation at long wavelengths and progressively lower attenuation as the wavelength becomes shorter. Another interesting feature of the ZBLAN glass is that it already contains rare earth ions (La^{3+}) as an integral component. La^{3+} can easily be substituted by an alternative rare earth ion without significantly affecting the properties of the glass. Doping up to 10 mol % is accepted by the fluoride framework [13]. In contrast, silica fiber is usually doped at less than 0.1 mol% [14]. If rare earth ions are incorporated in a silica glass network, the SiO_2 is distorted and does not well accept the doping ions which then tend to cluster. Therefore, SiO_2 can incorporate only very small amounts of rare earth dopants before microscopic clustering occurs and ion-ion interactions shorten the fluorescence lifetimes.

2.3 Nonradiative relaxation by the multiphonon emission process

Nonradiative relaxation caused by the multiphonon emission process greatly influences the radiative quantum efficiency of the transitions between the 4f states of rare earth ions. These phonons arise from the interaction of the electronic levels of the rare earth with vibrations of the host lattice. If the electronic states are spaced so closely that they can be bridged by one or more phonons, the transition will occur rapidly. This leads to thermal occupation of levels above the ground state or metastable states if the separations are in the order of the thermal energy. The ion undergoes a nonradiative transition to a lower electronic state through the emission of multiple phonons. If the nonradiative relaxation rate of a specific level is comparable to its radiative transmission rate, the efficiency of the luminescent process originating in that level is degraded. The lattice vibrations are quantized as phonons having excitation energies determined by the masses of the constituent ions and the binding energies between the ions which are extremely host dependent. If ΔE is the energy gap between two electronic levels, a number p_i of phonons, of energy $\hbar\omega_i$, is required for energy conservation; hence, the order of the process is determined by the condition [7]:

$$\sum p_i \hbar\omega = \Delta E \,. \tag{2.4}$$

The probability of such a transition decreases strongly with an increasing number of phonons needed. In materials with low phonon energy, the number of phonons required to bridge an energy gap is large, leading to a low multiphonon relaxation rate. The dependence of the multiphonon relaxation rates W_{mp} on the energy gap ΔE is expressed by [10]:

$$W_{mp} = C\left[n(T)+1\right]^{p} \exp\left(-\alpha\Delta E\right). \tag{2.5}$$

In this expression C and α are host dependent parameters, p is the number of photons required to bridge the energy gap and $n(T)$ is the Bose-Einstein occupation number for the effective phonon mode:

$$n(T) = \frac{1}{\exp(\hbar\omega / kT) - 1}, \tag{2.6}$$

where ω is the phonon angular frequency. In practice, C, α, and p are considered to be empirical parameters which are host dependent but insensitive to the rare earth ion and the energy levels involved. We see from the equation (2.5) that the multiphonon relaxation probability has a dependence which is approximately exponential on the energy gap between levels and decreases with decreasing temperature because of the temperature dependence contained in $n(T)$.

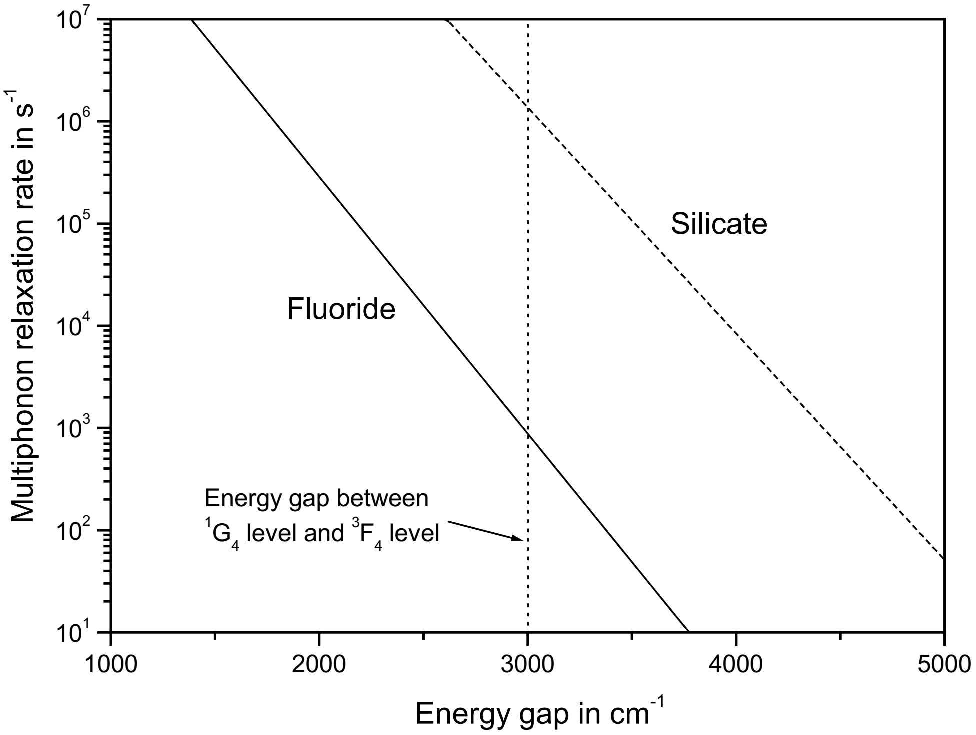

Figure 2.6: Energy gap dependence of multiphonon relaxation rate for silicate glass and fluoride glass [7]

Figure 2.6 shows the multiphonon relaxation rate as a function of the energy gap for silicate glass and fluoride glass. The energy gap between $^1G_4$ and neighbouring $^3F_4$ of Pr^{3+} was taken as an example for this consideration. In this case the energy gap is about 3000 cm^{-1}. The multiphonon relaxation rate in silicate glass is more than three orders of magnitude larger than in fluoride glass. These large differences originate mainly from the difference in phonon energies of the host glasses. The strong covalent bonds of silicate glasses result in a higher phonon energy (1100 cm^{-1}) compared to the weaker ionic bonds of fluoride glasses which lead to a much lower phonon energy (580 cm^{-1}). Owing to this lower phonon energy, more metastable levels are available in fluoride glasses. Therefore, many transitions that are laser-inactive in silicate glass can be active in fluoride glass. In silica the multiphonon relaxation rate is so high that any ion arriving in an upper level will undergo multiphonon emission before having a chance to show fluorescence. Only when the energy gap to the next lower level is larger than 4000-5000 cm^{-1} may a level in silica become fluorescent to any significant degree. By contrast, in fluoride glasses, where the phonon energy is smaller, an energy gap of only 2000-3000 cm^{-1} is needed before significant fluorescence decreasing occurs [9]. In addition this difference in multiphonon relaxation yields a better quantum efficiency for fluoride glasses in comparison to silica [15].

2.4 Ion-ion interaction

In the preceding discussions only isolated ions were considered. When the doping density of rare earth ions is increased, a level will be reached where the mean ion separation is sufficiently small to allow for a spatial migration of the excitation from one rare-earth ion to a neighbouring ion. The interaction range is typically of the order of 1-2 nm which corresponds to the mean distance between randomly distributed ions for concentrations of ~ 0.1 - 1 mol %. [15]. Such a transfer of excitation can be used to enhance the pumping of a laser transition and, thus, to increase the lasing efficiency. However, there are also situations where the presence of multi-ion phenomena can weaken the laser performance. In the following, different ion-ion interaction processes will be described in detail.

2.4.1 Energy transfer

The simplest case of energy transfer involves the transfer of energy from an excited ion to a nearby ion in its ground state without gain or loss of energy in the two-ion system as a whole. This is known as *resonant energy transfer* and is illustrated in Figure 2.7a. The activator ion (A) receives the energy from a nearby sensitizer (S). Also, *nonresonant energy transfer* can occur where the difference in energies between the initial and final ionic states is made up by the assistance of a photon or a phonon [5]. In the first case, one ion emits a photon which is then reabsorbed by another ion (Figure 2.7b). If the transition energies for the ions involved are not equal, absorption or emission of phonons becomes necessary in order to conserve energy. This process is schematically shown in Figure 2.7c.

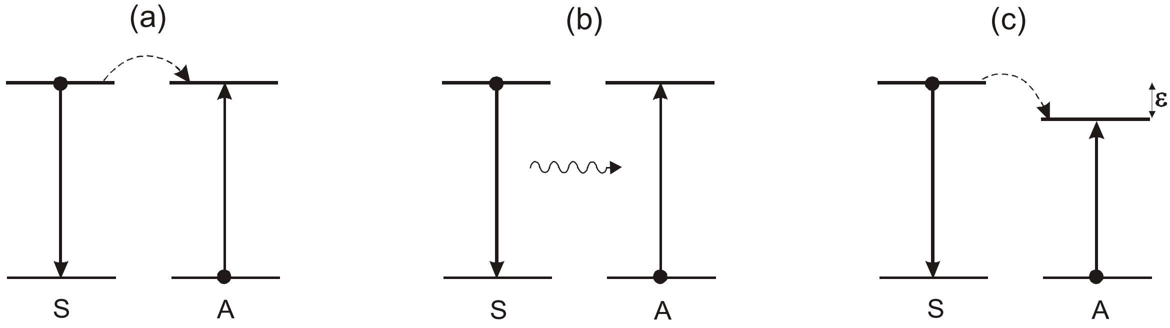

Figure 2.7: Ion-ion energy transfer mechanisms from a sensitizer (S) to an activator (A): (a) resonant energy transfer, (b) radiative transfer, (c) energy transfer assisted by phonons [16]

If energy transfer between two different kinds of ions takes place, the type of ion that is optically excited is referred to as the donor, and the one that receives the excitation is called the acceptor. The process can occur in a single step in which the particular donor ion that absorbs the pump photon transfers its energy to a nearby acceptor. If the donor concentration is high enough, another mechanism can occur: the migration of the excitation among the strong coupled donor ions (donor-donor transfer). This proceeds until the excitation reaches a donor which is close enough to an acceptor to complete the final step of the transfer process. This mechanism is commonly used for sensitising materials by using a large donor concentration (e.g. Yb^{3+}) in order to absorb the optical excitation and to transfer it to the activator (e.g. Pr^{3+}) if the latter has weekly or poorly placed absorption bands [10].

Processes which convert long-wave radiation into short-wave radiation by multiphoton mechanisms are called *upconversion* processes. Rare earth ions can be optically excited to several discrete energy states, each of which has a finite lifetime before decay occurs to a lower energy state. Therefore, energies of absorbed photons are added in the energy level scheme of a rare earth ion resulting in the population of a higher excited state than could be reached by one-photon absorption. The finite lifetimes can be usefully employed to allow for further interactions, e.g. the energy transfer to, or the absorption of a second photon. The general energy scheme related to the successive absorption of two photons is shown in Figure 2.8a.

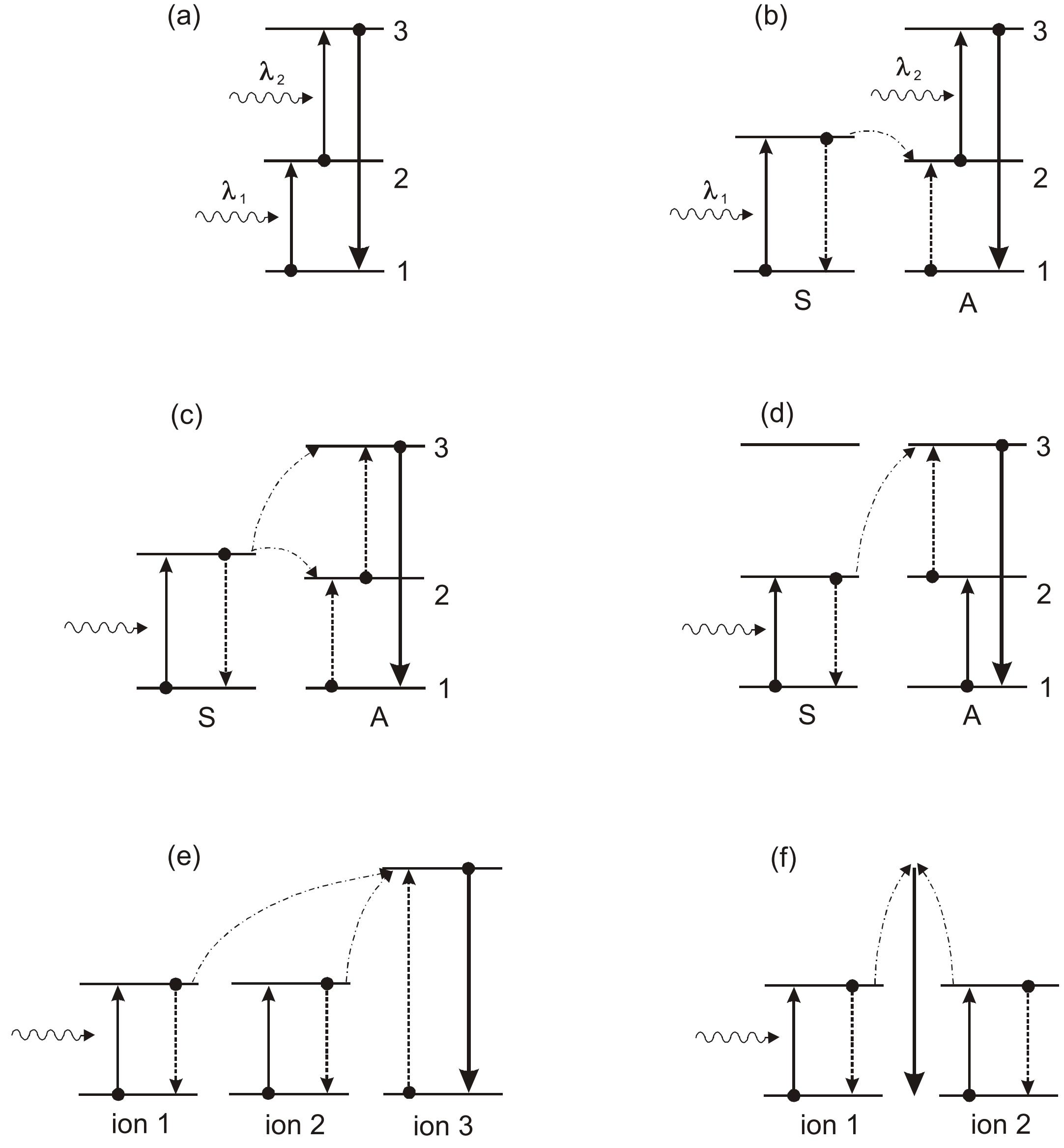

Figure 2.8: Schematic illustration of upconversion excitation mechanisms: (a) two-step absorption, (b) energy transfer followed by ESA, (c) successive energy transfers, (d) cross relaxation upconversion, (e) cooperative sensitization, (f) cooperative luminescence [17]

If a photon of wavelength λ_1 has an energy in resonance with the transition from the ground state 1 to the excited state 2, it is absorbed. This process is termed *ground state absorption (GSA).* After that, an incident photon with an energy resonant with the transition from state 2 to the higher excited state 3 may be absorbed by the previously excited ion. This process is known as *excited state absorption (ESA)*. It leads to an ion reaching a higher excited state. Again, the ion may be excited to a metastable level or to undergo decay to a lower level. Because of the broadening of rare earth ion transitions in glass at room temperature, overlapping GSA and ESA spectra are quite common. This may lead to a case, where only one pump wavelength is necessary ($\lambda_1 = \lambda_2$). In contrast, in rare earth doped crystals, rare earth absorption spectra are significantly less broadened, and it is much less likely that the GSA and ESA spectra overlap. Consequently, it is necessary to use two pump laser wavelengths, one resonant with the ground state absorption transition and the other resonant with the excited state absorption transition. Energy transfer can also occur between ions where both the sensitizer and activator ions are in one of their excited states. This allows for a possible fluorescence at a higher frequency than that of the excitation beam which is typical for upconversion processes. The different types of the energy transfer upconversion are schematised in Figure 2.8b-f. In Figure 2.8b the energy transfer between the sensitizer in its excited state and the activator in its ground state is presented. Activator is promoted to its excited state 2. Then ESA occurs from state 2 of the acceptor ion and is promoted to the higher excited state 3. This pumping process has an advantage: compared to pure ESA for most cases only one pump beam is necessary.

The next process shown in Figure 2.8c is called *successive energy transfer*. In this case, only the sensitizer ion may absorb photons. After that, the activator ion is promoted to its excited state 2 by a first energy transfer, and then it is promoted to its excited state 3 by a second energy transfer. Figure 2.8d depicts schematically the case which might be named *cross relaxation upconversion*. Indeed, *cross relaxation* usually refers to all types of energy transfers occurring between identical ions. If the sensitizer and the activator are identical ions, photons are absorbed both by the sensitizer and by the activator leading to these two ions reaching their excited state 2. Then, an energy transfer promotes the activator ion to its state 3 while the sensitizer goes down to a lower energy state. For the three cases b, c, and d, further energy transfers from the sensitizer to the activator may occur and populate higher energy levels of the activator [17].

If more than one centre is involved in the elementary process of sensitization or luminescence, one may speak of *cooperative effects*. Figure 2.8e shows the case of *cooperative sensitization*. Here, the energy accumulated by two excited ions is transferred to another ion which reaches a higher excited state from which it can relax to the ground state. When the process starts, ions 1 and 2 are in their excited states and ion 3 is in its ground state. The final state is reached when ions 1 and 2 are in their ground states and ion 3 is in its excited state. Conservation of energy requires that the photon emitted by ion 3 must carry the cumulated energy of the two photons absorbed by ions 1 and 2. If two excited interacting ions cause in a single process the emission of a photon, one speaks of *cooperative luminescence* [18] which is shown in Figure 2.8f.

2.4.2 Photon avalanche

The phenomenon called *photon avalanche* is shown in Figure 2.9. This is an unconventional pumping mechanism because it may lead to strong upconverted emissions from level 3 without any resonant ground state absorption. The pump wavelength is only resonant between a metastable state 2 and a higher energy level 3. This is the first characteristic of the photon avalanche process.

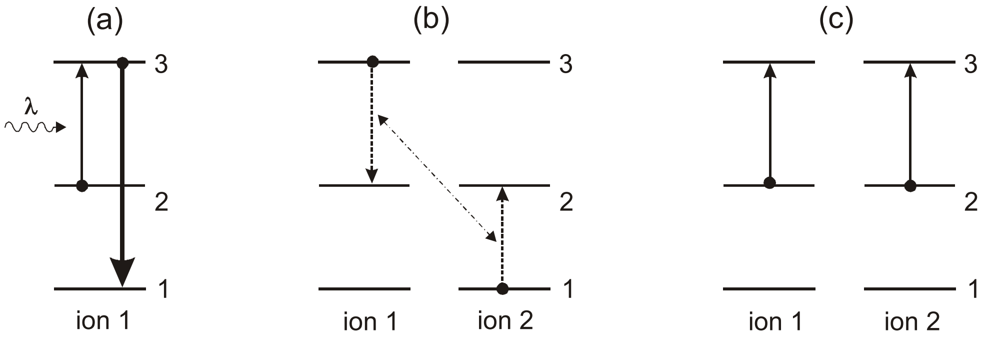

Figure 2.9: Energy scheme for the simplest photon avalanche process [17]

As all ions are initially in the ground state 1 (no thermal population of level 2), the effect of the pump is minimal. If an ion is promoted to the metastable state 2, it may be further excited to level 3 by absorption of a pump photon, regardless of the mechanism of population of this state. Then, the cross relaxation excites this ion as well as one of its neighbours in the metastable level 2 (Figure 2.9b). Now two ions are available for further ESA of the pump light. In the following, by the same feeding process, four ions will be in this metastable state. Thus, this process causes doubling of the population of level 2, and in the following, the number of ions in this level grows like an avalanche. The characteristic feature of an avalanche process is an excitation power threshold which clearly separates two different regimes. Below the threshold, the intensity of the upconverted fluorescence is weak and the doped material is transparent to the pump; above the threshold, the fluorescence increases by orders of magnitude and the pump light is strongly absorbed; it is a so-called *self-induced absorption* [17]. In addition, when the pump light is turned on, fluorescence builds up slowly on a time scale that is much longer than any of the lifetimes of the metastable states. Therefore, there is a noticeable delay between the onset of the pump power and the maximum of the fluorescence, and with increasing pump intensity this delay decreases [19, 20].

2.4.3 Upconversion pumping process in Pr^{3+}-doped glass

In a conventional optically pumped laser, the photon energy of the pump light is higher than that of the laser photons, and the absorption of one photon by an active ion is sufficient to excite the upper laser level. Upconversion lasers represent a class of optically pumped lasers that operate at wavelengths shorter than that of the pump laser. But, on the other hand, more than one pump photon is required to provide sufficient energy for the excitation of one laser ion. Using this non-linear excitation process, such lasers can convert infrared pump radiation from semiconductor diode lasers to a visible laser output. The operation of a number of such upconversion lasers has been demonstrated using rare-earth ions doped into crystals and glasses. Upconversion lasers can potentially provide practical all-solid state sources with output wavelengths from the ultraviolet to the infrared [20]. As already mentioned, lifetimes for many levels in fluoride glasses are longer than in other glass hosts, and this offers the possibility for realizing upconversion lasers. The longer lifetimes allow for a greater probability for two-photon (or more) absorption, e.g. IR to UV lasers become more feasible.

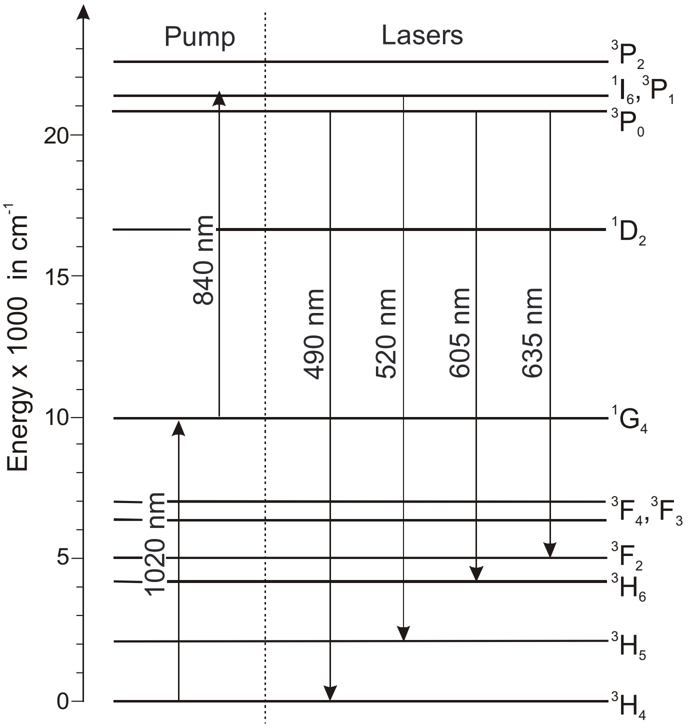

Figure 2.10: Energy level diagram for Pr^{3+}- doped ZBLAN glass with laser transitions

Praseodymium is a very interesting doping ion because it offers laser transitions in the blue, green, orange, and red using the same pumping scheme. Emission in the visible occurs with transitions originating from the $^3P_0$, $^3P_1$, and $^1I_6$ levels as shown in Figure 2.10. For simplicity, and because of the quasi perfect energy match between $^3P_1$ and $^1I_6$, these two levels will be collectively referred to as $^3P_1$ level in the further discussions, and all of the three levels ($^3P_0$, $^3P_1$, and $^1I_6$) will be addressed as ^3P_J. Owing to the small energy difference of ~600 cm^{-1} between $^3P_0$ and $^3P_1$ [21], these levels are thermally coupled following a Boltzmann distribution law, so that the population of $^3P_1$ is 5 % of the population of $^3P_0$ at ambient temperature. The lifetime of the $^3P_1$- and $^3P_0$-coupled manifold of Pr^{3+} in ZBLAN has been reported to be in the range of 39-47 μs depending on the concentration of the ions [22]. Therefore, we can treat it as a metastable level. In contrast to ZBLAN, $^3P_0$ is not metastable in silica because of non-radiative emission. However, a weak fluorescence from this level has been observed [23].

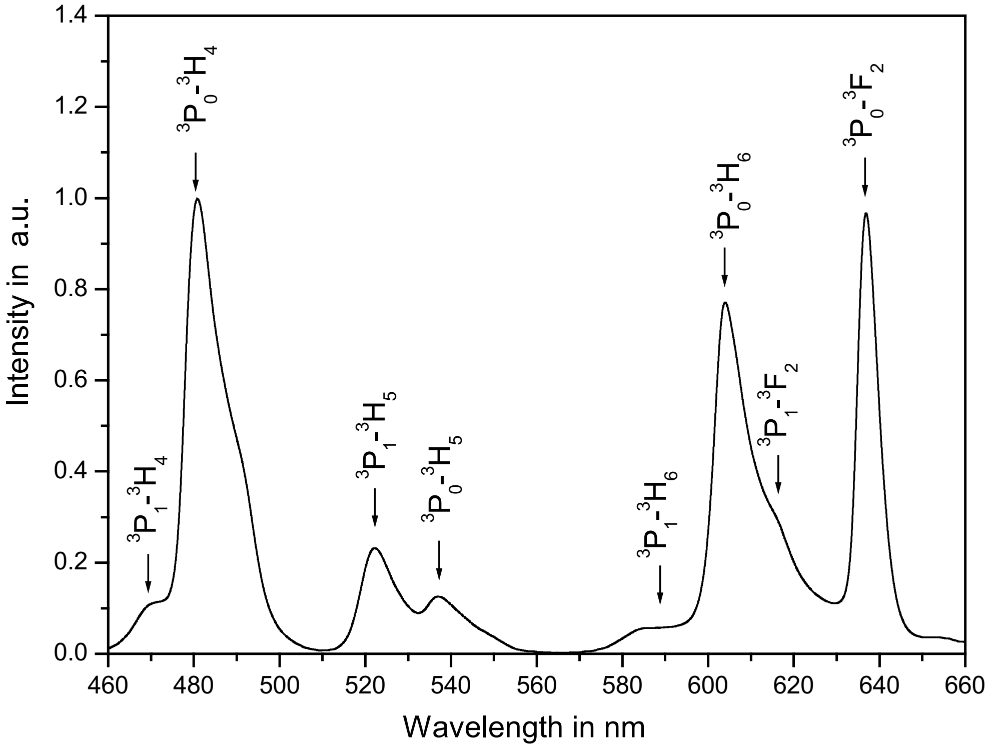

Figure 2.11: Fluorescence spectrum of Pr^{3+} in ZBLAN under excitation at 458 nm

In Figure 2.11, an emission spectrum of a ZBLAN glass sample doped with 3 mol% Pr^{3+} is shown together with the transition responsible for the fluorescent bands. The spectrum has been corrected for the spectral response of the detection system. The glass sample was pumped by the 458 nm line from an argon laser corresponding to absorption into the high energy side of the $^3P_1$ level. The $^3P_0$ level is also populated due to a non-radiative transition from the $^3P_1$ level. The 490, 605, 635 nm transitions all originate from the $^3P_0$ level and terminate in the $^3H_4$, $^3H_6$, $^3F_2$ and $^3F_4$ levels, respectively (see Figure 2.10). The 520 nm transition originates from the $^3P_1$ level and terminates in the $^3H_5$ state. Despite the fact that at room temperature only ~5 % of the population of the $^3P_1$- and $^3P_0$-coupled manifold resides in the $^3P_1$ level, the $^3P_1 \rightarrow {}^3H_5$ transition dominates the $^3P_0 \rightarrow {}^3H_5$ transition, centered at ~540 nm, because the latter is nominally forbidden and, therefore, much weaker [10, 40]. Each emission from $^3P_0$ is accompanied by the corresponding blue-shifted emission from $^3P_1$. The $^3P_1 \rightarrow {}^3F_2$ emission may be present under the tail of the $^3P_0 \rightarrow {}^3H_6$ band [21]. All these terminal levels lay close together, and therefore, they depopulate rapidly to the ground state by nonradiative relaxations. The radiative branching ratio from $^3P_0$ to $^1D_2$ is very low (a few percent at most), and hardly any of the visible emissions from Pr^{3+}-doped glass originates from $^1D_2$ if an argon laser is used for excitation [22].

For population of the ^3P_J levels the upconversion processes can also be used. Two-step absorption is an interesting alternative to an argon laser pump. It is not possible to pump these high levels by a single infrared pump source, because the energy levels are not suitably placed. An upconversion process is realized through two infrared excitations at different wavelengths, as shown in Figure 2.10. The pump light at 1020 nm excites the ions from the ground state to an intermediate level, $^1G_4$. This is a metastable level with a lifetime of about 100 μs [24]. This time span is long enough for further excitation of these ions to the upper levels, $^1I_6$, $^3P_1$ and $^3P_0$, by absorbing photons at 840 nm, the latter two by nonradiative relaxation [25, 26]. Most (96 %) of the oscillator strengths in these excited state absorption steps resides in the $^1G_4 \rightarrow {}^1I_6$ transition [27]. Finally, the Pr^{3+} ion decays from levels ^3P_J to other levels of smaller energies emitting light at various wavelengths. The great attraction of pumping at infrared wavelengths is that high power laser diodes are available, and so it is possible to construct an efficient and compact laser. The described pumping scheme is again ineffective in silica glass due to the small energy gap between $^1G_4$ and the next closest level $^3F_4$ ($\Delta E \approx 2800$ cm^{-1} [28]) and also due to a large phonon energy. The $^1G_4$ level in silica is strongly depopulated by multiphonon relaxation. On the other hand, the transition $^1G_4 \rightarrow {}^3H_5$ is of particular importance for optical telecommunication. Fiber amplifier working at 1.3 μm utilizes this transition, and only host glass with low phonon energy such as fluoride glasses assures proper operation of this amplifier. Therefore, the amplifier based on a silica glass has a poor efficiency.

It is possible to obtain a laser transition from ^3P_J levels by pumping only at one wavelength, but in this case the glass sample has to be co-doped with a sensitizer ion. Ytterbium is often used as a sensitizer for other rare earth lasers because of several useful properties. It has a very broad energy level which absorbs strongly in the region covered by high power GaAs laser diodes. The broad absorption band permits a wide pump wavelength range for activating the Yb^{3+}. This has a great practical importance, because a sophisticated temperature control of the diodes to suppress frequency changes is not needed. The Yb^{3+} ion has only one energy level above the ground state (see Figure 2.12). Consequently, it neither suffers from unwanted upconversion due to energy transfer within its own system, whatever the concentration quenching, nor the excited state absorption. The broad excited state overlaps with a range of energy levels in other rare earths where direct diode pumping is not possible. Thus, coupled with the long lifetime of its single excited state (1.7 ms in ZBLAN [29]), Yb^{3+} is a good sensitizer for transferring energy to nearly matched levels in other ions [30]. Isolated Yb^{3+} ions cannot transfer their energy, which is therefore lost. The Yb^{3+} concentration has to be relatively high to ensure a high probability of close nearness to a Pr^{3+} ion. The energy of Yb^{3+} can now migrate (by energy transfer) to a Pr^{3+} ion. Usually, a sufficiently high concentration of Yb^{3+} to obtain an efficient energy transfer is 2 % [31].

Several pumping paths are possible to excite the Pr^{3+} ion from the ground state to ^3P_J levels by co-doping it with Yb^{3+} ions. Weak absorption of the 840 nm pump in the short wavelength wing of the Yb^{3+} absorption band populates the $^2F_{5/2}$ level of Yb^{3+} as shown in Figure 2.12. The wing of the Yb^{3+} absorption band can extends to 800 nm at high Yb^{3+} concentrations [32].

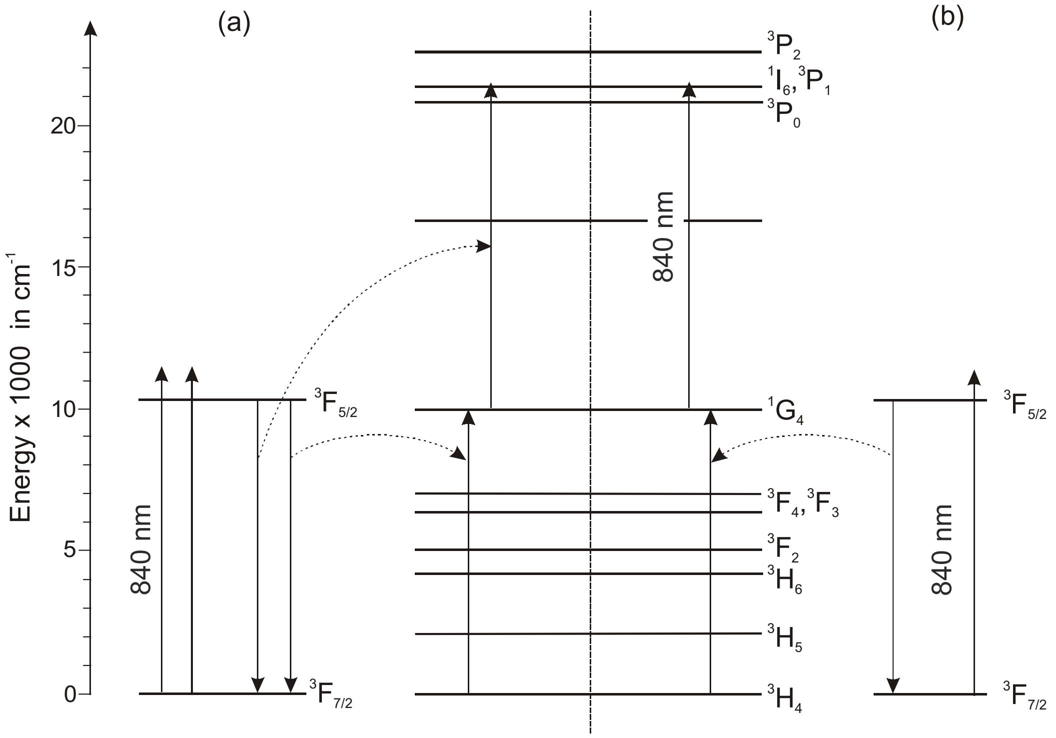

Figure 2.12: Upconversion pumping process for visible lasers in Pr^{3+}/Yb^{3+} co-doped ZBLAN glass: (a) two successive energy transfers, (b) the energy transfer followed by ESA

The energy transfer from an excited Yb^{3+} ion to a neighboring Pr^{3+} ion residing in the ground state results in a simultaneous occurrence of the transition, the Yb^{3+} ion relaxes to its ground state and, a Pr^{3+} ion is excited to the intermediate level:

$$Yb^{3+}\ (^2F_{5/2}),\ Pr^{3+}\ (^3H_4) \rightarrow Yb^{3+}\ (^2F_{7/2}),\ Pr^{3+}\ (^1G_4). \qquad (2.7)$$

There are two mechanisms possible for Pr^{3+} ions in the $^1G_4$ level to be promoted to the ^3P_J level. The first is that the next energy transfer occurs. As a result, an Yb^{3+} ion in the excited level decays to the ground state and simultaneously a Pr^{3+} ion in the intermediate level is promoted to the high lying ^3P_J levels (see Figure 2.12a):

$$Yb^{3+}\ (^2F_{5/2}),\ Pr^{3+}\ (^1G_4) \rightarrow Yb^{3+}\ (^2F_{7/2}),\ Pr^{3+}\ (^3P_J) \qquad (2.8)$$

The second mechanism possible is the excited state absorption which excites the Pr^{3+} ion from the $^1G_4$ level to the ^3P_J levels (see Figure 2.12b). Then these excited ions relax to lower states and emit photons at various wavelengths [33]. The question arises which step of the upconversion process is more likely, the second energy transfer or the excited state absorption. There are some indications in favour of the excited state absorption being the dominant process. First, as the pump wavelength was varied, local maxima in the pumping efficiency of the red transition around 840 nm were observed which corresponded to the $^1G_4 \rightarrow {}^3P_1$ transition. Another maximum of the upconverted light around 900 nm has been observed which can be attributed to the $^1G_4 \rightarrow {}^3P_0$ transition. If the ^3P_J excitation were due to the energy transfer, these resonances should not exist. Secondly, only Yb^{3+} ions in the higherlaying Stark sublevels of the $^2F_{5/2}$ level have sufficient energy to excite the Pr^{3+} $^1G_4 \rightarrow {}^3P_0$ transition by the energy transfer. However, at room temperature, intra-Stark relaxation processes (thermalisation via phonons) implies that the Boltzmann distribution of $^2F_{5/2}$ is reached well before the energy transfer can occur. This leads to negligible population in these higher-lying Stark sublevels so that the contribution of the energy transfer for an excitation of ^3P_J can be neglected, and the excited state absorption is dominant [10, 34]. However the Yb^{3+} absorption at 840 nm is very weak and both pumping paths have low efficiency.

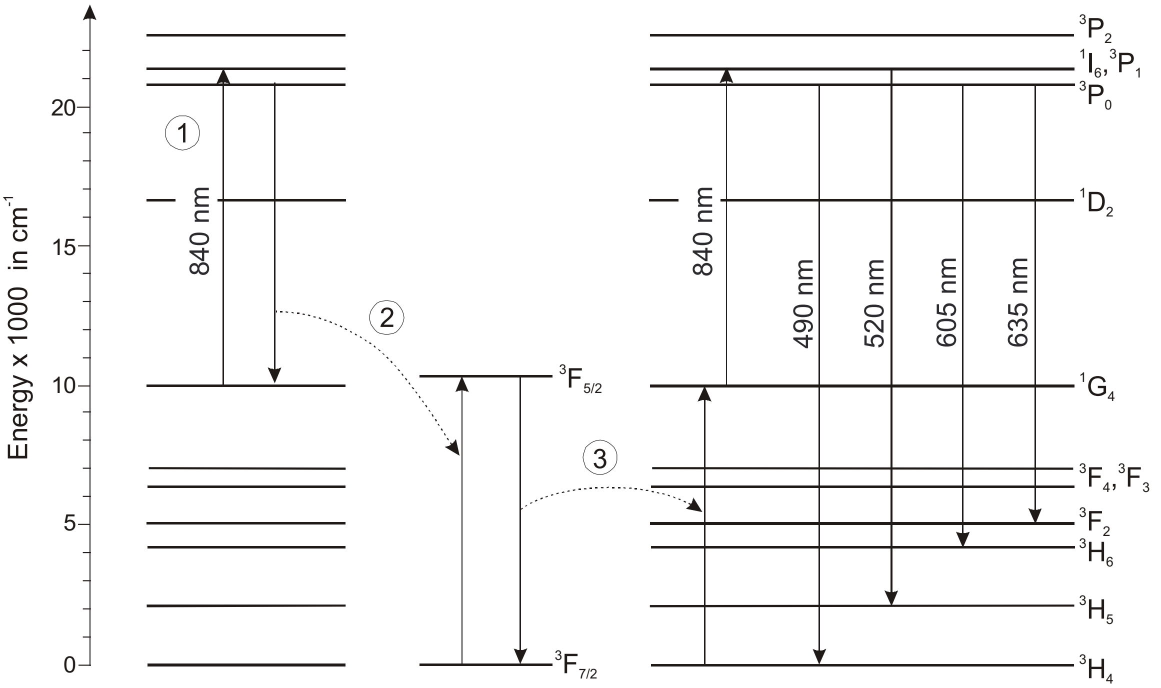

Figure 2.13: Photon avalanche upconversion in Pr^{3+}/Yb^{3+} co-doped ZBLAN glass [34, 35]

A third possible upconversion pumping mechanism is a photon avalanche upconversion which is summarized in Figure 2.13. The three steps of the excitation process are marked with numbers. At the beginning a pump photon is absorbed by an excited Pr^{3+} ion, and this ion is promoted from an intermediate state $^1G_4$ to the group of levels ^3P_J (step 1). This excited state absorption is followed by a cross relaxation from the Pr^{3+} ion to a nearby Yb^{3+} ion, raising the Yb^{3+} ion into an excited state and leaving Pr^{3+} in the intermediate level (step 2):

$$Pr^{3+}\ ({}^3P_J),\ Yb^{3+}\ ({}^2F_{7/2}) \rightarrow Pr^{3+}\ ({}^1G_4),\ Yb^{3+}\ ({}^2F_{5/2}). \qquad (2.9)$$

Subsequently, the Yb^{3+} ion can transfer its energy to another Pr^{3+} ion nearby, the Yb^{3+} relaxes to its ground state exciting a Pr^{3+} ion from its ground state to the intermediate level (step 3):

$$Yb^{3+}\ ({}^2F_{5/2}),\ Pr^{3+}\ ({}^3H_4) \rightarrow Yb^{3+}\ ({}^2F_{7/2}),\ Pr^{3+}\ ({}^1G_4). \qquad (2.10)$$

This excitation closes the pumping cycle in the Pr^{3+}/Yb^{3+} system. After each cycle, the number of ions excited to the $^1G_4$ state of Pr^{3+} are doubled. Therefore, this pumping scheme is called an avalanche process [36, 37].

Because the typical dopant concentration of Pr^{3+} and Yb^{3+} ions used in visible laser applications are about 0.3 % and 2 %, respectively, it is unlikely that any given Yb^{3+} will be located near two Pr^{3+} ions, assuming the doping to be spatially uniform. Generally, the energy from an excited Yb^{3+} ion may migrate through one or more nearby Yb^{3+} ions until a Yb^{3+} ion that lies near a Pr^{3+} ion is excited, at which point a Yb^{3+}-Pr^{3+} interaction can take place [10].

Although the photon avalanche upconversion process seems to be a very complicated one and therefore, minimally probable, there are many indications that, in reality, this is the dominant process in a Pr^{3+}/Yb^{3+} doped glass among the processes presented here. An important argument is the existence of a critical pump power. After reaching a threshold pump power, a considerably intense fluorescence is observed, and this is a typical feature of an avalanche process. Additionally, a self-induced absorption has also been observed [38]. Experimental results which confirmed a dominant role of the photon avalanche upconversion in the pumping process will be shown in the chapter 5.2.7.

3 Spectroscopic properties of doped glasses

Knowledge of the spectroscopic properties of rare earth ions doped in glasses is mandatory for predicting the characteristics of rare earth doped lasers and amplifiers or to understand the limitations of device efficiency. Laser performance depends strongly on the absorption and emission properties of the dopant in the host glass system; therefore, measuring these properties is helpful for finding an optimal host glass. Additionally, the lifetimes of the individual energy levels determine the efficiency of the pumping and laser transitions. In this chapter, transition cross-sections and lifetime measurements on Pr^{3+}-doped fluoride glasses will be presented.

3.1 Transition cross-section

Cross-sections quantify the ability of an ion to absorb and emit light. The cross-section of a particular transition between two states of an ion represents the probability for that transition to occur with the concurrent emission or absorption of light. Given two states, 1 and 2, with respective energies E_1 and E_2 (E_1 less than E_2), the transition probability for the absorption of a photon of energy E_2-E_1 is proportional to the cross-section σ_{12} and that for the emission of a photon is proportional to the emission cross-section σ_{21}. The dimension of the cross-section is an area. The absorption cross-section can be thought of as a sort of target area that can intercept a light flux by catching the photons that flow through it. The emission probability has an analogous interpretation. It should be noted that the emission and absorption probabilities are proportional to the light intensity, not to its power. The smaller the area on which the light is concentrated, the higher the probability for emission or absorption of light [5].

For two non-degenerate states 1 and 2, the absorption and emission cross-sections will be equal: $\sigma_{12} = \sigma_{21}$. Complications arise in the case of rare earth ions in solids because the absorption and emission cross-sections are different. The reason for this lies in the fact that, in case of rare earth ions, these two states are in reality a set of Stark sublevels that are populated to various degrees depending on the thermal distribution. The cross-section is then meant to specify the cross-section at a particular frequency within the spectral bandwidth of the transition.

The spectral shape of emission and absorption cross-section for transitions between two manifolds will be different since they depend on the thermal population in the various sublevels. The emission and absorption cross-section, at a particular frequency, are equal only if the various sublevels are equally populated, or if the transition strengths between any of the individual sublevels are all equal [39]. The cross-sections that are derived from an experiment yield the effective spectral absorption and emission strength for a given ion's transition which is usually needed to actually model and predict the performance of a laser. The key issue is how to correctly extract the emission and absorption cross-section from measured absorption and fluorescence spectra.

We will examine absorption and emission of light in a degenerate two-level system, where level 1 has degeneracy g_1 and level 2 has degeneracy g_2. The transition lines have a finite linewidth and are characterized by a normalized lineshape function $g_{ij}(v)$. The absorption cross-section at a frequency v is defined for a broadened line as [5]:

$$\sigma_{12}(v)=\frac{hvn}{c}B_{12}g_{12}(v)=\frac{h}{\lambda}B_{12}g_{12}(v), \tag{3.1}$$

where B_{12} is the coupling constant of radiation and matter for the absorption process and n is the refractive index of the medium. Similarly for the emission cross-section:

$$\sigma_{21}(v)=\frac{hvn}{c}B_{21}g_{21}(v)=\frac{h}{\lambda}B_{21}g_{21}(v), \tag{3.2}$$

where B_{21} is the coupling constant for the stimulated emission process. The transition lineshape function $g_{ij}(v)$ is normalized by the equation:

$$\int g_{ij}(v)\,dv=1, \tag{3.3}$$

where the integral spans the full spectrum of the transition line.

Furthermore, if we insert equation (1.13) into (3.2), we get formulas called the Fuchtbauer-Ladenburg equations [39, 40]. The absorption and emission cross-section may be written as follows:

$$\sigma_{12}(v)=\frac{g_2}{g_1}\frac{\lambda^2}{8\pi n^2}A_{21}g_{12}(v), \tag{3.4}$$

$$\sigma_{21}(v)=\frac{c^2}{8\pi n^2 v^2}A_{21}g_{21}(v). \tag{3.5}$$

The peak wavelength of the transition is λ. This last equation allows a normalized emission spectrum $g_{21}(v)$ to be scaled to the spectral emission cross-section by the use of the calculated emission rate A_{21}. This is very important, because absolute emission spectra are difficult to obtain. The analogue equation for the absorption cross-section is less useful, since the absorption cross-section can be measured exactly by spectral attenuation measurement in a known length of material.

The McCumber theory provides another method of transformation between the absorption and emission cross-section. The key assumption needed by the McCumber theory is that the time required to establish thermal distribution within each manifold is shorter compared to the lifetime of that manifold. The absorption cross-section is related to the emission cross-section by [41]:

$$\sigma_{21}(v)=\sigma_{12}(v)\exp[(\varepsilon-hv)/kT], \tag{3.6}$$

where ε is the temperature-dependent excitation energy. The physical interpretation of ε is the net free energy required to excite a rare earth ion from the ground state to an excited state at temperature T [7]. This equation implies that the emission and absorption cross-sections are equal only at one frequency ($\nu_c = \varepsilon/h$). At frequencies higher than the crossing point (shorter wavelengths), the absorption cross-section is larger than the emission cross-section, and at lower frequencies (longer wavelengths), the emission cross-section is larger. Another important characteristic of eq. (3.6) is that even a relative measurement of the spectrum of either cross-section is sufficient to generate a relative spectrum of the other cross-section. The McCumber theory was verified experimentally, in particular for Er^{3+}, and led to good agreement [42]. Figure 3.1 shows the measured and calculated cross-sections for the Er^{3+} $^4I_{15/2}\rightarrow{}^4I_{13/2}$ transition. The principal disadvantage of a McCumber analysis is that ε is related to the partition function and can be calculated only if the positions of all the Stark levels are known for both manifolds.

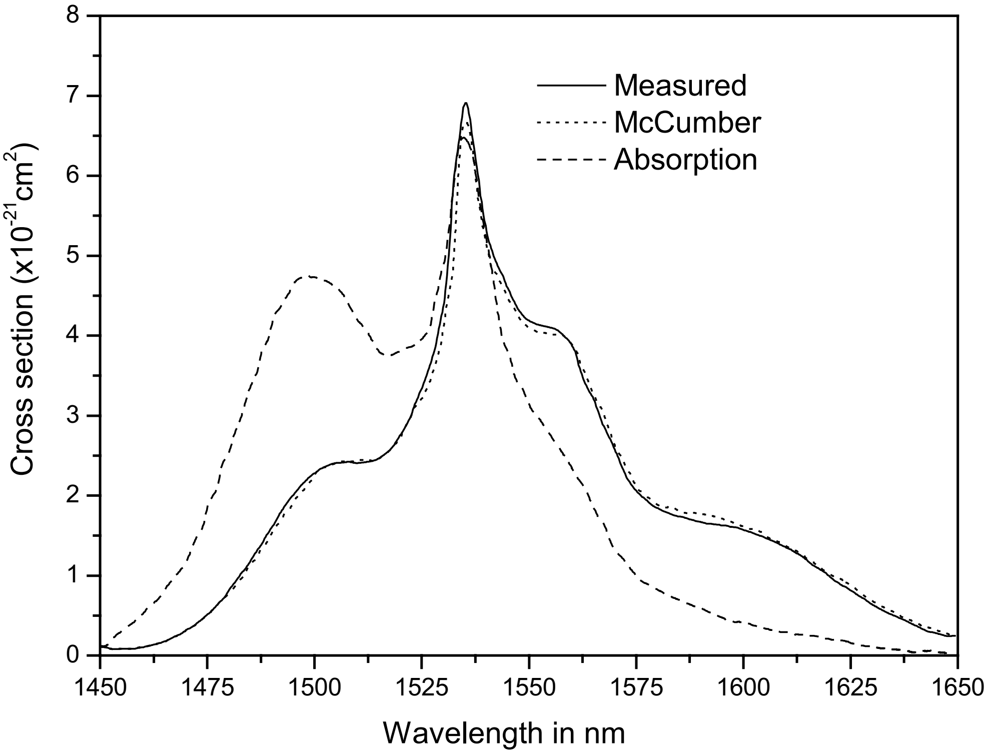

Figure 3.1: Comparison of the shape of the measured emission cross-section with that calculated from the absorption cross-section using the McCumber theory [42]

The integrated intensities of transitions of rare earth ions can be also obtained using the Judd-Ofelt theory [43, 44]. The intensity of a transition between two states is often characterized by its oscillator strength. The electric dipole contribution to the oscillator strength for a transition between levels i and j is given in the Judd-Ofeld theory as [45]:

$$f_{ij} = \frac{8\pi^2 m_e \nu \chi_{ed}}{3h(2J+1)} \sum_{t=2,4,6} \Omega_t \left| \left\langle i \left\| U^{(t)} \right\| j \right\rangle \right|^2, \tag{3.7}$$

where m_e is the electron mass, J is the angular momentum of the initial level in the transition, and $\chi_{ed}=(n^2+2)^2/9n$ is the Lorenz local field correction factor for the absorption. The three terms $< i \,||U^{(t)}||\, j >$ are the reduced matrix elements calculated in the intermediate coupling approximation. The Judd-Ofelt parameters Ω_2, Ω_4, Ω_6 are material parameters. They parameterize the oscillator strength for the transition between various multiples. The Ω_t are usually calculated to provide the best fit to the experimental data obtained by ground state absorption. The whole procedure is described in [40]. These three parameters are then used to calculate the electric dipole oscillator strength between any states and lead, for example, to the values of excited state absorptions or stimulated emission cross-sections. Except for the case of the so-called hypersensitive transitions, this is a good phenomenological model. The Judd-Ofelt analysis is accurate to about 10-15 %, although errors on the order of 50 % are found in certain cases.

From the oscillator strength one can calculate the transition rates for spontaneous radiative transition from an initial manifold i to a final manifold j using the following equation [46, 47]:

$$A_{ij} = \frac{2\pi v^2 e^2}{\varepsilon_0 m_e c^3} f_{ij}, \tag{3.8}$$

where ε_0 is the dielectric constant, and e is the electron charge. The radiative lifetime of an excited level is obtained from the sum of all transition probabilities:

$$\tau_i = \frac{1}{\sum_j A_{ij}}. \tag{3.9}$$

The luminescence branching ratios β are calculated according to the formula:

$$\beta_{ij} = \frac{A_{ij}}{\sum_j A_{ij}} = A_{ij} \cdot \tau_i, \tag{3.10}$$

which indicates relative intensities of transition from an excited level to all terminated levels. The branching ratio has an important influence on the performance of a device based on a particular transition. It has a significant effect on the threshold of a laser.

Although the Judd-Ofelt theory is successful for most rare earth doped materials, it is well known that its application to Pr^{3+} suffers from several problems. First, large deviations between calculation and experimental data are observed, and a difficulty to fit the $^3H_4 \rightarrow {}^3P_2$ hypersensitive transition is noticed. Moreover, a negative Ω_2 is sometimes obtained, a case which is impossible within the framework of the Judd-Ofelt theory [48]. The explanation for the inconsistent behaviour of Pr^{3+} is that an approximation made in the general case of the Judd-Ofelt theory is not valid for the praseodymium ion. This approximation states that the perturbing configurations of the outermost 5d electrons are degenerated and of much higher energy than the f-f transitions being considered, an approximation which is not completely valid for Pr^{3+}. In a CaF_2 host, for example, the first 4f-5d absorption of Pr^{3+} is located at an energy of about 45 000 cm^{-1} while, for any other lanthanides, it is at least 10 000 cm^{-1} higher in energy, thereby suggesting that a mixing effect may be significant [46]. Several authors proposed methods to improve the reliability of the Judd-Ofelt parameters for Pr^{3+} [45, 48, 49].

3.2 The glass samples

The samples investigated were Pr^{3+}-doped fluoride glasses, sometimes co-doped with Yb^{3+}. Beside the ZBLAN glass, already mentioned in chapter 2, spectroscopic measurements were also realized for another heavy metal fluoride glass called IBZP. This glass belongs to the family of fluoroindate glasses, and its name is an acronym built from the first letters of its main components. This compound shows very good optical quality, and it is very stable against atmospheric moisture. In addition, the fluoroindate glasses are characterized by a lower value of the phonon energy (~510 cm^{-1}) than conventional fluorozirconate glasses (~580 cm^{-1}) [50]. Therefore, fluoroindate glasses are more transparent in the infrared than fluorozirconates, and they can be used as a base for the design of efficient lasers.

The composition of both glasses in mol % used in spectroscopic experiments was as follows:

ZBLAN: 53 ZrF_4 - 20 BaF_2 - (3.875-x) LaF_3 - 3 AlF_3 - 17 NaF - 0.125 InF_3 - 2.5 PbF_2- xPrF_3,

IBZP: (28-x) InF_3 - 14 BaF_2 - 20 ZnF_2 - 16 PbF_2 - 5 YF_3 -7 AlF_3 - 2LiF - 8NaF - xPrF_3.

In the case of doped ZBLAN glass, LaF_3 was replaced with PrF_3 and YbF_3. For an IBZP glass, InF_3 was substituted by PrF_3. The molar concentration *p* and dimensions of the glass probes investigated are presented in Table 3.1. The geometrical dimensions are the main values of three measurements at different positions, and their uncertainty is ± 0.10 mm.

Table 3.1: Dopant concentration and dimensions of used glass samples

Glass no.	**p mol%**	**A mm**	**B mm**	**C mm**
Pr^{3+}: ZBLAN				
Z1118	0.112	8.20	15.15	18.63
Z1159	0.220	8.80	14.30	16.75
Z958	1.052	8.30	11.70	19.28
Z1109	3.003	7.98	14.08	18.80
Z1011	—	8.30	15.33	18.98
Pr^{3+}/ Yb^{3+}: ZBLAN				
Z1283*	0.301	8.85	16.00	n.p

* probe co-doped with 1.997 % Yb^{3+}

Glass no.	**p mol%**	**A mm**	**B mm**	**C mm**
Pr^{3+}: IBZP				
I546	0.117	8.98	14.50	n.p.
I549	0.301	8.70	14.10	n.p.
I550	1.004	8.95	13.05	15.90
I553	2.998	9.15	12.15	15.70
I544	—	8.67	14.94	18.05

n.p. - not polished

The probes Z1011 and I544 were not doped with any rare earth ions and were used both to determine the basic transition of the glass samples, and for refractive index measurements. The remaining probes were doped with Pr^{3+}, and sample Z1283 was additionally co-doped with Yb^{3+}. The glasses have been prepared by melting ultra pure powders in a platinum crucible at 800 °C for 30 min, followed by 30 min at 900 °C for refining under a dry nitrogen atmosphere. Nitrogen atmosphere ensures an absence of contaminations, e.g. water, hydrogen and hydroxyl radicals, in the melt [51]. The liquid was poured into a preheated brass mold at 260 °C and then cooled to room temperature. Samples were polished with diamond paste resulting in optical quality. Some probes were polished only from four sides; therefore, not all dimensions of the samples could be measured (see Table 3.1). Opposite surfaces were not exactly parallel in order to avoid interference effects. The polished bulk glasses were homogenous and without crystals or bubbles.

Table 3.2: Parameters for a Cauchy approximation of the refractive index measurements [47]

Parameter	ZBLAN	IBZP
A in µm^4	$2.30 \cdot 10^{-4}$	$6.70 \cdot 10^{-4}$
B in µm^2	$6.78 \cdot 10^{-3}$	$4.74 \cdot 10^{-3}$
C	1.4847	1.5057
D in µm^{-2}	$1.34 \cdot 10^{-2}$	$6.52 \cdot 10^{-3}$
E in µm^{-4}	$-7.91 \cdot 10^{-3}$	$-4.42 \cdot 10^{-3}$

The refractive index spectrum is an important quantity of glass material. The changes in refractive indices for undoped ZBLAN and IBZP samples were measured by a SOPRA spectroscopic ellipsometer. The results were then fitted using the Cauchy formula [52]:

$$n(\lambda) = A\lambda^{-4} + B\lambda^{-2} + C + D\lambda^{2} + E\lambda^{4}\,. \tag{3.11}$$

Calculated parameters $A - E$ are given in Table 3.2, and fits of refractive index spectra using the Cauchy formula are presented in Figure 3.2. The measured refractive indices are in good agreement with the control measurement performed for the glass samples using an Abbe refractometer at the wavelength of 589.3 nm. The results of the Cauchy fit were used for further spectroscopic calculations.

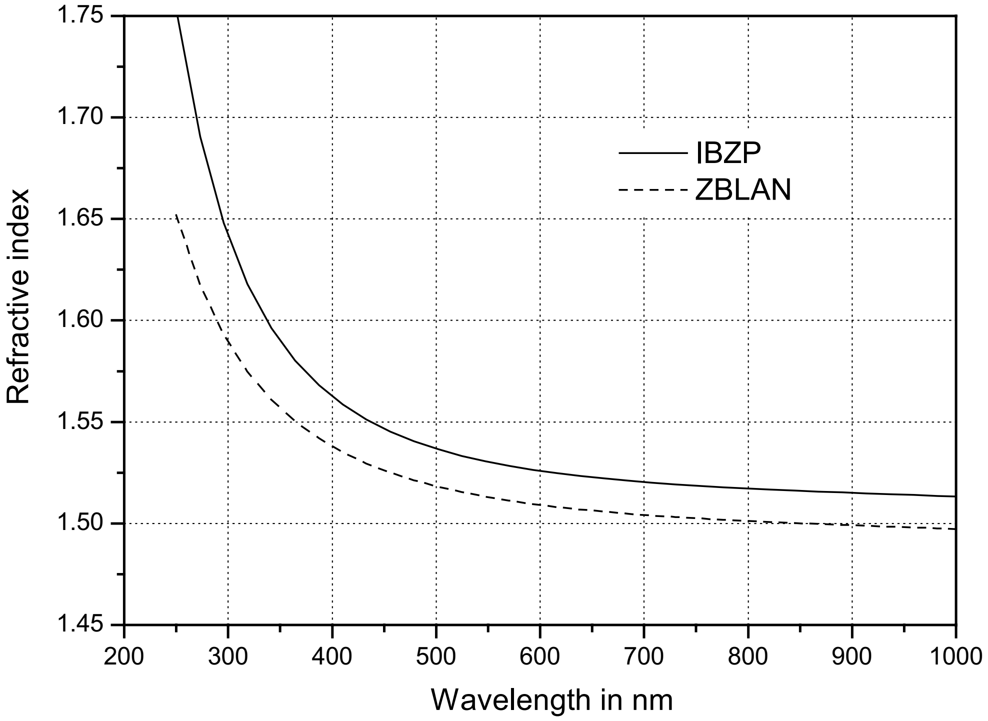

Figure 3.2: Fit of measured refractive indices spectra using the Cauchy formula [47]

3.3 Absorption measurements

After presenting theoretical issues and parameters of the glass samples, we will now continue with the practical part. Results of spectroscopic measurements are generally presented in wavenumbers k scaled in cm^{-1}. A wavelength in nm can be converted into a wavenumber by:

$$k\ in\ cm^{-1} = \frac{10^7}{\lambda\ in\ nm}. \tag{3.12}$$

Thus, the wavenumber is just the inverse of the wavelength. However, in order to make the interpretation easier, all measurement results given in tables are shown both in wavenumbers and nanometers.

Optical absorption measurements in the visible range were done with a Varian Cary 5G spectrometer. For all measurements the resolution was smaller than the observed linewidth. Absorption measurements in the infrared range were made with a Fourier transform (FT) spectrometer IFS 25 from Bruker. These two measuring instruments represent two different approaches to measuring the absorption spectrum. In both cases, a high temperature source with a broad and smooth spectrum is used, e.g. a halogen lamp. In the first measuring method, a monochromator is used as a narrow band filter selecting the wavelength of interest in the emission spectrum. With increasing resolution (decreasing bandwidth of the monochromator), the intensity of the usable radiation is decreasing. In the second method, the radiation from the source is made to interfere with itself in a Michelson interferometer, and the interference signal is detected. The intensity of the signal is recorded with respect to the position of the oscillating mirror and, therefore, the intensity spectrum of the source can be calculated via a Fourier transformation. Compared to the monochromator setup, the Fourier method uses the full spectrum of the source. This plays an important role in the infrared region where the spectral intensity of light sources and the sensitivity of available detectors are low. However, the drawback of high sensitivity is a low dynamic range compared to the monochromator setup [40]. Therefore, a monochromator spectrometer was used in the range 400-660 nm, and the absorption in the range 660-4500 nm was measured with the FT-IR spectrometer containing a Si-detector.

Regardless of the spectrometer used, the absorption measurement was made in two steps. First, the reference spectrum $I_0(k)$ without a sample was measured. This step allows determining the spectral characteristics of the light source, of the detector and of all optical components in the optical path. In the second step, the spectrum $I(k)$ with the glass probe is obtained. Using these two measurements the transmission of the sample may be calculated by:

$$T(k) = \frac{I(k)}{I_0(k)}. \tag{3.13}$$

Consequently, the absolute attenuation spectrum is given by:

$$\alpha_{abs}(k) = \ln\left(\frac{I_0(k)}{I(k)}\right). \tag{3.14}$$

3.3.1 Analysis of measured spectra

The measurements on glass probes include not only the raw absorption spectra, but also an attenuation caused by the host glass and Fresnel reflections from both surfaces of the glass. Here, we are only interested in the rare earth dopants and not in the properties of the glass host. Therefore, the baseline of each spectrum had to be corrected. First, each spectrum was split into pieces, each of which contained an individual absorption line or a group of overlapping lines. Then the base line correction was made. The original absorption measurement and the corrected spectrum for the $^1D_2$ line of Pr^{3+}:IBZP glass are shown in Figure 3.3.

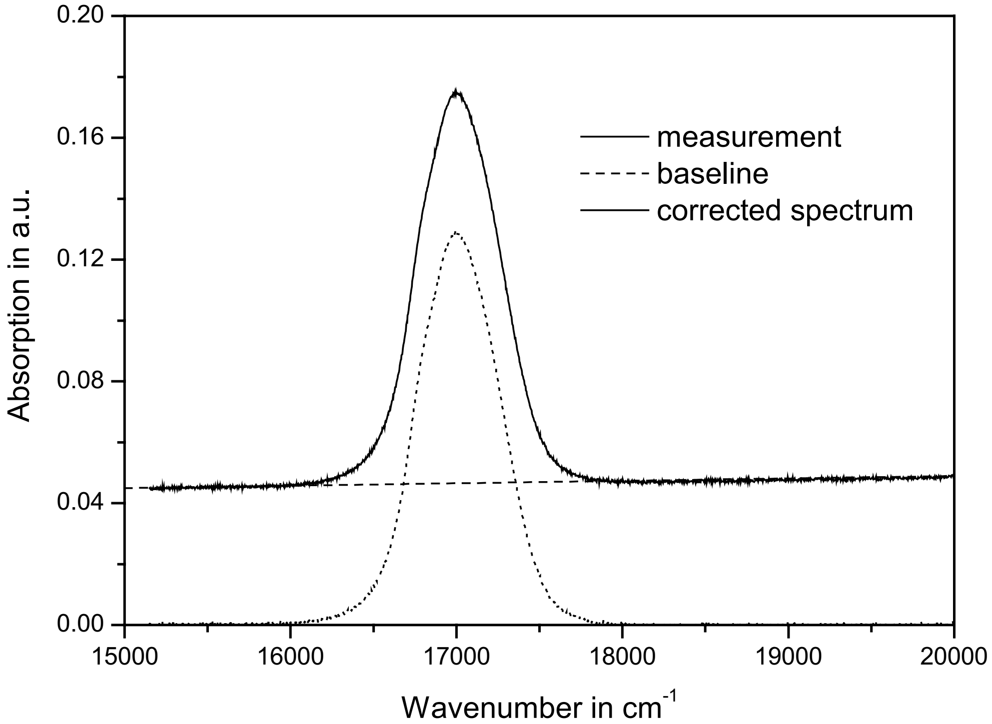

Figure 3.3: Baseline correction for the Pr^{3+} line $^1D_2$ IBZP glass sample (I549)

In the next step, the absorption cross-section was estimated from the corrected spectra using the equation [40]:

$$\sigma_{12}(k) = \frac{\alpha_{abs}(k)}{l\gamma p}, \tag{3.15}$$

where l is the length of the sample and p the molar concentration. The conversion factor γ is given by:

$$\gamma = \frac{\rho N_A}{m}, \tag{3.16}$$

where ρ is the mass density, N_A Avogadro's constant and m the molar mass of the glass composition.

The mass density of ZBLAN glass was found to be 4.33 g/cm^3 which is comparable to the value 4.37 g/cm^3 published in [53]. This yields a conversion factor of $1.84 \cdot 10^{22}$ cm^{-3}. In the case of IBZP, the mass density was found to be 5.2 g/cm^3 and is in good agreement with 5.1 g/cm^3 found in the literature for a slightly different composition [54]. This leads to a conversion factor of $2.27 \cdot 10^{22}$ cm^{-3}.

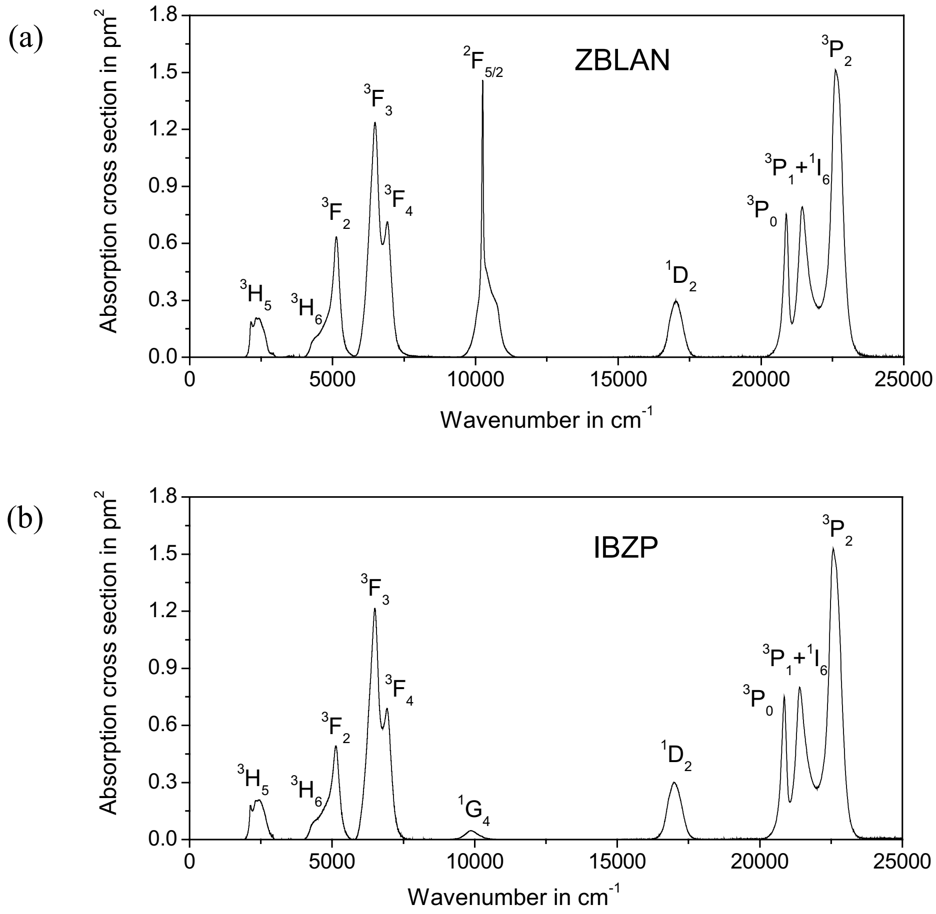

Figure 3.4: Spectrum of the ground state absorption cross-section for (a) Pr^{3+}/Yb^{3+}: ZBLAN, (b) Pr^{3+}: IBZP

The results of the calculation of the absorption cross-section from the ground level $^3H_4$ to higher levels are shown in Figure 3.4. The ZBLAN glass was doped with 0.3 % Pr^{3+} and 2 % Yb^{3+} (sample Z1283). The IBZP glass was doped with 0.3 % Pr^{3+} (sample I549). The ZBLAN glass has one additional absorption peak which causes the $^2F_{7/2}\rightarrow^2F_{5/2}$ transition in Yb^{3+} located at 975.3 nm (10 254 cm^{-1}). An absorption band due to the transition $^3H_4\rightarrow^1G_4$ in Pr^{3+} exists in the same range (see IBZP), but its cross-section is two orders of magnitude smaller than the transition in Yb^{3+}. Thus, its contribution to the spectrum is negligible. The transition to level $^3H_5$ shows two peaks which are related to three groups of Stark levels [40]. Level $^3H_6$ shows no separate peak, because the $^3F_2$ line is very narrow and large. There are three particularly interesting absorption peaks grouped near 450 nm (22 200 cm^{-1}) which correspond to the $^3P_2$, $^3P_1$, $^1I_6$ and $^3P_0$ multiplets. This broad and strong absorption band absorbs the blue part of the visible spectrum, and it plays an important role for a blue laser line which will be discussed in detail in chapter 5.2.4. The $^3P_1$ and $^1I_6$ levels have a considerable overlap and can be simply referred to as the $^3P_1$ state. The absorption band position and its relative intensities agree with previous reports on Pr^{3+} ions in other fluoride glasses [40, 55, 56].

Table 3.3: Calculated absorption cross-sections for ZBLAN and IBZP glasses

Level	**RE**	**ZBLAN**			**IBZP**		
		k_p in cm^{-1}	**λ_p in nm**	**σ_{12} in pm^2**	**k_p in cm^{-1}**	**λ_p in nm**	**σ_{12} in pm^2**
$^3H_5$	Pr^{3+}	2413	4144.2	0.206	2425	4123.7	0.209
$^3F_2$	Pr^{3+}	5128	1950.1	0.635	5119	1953.5	0.491
$^3F_3$	Pr^{3+}	6483	1542.5	1.238	6495	1539.6	1.215
$^3F_4$	Pr^{3+}	6923	1444.5	0.714	6918	1445.5	0.689
$^1G_4$	Pr^{3+}	——	——	——	9883	1011.8	0.046
$^2F_{5/2}$	Yb^{3+}	10254	975.3	1.043	——	——	——
$^1D_2$	Pr^{3+}	17021	587.5	0.297	16998	588.3	0.301
$^3P_0$	Pr^{3+}	20890	478.8	0.753	20855	479.5	0.750
$^3P_1$, $^1I_6$	Pr^{3+}	21445	466.3	0.792	21404	467.2	0.801
$^3P_2$	Pr^{3+}	22604	442.4	1.513	22578	442.9	1.527

The peak wavenumbers k_p, appropriate wavelengths λ_p and values of absorption cross-sections σ_{12} for transitions in visible range are collected in Table 3.3. No big changes in the wavelengths of maximum absorption between the two host glasses were observed. This is due to the fact that the absorption bands arise from electronic transitions within the 4f shell which is not very sensitive to the crystalline field [57]. Additionally, there are only small differences in absorption cross-sections.

3.3.2 Excited state absorption

In the previous section, we discussed the absorption from the ground state, but an excited state absorption (ESA) in our laser system is also of interest. This is an undesirable process if the signal light is absorbed from the upper level instead of being amplified; whereas, it is a desirable process if used for stepwise pumping of the upper level. In our case, the absorption from the excited state $^1G_4$ to ^3P_J levels plays an important role in the pumping process, and we will concentrate only on this transition. ESA spectra are usually obtained using a pump-probe technique in which the transmission of a tunable probe beam is monitored while the upper level population is modulated by chopping the pump beam. The authors in [27] proposed a new technique. In order to determine the ESA spectrum, the fluorescence from $^3P_0$ to $^1G_4$ as well as the fluorescence from the thermally populated $^3P_1$ and $^1I_6$ levels was measured around 900 nm. The $^3P_0$ level was pumped with 488 nm argon laser light.

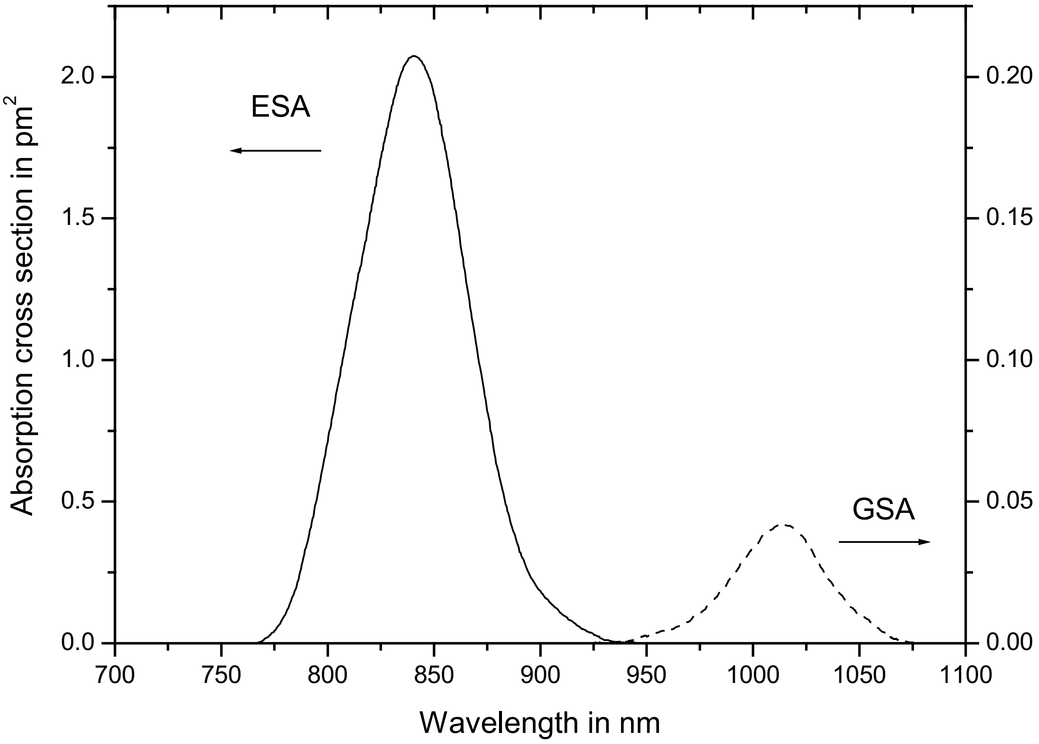

Figure 3.5: Cross-section spectra for $^3H_4 \rightarrow {}^1G_4$ ground state absorption (dotted line) and excited state absorption for $^1G_4 \rightarrow {}^3P_J$ (solid line) [27]

The theory of McCumber was used to calculate the ESA spectrum from the measured fluorescence, and the results of this procedure are shown in Figure 3.5. For comparison, the ground state absorption cross-section spectrum is also presented. This transition $^3H_4 \rightarrow {}^1G_4$ is weak, and the cross-section is more than an order of magnitude smaller than the ESA cross-section. The ESA spectrum shows a peak at a wavelength of 842 nm which corresponds to reports of 835 nm in [25] and 845 nm in [34] as the optimum wavelength for upconversion pumping of a visible Pr^{3+}:ZBLAN laser. This method may determine ESA-band profiles more reliably than absolute magnitudes. The Judd-Ofelt theory is known to give a poor fit for some Pr^{3+} transitions. The measurement of the optimum pump wavelength for our laser setup was also realized, but it will be described later on in chapter 5.2.6.

3.4 Emission measurements

The knowledge of possible emission lines is of a great importance for designing laser systems. For emission measurements, a fluorescence spectrometer was used, and the measurement setup used is sketched schematically in Figure 3.6. It is described in [40].

For measuring the emission spectrum of a rare earth doped glass, first it is necessary to excite the rare earth ions with a suitable pump source. Next, the spectrum emitted due to relaxation to lower energy levels is measured. An excited ion may decay spontaneously to all lower lying energy levels. Therefore, the emission spectrum contains, in principle, the emission lines for all energy levels between the pump level and the ground state. Our glass probes were pumped at the 457 nm line of an argon ion laser. The argon laser emits several lines simultaneously. Therefore, a prism and an iris diaphragm were used to select the interesting laser line. All powerful argon lines (e.g. 514 nm and 488 nm) lie very close to expected Pr^{3+} emissions in the blue and green range. Hence, we had chosen a line which was sufficiently far from an expected emission in order to avoid an overlap of pump and fluorescence.

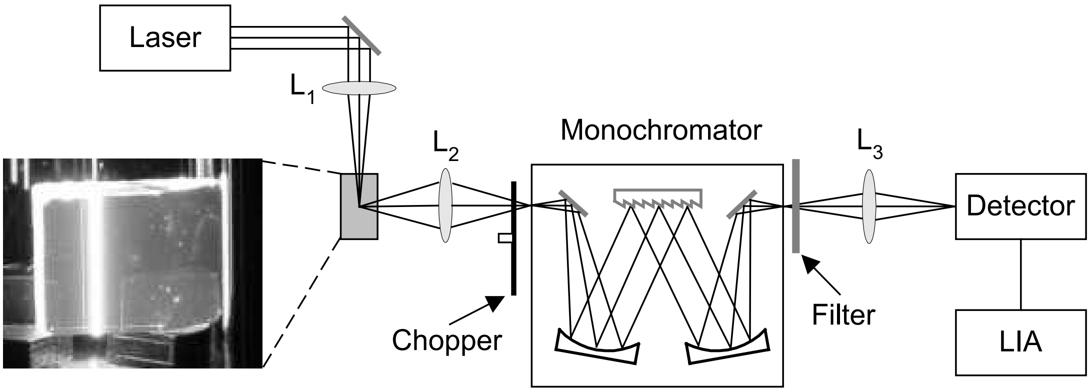

Figure 3.6: Setup of the fluorescence spectrometer

The pump beam was focused onto the glass sample by a lens L_1, and the sample was pumped from the top. Hence, the source of fluorescence was a cylinder with a Gaussian intensity distribution across the diameter. The diameter of the cylinder was considered to be constant across the full length as shown in the attached photograph. The light emitted from this cylinder was then collected by another lens L_2, and was imaged onto the entrance slit of a monochromator (Photon Technology International) with one grating. The monochromator acts as a band-pass filter suppressing large parts of the background noise. Before entering the monochromator, the beam was chopped in order to synchronize the lock-in amplifier (LIA). A filter was placed behind the monochromator for blocking the higher diffraction orders of the monochromator grating or remaining pump power. The lens L_3 was used to image the exit slit of the monochromator onto the Si detector. The detected signal was then amplified by a transimpedance amplifier and finally measured with the lock-in amplifier. It can recover signals in the presence of a large noise background. The setup described was also used to measure the fluorescence from fibers.

Emission spectroscopy is somewhat more difficult than absorption measurements. Instead of absorption measurements, fluorescence spectroscopy delivers unscaled intensity spectra. The drawback of such a one-way measurement is the fact that spectral responses of all optical parts are contained in the measurement results. In reality, our measured spectrum $I_M(\lambda)$ is the real spectrum $I_R(\lambda)$ multiplied by some transition function $T(\lambda)$:

$$I_M(\lambda) = I_R(\lambda) \cdot T(\lambda). \qquad (3.17)$$

This T-function describes spectral characteristics of all the elements used in the setup; i.e. lenses, mirrors, the monochromator, filter and detector. In order to obtain the true spectrum, we have to divide our measured spectrum by this T-function. However, first we have to know this function. For determining the T-function, we need a calibrated light source, e.g. a light source with a well known spectral characteristic $I_{CR}(\lambda)$. The calibrated light source is used instead of our fluorescent glass sample, and the spectrum of this light source $I_{CM}(\lambda)$ is measured by our setup. If we know these two spectra, we can determine the T-function by:

$$T(\lambda) = \frac{I_{CM}(\lambda)}{I_{CR}(\lambda)}, \tag{3.18}$$

and obtain a correct fluorescence spectrum from our glass sample.

We used a 100 W halogen lamp HLX 64342 from OSRAM, driven with 6.3 A from a stabilized current source. The spectral response $I_{CR}(\lambda)$ of this lamp was measured in the German Institute of Standards (PTB) and collected in [58], with 20 nm measurement steps, but our fluorescence measurement was made with 0.5 nm resolution. Sources like the halogen lamp have blackbody-like emission spectra, and the spectral intensity of such a radiation source can be given by:

$$I(\lambda) = \frac{A}{\lambda^5} \frac{1}{\exp(hc/\lambda kT) - 1}. \tag{3.19}$$

This equation was used to fit the $I_{CR}(\lambda)$ points. The fit parameters were A and T, and the results are shown on Figure 3.7.

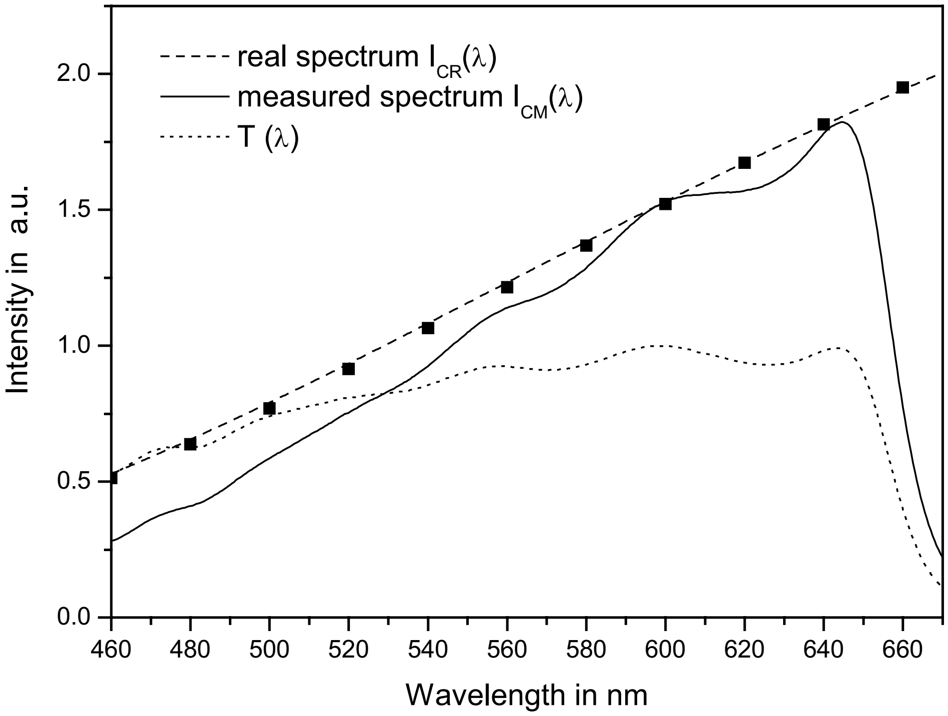

Figure 3.7: Real and measured spectrum of the calibrated lamp

These measurements allow determining the T-function. The squares are measured points, and the dashed line results from the fitting procedure. The fit agrees very well with the measurement. The straight line represents the halogen lamp spectrum as measured with our setup and normalized to the real spectrum of the calibrated lamp. Several differences are noticeable. For wavelengths below 600 nm, deviations become larger and larger with decreasing wavelengths. This is caused mainly by the spectral sensitivity of the Si diode. The maximum sensitivity for this diode is about 850 nm and is reduced with deceasing wavelength. Additionally, the measured spectrum is slightly wavy. This is due to of the filter used which does not have a flat transmission spectrum. The short-pass filter is also responsible for a sudden reduction in the intensity measured above 640 nm. It was especially useful for fluorescence measurements on a fiber pumped at 840 nm. By means of this filter, all remaining pump power was reflected. Without the filter, the detector would measure the fluorescence signal and the scattered pump power. Since we know the real $I_{CR}(\lambda)$ and the measured $I_{CM}(\lambda)$ spectrum of the calibrated lamp, we can calculate the T-function using eq. (3.18). Thus, we are able to determine the correct fluorescence spectrum $I_R(\lambda)$. We must only divide the measured spectrum $I_M(\lambda)$ by the assigned T-function. The results of a spectrum correction are shown in Figure 3.8. The difference between the measured and the calibrated spectra in orange (605 nm) and red (635 nm) emission peaks is small. For the orange line there is hardly any discrepancy, and the red line is corrected by only 4 %. The influence of the calibration procedure is more visible in the green and blue ranges which correspond to emission peaks at 625 and 490 nm, respectively.

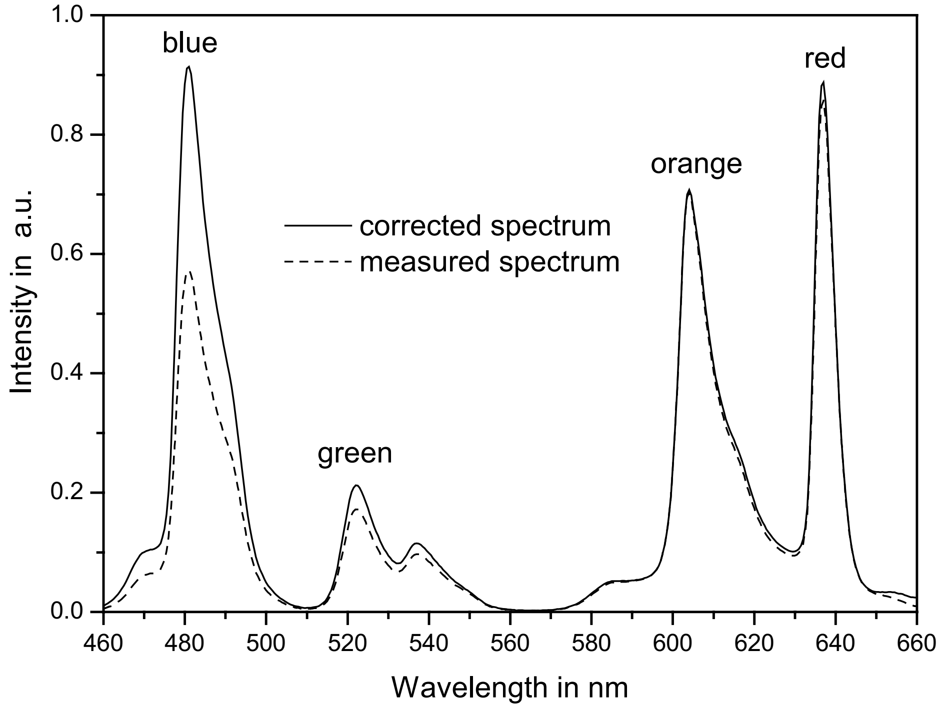

Figure 3.8: Measured fluorescence of Pr^{3+}:ZBLAN (dashed line) and spectrum after the calibration procedure (solid line)

The calibrated green line has 25 % more intensity than that without a correction; whereas, in the case of the blue line, the intensity increase reaches 60 %, a significant improvement. In our case, the calibration procedure plays an important role in precise measurements of fluorescence spectra, especially in a blue-green emission range. Nevertheless, skipping the calibration for an orange-red area does not cause significant errors.

The emission cross-section is an important parameter for the laser gain of materials, as it determines the laser gain for a given population inversion [59]. As already mentioned, emission spectroscopy is slightly more complicated than absorption measurement. Even corrected emission spectra are still relative spectra, because a sample emits in all directions in contrast to absorption measurements where the intensity of a transmitted radiation beam is measured. Therefore, we used the Fuchtbauer-Ladenburg eq. (3.5) together with the calculated radiative spontaneous emission rate A_{21} from eq. (3.5) to scale the measured lineshape $g_{21}(k)$ of a transition to a cross-section spectrum [40]:

$$\sigma_{21}(k) = \frac{1}{8\pi c k_{cm}^2 n^2} A_{21} g_{21}(k). \tag{3.20}$$

In eq. (3.9), the frequency v was replaced by the wavenumber $k = v/c$, and the lineshape $g(k)$, due to the different normalization $\int g(k)dk = 1$, has the dimension of an inverse wavenumber in contrast to $g(v)$. Therefore, a factor c is introduced. The center of mass wavenumber k_{cm} divides the area into two equal parts:

$$\int_{-\infty}^{k_{cm}} g_{21}\, dk = \int_{k_{cm}}^{\infty} g_{21}\, dk. \tag{3.21}$$

The refractive index n was measured for ZBLAN as well as for IBZP glass. The results are shown in Figure 3.2. The values of the radiative spontaneous emission rate A_{21} for particular transitions were taken from [40]. The emission measurements were made on the same glass probes as in the case of the absorption measurements. The results of calculations are shown in Figure 3.9, and the transition wavenumbers k_p, appropriate wavelengths λ_p, and the values of emission cross-sections σ_{21} for transitions in the visible range are listed in Table 3.4.

Table 3.4: Calculated emission cross-sections for ZBLAN and IBZP glasses

Transition	**Pr^{3+}/Yb^{3+}:ZBLAN**			**Pr^{3+}:IBZP**		
	k_p in cm^{-1}	**λ_p in nm**	**σ_{21} in pm^2**	**k_p in cm^{-1}**	**λ_p in nm**	**σ_{21} in pm^2**
$^3P_0 \rightarrow {}^3F_2$	15686	637.5	7.191	15674	638.0	2.459
$^3P_0 \rightarrow {}^3H_6$	16515	605.5	2.545	16529	605.0	3.865
$^3P_1 \rightarrow {}^3H_5$	19029	525.5	3.055	19102	523.5	2.952
$^3P_0 \rightarrow {}^3H_4$	20833	480.0	4.380	20812	480.5	4.493

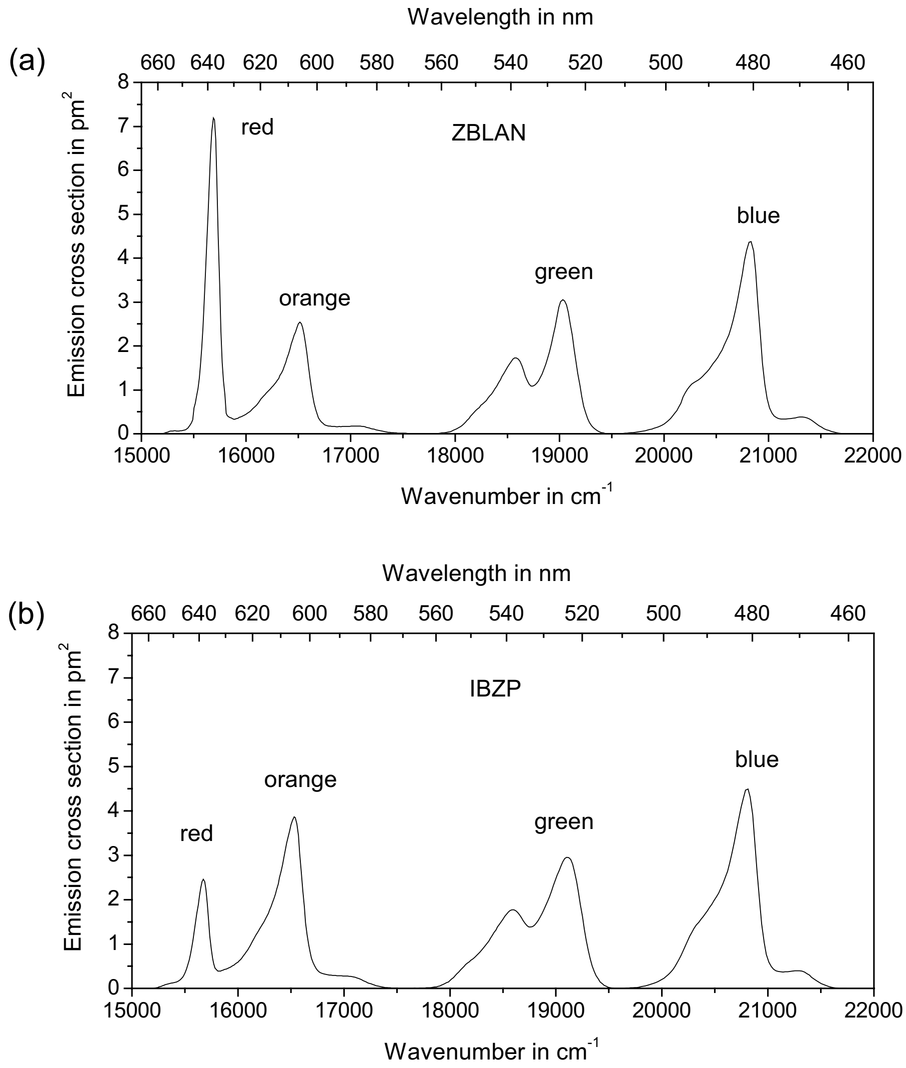

Figure 3.9: Spectrum of the emission cross-section for (a) Pr^{3+}/Yb^{3+}:ZBLAN, (b) Pr^{3+}:IBZP

The emission wavelengths and emission cross-section values are comparable with previous reports on Pr^{3+} ions in fluoride glasses [35, 60, 61]. The emission cross-sections obtained are large and indicate that the Pr^{3+}-doped fluoride glasses are good laser materials in visible region. Comparing the position of the emission peaks for ZBLAN and IBZP glasses, no significant discrepancy is noticeable. Also, the emission cross-sections at blue and green lines are comparable. The largest differences between these two kinds of glasses are visible at red and orange emissions. The emission cross-section of the red line in IBZP glass is smaller by 66 % in comparison to ZBLAN glass. Simultaneously, the emission cross-section of the orange line increases by 52 %. The results indicate that the fluorescence properties of Pr^{3+}-doped fluoride glasses are dependent on the glass composition. The red line in ZBLAN glass is clearly dominant, and consequently, the red laser is simple to excite. Nevertheless, laser mirrors have to be selected very carefully if a laser emission other then red is required.

The mirrors should have a reflection as small as possible in the red range. In another case, the red laser competes with the desired laser line. This was experimentally observed and will be discussed in further chapters. All laser emissions in the IBZP host have similar cross-sections, and there is no clear dominant emission.

3.5 Lifetime measurements

The fluorescence lifetime is a very important parameter and a key to the qualitative understanding of laser properties. Besides this, detailed measurements of the fluorescence from the upper level can provide information on the relative importance of ion-ion interactions such as upconversion and quenching processes. The decay of the population in a given level drops exponentially with a time constant equal to the lifetime. There are several ways for the population to decay. The total probability of the decay is equal to the sum of the individual probabilities for each path. Usually, the lifetime for a given rare earth level follows from consideration of the three main paths for decay; i.e., radiative, nonradiative and energy transfer [46]:

$$\frac{1}{\tau}=\frac{1}{\tau_r}+\frac{1}{\tau_{nr}}+\frac{1}{\tau_{ET}}, \tag{3.22}$$

where τ is the total lifetime, τ_r is the radiative lifetime, and τ_{nr} is nonradiative lifetime. The τ_{ET} represents the energy transfer processes. The radiative lifetime is determined by the fluorescence from the excited level to all the levels below it. It can be calculated with the help of the Judd-Ofelt analysis. In the nonradiative process, the deactivating process from the excited rare earth level is accompanied by the emission of one or several phonons. Nonradiative processes are described in chapter 2.3.

The lifetime τ in the upper laser level may be measured simply by monitoring the decaying fluorescence from a glass sample pumped by a chopped laser beam. The only requirement is that the pump light be turned on a sufficiently long time for a significant ratio of the rare earth to be excited. This ensures a realistic fluorescence level for the measurement. Ideally, the pump light should then be turned off completely, and the fluorescence intensity would then decay exponentially according to $\exp(-t/\tau)$, where t denotes the time [62]. However, in practice, the pump will always have a given decay time, but depending on the requirements of accuracy and the involved lifetime, different choppers may be used. This means that if the lifetime is very long (for instance, around 10 ms), realistic lifetime estimates may be obtained by a mechanical chopper. On the other hand, if the pump has to be turned off much faster, then an acousto-optical modulator (AOM) may be used. For our laser application, the lifetime of upper laser levels ($^3P_{0,1}$) is of highest interest. Based on the literature, we expected a lifetime in the range of tens of μs; therefore, the acousto-optical modulator was applied. The lifetime measurements were performed using, in principle, the same setup as for emission spectroscopy, only with small modifications. The mechanical chopper was removed and the acousto-optical modulator was located in front of a glass sample to modulate the pump signal, and therefore, the excitation. The samples were excited as before by the 456 nm line of an argon ion laser. The AOM from Isomet had a fall time of only 2.2 ns, which was 4 orders of magnitude shorter than the expected lifetime. The AOM makes use of the acousto-optic effect. Acousto-optic interaction occurs if an acoustic wave and a laser beam are present in the medium. The acousto-optic effect is the change in the refractive index of a medium caused by the mechanical strains accompanying the passage of an acoustic (strain) wave through the medium. The strain, and hence the refractive index, varies periodically with a wavelength Λ equal to that of the acoustic wave.

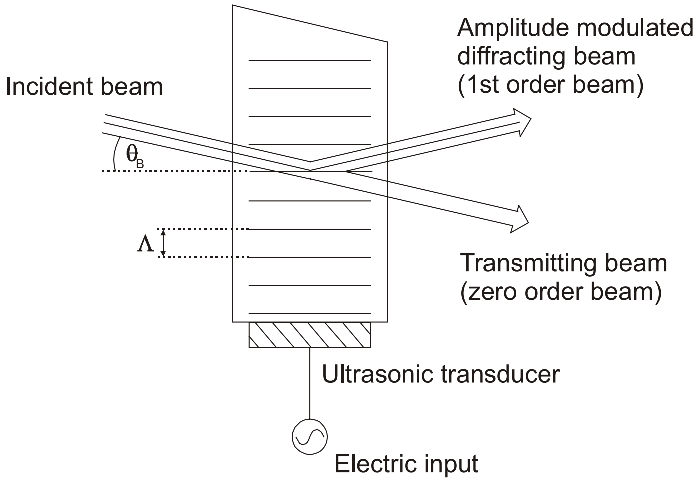

Figure 3.10: Schematic illustration of acousto-optic effect

The situation is shown in Figure 3.10, where the solid horizontal lines represent acoustic wave maxima. Because these variations occur at regular intervals, they act like a phase grating, and incoming light is diffracted into the various orders. At one particular incidence angle only one diffraction order is produced, the others are annihilated by destructive interference. This is the so-called Bragg angle θ_B defined by [63]:

$$\sin\theta_B = \frac{\lambda}{2\Lambda}. \tag{3.23}$$

An acousto-optic modulator is fabricated from a material with a high acousto-optic figure of merit such as lead molybdate ($PbMbO_4$), to which a piezoelectric transducer such as lithium niobate ($LiNbO_3$) has been bonded. The piezo transducer inducts ultrasonic waves in the crystal by applying an RF signal generated by the driver electronics as shown in Figure 3.10. In our setup, the AOM position was aligned to obtain maximum power in the first order, and this modulated beam was used to excite glass samples.

3.5.1 Lifetime measurements of ^3P_J levels

The fluorescence signal was measured with a Si diode connected to a transimpedance amplifier. Usually, in order to determine a fluorescence lifetime, a decay curve is measured and stored using an oscilloscope. In the next step, an exponential fit is applied to determine the value of the lifetime. Unfortunately, our transimpedance amplifier has a large amplification but only a small bandwidth of 20 kHz. This was insufficient to measure lifetimes of the ^3P_J levels in the range of tens of µs. Therefore, we had to apply another method which is described in detail in [64].

The change of the upper level population N_2 is described by equation (1.7). If we take equation (1.5) into account and ignore the stimulated emission, we obtain the following equation:

$$\frac{dN_2}{dt} = B_{12}\rho(\nu)N_1 + \frac{N_2}{\tau}. \tag{3.24}$$

The population density N of a specific level is proportional to energy z accumulated in it. Hence, equation (3.24) can be interpreted as:

$$\frac{dz}{dt} = p_{abs} - \frac{z}{\tau}, \tag{3.25}$$

where p_{abs} is absorbed power and z/τ is emitted power. The difference corresponds to a temporal change of the energy accumulated. The absorption probability and the quantum efficiency are considered to be constants. Consequently, for the supply pump power $p(t)$:

$$p(t) \propto p_{abs}, \tag{3.26}$$

is valid, and for the emitted power $e(t)$:

$$e(t) \propto \frac{z(t)}{\tau}. \tag{3.27}$$

The sample is excited until time $t = 0$. Then the pump beam is blocked, and the emission decays with the time constant τ. As already mentioned, the measurement of the lifetime τ in the time domain was impossible; therefore, we performed it in the frequency domain. For the fluorescence measurement, the lock-in-amplifier was used, and the amplitude as well as the phase were measured. The amplitude was not important for us, but we could use the phase to determine the lifetime. A phase θ_p at the pump wavelength and a phase θ_s at the signal wavelength were measured for different modulation frequencies f. The knowledge of differences between these two phases permits to calculating the lifetime as shown below.

For the calculation, a Laplace transform was used. The Laplace transform is often interpreted as a transformation from the time domain (in which inputs and outputs are understood as a function of time) to the frequency domain where the same inputs and outputs are seen as functions of complex angular frequencies. The Laplace transforms of the pump power $p(t)$ and the emitted power $e(t)$ are $P(s)$ and $E(s)$, respectively. There exists exactly one transfer function $H(s)$ which defines the temporal ratio of signal to pump power, converted by the Laplace transform:

$$H(s) = \frac{E(s)}{P(s)}. \tag{3.28}$$

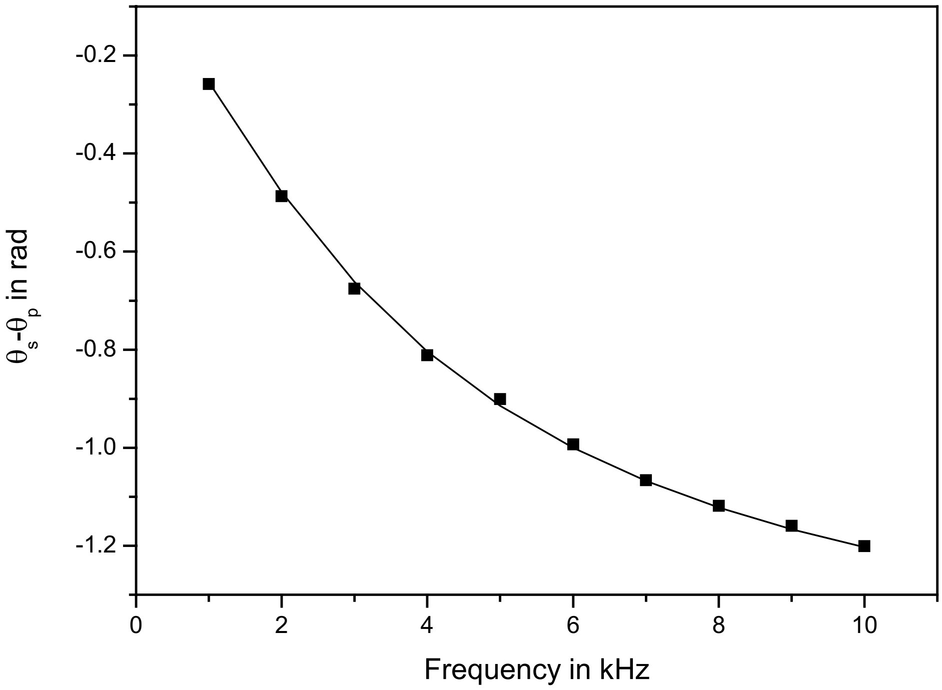

Figure 3.11: Phase difference versus modulation frequencies for a 0.1 % Pr^{3+}: ZBLAN glass

Thus, the transfer function is determined only by the spontaneous emission and not by the setup used. With the Laplace transform of equation (3.25), we obtain:

$$sZ(s) = P_{abs}(s) - \frac{Z(s)}{\tau} . \qquad (3.29)$$

Taking into account assumptions (3.26) and (3.27), we receive:

$$\frac{\frac{Z(s)}{\tau}}{P_{abs}(s)} = C\frac{E(s)}{P(s)} , \qquad (3.30)$$

and application of equations (3.28) and (3.29) leads to:

$$= CH(s) = \frac{1}{1+s\tau} . \qquad (3.31)$$

The unknown constant in the transfer function has no influence on the phase course. Therefore, we can assume that it is equal to unity. The transfer function of the system is:

$$P(s) \longrightarrow \boxed{\frac{1}{1+s\tau}} \xrightarrow{E(s)} \qquad H(s) = \frac{1}{1+s\tau} . \qquad (3.32)$$

With the knowledge of the transfer function, we can take the inverse Laplace transform to find the general solution in the time domain. Our system has the output function *g(t)* with a normalization $g(0) = 1$ as follows:

$$g(t) = \exp\left(\frac{-t}{\tau}\right) . \qquad (3.33)$$

The phase course $\theta(\omega)$ of system is an argument of the transfer function at point $s=j\omega$ [64]:

$$\theta(\omega) = \arg\{H(j\omega)\} = -\arctan(\omega\tau). \tag{3.34}$$

The measured phase $\theta(\omega)$ is the difference between a signal phase θ_s and a pump phase θ_p at different modulation frequencies f [64]:

$$\theta(\omega) = \theta_s(2\pi f) - \theta_p(2\pi f). \tag{3.35}$$

The results of phase measurements are shown in Figure 3.11 as squares. The straight line is a fit to the function (3.34). The measurement results and the fit show very good agreement.

Using this method, we were able to determine the lifetime of the $^3P_0$ level for different dopant concentrations in ZBLAN and IBZP glasses. The results of the measurements are shown in Figure 3.12. The lifetimes presented were measured for a blue emission line which corresponds to the $^3P_0 \rightarrow {}^3H_4$ transition. The results obtained are comparable to others reported in the literature [22, 51, 65]. Orange and red lines were also used to determine the lifetimes, and the results show the same values as for the blue line. The green line emission was also used to determine the lifetime of the $^3P_1$ level, and the results were the same as for the $^3P_0$ level. This is caused by the strong thermal coupling between these two levels. The lifetime for the ZBLAN and the IBZP glass are very similar, but the lifetime of the IBZP is a little shorter. The lifetime depends strongly on the content of Pr^{3+} ions. An increase of the dopant concentration from 0.1 % to 1 % reduces the lifetime by half. This plays an essential role for selecting the dopant concentration in a laser design. Here the fluorescence lifetimes should be taken into account.

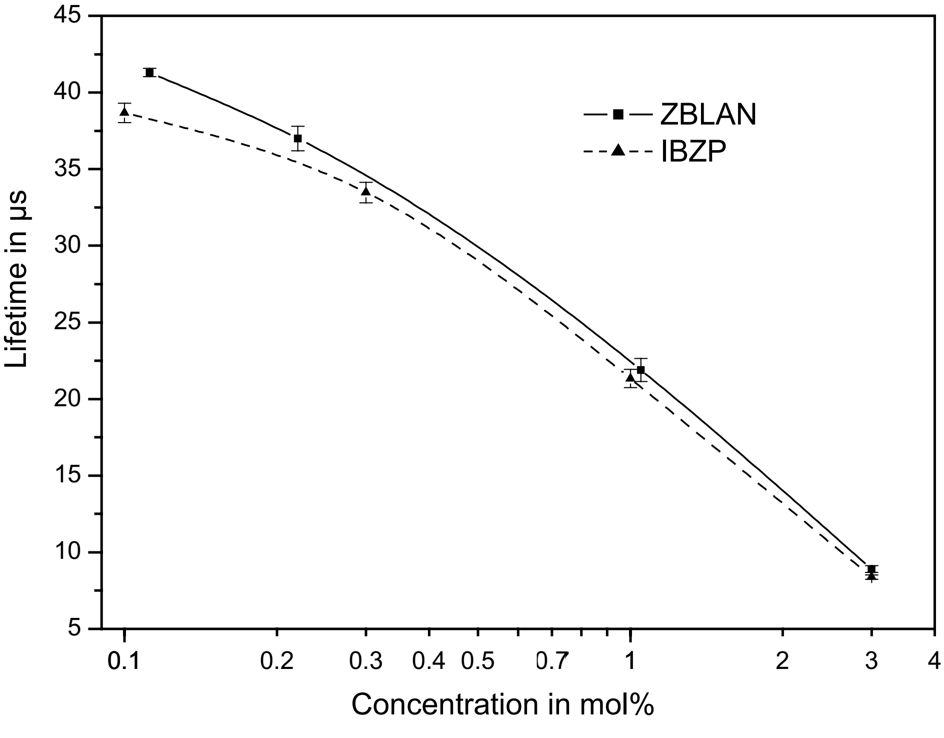

Figure 3.12: The $^3P_0$ lifetime dependence on Pr^{3+} concentration for ZBLAN and IBZP

For both host glasses, the lifetime dependence on concentration is very similar, and the traces run nearly parallel. The shortening of the lifetime with increasing dopant concentration is known as *concentration quenching*. It can arise from upconversion effects between Pr^{3+} ions described in detail in [66]. An ion in the excited state interacts with another neighboring ion in the ground state with the result that both ions end up in some intermediate states, thereby quenching the fluorescence from the excited state. Quenching can also arise from the fact that, in high concentration samples, the excitation can migrate from one ion to another and has, thus, a greater probability of encountering a quenching center where a local phonon or deformation can deactivate the excitation [5]. For ion concentrations sufficiently low for negligible ion-ion interaction, the measured lifetimes should follow directly from the sum of the radiative and nonradiative rates, and should be independent of dopant concentration. Our glass sample with the lower concentration contains 0.1 % Pr^{3+}. In literature, this concentration is reported as boundary concentration because above it, quenching is usually observed [67]. Consequently, all our glass probes are probably subject to quenching. We can expect that in glass samples with concentrations below 0.1 %, quenching will be not so significant, and dopant concentration will not influence the lifetime.

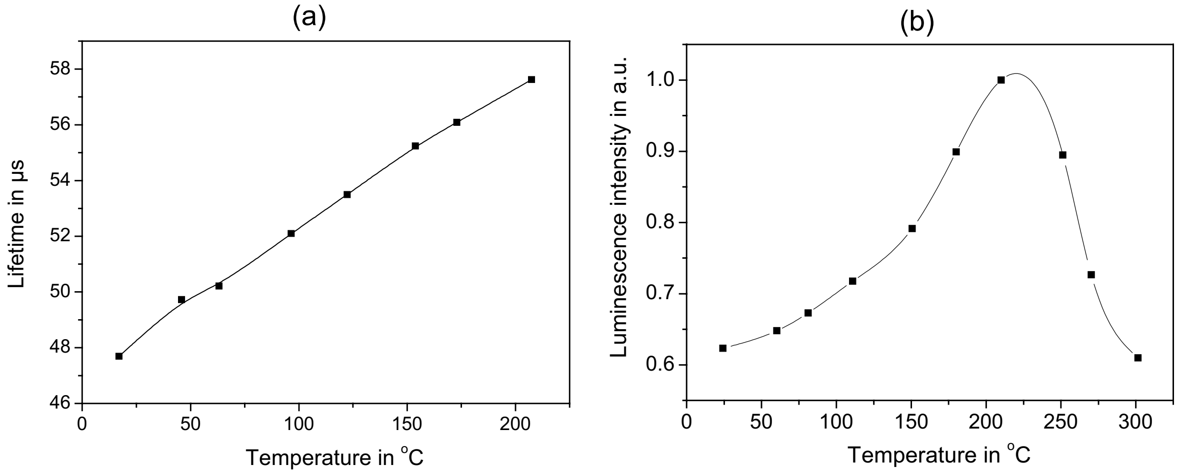

Figure 3.13: Influence of temperature on: (a) lifetime of the $^3P_0$ level [68] and (b) luminescence from Pr,Yb: ZBLAN pumped at 960 nm [72]

The measured lifetime is influenced not only by the dopant concentration, but also by temperature. In Figure 3.13a the fluorescence lifetimes from the $^3P_0$ excited state are depicted as a function of temperature [from 68]. As the temperature increases, the measured lifetimes are also seen to increase slowly. This phenomenon is used in temperature sensors based on Pr^{3+}: ZBLAN glass. This behaviour, the opposite to the one corresponding to multiphonon decays, can by understood as due to the thermal population of the $^3P_1$ and $^1I_6$ levels at high temperatures, and to the different decay probabilities of these levels as compared with that of $^3P_0$ [69]. Nguyen et al. reported that there occurs a critical concentration of 6900 ppm [70] at which the fluorescence lifetime is independent of temperature. The fluorescence lifetime increases with temperature at dopant levels below this critical level, and decreases with temperature at dopant levels higher than this critical level. The increase of the lifetime with growing temperature was also observed for a Yb^{3+}-doped fluorophosphates glass [71]. The lifetime was found to increase from 1.7 ms at 77 K to 2.0 ms at 380 K.

There is also an influence of the temperature on the emission intensity. The analysis of this phenomenon in Pr, Yb: ZBLAN, pumped at 960 nm, is reported in [72] and shown in Figure 3.13b. The intensity of the upconversion emission first increases with temperature, reaches a maximum value, and then decreases. This indicates that the energy transfer probability among Pr^{3+} ions depends on temperature. It supports the assumption that the energy transfer among the Pr^{3+} ions under IR excitation is caused by a phonon-assisted energy transfer process.

The increase of intensity with increasing temperature is due to an increase in the probability of the non-resonant multiphonon process which is involved in the transfer of electron-excitation energy among the activator ions. This results in populating the highly excited levels of the activator. However, an increase in the temperature also causes both an increase in the probability of multiphonon relaxation transitions, and also an increase of processes involved in the reverse transfer of electron excitation energy among the activator ions. This depletes the radiative levels of the activator. As a result of the combined competitive action of such processes, a maximum value of the intensity is obtained at a certain temperature, and the value of the intensity drops with further increase of the temperature [73].

3.5.2 Lifetimes of $^1G_4$ level

The $^1G_4$ level plays an important role in the upconversion pumping process in the Pr^{3+}/Yb^{3+} system. The transition from $^1G_4$ to $^3H_5$ was of great interest because of the possibility of realizing fiber based amplifiers for the 1.3 µm telecommunication window. Figure 3.14a shows the dependence of the $^1G_4$ lifetime in ZBLAN on the Pr^{3+} concentration [74].

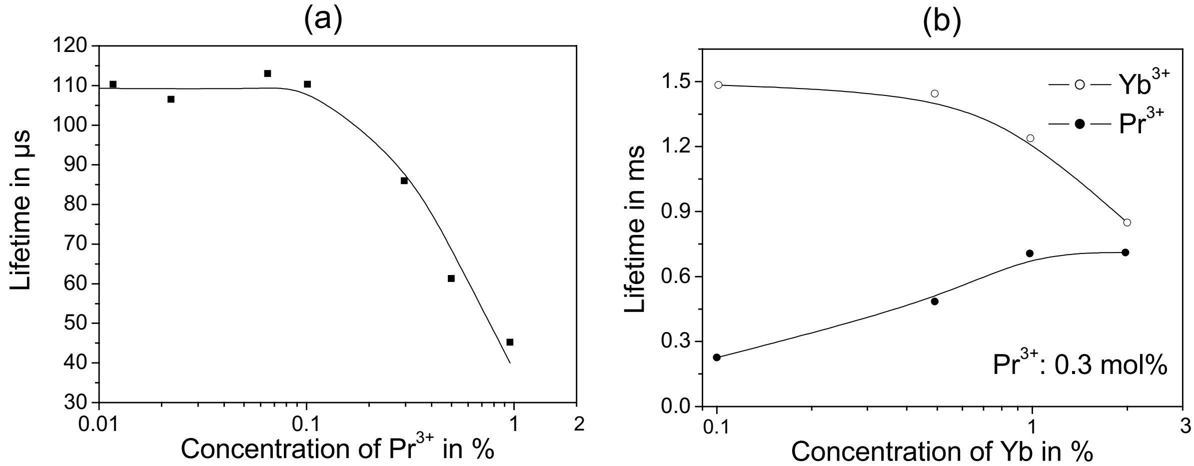

Figure 3.14: (a) The $^1G_4$ lifetime dependence on Pr^{3+} concentrations [74], (b) Pr^{3+} and Yb^{3+} lifetime dependence on Yb^{3+} concentrations [76]

The fluorescence lifetime decreases noticeably at concentrations of more than 0.1 %. At lesses concentrations, the fluorescence lifetime becomes constant at 110 μm, within measurement errors. This result indicates that the $^1G_4$ level is quenched at a concentration of more than 0.1 %, similar to the case of ^3P_J transitions. Remillieux et al. report that a slight reduction of the $^1G_4$ level also is observed in the 0.02 - 0.1 % concentration range [75]. This suggests that there are still some interacting Pr^{3+} ions which degrade the lifetime. Pr^{3+} ions become isolated from each other at concentrations below 0.02 %.

Figure 3.14b shows the Pr^{3+} and Yb^{3+} lifetime dependence on Yb^{3+} concentrations for the $^1G_4 \rightarrow {}^3H_5$ fluorescence of Pr^{3+} and the $^2F_{5/2} \rightarrow {}^2F_{7/2}$ fluorescence of Yb^{3+} in ZBLAN [76]. The concentration of Pr^{3+} remained constant (0.3 %), and that of Yb^{3+} changed from 0.1 to 2 %. The fluorescence lifetime was determined as the first *e*-folding time of the fluorescence decay curve. The lifetime of the $^1G_4 \rightarrow {}^3H_5$ fluorescence for the Pr^{3+} (0.3 %)–Yb^{3+} (0.1 %) system was 0.225 ms and was longer than that of single 0.3 % doped Pr^{3+}. On the other hand, the fluorescence lifetime of $^2F_{5/2} \rightarrow {}^2F_{7/2}$ of Yb^{3+} for Pr^{3+} (0.3 %)–Yb^{3+} (0.1 %) co-doped glass was 1.49 ms and was shorter than (1.89 ms) of single 0.1 % doped Yb^{3+}. The fluorescence lifetime of Pr^{3+} increased and that of Yb^{3+} decreased with an increase of the Yb^{3+} concentration. The energy transfer efficiency in the Pr^{3+} (0.3 %)–Yb^{3+} (0.2 %) system was estimated from a fluorescence lifetime measurement of Yb^{3+} [77] to be 22 %, a result which is apparently due to the low concentrations of Yb^{3+} employed. The energy transfer from Yb^{3+} to Pr^{3+} increases to about 56 % if 0.3 % Pr^{3+} is co-doped with 2 % Yb^{3+} [78]. Therefore, the pumping efficiency can be improved by optimizing the concentration of Pr^{3+} and Yb^{3+}. Forward transfer of energy from Yb^{3+} to Pr^{3+} is relatively likely, while back transfer of energy from Pr^{3+} to Yb^{3+} is relatively unlikely, largely as a consequence of the short lifetime of the Pr^{3+} $^1G_4$ level. The Pr^{3+} ion concentration, if doped alone, should not be more than 0.1 % because of concentration quenching. However, if Yb^{3+} ions are added, the energy transfer rate from Yb^{3+} to Pr^{3+} following an increase of Pr^{3+} effective lifetime. The increase of energy transfer rate compensates absorbability reduction due to Pr^{3+} ion concentration quenching. This shows it is possible to increase the concentration of Pr^{3+} [79]. Loyano et al. describe a linear dependence of the fluorescence emitted by the Pr^{3+} ions by increasing Yb^{3+} concentration in fluoroindate glass pumped at 976 nm [55]. For Yb^{3+} contents larger than 1.5 %, a deviation from the linear behaviour is observed. The fluorescence intensities increase slower and reach some saturation. All these results suggest that the optimum dopant concentration is 0.3 % of Pr^{3+} with 2 % of Yb^{3+}.

4 Fiber lasers

After concentrating on theoretical considerations and spectroscopic properties of laser materials doped with rare earth ions, we will now consider lasers which emit in the visible range of the spectrum with a focus on fiber lasers doped with Pr^{3+}. However, at first we will recall the main properties of optical fibers.

4.1 The structure of an optical fiber

An optical fiber is a cylindrical dielectric waveguide made of low-loss materials such as silica glass. It consists of a central part called the *core* in which the light is guided, surrounded by a material called the *cladding*, as shown in Figure 4.1 for a step index fiber.

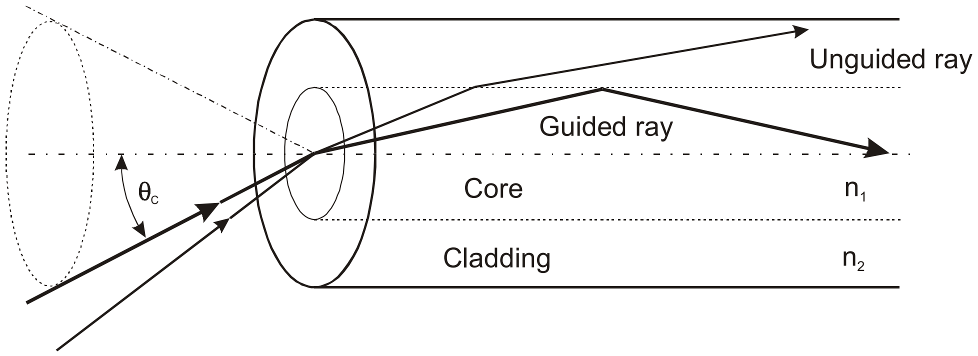

Figure 4.1: The schematic structure of an optical step index fiber

The core has a refractive index n_1, which is higher than that of the cladding n_2. Therefore, electromagnetic waves can be confined in the core region and are transmitted by total internal reflections at the boundary between the core and cladding. Additionally, the fiber is shielded by an acrylate coating. The coating protects the fiber from physical damage and chemical attacks by moisture. Optical fibers replaced copper coaxial cables as the preferred transmission medium for electromagnetic waves and revolutionized communications. Applications range from long-distance telephone and data communications to computer communications in a local area network. If a fiber core is doped with rare earth ions it can be used as an active material in fiber amplifiers and lasers.

An important parameter of the fiber is the numerical aperture (*NA*) which is defined as:

$$NA = \sin\theta_c = \sqrt{n_1^2 - n_2^2} \ . \tag{4.1}$$

So, the *NA* is a measure for the refractive index difference. The importance of the *NA* becomes clear when we realize that it is related to the maximum acceptance angle θ_c at which radiation can be trapped in the fiber core and at which it radiates into space when escaping from the end of the fiber. If the angle of the ray to the axis inside the core is smaller than the θ_c, then complete reflection occurs and the ray continues to propagate along the core, since all subsequent reflections occur at the same angle and therefore with no additional loss of energy. On the other hand, if a ray enters at an angle greater that θ_c, then the energy is lost by refraction into the cladding and possibly beyond. It may, however, undergo total internal reflection at the cladding-air interface and, thus, be able to propagate down the fiber to some extent, although the attenuation is expected to be high. This is an example of a *cladding mode*.

Optical fibers can support a number of guided waveforms called modes. Single mode fibers support only one waveform, the fundamental mode, which can exist in two mutually orthogonal polarisations [80]. Multimode fibers support a large number of modes. The relations between the properties of a given dielectric optical waveguide and the properties of the waves guided by it, can most easily be described by introducing a dimensionless quantity, the so-called *normalized frequency V* [81]:

$$V = \frac{2\pi a}{\lambda} NA. \tag{4.2}$$

The normalized frequency combines in a very useful manner the information about three important experimental design variables: the core radius a, NA and the operating wavelength λ. When $V < 2.405$, the fiber supports only the fundamental mode, and all higher modes are cut off. From the definition of the normalized frequency (4.2), the corresponding cut-off wavelength λ_c is defined as:

$$\lambda_c = \frac{2\pi a}{2.405} NA. \tag{4.3}$$

For wavelengths larger than the cut-off value, the fiber operates as a single mode waveguide. Single mode operation is achieved by using a small core diameter and small NA, or by operating at a sufficiently long wavelength. The fundamental mode has a bell-shaped spatial distribution similar to Gaussian distribution. This mode provides the highest confinement of light power within the core.

To calculate the power launched into the fiber input end one needs to know the radial amplitude distribution both in the core and in the cladding. From the fact that the fundamental fiber mode is very similar to a free Gaussian beam, one can conclude that the Gaussian function is a close approximation [81]:

$$E(r) \approx E_0 \exp\left[-\left(\frac{r}{\omega_0}\right)^2\right], \tag{4.4}$$

where ω_0 is the field radius of the fundamental mode or the *spot size*. The *mode field diameter (MFD)* is two times the spot size. The mode field diameter usually is slightly larger than the core diameter. The *MFD* can be determined from an analytic approximation accurate to within 1 % for $1.2 < V < 2.4$ and given by [82]:

$$MFD = d\,(0.65 + 1.619/V^{1.5} + 2.879/V^6), \tag{4.5}$$

where d is the core diameter and V is the normalized frequency mentioned above.

4.2 Loss mechanisms in optical fibers

The optical attenuation or power losses which occur as a light beam passes through a fiber are due to a variety of mechanisms and a function of the wavelength of radiation. Several factors contribute to the overall loss as shown in Figure 4.2.

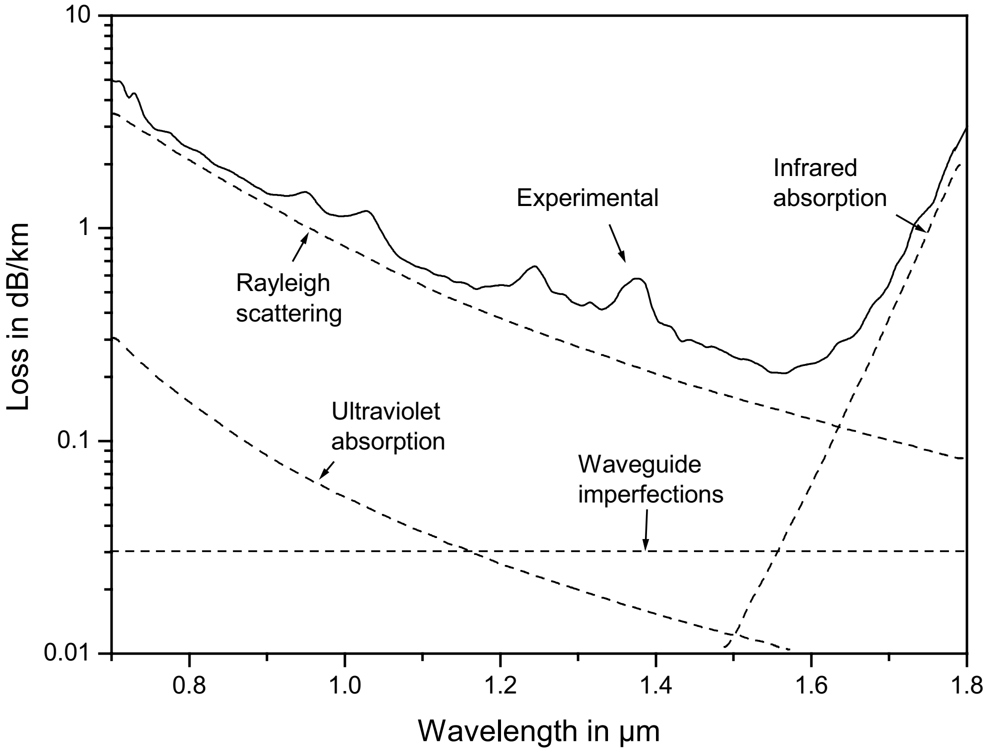

Figure 4.2: Contribution of various mechanisms to the spectral loss of optical fibers [83]

The transmission loss of the fiber consists of intrinsic and extrinsic losses. Intrinsic losses are inherent in the material and hence unavoidable. The most important among them are ultraviolet and infrared absorptions, and Rayleigh scattering. At short (usually ultraviolet) wavelengths, optical absorption occurs if the energy of a single photon causes electrons in the material to jump from the valence to the conduction band. The details of this electronic absorption process are not well understood, but experimental data for many materials show that the attenuation caused by it decreases exponentially with increasing wavelength [12]. This electronic absorption intensity decreasing with wavelength is a negligible contribution to the overall attenuation beyond about 1 µm.

Scattering of light is the second process contributing to the intrinsic transparency curve. Rayleigh scattering is a fundamental loss mechanism arising from local microscopic fluctuations in density. In glass, individual atoms are arranged in a random, non-periodical fashion that reflects the disordered structure of the liquid from which they are formed upon cooling. There exist small, localized fluctuations in the refractive index of the material caused by variations in density or composition on a scale that is small compared with the wavelength of transmitted light. This small scale granularity results in Rayleigh scattering of light. The scattering loss is proportional to λ^{-4}. This means that the amount of scattered light increases as the wavelength decreases.

In the infrared range, the transparency of an optical material is limited by loss due to lattice vibrations. The loss depends on the vibration modes of the constituent atoms and molecules. If the frequency of the incident light is the same as that of the intrinsic lattice vibration, the light is strongly absorbed by the material. This was described in chapter 2.2 in detail.

Extrinsic factors include absorption due to impurities and contamination in the material, such as transition metal, rare earth ions, hydroxyl (OH) groups and water, as well as light scattering from particles, crystals or bubbles in the glass. An ideal fiber with a perfect geometry guides a mode without energy leakage into the cladding layer. In practice, imperfection at the core-cladding interface (e.g. random core-radius variations) can lead to additional losses, the so-called waveguide imperfection losses [83].

4.3 Comparison of bulk and fiber lasers

Even though the basic active media are identical, there are important differences between bulk glass lasers and glass fiber lasers. Generally, the gain coefficient will scale monotonically with pump intensities. Obviously by focusing more strongly into the gain medium, a smaller spot can be produced but only at the expense of a more rapidly diverging pump beam. For a given length of the gain medium, there exists an optimum focusing condition for a bulk glass.

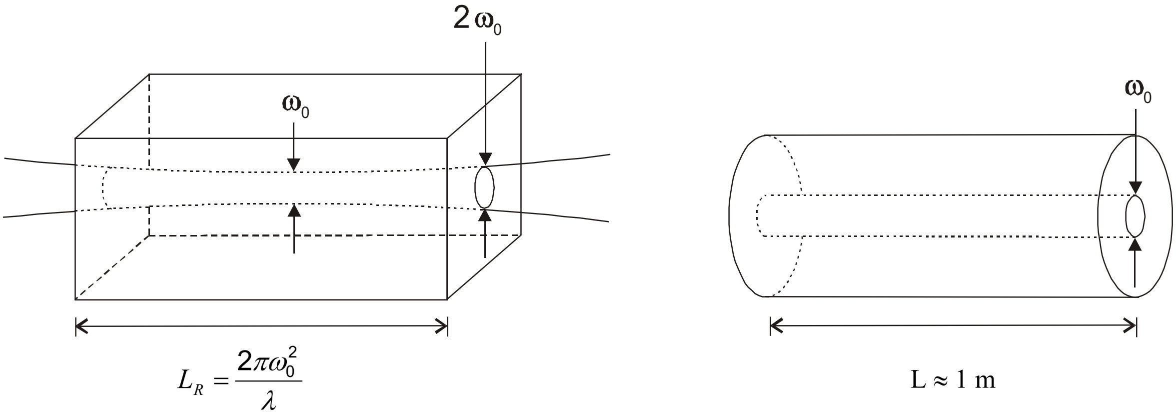

Figure 4.3: Sketch of: (a) a bulk glass laser, (b) a fiber laser [84]

This is shown in Figure 4.3a. Since the length needed for the active medium is determined by pump absorption requirements, the length and the pump spot size are not independent parameters when designing a bulk device. In a fiber laser the situation is somewhat different (Figure 4.3b). The considerable advantages of the fiber configuration arise from the fact that the pump radiation travels along the axis of the fiber and is guided by the core together with the lasing radiation. Once power has been launched into the core, then that power continues to propagate down the fiber until it is completely absorbed. There is, therefore, a very efficient coupling between the pump radiation and the ions. Fibers offer a convenient means for confining the pump beam as it interacts with the rare earth ions over lengths exceeding several meters. This is an attractive property of fiber lasers since the lengths of bulk crystal are, in contrast, generally limited to a few centimeters. This allows choosing a laser cavity length for optimum performance, rather than being restricted to crystal growth size. Another advantage of a fiber is that the pump spot size and the device length are now independent parameters. For fiber lasers pumping efficiencies approaching 100 % become possible, and slope efficiencies exceeding 60 % have been measured, as have threshold pump powers of a few hundred microwatts. In a conventional crystal laser, on the other hand, high power is achieved by tight focusing which then limits the effective pumping length through divergence [85].

The fiber geometry is particularly beneficial when the pump absorption is weak or the stimulated emission cross section for the rare earth transition of interest is small. In a large number of cases, transitions which have been demonstrated to lase at room temperature in fiber lasers have required cooling for lasing to occur in a crystal. Fiber hosts also allow for reduced rare earth concentration to be used in those situations in which ion-ion interactions are bad for the pumping efficiency or increase the upper level deactivation rate [86]. Furthermore, since the cross-section area of the core for a single mode fiber is on the order of 10 μm^2, enormous power densities can be achieved, around $1.5 \cdot 10^8$ W/m^2, for only 1 mW input power. This combination of power density with long interaction lengths leads to a low lasing threshold and permits CW diode-laser-pumped operation of three-level lasers; whereas, bulk lasers with glass hosts usually operate only with a pulse output and often require a supply of considerable pumping energy to obtain significant depletion of the ground state population necessary to achieve lasing. The small core diameters for the fiber also account for the beam quality of fiber lasers which typically produce radiation in the fundamental Gaussian mode. Because the host is a disordered medium, rare earth-doped glass fibers exhibit absorption and emission profiles that are broader compared to the characteristics of crystals. The width of the emission spectrum and its negative impact on the stimulated emission cross section are compensated by the fiber length and the pumping intensities discussed earlier. The broad absorption spectra associated with rare earth ions in glass have favorable implications for pumping lasers with diode lasers. Fiber lasers are small, robust, flexible, and give easy access to the laser cavity which allows great flexibility in laser design, thus enabling the operation of Q-switching, mode-locking and line-narrowing to be carried out. Because of the large fluorescent linewidths, large tuning ranges have been reported, over 70 nm in erbium, 150 nm in ytterbium, and 300 nm in thulium [87]. Moreover, fiber lasers are ideal for medical applications in which the flexibility and small size of the fiber leads to ease of insertion, for example, into the stomach [8]. Fiber-to-fiber compatibility is also a clear advantage particularly in fiber telecommunications systems, allowing all-optical circuitry to be assembled with both active and passive components.

Thermal advantages offer another reason for considering fiber geometry. Simply as a result of the fiber dimensions, heat dissipation from the fiber core is far more efficient than from the pumped regions of bulk glass lasers. Heat removal and thermal management are much simpler with a thin elongated fiber, and the waveguide nature helps to prevent thermally inducted beam distortion. Thermal lensing and stress problems as well as decreases in fluorescence occurring at higher temperatures that can be encountered in bulk devices, are rarely a problem for fiber devices. The development of the double-clad fiber geometry, which allows efficient coupling of the output of high-power diode lasers bars into a single mode fiber core, has led to the demonstration of a Yb^{3+}-doped silica fiber laser producing over 1 kW of output power in single mode CW at 1.1 μm [88]. High efficiency of low-loss Yb-doped fiber lasers over 80 % is possible. That means that even a 1 kW fiber laser generates no more than ~200 W of heat.

In comparison to many solid-state and glass laser systems, fiber lasers are simpler and more compact. Glass lasers have high power consumption, low efficiency and low output power. Compared to laser diodes, fiber lasers are spectrally cleaner and can be modulated with less signal distortion. Semiconductor lasers do not cover the entire spectral range. In fiber lasers, the emission wavelength depends on the rare earths doped and the transition selected. Fiber lasers can generate radiation in a span from 0.38 to 3.9 μm [89]. Therefore, fiber lasers are also of interest because they provide a means of generating laser radiation at wavelengths for which there are currently few or no solid-state lasers sources, particularly in the spectral regions lower than 0.63 μm and higher than 2.0 μm. Semiconductor lasers suffer from intrinsic limitations such as low power density, unstable temporal behaviour and low beam quality [90]. The beam cross section of a semiconductor diode is elliptical, which is a disadvantage in some applications.

4.4 Fiber laser applications in the visible spectrum range

Many applications in industry and life science have initiated the development of sources in the visible spectral range. Important biotechnological, pharmaceutical and medical measuring procedures, such as the confocal microscopy and flow cytometry, are based on laser-induced fluorescence detection technologies. Fluorescent dyes are used for marking specific components of cells or specific parts in solution. The dyes can be stimulated with a laser and then re-emit the light with an offset to the red, a longer wavelength, which will be detected. Doing so, it is possible to perform very sensitive, efficient and automatic measurements or visualizations on the biological sample. A lot of different fluorescent dyes are common, each with a specific range of absorption and emission mainly in the visible spectral range. Upconversion fiber lasers have the potential to replace gas lasers or to open this application to further dyes by the availability of new laser wavelengths [84]. Almost all known human life-threatening diseases can be diagnosed by cytology, the study of the properties of single cells, using tunable visible lasers of a few mW power.

Fluorescence correlation spectroscopy is an application example for fiber lasers. It is a procedure to measure the mobility of individual molecules. To detect molecules in a chemical solution, a sharply focused laser beam is obligatory. Molecules marked with a fluorescent dye light up as soon as passing the focus. The emitted photons are counted by using a sensitive detector. The real time signal depends directly on the number and the brightness of the molecules in the focus. The temporal variation of the signal indicates the average number of the molecules in the focus as well as the speed of the molecules. So the fraction of small sized, fast moving molecules and larger, lower speed molecules, can be determined. This bonding behavior is typically for the chemical characteristics of the chemical reaction investigated as well as for the influence of other substances; for instance, potential active substances for ethical drugs. Optical parameters of argon ion lasers can be well reproduced by upconversion fiber lasers. Therefore, they are excellently suited for use in analytical or medical instrumentation systems [91].

For small hand-held displays red, green, and blue lasers emitting less than 1 mW of total optical power will probably be sufficient, though for larger displays several watts of optical power are required [30]. Three laser beams (blue, green, red) are used for exposing photographic paper, films or printing plates. Depending on the spectral sensitivity of the materials used for these colors, upconversion fiber lasers have the potential to replace one or more lasers in the different setups being used today. Further applications of upconversion fiber lasers are in the field of imaging, metrology, sensing and spectroscopy [84].

4.5 Praseodymium-doped ZBLAN fiber lasers

The first rare earth-doped fiber for use as an optical amplifier was developed as early as 1964, only four years after the invention of the laser, when light amplification in a neodymium-doped multimode fiber was reported by Koestler and Snitzer [92]. Little interest was shown in such devices, however, until the mid 1980s when two key events took place. These where the development of chemical vapour deposition techniques for the manufacture of high quality doped fiber preforms, and the recognition that erbium-doped fibers could be used as optical amplifiers for telecommunication systems. Since 1987 a huge amount of research has been carried out worldwide in the development and applications of rare earth-doped fiber amplifiers and lasers. The discovery of fluoride glass in 1974 originated a new class of active components in the visible range. This was due to a lower energy of phonons that implied a smaller contribution to multiphonon relaxation, thus increasing the number of metastable excited levels in fluoride glasses as compared to silica. A summary of the visible wavelengths at which upconversion fiber lasers have operated in silica and fluoride glass hosts is shown in Figure 4.4. Silica fibers incorporating rare-earth ions as the active medium are not particularly good for visible lasers. There is only one wavelength in visible range demonstrated in a silica fiber doped with Sm. Compared with silica fiber lasers, fluoride fiber lasers offer a wider range of wavelengths. The shortest wavelengths yet generated from a glass fiber laser are those available from Nd^{3+}-doped ZBLAN. In 1994, Funk et al. reported the first fiber laser on the edge of ultraviolet, operating at 381 nm, when pumped at ~590 nm [93]. Lasing was also observed at 412 nm by the same authors [94]. In 1990, the first upconversion-pumped visible fiber laser was demonstrated in Tm^{3+}-doped ZBLAN fiber cooled to 77 K [95]. When pumped simultaneously at 647.1 and 676.4 nm, it emitted at 455 nm or 480 nm.

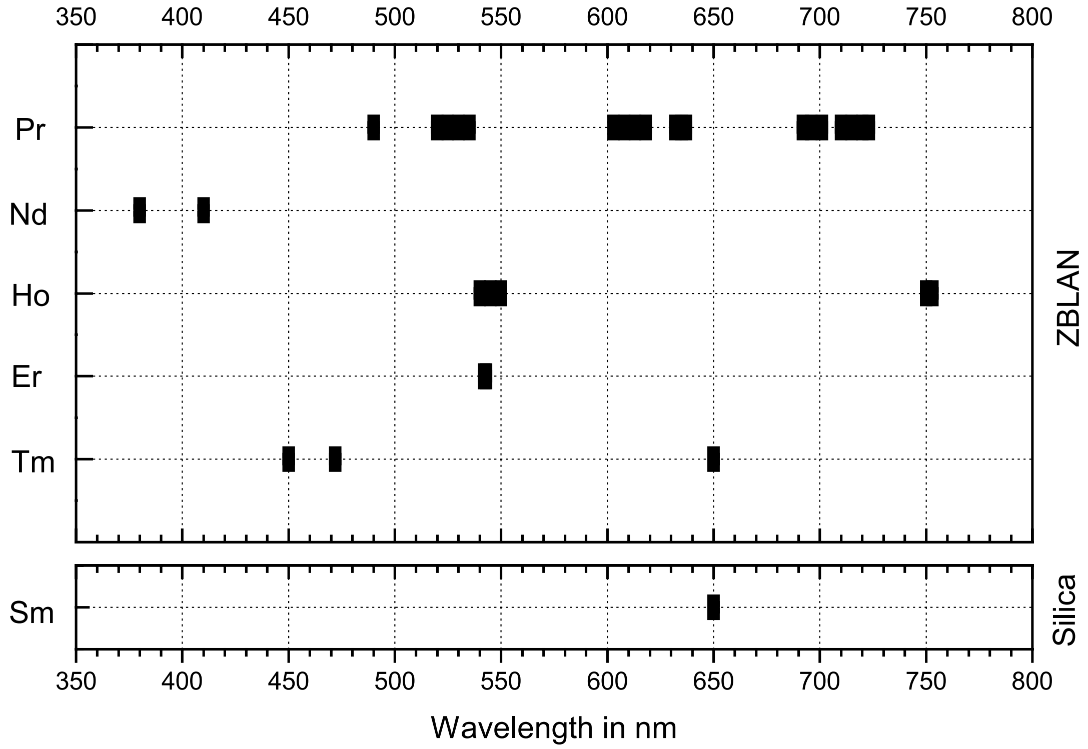

Figure 4.4: Wavelengths of visible laser and near-ultraviolet laser transitions demonstrated in rare earth doped fluoride and silica fibers [10]

In 1992, the first room temperature operation of the 480 nm line in any Tm^{3+}-doped host was demonstrated in ZBLAN fiber; it was pumped by a Nd^{3+}-doped YAG laser operating in the 1112-1123 nm spectral region [96]. The room-temperature, upconversion pumped green Er^{3+}-doped ZBLAN fiber laser attracted much attention when it was first demonstrated by Whitley and co-workers in 1991 [97]. The emission at 546 nm was obtained only at single pump wavelength, typically 800 nm or 970 nm, which was accessible by existing laser diodes. Ho^{3+}- upconversion emission is also a potential candidate for realizing green lasers. The green transition at around 550 nm has been successfully pumped in the near-infrared (750 nm or 890 nm), but it is most efficient when pumped in the red (640 nm-645 nm) [98]. However, the broadest emissions in the visible range of the spectrum show fibers doped with Pr^{3+}. This dopant offers laser transitions in blue, green, orange and red by the same pumping scheme. In view of the significance of this dopant, we will describe in further considerations the development of Pr^{3+}-doped fiber lasers in detail. A summary of the laser characteristics of Pr^{3+}-doped ZBLAN fiber lasers reported in the literature is given in Appendix A.

The first demonstrations of lasing in the red, orange [21] and subsequently, the green and blue [28], in Pr^{3+}-doped ZBLAN fiber was reported in 1991. In these initial experiments the upper laser levels were populated by direct excitation from the ground state using the 476.5 nm line of an argon laser. In the same year, two methods for upconversion pumping of the visible lasers were demonstrated [10]. Smart and co-workers pumped a Pr^{3+}-doped fiber simultaneously at 1020 nm and 835 nm [25]. Lasing was then observed at blue (491nm), green (520 nm), orange (605 nm) and red (635 nm) wavelengths. In the work of Allain and co-workers, a pumping scheme requiring only one pump source was demonstrated [34]. In this case, the Pr^{3+}-doped ZBLAN contained Yb^{3+} as a co-dopant. The pumping process was already described in chapter 2.4.3. The ability to achieve pumping with a single pump source represents a significant advantage.

Since these first demonstrations of lasing in Pr^{3+}-doped ZBLAN, steady progress has been made in developing this laser in large part due to improvements in fiber fabrication. Reduction in fiber core diameter has been achieved by going to a larger numerical aperture, and fiber propagation losses have been reduced. Improved fibers, combined with improved pumping schemes, have now lead to greatly improved results [99]. One approach, described by Pask, involves a pumping scheme requiring a single initial pump source, based on the use of an Yb-doped silica fiber, itself pumped at 835 nm, and selected to lase at 1020 nm by way of a fiber Bragg grating [100]. The Yb fiber output then consists of unabsorbed 835 nm and 1020 nm light, both of which are needed to pump the Pr^{3+}:ZBLAN upconversion laser.

Several of the most efficient and highest power upconversion pumped fiber lasers have been observed in the Pr^{3+}/Yb^{3+}-codoped ZBLAN fiber pumped at about 840 nm. Xie and Gosnell reported efficient and high-power operation of the 635 nm transition [33]. 300 mW of output power was generated for 760mW of launched Ti:Sapphire pump power yielding an optical conversion efficiency of 39 %. The authors show also a possibility of continuous tunable laser operation over each emission line.

For most applications output power plays an important role. The output power of upconversion fiber lasers was for a long time restricted to direct pumping of a small (3-5 µm) fiber core that supports only a single spatial mode. Therefore, pump diodes had to be single mode diodes. However, the power of single mode pump sources is limited to 0.2-0.3 W. This drawback was overcome by a double-clad fiber design. In these fibers, the active fiber core is surrounded by a second fiber core which acts as a large diameter waveguide for the pump light. Using this technique, the multimodal pumping radiation from the high-power diode lasers can be effectively converted into laser radiation with excellent beam quality. The main design problem of the double clad fiber is to find a geometry for an efficient coupling of the pump light from the pump core to the laser core [101]. Zellmer et al. demonstrated a cladding-pumped upconversion laser in Pr^{3+}/Yb^{3+}-co-doped ZBLAN [102]. With a pump power of 6.5 W, an output power of around 2 W at 635 nm and 0.3 W at 520 nm has been achieved. The drawback of the double clad design is a poor pump light absorption resulting in low optical efficiency since only a small area of the pump core is doped with active ions. This causes a large laser threshold of 2 W.

The Pr^{3+} system offers the advantage of having a single manifold (^3P_J) that undergoes several radiative decay processes to produce emissions across the visible spectrum. This is an advantage because a single upconversion pumping scheme can potentially be used to simultaneously produce laser output at widely spaced, multiple wavelengths in the visible spectrum. Baney et al. demonstrated a Pr^{3+}/Yb^{3+}-doped ZBLAN fiber laser which emitted simultaneously at 521 nm and 492 nm [103]. Similar results were presented by Zellmer and co-workers [35]. At a pump power of about 1.6 W, a multi-line output power of 230 mW was achieved. The distribution of the power was approximately 75% in the 491 nm line and 25 % in the 520 nm line. Salewski in his Ph. D. thesis demonstrated the possibility for color switching between blue and red laser emission [104]. A combination of dielectric mirrors mounted on the fiber end faces with external feedback optics, together with direct modification of the mirror reflectivity by variation of the thickness of a dielectric mirror layer (adjustable air gap between fiber end face and cavity mirror) enabled both a variation of the wavelength-dependent losses of the laser resonator and switching continuously between different colors of laser emission or even achieving simultaneous operation at different wavelengths.

Active mode locking of Pr^{3+}/Yb^{3+}-doped fluoride fiber laser with an all-fiber ZnO acousto-optic modulator was demonstrated by Costantini and co-workers [105]. Optical pulses of ~550 ps duration with a repetition rate of 239MHz at a wavelength of 635 nm have been generated. The piezoelectric fiber-optic phase modulator consisted of concentric Cr/Au electrodes and a ZnO piezoelectric coating that formed a cylindrical actuator around a standard telecommunication fiber. The active ZBLAN fiber and the all-fiber phase modulator were butt-coupled to each other.

Pr^{3+}-doped fibers can also be used for the design and the realization of a fluoride glass optical fiber amplifier for signal light at a wavelength in the red spectral region. Petreski and co-workers described small-signal amplification at the 635.8 nm He-Ne wavelength with a slope efficiency of 0.15 dB/W and up to 14 dB gain [106]. Scheife reported about 1.38 W of maximum signal power extracted from an amplifier based on Pr^{3+}/Yb^{3+}-doped ZBLAN fiber [107]. The amplifier responds to the intensity modulation of the signal light with frequencies ranging from 10Hz to 100 MHz.

4.6 Semiconductor diode lasers for the visible spectrum range

In order to generate the light in visible spectrum range, semiconductor materials could also be used. Semiconductor diode lasers have many attractive characteristics. They are small and efficient and they have long operating lifetimes. They are also capable of producing high powers of up to several watts cw from a very small laser. Unfortunately, most semiconductor lasers operate in the near-infrared spectral region due to the inherent nature of their energy levels. However, in recent years significant progress has been made in engineering special semiconductor materials that provide energy levels in the visible spectral region which can lead to population inversion and gain [118].

Semiconductor laser materials are manufactured by doping the semiconductor with other materials having either an excess (*n*-type) or a deficiency (*p*-type) of electrons when compared with the pure semiconductor materials. Such doping involves implanting a small amount of *p* and *n* materials in the semiconductor in a narrow spatial region located adjacent to each other. Such a spatial region is referred to as a junction. If an electric field is applied across this junction, the excess electrons in the *n*-type material are pulled into the *p*-type material creating an overpopulation of electrons or a population inversion in the medium.

These electrons then recombine with vacancies (holes) of that material and produce a recombination radiation. This radiation leads to the generation of laser radiation if the geometry of the semiconductor is suitably designed.

The approach of making visible semiconductor lasers has been to use special mixtures of materials that lead to large energy gaps consistent with a visible emission. Red and orange diode lasers have been made in InGaP/InGaAlP strained layer quantum well materials at a wavelength as short as 0.6 µm. The quantum well is a special class of heterojunction in which the thickness of the active region is less than the deBroglie wavelength of the electron in the semiconductor materials. Basically, the electron and the hole are confined so tightly in space that discrete energy levels arise due to the wave-particle nature of the electron-holes. This effect causes electrons and holes in the subbands to recombine, and the emission is blue-shifted to larger energies than the bulk junctions [119]. Also, lasers have been made in AlGaAs lattice matched materials at wavelengths as short as 0.68 µm. The semiconductors based on GaAs, which also consist of III-V compounds, cannot reach the shortest wavelengths; the only choice is offered by II-VI semiconductors centered around zinc selenide, as shown in Figure 4.5. The first diode lasers at short visible wavelengths (in the blue-green, 480 nm - 520 nm) were indeed demonstrated in ZnSe. Among II-VI semiconductors, ZnSe appears to be well-suited for blue light emitting devices, not only because of its band gap, but also because it is very close to that of GaAs. ZnMgSSe-, ZnSSe- and ZnCdSe-based materials have been studied for blue and green light emission devices [120].

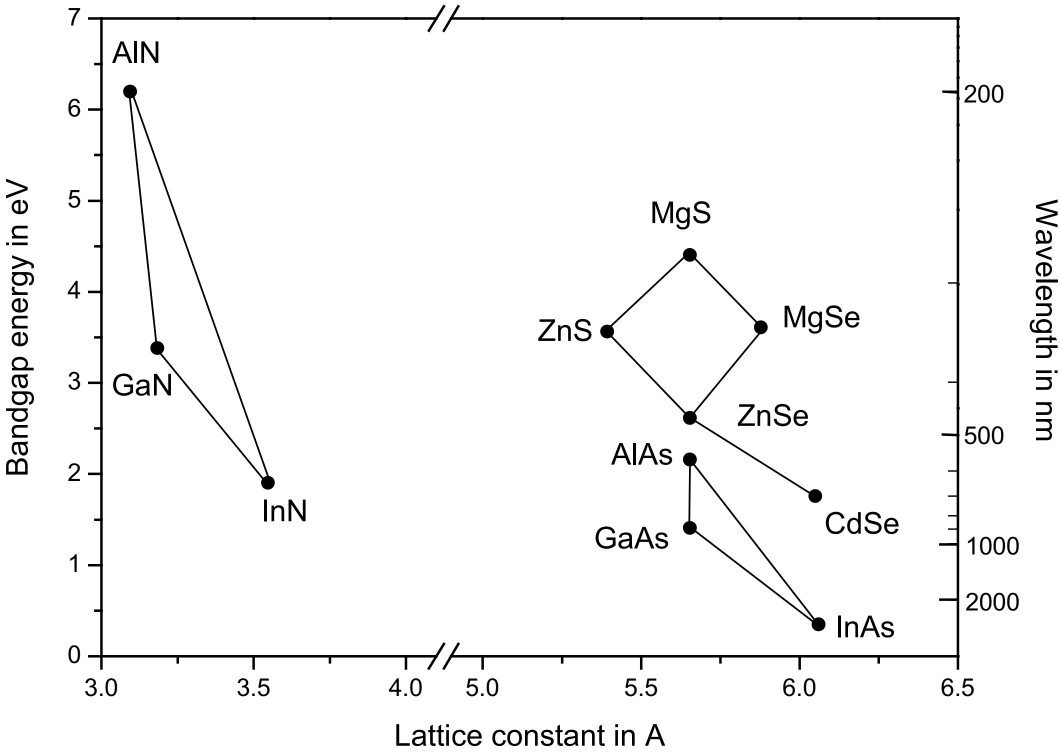

Figure 4.5: Bandgap energy versus bond length for various semiconductors [120, 121]

The nitride materials represent the next group of wide bandgap semiconductors anchored at GaN with its room-temperature bandgap of 3.4 eV, corresponding to the wavelength of 365 nm, in the ultraviolet. The other constituent materials are aluminum and indium alloys, $Al_xGa_{1-x}N$ and $In_xGa_{1-x}N$, which have bandgaps that are compositionally over much of the near-ultraviolet and visible range [121]. So far, AlGaInP laser diodes in the 650 nm red-light range have been commercialized, and 400 nm range blue-light AlGaInN laser diodes have been developed to the stage of practical use. It is, however, difficult to realize laser diodes in the middle visible range (green-to-yellow); i.e., 500 nm-630 nm in wavelength.

4.7 Second harmonic generation

In addition to the fiber lasers and semiconductor diodes, another method to obtain the light in the visible spectrum range is a second harmonic generation. This process occurs only in those materials which have a nonlinear response to an electric field. The explanation of nonlinear effects lies in the way in which a beam of light propagates through a solid. The nuclei and associated electrons of the atoms in the solid form electric dipoles. The electromagnetic radiation interacts with these dipoles causing them to oscillate which, by the classic laws of electromagnetism, results in the dipoles themselves acting as sources of electromagnetic radiation. If the amplitude of vibration is small, the dipoles emit radiation of the same frequency as the incident radiation. However, as the irradiance of the radiation increases, the relationship between irradiance and amplitude of vibration becomes nonlinear, resulting in the generation of harmonics of the frequency of the radiation emitted by the oscillating dipoles. Thus, frequency doubling and higher order frequency effects occur as the incident irradiance is increased. Harmonic generation is only observed in those solids that do not possess a center of symmetry [63].

A nonlinear process can be described in terms of a photon model, according to which we can view harmonic generation as the annihilation of two photons of angular frequency ω and the simultaneous creation of one photon of frequency 2ω. The simplest nonlinear optical effect is harmonic generation, the production of light waves at integral multiples of frequency of the original wave. The second harmonic is at twice the frequency of the original wave or, equivalently, at half its wavelength. Most materials have small nonlinear coefficients, so only a few materials are usable for second harmonic generation. Special conditions must be met for the interaction between input and output beams. Because nonlinear effects are small, they usually appear only at high input powers. This makes it easier to generate harmonics from short pulses with high peak power than from continuous wave beams with a much lower steady power [122].

Frequency doubling of 1.06 μm-Nd-lasers is one of the methods for generating the green color. The simplest devices are sandwiched laser systems of microchip laser material and frequency doubler. Another simple approach is self-frequency doubling in nonlinear crystals doped with laser active ions [123]. The blue light can be produced using $KNbO_3$ crystals to frequency double GaAlAs diode lasers.

Unfortunately, radiation in the spectral region between 550 and 650 nm cannot be generated with second harmonic generation because of the absence of efficient fundamental lasers. Other ways of generating coherent light at these wavelengths have to be found. One possibility is sum frequency generation in which coherent radiation of frequencies ω_1 and ω_2 is mixed, generating radiation of frequency $\omega_3 = \omega_1 + \omega_2$. Sum frequency mixing of diode pumped Nd-lasers operating near 1.06 µm and 1.44 µm can be used to generate light in the red spectrum at the 618 nm wavelength [123].

The most important disadvantage of second harmonic generation is the phase matching condition which requires a strict control of the temperature of both the second harmonic generation material and the laser diode, and an accurately defined pumping wavelength of the laser diode.

5 Results of measurements on visible fiber lasers

In previous chapters we concentrated on the theoretical aspects of laser operation and spectroscopic measurements on Pr^{3+}/Yb^{3+} glass probes. The knowledge gained there is useful for this chapter, where results of measurements on blue, green, and red lasers will be presented in different configurations. At first we will present lasers based on the most simple configuration, the Fabry-Perot setup.

5.1 Fiber laser configuration

Most investigations on lasing action, in which a rare earth doped fiber lasers was the active medium, are using a Fabry-Perot resonator. The fiber laser is a waveguiding, resonant device. The waveguide is the optical fiber, with a Fabry-Perot cavity formed by mirrors at both ends of the fiber. A fiber laser is, in effect, a wavelength converter. Photons at the wavelength of the pump beam are absorbed and produce the population inversion and stimulated emission necessary to give a lasing output at a wavelength which is characteristic for the dopant in the fiber. The experimental fiber laser setup is illustrated in Figure 5.1.

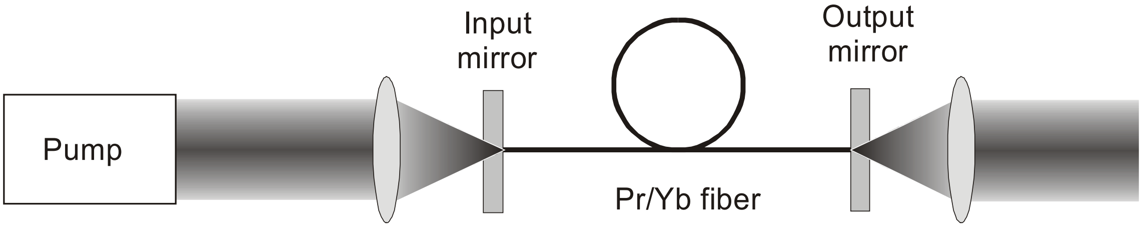

Figure 5.1: Schematic diagram of the Fabry-Perot fiber laser setup

In order to generate visible light using an upconversion process a pump laser source of lower frequency is needed. In our case it was a Ti:Sapphire laser. The pump light was focused on the fiber end by a lens and launched into the fiber core through an input laser mirror, which was butted against the fiber front face. Care had been taken to maximize the power launched. The core of this fiber was doped with Pr^{3+} and Yb^{3+}. In order to obtain best results the input mirror should be highly reflective at the emission wavelength and highly transparent at the pump wavelength. A second, partially reflective laser mirror completed the fiber laser cavity. The choice of the optimum reflectivity at the lasing wavelength of this output mirror depends on the gain of lasing medium [124]. In a low gain system it should be 95 % or more, but when high gain values are available, the reflectivity to maximize the lasing output power even 4 % Fresnel reflection may be sufficient. In many reports the output mirror is transparent at the pump wavelength so that any unconverted light is coupled out of the system. However, in most situations it is preferable that the output mirror reflects the pump light to maximize the pump absorption and hence the excitation [125]. A second lens collimates the light coming out from the fiber laser. Figure 5.2 shows a photograph of the fiber laser setup used.

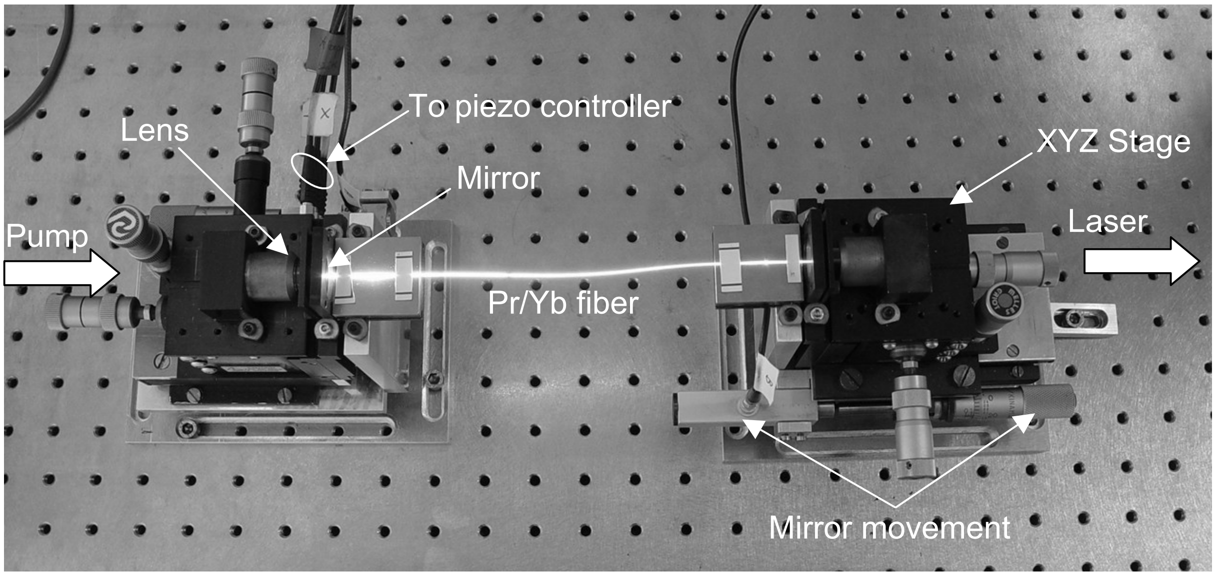

Figure 5.2: The fiber laser setup used to a characterize of a laser

The input lens system is assembled in a special holder which is placed on the XYZ stage. With the help of three micrometer screws it was possible to adjust for an optimum position of the lens. The pump laser had to be focused on the fiber core of only few micrometers in diameter, and therefore built-in actuators were used for fine adjustment. In Figure 5.2 we see the wires which were connected to the piezo controller. The fiber has shown a bright, white luminescence when the pump power was launched into the core at optimum. An additional micrometer screw and a piezoelectric actuator were used to adjust the butt coupling between the fiber ends and the mirrors. Below we will discuss individual components of the experimental setup in detail.

5.1.1 Ti:Sapphire laser

The titanium sapphire ($Ti:Al_2O_3$) laser is the most widely used tunable solid-state laser. It can be operated over a broad tuning range. However, a tuning range from about 700 to 1050 nm requires several sets of cavity mirrors. The Ti:Sapphire laser used in our experiments was pumped by an argon ion laser and can be tuned over a range of 750 to 860 nm, with the peak of the gain curve around 800 nm. The optimum pump wavelength for our Pr^{3+}/Yb^{3+} fiber was around 840 nm, and this pump wavelength was used in the experiments described below. The Ti:Sapphire laser was able to emit over 1 W of output power, but the main problem was the the poor beam quality as shown in Figure 5.3.

A single mode fiber, as used in the experiments, can be matched well only to the fundamental Gaussian mode TEM_{00}, the so-called Gaussian beam. With this beam we obtain the largest coupling ratio. If the shape of the laser beam departs from the Gaussian profile the coupling ratio decreases. During the experiments, the beam quality of the pump laser was continually monitored by a beam analyser, and if necessary, the beam quality was corrected by adjustment of the laser mirrors. This assured always a maximum coupling to the fiber.

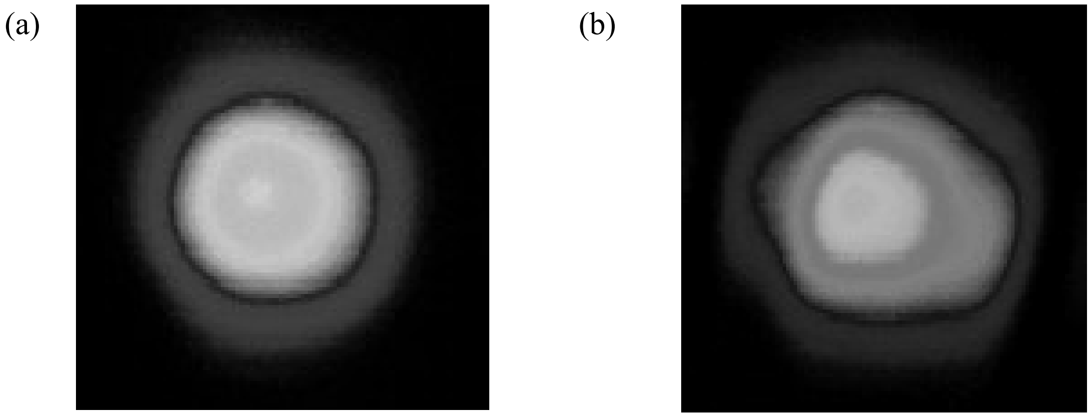

Figure 5.3: Cross-section of the pump laser beam at (a) 400 and (b) 600 mW

However it was difficult to obtain a sufficiently good Gaussian beam above 500 mW of output power as it is shown in Figure 5.3b. Therefore, fiber laser characteristics were usually measured only with pump powers below 500 mW. Above this value a pseudo-saturation of the fiber laser was noticeable. In reality it was not a fiber laser saturation but a decrease of the coupling ratio, caused by a degradation of the beam quality of the pump laser.

5.1.2 Coupling of pump power to a fiber

In order to couple radiation from a pump source into a fiber, the beam must be matched as close as possible to the lateral intensity profile and phase front of the mode that is to be excited in the fiber. For optimum coupling a circularly symmetric Gaussian laser beam should be focused so that its beam waist is matched to the equivalent Gaussian profile of the propagating mode, which means to the mode field diameter of the fiber. Additionally, the beam axis must coincide with the fiber axis, and the beam waist must be located in the fiber front face [126]. If the front end of the fiber is illuminated with a focus spot, which is too large, a significant amount of energy enters higher order modes which leak out to the fiber cladding and possibly beyond. The same happens when the focus spot is too small.

Several types of misalignment are possible. First, there may be a mismatch of the field widths of the focusing laser beam ω_0 and the fundamental fiber mode ω_G. A 15 % mismatch of the spot sizes causes a launching loss of 0.1 dB. Second, a transverse offset may exist between the beam and the fiber axis. For the launching loss to be smaller than 0.1 dB, the offset must be smaller than $0.15\omega_G$, i.e. for $\omega_G = 5$ µm, smaller than 0.8 µm [81]. Therefore, for efficient coupling of pump light into a fiber core piezoelectric actuators are very useful, because they assure submicrometer movement accuracy. Third, there may be a longitudinal offset between the beam waist and the fiber input face. However, a slight defocusing of the laser beam causes only a small increase of loss. Finally, there may be a tilt between the beam axis and the fiber axis. In order to ensure launching losses to remain smaller than 0.1 dB, the tilt angle must be smaller than 1°. Usually, different sources of mismatch loss will exist simultaneously. Nevertheless, the coupling loss is significantly more sensitive to lateral misalignment than to either longitudinal or angular misalignments.

Let us consider a Gaussian beam with spot size ω_I entering a lens of focal length f. The spot size value ω_0 in the waist position after the lens is given by [127]:

$$\omega_0 \cong \frac{\lambda f}{\pi \omega_I}. \tag{5.1}$$

Hence, by selecting a lens with a suitable focal length f it is possible to transform an input spot size ω_I to an output spot size ω_0 equal to the fundamental fiber mode ω_G. Unfortunately, our case it is more complicated. Between the lens and the fiber end a laser mirror is located. This mirror consists of multilayered dielectric stacks that have been deposited onto a glass substrate, which in our case had a thickness of 2 mm. The calculated optimal focal length for our setup (ω_0=ω_G=2 µm, ω_I=1.1 mm, λ=840 nm) amounts to 8 mm. This lens was installed in a housing, and the working distance was only 1.1 mm, which was too small. Looking to equation (5.1) we can notice that if we want to use a lens with a larger focal length we need to increase the input spot size. Therefore, we constructed a beam expander using two lenses. These lenses were selected in such a way that the enlarged spot size enabled an optimum match between the focused beam and the fundamental fiber mode (ω_0= ω_G) when a lens with a focal length of 14.5 mm was used.

5.1.3 The fiber end-mirror interface

The fiber endfaces must be prepared to a high quality. As far as possible, they must be flat and perpendicular to the fiber axis. In brittle materials like glass breaking occurs by the propagation of surface cracks, thus producing a flat and perpendicular fracture surface. Our ZBLAN fiber was cut with a special fiber cleaver (FK 12, York). The fiber was first fixed, a longitudinal tension was applied and then a blade made a score to initiate the brake. The cleaver used allowed to control the tension applied. This was important for obtaining a good surface quality as shown in Figure 5.4.

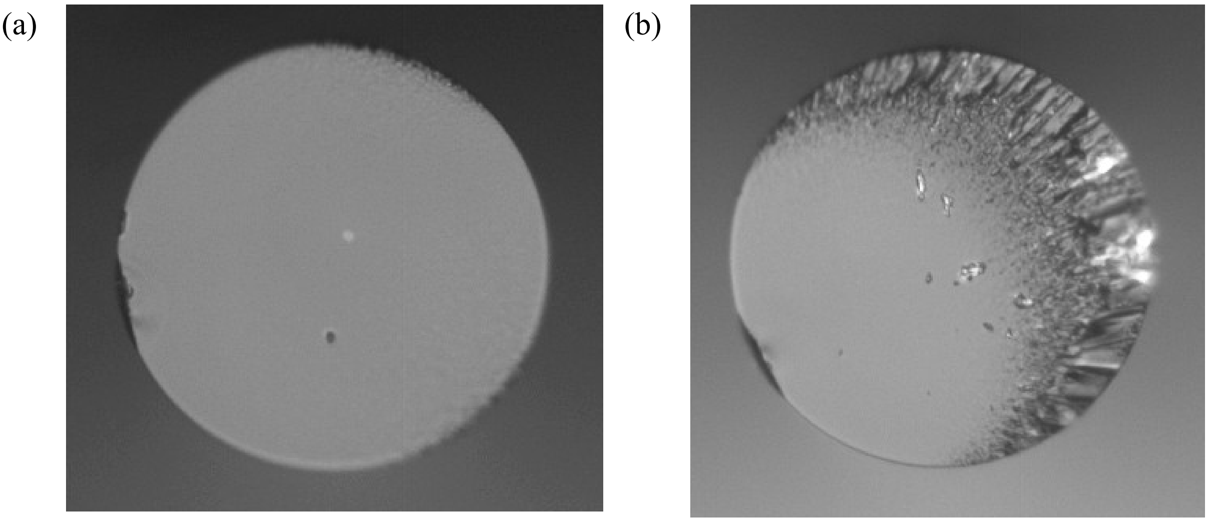

Figure 5.4: Microphotograph of a ZBLAN fiber end face done by:
(a) optimum tension (60 g), (b) too large tension (90 g)

We found that for our ZBLAN fibers a pulling tension of around 60 g produced good and reproducible results (Figure 5.4a). The surface was smooth and homogeneous. If the tension was too large, only part of the surface was mirror-like, and in Figure 5.4b we see also an area where the surface is inhomogeneous and rough. We see also small pieces of glass on the surface. Even when the fiber core was free from inhomogeneities we never obtained a good physical contact between fiber end and mirror surface in such cases.

The fiber end and the mirror must be mounted in such a way that they meet at an angle as close as possible to 0°. It is also desirable to avoid any air gap or tilt between fiber end and mirror surface. Another difficulty that arises in practice is fiber buckling which occurs if excessive force is applied in an effort to avoid separation. If we neglect the interferences the effect of a 2-3 μm gap between fiber end face and mirror surface may be one order of magnitude less serious than the effect of 1° of tilt. On its way through the small gap the Gaussian beam has merely diverged, but the peak intensity is still coincident with the fiber axis, and therefore the overlap with the guided fiber mode is high. In contrast, if a Gaussian beam meets a tilted endface, the intensity peak is off-axis and has a poor spatial overlap. So a few micrometers of separation can be acceptable, but even a small tilt may impose serious intracavity loss [128, 129]. In our experimental setup we used a fiber clamp which ensured an appropriate location of the fiber with respect to the mirror, and this setup is shown in Figure 5.5. The fiber is placed on a metal plate and it is clamped in a V-groove by two magnetic bands. The left magnet delicately holds down the fiber and prevents fiber movements. On part of the fiber the coating is removed, and this bare fiber is hold down by the second magnet. However, the diameter of the bare fiber and the V-groove size is matched in such a manner that the fiber can be moved inside the V-groove.

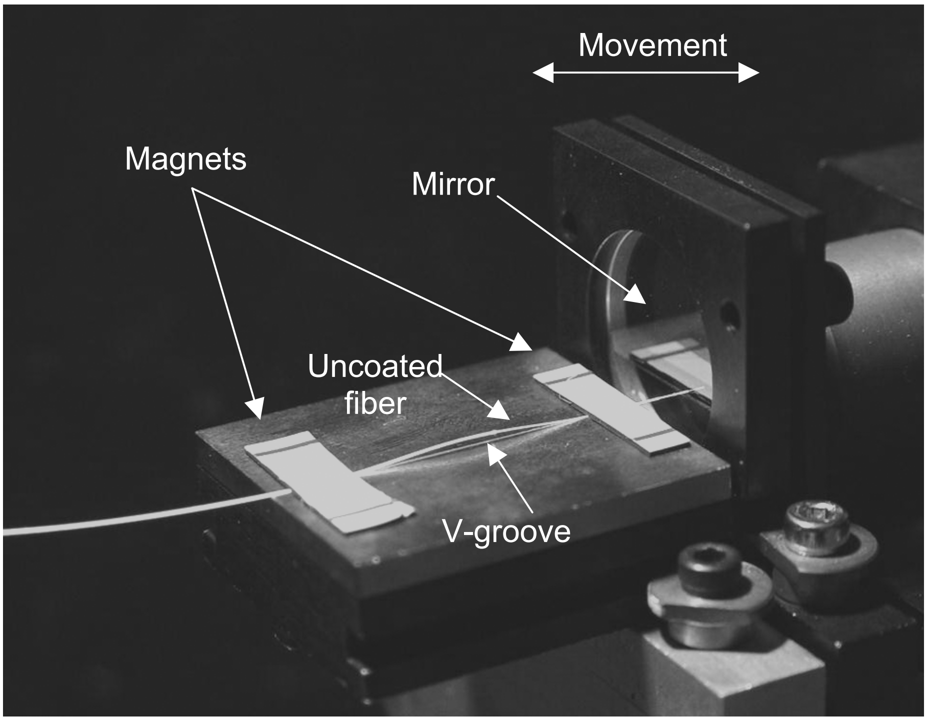

Figure 5.5: Photograph of our setup to connect a fiber end to a mirror by physical contact

In our setup it was possible to move the mirrors. We moved a mirror against a fiber end until physical contact was obtained. The possibility to move the fiber inside the V-groove assures that the fiber can be pressed against the mirror without a fiber break. We can be sure that the fiber has a good physical contact with a mirror when a part of the fiber between the two magnets buckles slightly. This buckling was usually very small, and was made large only for this photograph. The bare fiber was placed in the V-groove and pressed down by a magnet. Therefore, the fiber could be moved only perpendicularly to the mirror surface, and the probability for a tilt between fiber end face and mirror was minimized. Additionally, it was possible to move the mirror precisely by piezo actuators (see Figure 5.2). For input and output mirrors the same setup was used. The position of the mirrors was always optimised to obtain maximum output power from the fiber laser. The setup used here ensures reproducible contact at normal incidence. Evidence for the reliability of our fiber clamp system is the fact that after coupling a pump signal into the fiber it was possible to move the input mirror without significantly decreasing the power in the fiber.

An alternative method for providing the fiber with an end reflector is deposition of a multilayer dielectric mirror directly on its end face [130]. However end-coated mirrors are more sensitive to imperfections in the fiber endface, and cleaving must be performed to a higher standard. Secondly, if damage to the coating is caused by using excessively high power in the focused pump light, the whole fiber laser is in effect destroyed. In contrast, pump laser damage to bulk mirrors is usually restricted to a small area, and the fiber end can be moved relative to the mirror surface to reinitiate lasing.

5.1.4 Properties of ZBLAN fibers doped with Pr^{3+}/Yb^{3+}

Different active fibers, all made in the fiber technology department of our institute, were used for fiber laser investigations. In the above chapter on spectroscopy many interesting properties of IBZP glass were shown. Unfortunately, due to technological problems, it was impossible to make an IBZP fiber of sufficient quality here. Therefore, we will concentrate only on ZBLAN fibers. The fibers were fabricated using a 2-step rotational casting method. The first step was to melt a cladding material of appropriate composition. The melt was then poured into a cylindrical mold which was then spun around its axis to form a tube of cladding material. This tube was cooled, and the melt solidified at the wall, leaving a hole in the centre. The melt of the core composition containing rare earth ions was then poured into the hole and the whole structure cooled to room temperature. After removing the resulting rod from the mold, it was drawn to tiny sticks with diameters of 2-3 mm. Afterwards, such a stick was placed in the center hole of a second cladding tube, and a single mode fiber was drawn from this perform structure. Fiber drawing techniques for ZBLAN are similar to those established for silica preforms, but performed at lower temperatures (300 to 320°C). The parameters of the fibers used for our investigations are collected in Table 5.1.

Table 5.1: Parameters of the fibers used for fiber laser experiments.

Fiber	d in µm	NA	λ_c in nm	α @ 750 in dB/m	MFD @ 635 in µm	MFD @ 840 in µm	Pr^{3+} in %	Yb^{3+} in %
A	2.4	0.25	784	3.3	2.3	2.8	0.3	2
B	2.2	0.25	718	1.5	2.2	2.7	0.1	2
C	3.4	0.16	710	2.7	3.5	4.2	0.3	2
D	3.8	0.16	794	1.2	3.7	4.3	0.3	2

The fiber core diameter *d* and the NA were measured indirectly. These parameters were calculated for several wavelengths in range 750-1300 nm from mode field diameter (MDF) measurements with the fiber characterization device S25 from York. Knowing the MFD for different wavelengths and using equation (4.5) we were able to determine *d* and NA.

To obtain a waveguiding effect a fiber core must have a higher refractive index than the cladding. This was realized by adding PbF_2 to the core glass composition. An amount of 4 % Pb in the ZBLAN core glass yields a NA of 0.16. In order to further increase the NA, we can theoretically increase the amount of Pb in the core glass. However, this is not advisable because incorporating more than 4% Pb in ZBLAN causes the glass composition to become unstable, and microcrystals appear in the core. Therefore, to obtain a fiber with the high NA of 0.25, Zr was replaced by Hf in the cladding glass which lowers the refractive index. The fiber core was doped with the optimum amount of rare earth ions as determined by spectroscopic investigations, e.g. 0.3 % Pr^{3+} and 2 % Yb^{3+}. This is also the most frequently reported doping composition published in the literature (see Appendix A). Only fiber B in Table 5.1 has a reduced Pr^{3+} concentration of 0.1 %.

The cut-off wavelength λ_c was calculated from equation (4.3), and the MFD for the signal (635 nm) and the pump wavelength (840 nm) was determined using equation (4.5). An important parameter is the fiber loss α per unit length. We used a cut-back method for this measurement. A fiber of several meters in length was excited at 750 nm, the shortest wavelength emitted by our Ti:Sapphire laser. At first, the output power from the fiber was measured by a detector. Next, a piece of fiber (around 50 cm) was cut off without changing the launching condition. The output power from the remaining fiber was measured then. The difference between the results from these two measurements can be attributed to the length of fiber removed, and hence the absorption per meter can be calculated. This procedure was repeated several times, and an average loss was calculated.

The spectral loss distribution was also measured, and the results are shown in Figure 5.6. We can see that the background attenuation is larger for shorter wavelengths. This is caused by Rayleigh scattering and the ultraviolet absorption edge as discussed in chapter 4.2. Additionally, we see a large absorption peak at around 585 nm. This is caused by absorption of the $^1D_2$ level of Pr^{3+}. The attenuation increases also above 850 nm. This is caused by the Yb^{3+} absorption.

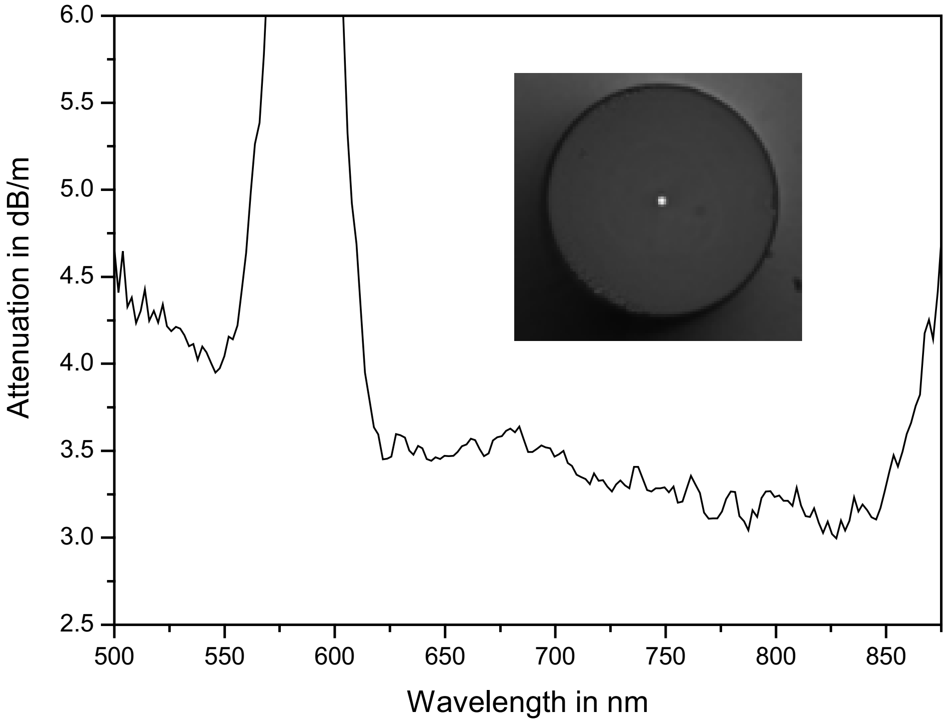

Figure 5.6: Measurement results of spectral losses of fiber A

In section 5.2.6 it will be shown that the optimum pump condition was obtained at 840 nm in spite of the fact that there is no noticeable small signal absorption at this wavelength. The reason is an avalanche pumping scheme of the Pr^{3+}/Yb^{3+} system. This absorption is induced at high pump power, as it was discussed in chapter 2.4.3. Spectral loss measurements showed a low repeatability, therefore the loss measurement at 750 nm was taken as an indicator of the fiber quality. Figure 5.6 contains also a photograph of a fiber endface. The luminous fiber core is circular and placed in the centre.

5.2 Visible fiber lasers in Fabry-Perot configuration

The Fabry-Perot setup, as described above, is the most simple and flexible resonator configuration. Therefore initial investigations were made using this construction. Blue, green and red fiber lasers were realized; the measurement results will be presented below. All lasers presented here were obtained using fiber A, pumped at 840 nm. We will start with a description of the setup used to measure the characteristics of the fiber laser.

5.2.1 Setup for fiber laser characterization

The laboratory setup used to measure the characteristics of fiber lasers is shown in Figure 5.7. Because of problems with the stability of the Ti:Sapphire laser a small fraction of the pump beam was directed to a beam analyser in order to monitor the shape of the pump beam online. Filter 1 was used to protect the pump laser from fiber laser radiation. For some setups the fiber laser emitted also in backward direction to the pump. Therefore we used a RG780 filter which was transparent for wavelengths above 780 nm, and below this wavelength the light was absorbed. Unfortunately, we had no isolator in our setup to protect the Ti:Sapphire laser from pump radiation reflections from a input mirror and the fiber end face. Such back reflections into the pump laser cavity deteriorate the beam quality. Nevertheless, if reflected radiation was exactly on the optical axis, the influence on the beam quality was at minimum, and thanks to a beam analyser we were able to obtain the optimum adjustment. However, this back reflection caused that a slightly higher pump power was obtained (about 5-15 %) than without reflections.

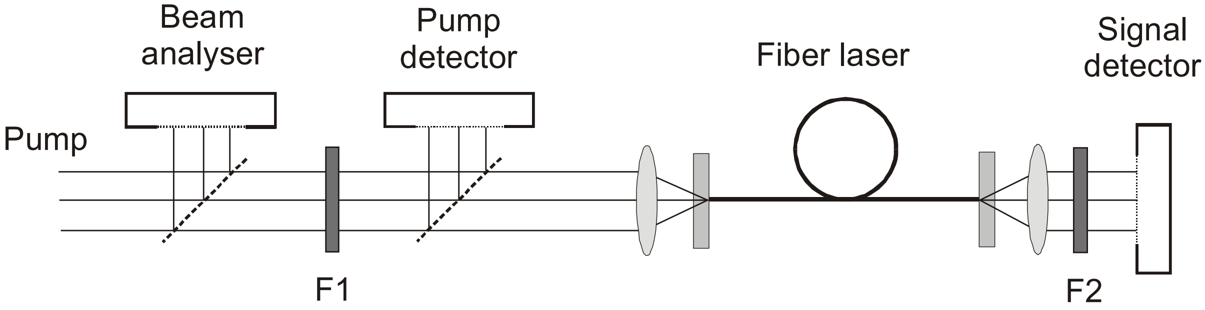

Figure 5.7: Setup used to characterize the fiber laser

In order to measure the pump power precisely, we used a pellicle beamsplitter to reflect a small fraction of the pump power to a detector (Thorlabs S120). After detector calibration we were able to make an online measurement of the pump power without touching the radiation coupled to the fiber laser. In this way an accurate measurement of the pump power was assured. The fiber laser output power was measured by a second detector (Newport 840). Radiation from the fiber laser contained not only the signal but also some amount of not absorbed pump power which was reflected by a second filter F_2 (03SWP412). This filter has a high transmission in the range below 650 nm and rejects wavelengths above. Therefore, only radiation from the fiber laser reached the detector.

5.2.2 Red fiber laser

The red transition ($^3P_0 \rightarrow {}^3F_2$) has the largest cross-section among all transitions starting from the ^3P_J levels (see chapter 3.4). Therefore, a red laser is very easy to realize. The gain for this transition is so large that it is possible to obtain laser oscillations without external mirrors, the Fresnel reflection is sufficient to excite laser oscillations. The Fresnel refection arises when a light beam passes through the interface between two transparent media with different refractive indices n_1 and n_2. The power reflection factor R is defined by:

$$R = \frac{(n_1 - n_2)^2}{(n_1 + n_2)^2} . \tag{5.2}$$

The power reflection factor R of a single interface between a ZBLAN fiber core glass ($n = 1.51$) and air ($n = 1$) amounts to 4.1 %.

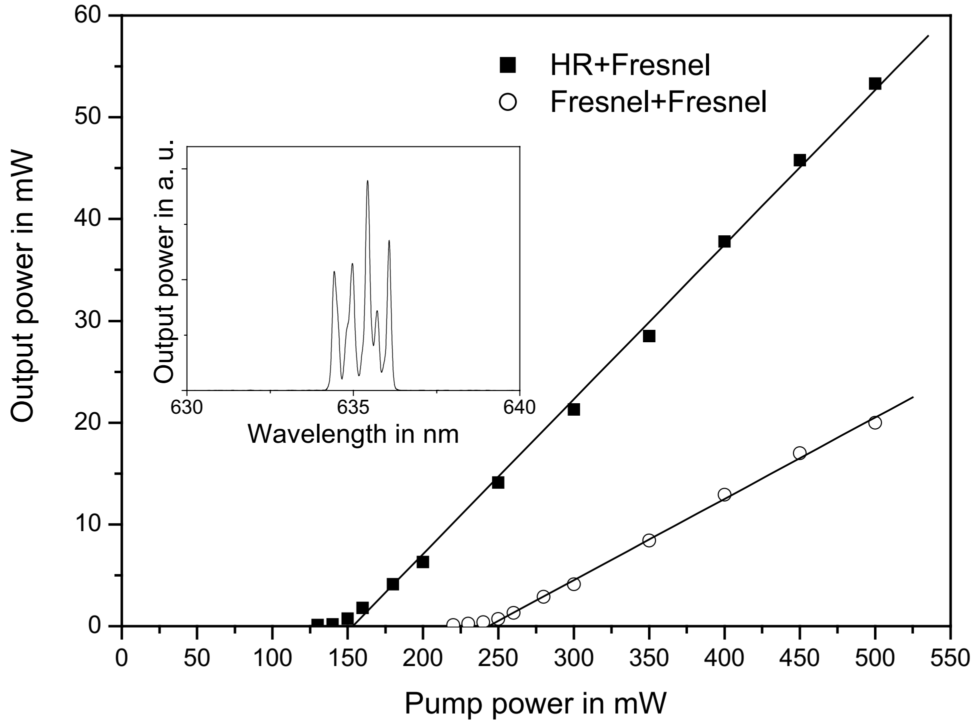

Figure 5.8: Laser characteristic of a red fiber laser

The setup of a red laser with Fresnel reflectors is very simple. It consists only of a piece of fiber with the fiber ends cut to good quality. No external mirror is needed. The photograph of such a fiber setup is shown in Figure B.1 in Appendix B. In the upper right corner we can see firstly a spectrum below threshold power. We can recognize blue, green, orange and red emissions as typical for a Pr^{3+}/Yb^{3+} ZBLAN fiber. This spectrum was obtained with the help of a diffraction grating (not visible on the photograph). Therefore we see two identical spectra. There are successive diffraction orders of this grating. However, if the pump power is high enough, we can obtain a red laser oscillations. We see in the photograph large red spots. Of course, a fiber laser cavity with two endfaces reflects only 4 % of the light and has a large round trip loss of 28 dB. Hence, such a laser has a large threshold power. In Figure 5.8 the red fiber laser output power is plotted versus the incident pump power. The fiber used in this experiment was around 40 cm long. This fiber laser had a threshold power of 244 mW, and 20 mW of output power were obtained with a pump of 500 mW. This leads to a slope efficiency of 8 %. We were able to improve the laser parameters significantly when we applied a special input mirror. This mirror had a high reflectivity (99 %) in the range 600-690 nm, and it was transparent for the pump wavelength. The fiber was butted against this input mirror, and the cavity was completed by the 4 % Fresnel reflection like before. Applying the HR input mirror caused the threshold power to decrease to 153 mW, and we obtained 53 mW of the output power when the incident power was 500 mW. Also the slope efficiency was doubled to 15 %. This laser with a highly reflecting mirror and cleaved ends showed the best performance as a strongly pumped red fiber laser as it will be shown in chapter 5.2.8. Figure 5.8 presents also a spectrum of fiber laser.

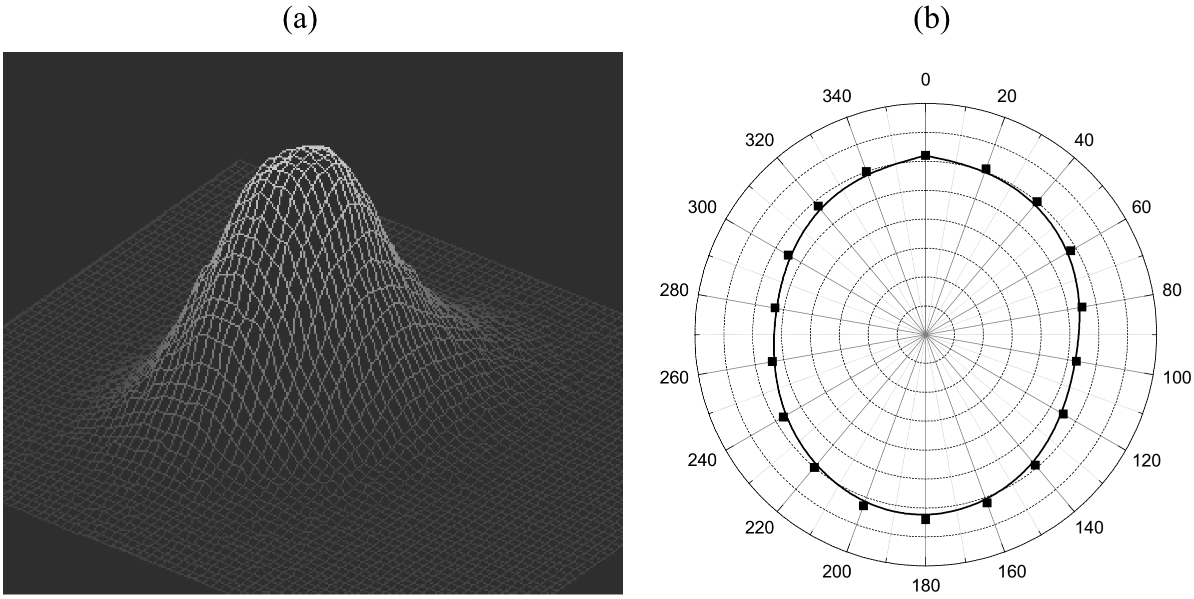

Figure 5.9: Red laser (a) intensity profile, (b) results of polarization measurement

The laser emitted at around 635 nm, and we see many longitudinal modes as typical for a Fabry-Perot setup. For a red laser we observed also an intensity profile by means of the beam analyser. Results of this measurement is presented in Figure 5.9a. For this experiment 58 cm of a fiber A were taken and the laser cavity consisted of a high reflecting input mirror and the output mirror had a reflectivity of 26 % at the signal wavelength. The fiber was slightly multi mode for 635 nm because the cut-off wavelength was 784 nm (see Table 5.1). Nevertheless, the intensity profile measurement indicated that only the fundamental mode was excited, however the cross-section of the laser beam was slightly elliptical. An important point was the fact that the fiber was single mode for the pump wavelength. Therefore the ion excitation distribution in the core reflected the fundamental mode of pump intensity and laser oscillation on the fundamental mode was a privileged compared to higher modes. We also investigated the polarization of this fiber, and results are presented in Figure 5.9b. As usual for fiber laser the polarization was not linear. The fiber core was not perfectly circular and this is the reason of the slightly elliptical cross-section of the intensity profile and probably also for the polarization profile.

5.2.3 Fiber laser emitting green light

The easiness to obtain a red laser is very helpful for designing a setup for red emissions. On the other hand, when other than red emissions are required, it is troublesome to suppress the red emission and one has to be very careful in selecting lasers mirrors. The reflections of these mirrors for red light should be as small as possible, otherwise the threshold of the red laser will be lower than that of the desired laser. The reflectivity of the mirror for a green laser as a function of the wavelength is shown in Figure 5.10.

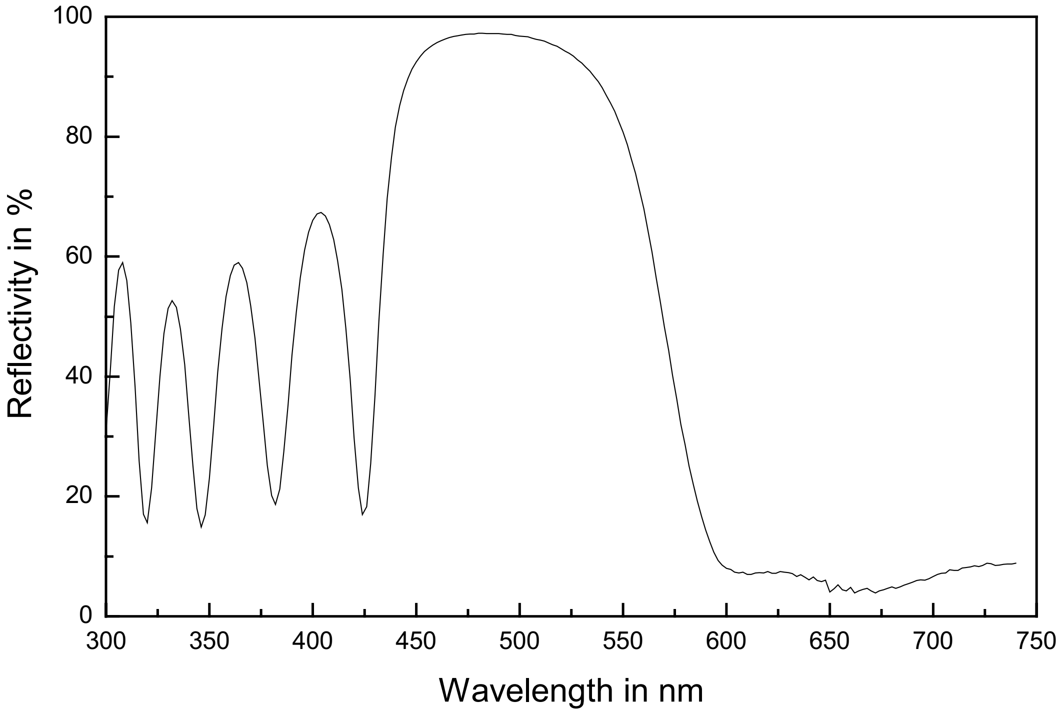

Figure 5.10: Reflectivity versus wavelength for a blue-green laser mirror

This mirror provided a high reflection of 95 % for the green (520 nm) and blue emission (490 nm). The reflection of around 5 % for the red transition at 635 nm was very small. This mirror had also good transmission at the pump wavelength. The cavity used to demonstrate laser emission at 520 nm consisted of two such mirrors butt-coupled to the fiber ends. A picture illustrating this setup is presented in Figure B.2 in Appendix B. As before we see a output spectrum below and above the laser threshold.

The $^3P_1 \rightarrow {}^3H_5$ transition has a much higher gain than the $^3P_0 \rightarrow {}^3H_5$ transition since the latter forbidden by quantum mechanical selection rules [40]. Thus, despite of the fact that the population of the $^3P_1$ level is only 5 % of the $^3P_0$ level at room temperature (Boltzmann distribution), the green emission is dominated by the $^3P_1 \rightarrow {}^3H_5$ transition. Laser action at 520 nm using the transition $^3P_1 \rightarrow {}^3H_5$ was investigated with two lengths of the fiber: 14 cm and 28 cm. In Figure 5.11 the output power versus pump power of the green laser is shown. The best performance was achieved with 14 cm of fiber length, for which a threshold of 173 mW and a slope efficiency of 3 % were obtained with respect to the incident power. A maximum power of 9.3 mW was achieved when the incident power was 500 mW. In the case of a fiber length two times longer than before, the laser was less efficient. We measured a threshold of 194 mW, and achieved a maximum of 5.4 mW as output power. For our laser cavity with 5 % output coupling an optimum fiber length exists. This will be discussed in chapter 5.2.5. The laser with the 14 cm fiber is closer to this optimum, therefore it shows better results. The spectrum of the green laser is also shown in Figure 5.11. We see several longitudinal modes around 520 nm.

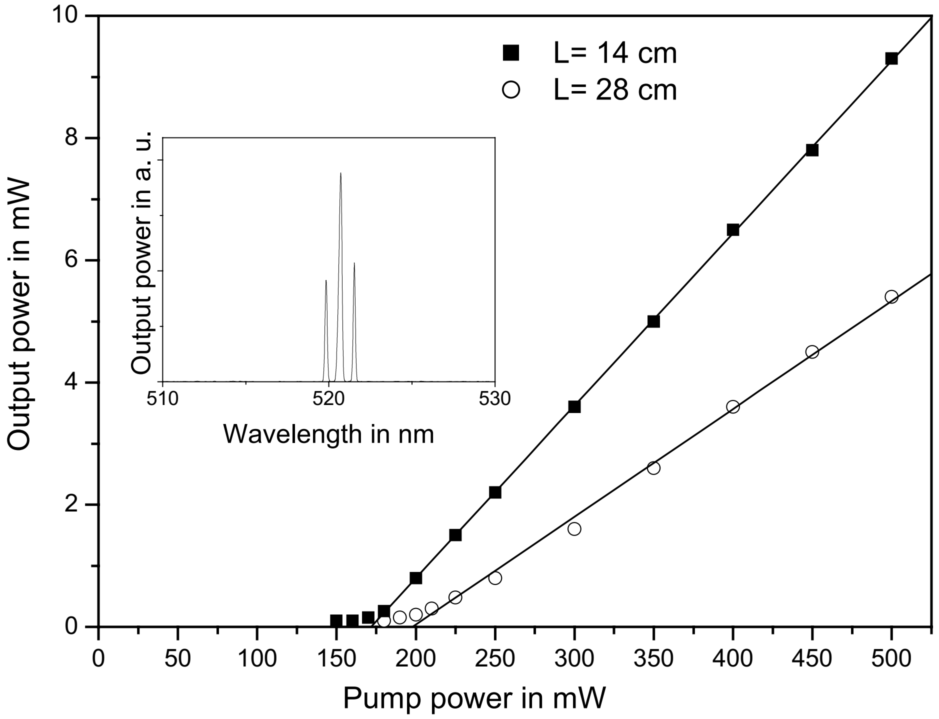

Figure 5.11: Output power at 520 nm as a function of pump power for two fiber lengths

We measured the output power from one end of the fiber. In our experiment both laser mirrors had the same parameters, which means that the same output power was emitted from the other end of the fiber towards the pump laser. So the full output power in this case actually was twice as large. Additionally taking into account a launch efficiency of 50 %, the total slope efficiency should be 4 times larger than measured.

5.2.4 Fiber laser emitting blue light

Blue laser action on the 3-level transition $^3P_0 \rightarrow ^3H_4$ has also been investigated. The same mirrors have been used as for the green laser, only the fiber length of 5.5 cm was considerably shorter. This can clearly be seen in Figure B.3 in Appendix B, where also a laser spectrum below and above the pump threshold is shown. A laser characteristic for the blue laser together with a laser spectrum is presented in Figure 5.12. The threshold power of 134 mW was measured, and a maximum output power of 4.8 mW was obtained when the incident power was 500 mW. The slope efficiency is small and amounts to just 1.3 %. Like in the previous experiment, the laser emits in booth directions. Of course, the performance of this blue laser could be further improved by using mirrors of appropriate design. It should be possible to improve the efficiency significantly by using an input mirror of high reflectivity at the signal wavelength. Taking into account a launch efficiency of 50 % and the loss of half of the laser power by the input mirror, the slope efficiency of our laser would be 4 times larger and amount to 5.2 %.

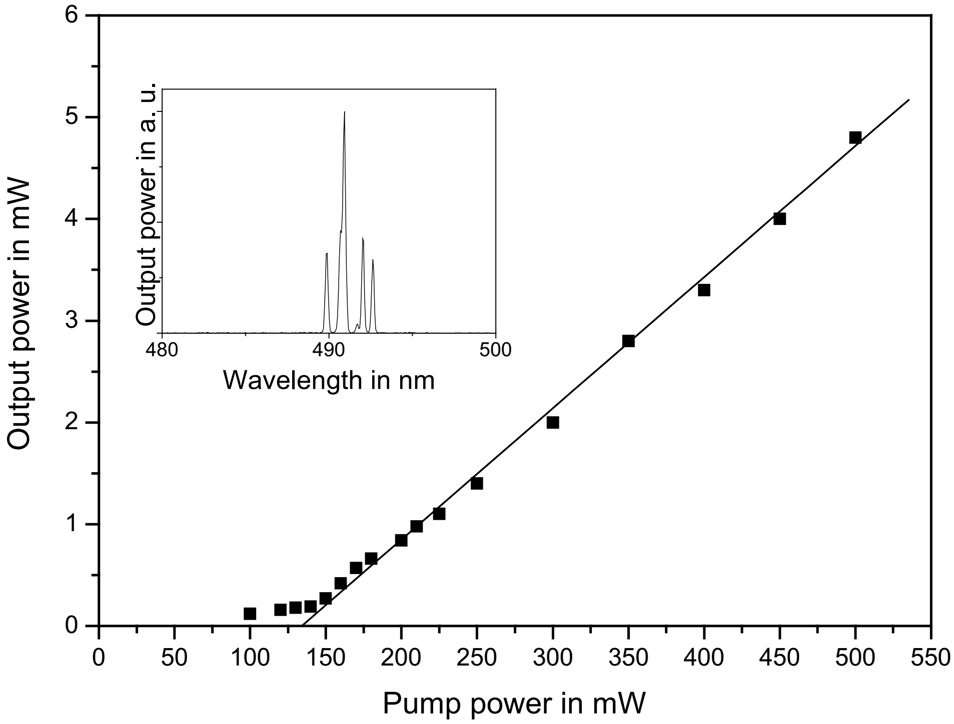

Figure 5.12: Laser output at 490 nm versus incident pump power (L = 5.5 cm)

The laser emitted at around 490 nm, but if we compare these results with fluorescence measurements (see chapter 3.4) we can notice that for a bulk glass the maximum emission in the blue range was measured at 480 nm. This discrepancy of 10 nm between fluorescence and laser emission peak is significant. The reason for this difference is the fact that the blue laser works in a 3-level system where we have not only emission from $^3P_0 \rightarrow {}^3H_4$, but also the ground state absorption $^3H_4 \rightarrow {}^3P_0$ with a maximum absorption peak at 479 nm (compare with chapter 3.3.1). This causes a competition with the emission of lasing photons. The influence of this ground state absorption is shown in Figure 5.13. The straight line shows the side-light spectrum from the fiber, e.g. the fluorescence in transversal direction was collected. Photons generated by spontaneous emission are emitted in all directions, and some of them are not guided in the fiber core, e.g. they leak to the cladding and eventually out of the fiber. The spectrum of this side-light fluorescence is the same as that obtained from a bulk glass. The maximum emission peak is reached at 480 nm. We measured also a fluorescence spectrum for the same fiber as before, but this time we collected light leaving the fiber end face (dashed line). The fiber investigated had a length of 30 cm, so the light excited near the fiber front face had to travel a long distance to the fiber end face. During this travel the light suffered from ground state absorption (reabsorption), and the maximum emission peak in the blue range is shifted to 490 nm. For green light there is no difference between transverse and longitudinal fluorescence because it is a 4-level system, and the excited state absorption is negligible. Since the $^3H_4 \rightarrow {}^3P_0$ transition at 490 nm corresponds to a 3-level laser scheme, the fiber could not be arbitrary long because of a reabsorption loss on passing down the fiber.

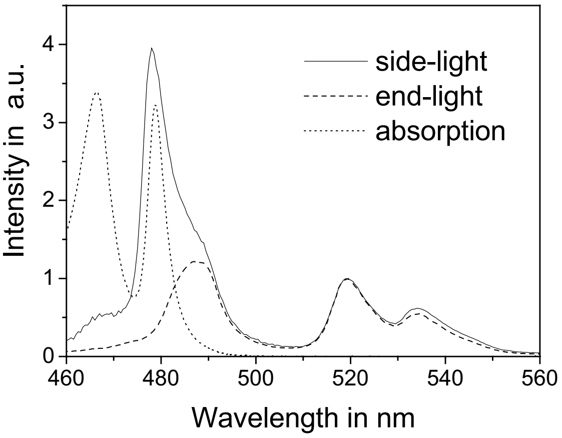

Figure 5.13: Spectrum of fiber emissions

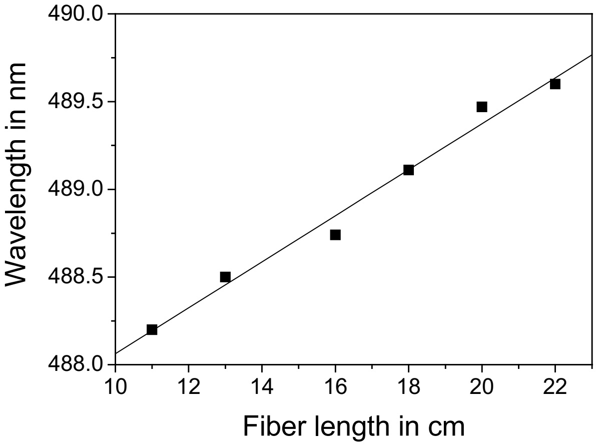

Figure 5.14: Emission wavelength vs. length

The blue laser requires a very short fiber length to obtain a laser emission which causes problems for the handling. Therefore, in the next experiment a fiber B with a reduced Pr^{3+} concentration was chosen. For this fiber the optimum fiber length was around two times longer than for the fiber A. This made the handling easier. The reabsorption has also an influence on the wavelength emitted, as it is shown in Figure 5.14. At the beginning the fiber was quite long (22 cm), and we obtained a maximum emission at 489.6 nm. Then the fiber was successively cut back, and we measured the emission wavelength of a blue fiber laser with a still shorter fiber. By increasing the fiber length the peak gain is shifted to longer wavelengths where reabsorption from the extra fiber length is minimized. And finally, when the fiber was 11 cm long, the maximum emission occurred at 488.2 nm.

5.2.5 Laser characteristic for different fiber lengths

In order to obtain an optimum fiber performance the fiber length for specific mirrors has to be found. Figure 5.15 depicts the output powers and the threshold powers of fiber lasers versus the fiber lengths. The output power was always measured at 500 mW of pump power, and we used the same mirrors as for the blue and green lasers. The x-axis in the graph is presented in a logarithmic scale in order to show better the changes for a blue laser. The experiment started with a fiber length of 150 cm and proceeded by cutting pieces from the fiber end without changing the pump conditions. After each cut back the optical contact to the mirror at the newly cleaved end was again optimized. It was difficult to obtain always the same conditions for the connection between the fiber and the output mirror for each measurement, therefore the measurements have a large uncertainty. Additionally, it was impossible to cut a fiber shorter than 11 cm without taking it out of the laser setup. With such a short fiber the pump power had to be aligned after every cut, which leaded to additional errors. Despite of these experimental difficulties these measurements can show a general tendency. With the long fiber we obtained red lasers although the reflection of the laser mirrors at this wavelength was only around 5 %. However, the gain of the red laser was so high that a tiny reflection was sufficient to excite laser oscillations.

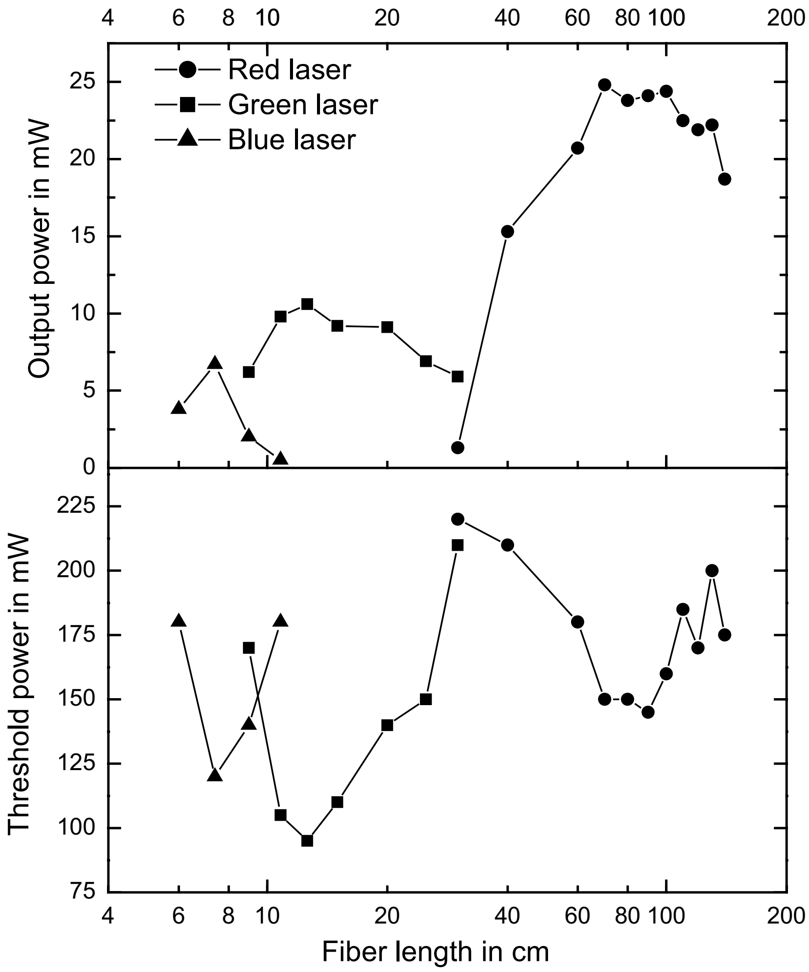

Figure 5.15: Output power and threshold power as a function of the fiber length

It can be seen that a fiber length around 80 cm is at optimum for the red laser, e.g. to get the maximum output power of 24 mW at the minimum threshold power of 150 mW. If the fiber length is shortened further, the output power of the red laser decreases and the threshold power increases. Finally, we obtain a red laser simultaneously with a green one. The losses caused by coupling out a large percentage of red radiation are constant, but a shorter fiber provides lower gain, and finally the losses exceed the gain, and only the green laser remains. The green laser has also an optimum fiber length, where an output power maximum of 12 mW at a threshold power minimum of 95 mW was obtained. This optimum fiber length is around 12 cm. When the fiber is shortened further, the green laser becomes weaker, and the blue laser starts. This laser has an optimum fiber length of around 7 cm. For very short fibers it was difficult to achieve just one, clear blue laser emission because the green laser runs often simultaneously with the blue one. A solely blue emission was reached by gently changing the connection conditions between the fiber and the mirrors. The blue laser is a 3-level system, and therefore it is necessary to pump with higher power to obtain a population inversion. The number of available pump photons, and hence the population inversion, is greatest at the launch end. If the fiber is too short, there it will be insufficient absorption of the launched pump radiation and hence low gain. If, on the other hand, the fiber is too long at the output end, there will be reabsorption of lasing photons to repopulate the upper lasing level, and so the available output power is decreased. The optimum length of fiber for a 3-level laser is that which reduces the pump power to the saturation power at the output end. By saturation power we mean that the power needed to excite half of the ions into the upper level [131]. The green and red lasers are 4-level lasers, and the reabsorption does not occur. Therefore, after reaching the optimum length, a further fiber elongation should not play a significant role. However, the fiber A used had large background losses, and if the fiber was too long, the laser emission was attenuated. Nevertheless, using the same setup we where able to obtain red, green and blue lasers by changing only the fiber length. Additionally, simultaneous emission of two lasers was possible by choosing only a suitable fiber length. This was possible due to the fact that all these emission lines started from the same manifold ^3P_J, and only by changing the laser cavity parameters we could select the emission wavelength.

5.2.6 Optimal pump wavelength

In order to obtain the best laser performance, the optimum pump wavelength had to be found. We pumped the 33 cm long fiber A by the Ti:Sapphire laser and measured the fluorescence signal at 635 nm. The pump laser was tuned in the spectral range between 800 and 860 nm. Results of this measurement are presented in Figure 5.16. The pump power at the fiber front face was held a constant 100 mW. During this measurement, the main difficulty was to maintain a constant coupling ratio. The focal length of the lens was slightly dependent on the wavelength. Therefore, after changing the pump wavelength, coupling conditions had to be realigned.

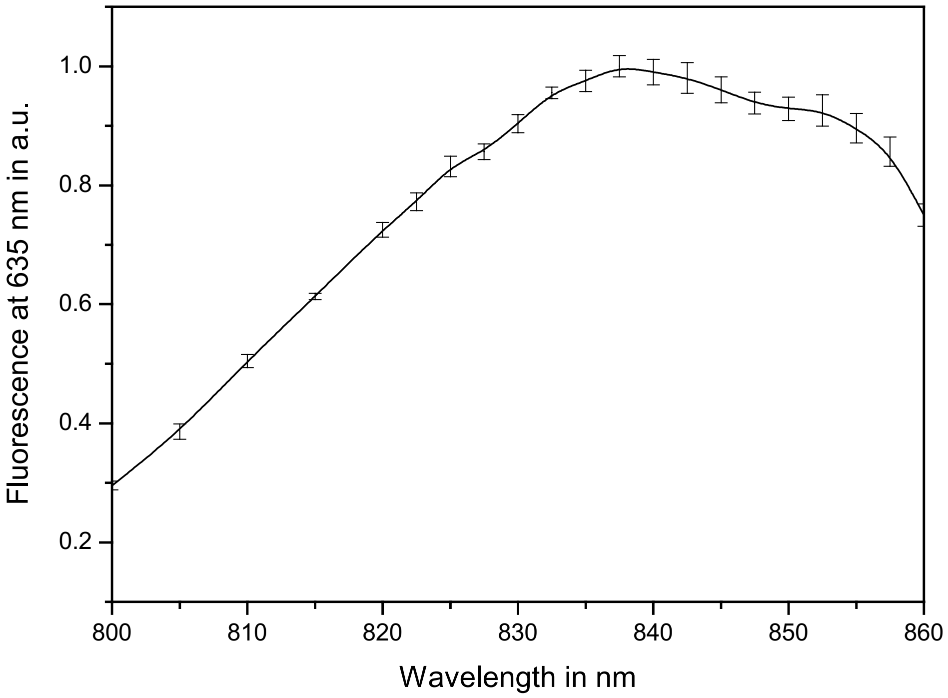

Figure 5.16: Normalized fluorescence signal at 635nm versus pump wavelength

The measurement was carried out three times to reduce the influence of a coupling error. The graph shows mean values with standard deviations. Starting at 800 nm, an increase of the pump wavelength caused a nearly linear increase of the signal at 635 nm. The optimum pump wavelength was found around 840 nm, and therefore, this pump wavelength was used for all fiber laser experiments. Pump wavelength changes from 830 to 850 nm caused intensity deviations of only around 10 %. This property is very important for diode-laser pumping, because an exact pump wavelength is not required for optimum pump efficiency. Increasing the excitation wavelength beyond 855 nm caused a clear decrease of the pump efficiency. Results published in the literature show a similar behaviour [33-36]. Unfortunately, the mirror set available for the Ti:Sapphire laser allows to reaching a maximum pump wavelength of 860 nm only. Therefore, measurements for longer wavelengths were not possible. The pump tuning curve confirms that, in a Pr^{3+}/Yb^{3+} ZBLAN fiber, an avalanche process and not an energy transfer from Yb^{3+} to Pr^{3+} is the dominant pumping mechanism (compare with chapter 2.4.3). Firstly, the optimum pump wavelength corresponds to the excited state transition $^1G_4 \rightarrow ^1I_6$. Additionally, the Yb^{3+} absorption is slowly increasing at 850 nm, and the strong central peak of the Yb^{3+} absorption in ZBLAN occurs at 975 nm [33]. In the case of an energy transfer process, the pump efficiency should have been higher and not lower above 850 nm.

5.2.7 An avalanche process in the fiber

There is also another indication that an avalanche process plays the dominant role in the pumping process of a Pr^{3+}/Yb^{3+} ZBLAN fiber. It is self-induced absorption which was measured in fiber A with a length of 35 cm. The fiber transmission as a function of the input power is shown in Figure 5.17.

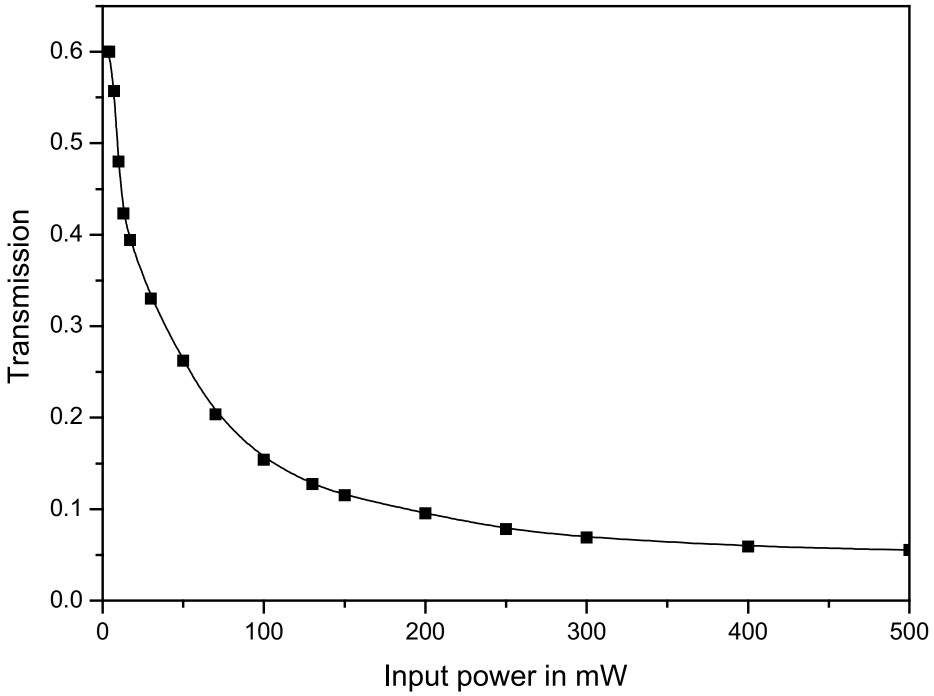

Figure 5.17: Self-induced absorption due to excited state absorption

The transmission is defined as the ratio of the input power to the remaining pump power as measured at the fiber end. The low signal transmission is close to 60 %. This value results from launching efficiency, Fresnel reflection and background losses. Thus, for low pump power, the fiber is nearly transparent for the pump wavelength. In ambient temperature conditions, the population of level $^1G_4$ is low. Therefore, for a very low pump power, the absorption of the pump radiation is also small. However, as it has already been mentioned in chapter 2.4.3, every pumping cycle doubles the population of this state. Hence, the population of $^1G_4$ grows very fast with increasing pump power. This causes an increase of the exciting state absorption, and the transmission of the fiber drops significantly below 10 %. Additionally, we can see saturation at around 150 mW which indicates that the ground level is depopulated.

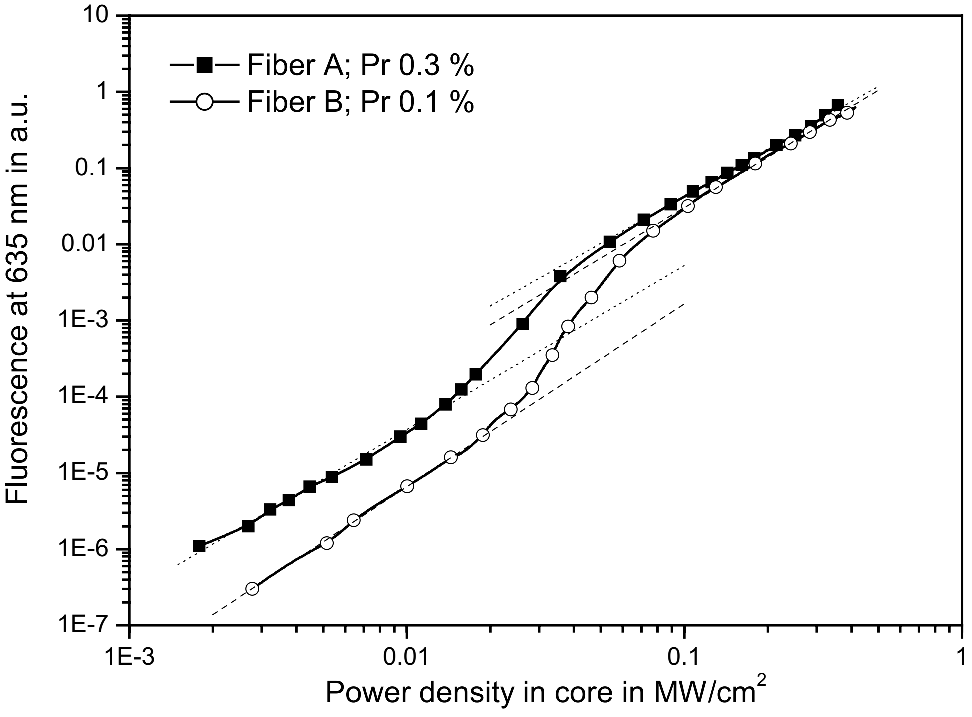

Figure 5.18: Red fluorescence signal as a function of power density

The avalanche process is characterized by a non-linear dependence of the upconversion fluorescence emission upon the pump intensity with the existence of a critical pumping threshold. This effect is shown in Figure 5.18, where the fluorescence measured at 635 nm is presented versus the power density in the fiber core. Two different fibers were used in this experiment, and in order to compare them, the pump power was recalculated to the power density in the core. The core diameter and the part of the pump power in the core were taken into consideration. The graph is shown in a double logarithmic scale in order to expose the avalanche process. For a start, we will concentrate on fiber A only. At low power density, an increase of the pump power causes a proportional growth of the fluorescence at 635 nm.

This dependence is linear in a logarithmic scale, and on a linear scale, it is quadratic dependence. When we pass the power density of 0.013 MW/cm^2, the fluorescence increases rapidly. This indicates that the critical threshold power required for the avalanche process is obtained. The threshold power is reached when the process populating the $^1G_4$ level are stronger than the decay processes of this state. This makes it possible to start the avalanche. However, at first the threshold power is exceeded only near the front end of the fiber. The large pump absorption at the front end means that at a certain position in the fiber the threshold power is no longer reached. To reach the threshold along the whole fiber, the power density needs to be properly high. For fiber A, this occurs at a power density of around 0.06 MW/cm^2. Further increase of the power density causes, ones again, a linear growth of the fluorescence (in a logarithmic scale). The presence of a pump threshold is typical for an avalanche pumping scheme as was described in chapter 2.4.3 in detail.

Figure 5.18 shows a comparison of the two fibers A and B. They had similar core diameters and NA, and both fibers were 30 cm long. The main difference was the praseodymium dopant. Fibers A and B contain 0.3 % and 0.1 % Pr^{3+}, respectively. Fiber B also had a lower attenuation at 750 nm (compare with Table 5.1). At low power density, fiber B showed less fluorescence than fiber A. This is due to the smaller Pr^{3+} concentration at equal fiber length. Additionally, the slope of the curve was larger for fiber B. The lower slope of fiber A indicates that statistically fewer pump photons were needed for one red photon; i.e., pumping was more effective. However, the measured fluorescence signal from both fibers was nearly the same in the range above the avalanche threshold powers. Nevertheless, the avalanche effect proceeded in fiber B more effectively. A 1-order-of-magnitude increase of the power density caused an increase of 3-orders-of-magnitude of the fluorescence signal from fiber A, and nearly of 4-orders-of-magnitude from fiber B. This was caused by concentration quenching of level $^1G_4$ at higher concentrations of Pr^{3+} ions, as it was explained in chapter 3.5.2. For a 0.3 % concentration of Pr^{3+}, the lifetime of level $^1G_4$ was shorter than in the case of a smaller doping. Therefore, the population of this level was also smaller, and that caused the avalanche process to operate less efficiently. On the other hand, a higher Pr^{3+} concentration allows for a better operation of the energy transfer. Therefore, for strong pumping conditions, the difference between both fibers was quite small.

5.2.8 Influence of mirror reflectivity on the laser performance

Output coupling is a critical parameter because it represents a loss of a laser cavity, but it is also the mechanism for converting intracavity signal power to useful output power. The reflectivity of the mirrors has to be optimized to find the best laser performance at a particular fiber length. In our experiment, the input mirror was the same all the time. It was highly reflective at 635nm and nearly transparent at the pump wavelength. However, several output mirrors with different reflectivities at the lasing wavelength were used.

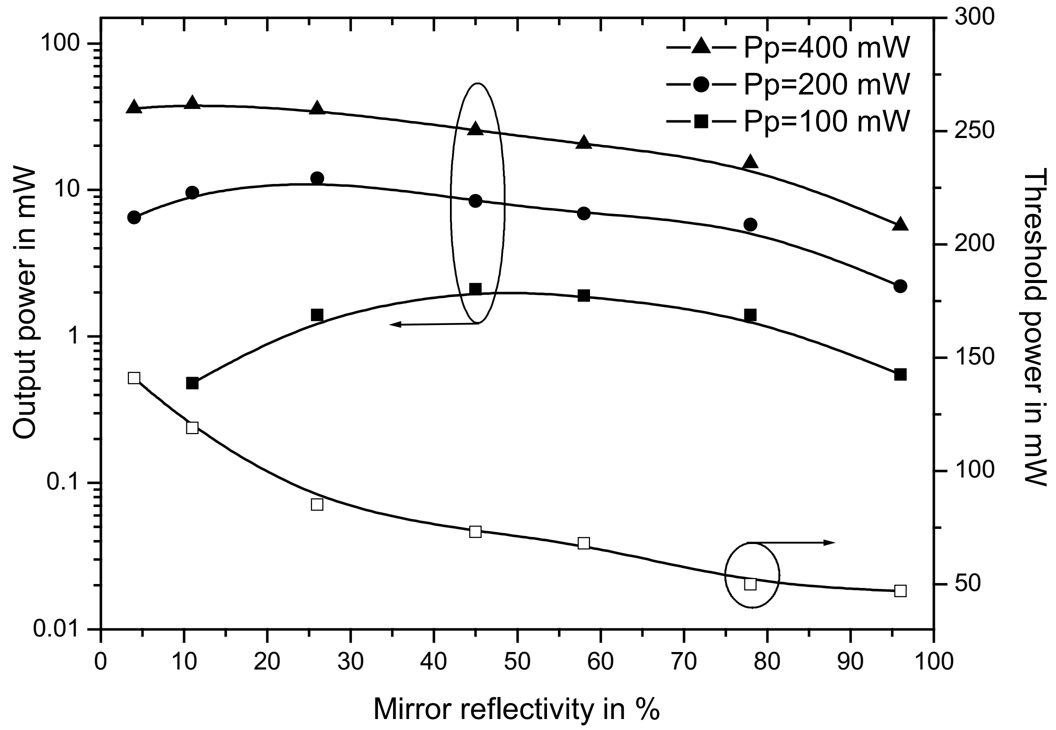

Figure 5.19: Output power and threshold power versus mirror reflectivity

Figure 5.19 shows the evolution of the output power and the threshold power as a function of mirror reflectivity. This measurement was made for several pump powers and fiber A with a length of 57 cm. The output power is shown on a logarithmic scale in order to allow a better distinction of output powers for different pump powers. There are some values of reflectivity at which the maximum output power was achieved. For a small pump power of 100 mW, the maximum output power was obtained with a reflectivity of about 45 %. When the pump power was increased, the optimum reflectivity shifted to lower values. For pump powers of 200 and 400 mW, the best mirror reflectivity was about 25 % and 10 %, respectively. The reason for this optimum arises from the fact that we had two contradicting circumstances. At one extreme, if both mirrors have zero transmission, the power emitted by the atoms in the cavity will be at maximum, while the threshold will be at its minimum value. But no power leaves the cavity. On the other hand, any attempt to increase the fraction of photons allowed to escape from the resonator results in increasing losses so that the power in the resonator decreases. This causes an increasing pumping threshold, and this threshold will, at some point, exceed the actual pumping level. When this happens, oscillation will cease and the power output will again be zero. Between these two extremes there exists an optimum value of mirror reflection at which the power output is at maximum [4, 132]. The reduction in output power as a result of non-optimum reflectivity becomes important while working very close to threshold. However, well above the threshold, the output power becomes rather insensitive to a change in output coupling around the optimum value.

As already mentioned, the reduction of mirror reflectivity causes an increase of the threshold power. In our experiment ,the threshold power reached its minimum of 47 mW for a very high reflectivity. But when the reflectivity was decreased, the threshold power increased exponentially. With a reflection of 4 % only, the threshold power is nearly three times as large as for the high reflectivity.

5.2.9 Optimization of fiber length

For a given fiber, parameters such as core diameter, ion concentration and NA are fixed, and fiber length and output coupling become key parameters to be optimized. If we assume a specific length of fiber, there exists a particular range of the reflectivity that yields a maximum output power, as discussed above. It is obvious that the optimum for this set of parameters varies with given pump powers. There exists a general rule of selecting a fiber length and an output coupling factor. For short lasers, high reflection coefficients have to be used for optimum output coupling. On the other hand, for long lasers, optimum output coupling is achieved with a low reflection coefficient of the output mirror [24, 133]. We made a series of measurements for three different fibers. The results are presented in Figure 5.20.

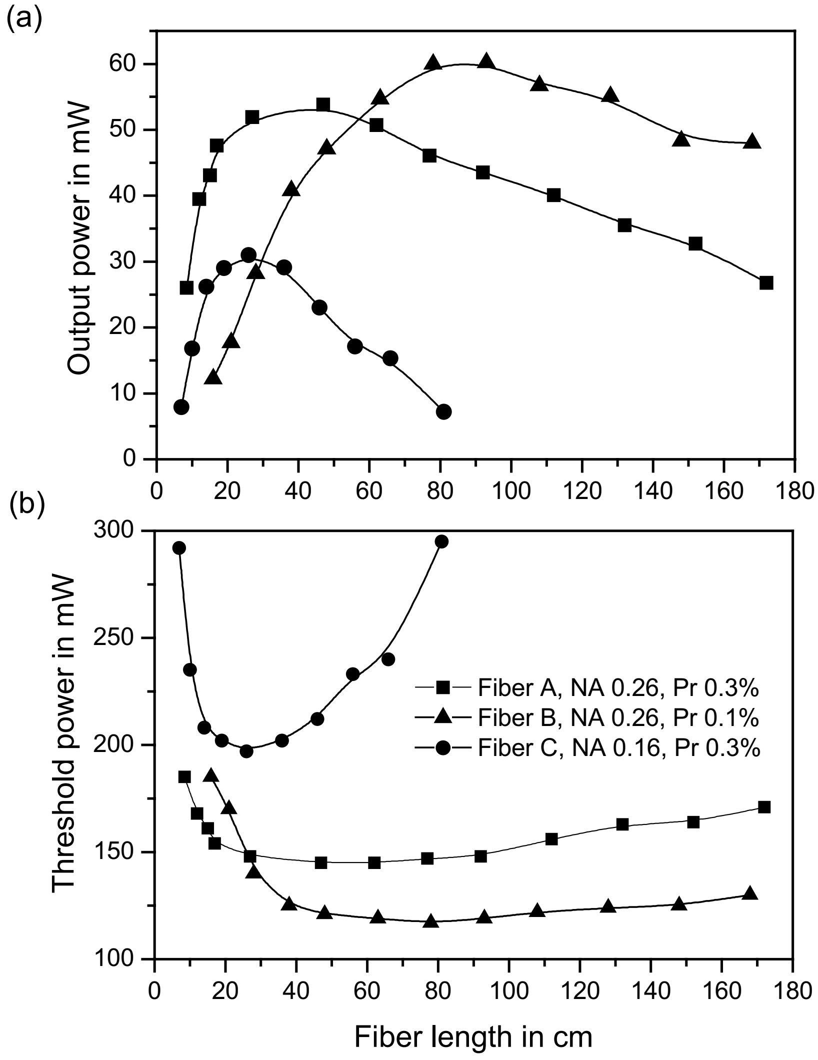

Figure 5.20: Influence of fiber length on (a) the pump power and (b) the threshold power

This graph shows an evolution of the output power and the threshold power when a fiber was cut back. The output power was measured each time at a pump power of 500 mW. In this experiment, the pump power was launched into the front end of the tested fiber. Both the coupling ratio and the input mirror remained constant during whole measurement; only the end of the fiber was cut back to a shorter length. A cleaved fiber end with 4 % Fresnel reflection was used as the output mirror. This reflectivity results in a large threshold power. But if the fiber was properly cleaved, the reflection from the fiber end after each cutting was the same. Using a butt coupled external mirror would result in additional reflection uncertainties depending on the repeatability of the realignment procedure. Therefore, to limit this error, the Fresnel reflection was used.

We will start with the investigation of fiber C. This fiber has a relatively large core diameter of 3.4 μm and small NA. A study of measurement points shows that there exists an optimum fiber length where the maximum output power is obtained by the minimum threshold power. This optimum fiber length was 26 cm, and the measured output and threshold powers at this length were 31 mW and 198 mW, respectively. When the fiber was shorter than the optimum length, the pump power was not sufficiently absorbed resulting in a smaller gain. On the other hand, if the fiber was too long, almost all pump power was already absorbed in the front part of the fiber, and the pump power at the fiber end was too low to produce an appropriate population inversion. However, increasing the fiber length caused an increase of total cavity losses because of a large fiber attenuation. So, if we enlarged the fiber length, the gain stayed nearly constant, but the total cavity losses were growing. Of course, this caused a drop of the output power and an increase of the threshold power.

If we examine fiber A in Figure 5.20, we can notice that for this fiber, the optimum length is a little longer and amounts to 47 cm, but the maximum output power is nearly doubled to 54 mW. The threshold power of 145 mW is definitely smaller in comparison to fiber C. Also, the slope efficiency is larger for fiber A than for fiber C and amounts to 15 % and 10 %, respectively. If we compare the parameters of fibers as collected in Table 5.1, we see that both fibers have a similar attenuation, but fiber A has a smaller core and a higher NA than fiber C. Small core and high NA assure a high pump power density in the core resulting in a high gain. An increasing NA improves overlap between pump radiation and fiber core [134]. The fraction of the pump power contained in the fiber core for fiber A amounts to 80 %; for fiber C it is lower and equals 75 %. A lower overlap in a low NA fiber results in an inefficient pump power absorption because there is a large fraction of the pump power in the cladding. In a high NA fiber, however, the overlaps are improved, and greater pump absorption efficiency decreases the threshold. Therefore, in spite of a similar attenuation, fiber A is more effective than fiber C. In order to keep the fiber in single mode at the pump wavelength, one must choose the fiber V value at the pump wavelength to be less than 2.405. For a fixed fiber V value, a smaller fiber core radius is used for a higher NA fiber (compare with equation (4.2)). Fibers A and C have similar attenuations, but the influence of the fiber length on the threshold power was smaller for fiber A than for fiber C. A slight elongation of fiber C beyond the optimum length caused a considerable growth of the threshold power, but not in the case of fiber A.

We obtained even better red laser performance with fiber B. The optimum fiber length was nearly two times larger than for fiber A, and we obtained a slightly larger output power and smaller threshold power of 60 mW and 117 mW, respectively. The improvement in laser performance was possible thanks to the small attenuation of fiber B. The larger optimum fiber length is caused by a smaller concentration of Pr^{3+}. Fiber A was doped by 0.3 %, and fiber B contained 0.1 % of Pr^{3+}. Yb^{3+} doping in both fibers was the same and amounted to 2 %.

We have shown that optimum output coupling is fixed by the values of three control parameters; i. e., the output coupler reflectivity, the pumping power, and the fiber length. As a general rule, the longer a lasing fiber, the greater the output that can be extracted at higher pump levels with low output coupler reflectivity. In other words, with increasing lengths and pump inputs, the optimum output operation is attained with a decreasing reflectivity.

5.3 Laser output stability

In this part, we will examine another aspect of laser operation; that is, that is the short- and long-term stability of the laser output radiation. Laser devices very often show severe stability problems which may be associated with optical damage problems, mechanical vibrations, acoustic noise and other sources of a so-called technical noise. Especially, laser amplifiers do not show a particularly good noise performance because of the unavoidable added noise that comes from spontaneous emission in the laser medium. It is not possible to have an inverted laser population without also having spontaneous emission from the upper level. However, relaxation oscillations are the most predominant mechanisms causing fluctuation in the output of a solid-state laser; therefore, we will describe this effect in detail. At the beginning, we will compare the stability of blue, green and red lasers.

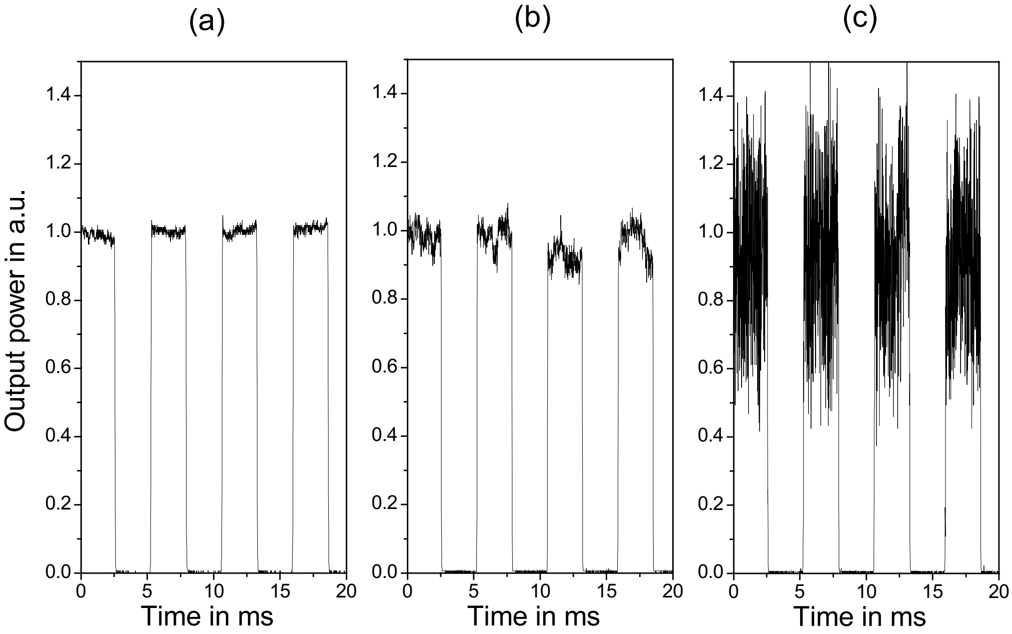

Figure 5.21: Output power stability of (a) red, (b) green and (c) blue fiber lasers

5.3.1 Stability of fiber lasers

The results of measurements of the output power stability on red, green and blue lasers are shown in Figure 5.21. The output power was measured with a fast photodiode S6468 from Hamamatsu with a cut-off frequency of 15 MHz. The signal was saved using a digital storage oscilloscope. Additionally, the output signal was mechanically chopped in order to obtain a better visualization of the noise level. The red laser, pumped by 300 mW, showed a low noise level. The output signal changed only about ± 3 %. The green laser was pumped by 200 mW, and for this laser the noise was slightly larger, and the output power varied in the region of ± 8 %. In the case of the blue laser, pumped at 350 mW, the output noise was much larger than that from both previously mentioned lasers. The output power fluctuated by approximately ± 40 %. In this case, only a quasi-cw mode was achieved with a strong self-pulsing behaviour. The reason for such a large amount of noise is the three-level laser system of the blue laser, because for such a laser, it is difficult to obtain a stable population inversion.

5.3.2 Relaxation oscillations

The laser output is a highly irregular function of time. The output consists of individual bursts with random amplitudes, durations and separations. This is termed "spiking" in the output. We will explain the spiking phenomenon with the help of Figure 5.22.

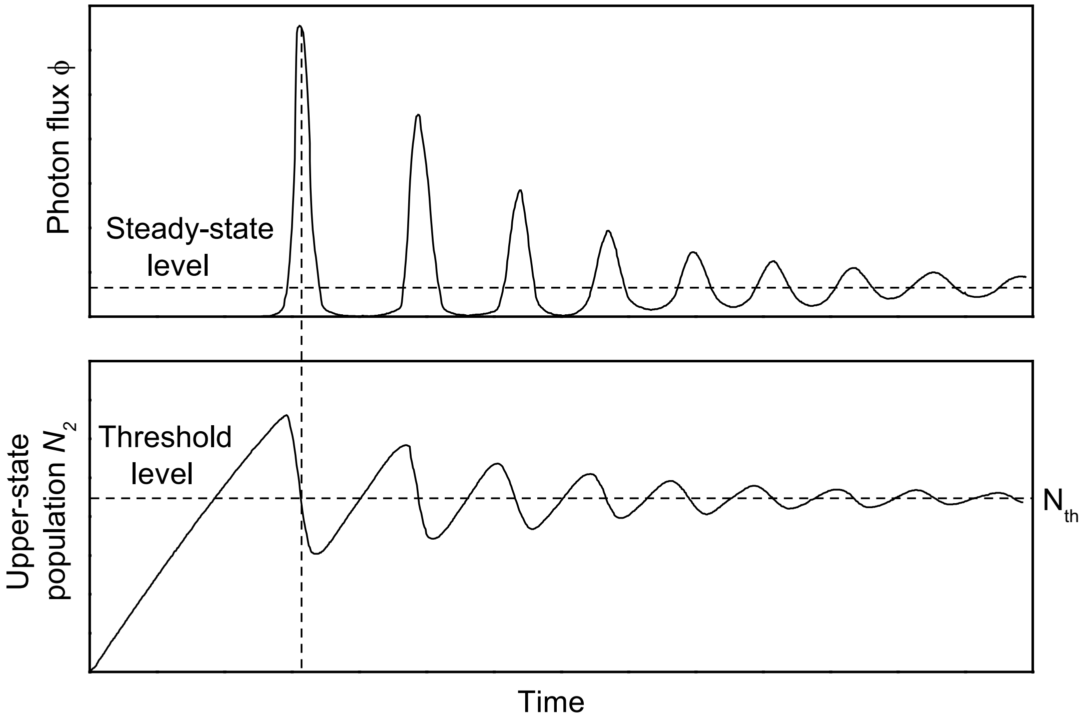

Figure 5.22: Spiking behaviour of a laser oscillator [2, 135]

When the laser pump source is switched on, there are a negligible number of photons at the appropriate frequency. The pump radiation causes a linear buildup of excited atoms, and the population is inverted. Although under steady-state oscillation conditions N_2 can never exceed N_{th}, under transient conditions, the pump can raise N_2 above the threshold level. No laser oscillation has yet been built up, and no radiation yet exists in the cavity to pull N_2 back down by means of stimulated emission.

The laser oscillation does not build up until after N_2 passes N_{th}, so that the net round-trip gain in the laser exceeds unity. Then, however, because N_2 is considerably in excess of N_{th}, the oscillation level will actually build up very rapidly to a value of the photon flux ϕ substantially in excess of the steady-state value for the particular pumping level. But, when $\phi(t)$ becomes larger, the rate of depletion of the upper-level atoms due to stimulated emission becomes correspondingly large, in fact considerably larger than the pumping rate. As a result, the upper-level population $N_2(t)$ passes through a maximum and begins to decrease rapidly, driven downward by the large radiation density. The population $N_2(t)$ is driven back below the threshold level N_{th}; the net gain in the laser cavity becomes less than unity, and the existing oscillation in the laser cavity begins to die out.

To complete the cycle of this relaxation process, once the radiation level has decreased below the proper steady-state level, the stimulated emission rate again becomes small. At this point, the pumping process can begin to build the population level N_2 back up toward and beyond the threshold value again. This causes the generation of another burst of laser action, and the system can again go through a repeated, similar cycle. As time passes, the peaks become smaller, and the curve becomes damped sinusoidally [2]. The output power shows a sequence of peaks (or laser spikes) of decreasing amplitude. This aspect of regular oscillations for the output power is usually referred to as relaxation oscillations [127].

However, most lasers show completely irregular, undamped spikes. This discrepancy between theory and experiment is due to the fact that the spiking behaviour dies out very slowly. In cw-pumped lasers, the relaxation oscillations are weak and usually consist of damped sinusoidal oscillations around the steady-state value. However, any kind of small disturbance, such as a sudden change in pumping rate, fluctuation in gain, cavity loss, or cavity alignment, will trigger a transient relaxation oscillation of the same general character which will again die away exponentially in the same oscillatory fashion [135].

The relaxation oscillations are due to a coupling of the cavity lifetimes τ_{cav} and the lifetime of the upper level laser level τ_2. Its frequency is given by [35]:

$$v_{rel} = \frac{1}{2\pi}\sqrt{(r-1)\frac{1}{\tau_2 \tau_{cav}}}, \tag{5.3}$$

with the pump rate r given by the pump power divided by the pump power at the laser threshold. The cavity lifetimes can by estimated as [35]:

$$\tau_{cav} = \frac{2nL}{c\alpha}, \tag{5.4}$$

with the fiber length and refractive index L and n, respectively, and the round trip losses α.

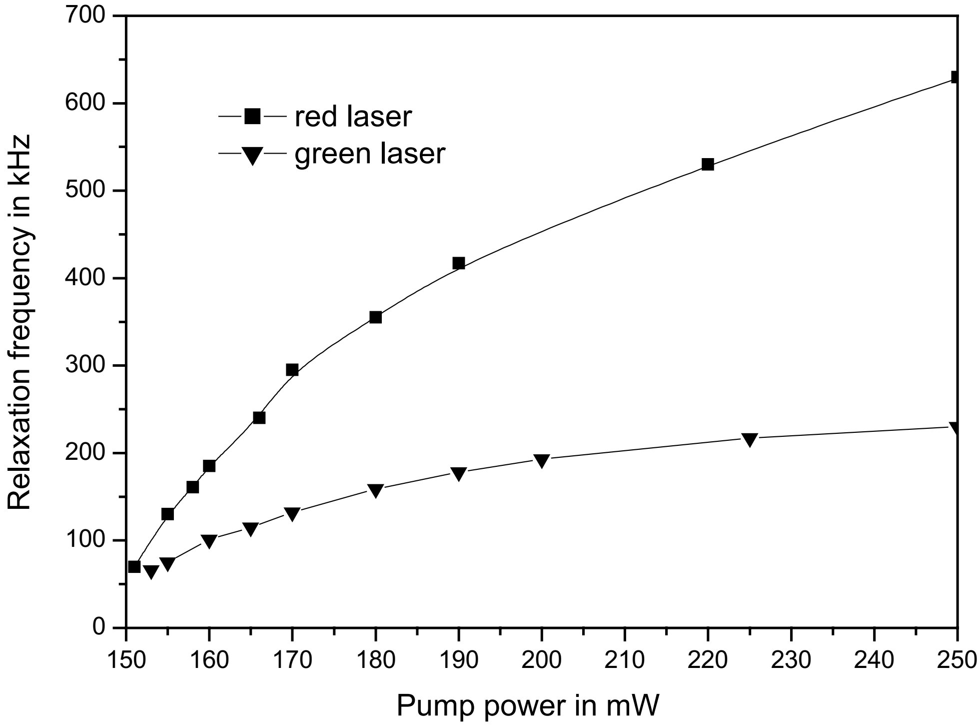

Figure 5.23: Relaxation frequency as a function of the pump power for red and green lasers

The measured relaxation frequency of red and green fiber lasers versus pump power is shown in Figure 5.23. Analysing the plot, we can observe that the greater the pump power the higher the oscillation frequency. The relaxation oscillations are in the range of a few hundred kilohertz depending on the laser. The graph has the typical shape of the natural root function. This results form a square root relationship between relaxation oscillations and pump rate as expressed in equation (5.3).

The green laser had two highly reflecting mirrors at the signal wavelength, as discussed in chapter 5.2.3, butted against 13 cm of fiber A. The red laser was made using 51 cm of fiber A. The input mirror had high reflection in the red range, and a cleaved fiber with 4 % Fresnel reflection was used as the output mirror. Due to a low reflection of the output mirror and a longer fiber, the round trip losses α of the red laser were definitely larger (17 dB) than for the green laser (1.2 dB). Therefore, the relaxation oscillations were also larger.

Relaxation oscillations are, in general, more a troublesome than a useful phenomenon. However, measurements of the relaxation oscillations have also been used to calculate the losses in fiber laser cavities [136, 137].

5.3.3 Noise suppression

A free running upconversion fiber laser unfortunately shows a strong amplitude noise. Due to the coupling of the upper laser level to the photon field in the laser resonator, fiber lasers show relaxation oscillations in the range of a few hundred kilohertz, as it was discussed above. In addition to the relaxation oscillations fiber lasers show noise features due to the nonlinear multi photon pump process, mode competition of longitudinal modes and technical noise from mechanical instabilities of the whole setup [138]. For some laser applications, it is desirable to have a smooth output power with very little modulation. The noise amplitude can be suppressed by applying a noise controlling opto-electronic feedback loop. The amplitude noise can be suppressed up to 45 dB which corresponds to a noise reduction from 10 % rms to 0.3 % rms [84]. The setup used for noise suppression in this work is shown in Figure 5.24.

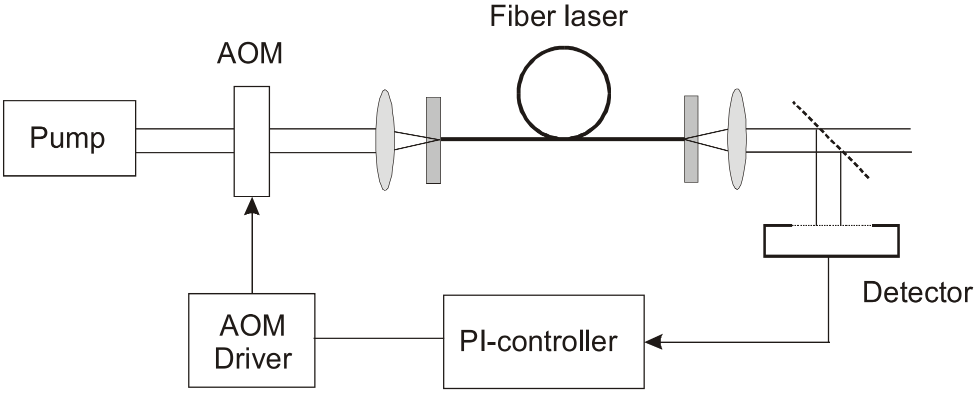

Figure 5.24: Configuration of a fiber noise reduction setup

An active feedback system consists of a beam splitter which guides a small part of the output power to a photodiode. The photodiode provides a feedback signal to a Noise Eater miniNE 100 from TEM Messtechnik. It contains a controller with a proportional and integral part which controls the AOM driver. The AOM allows for pump power modulation in order to minimize the noise from the fiber laser. The described setup was used to stabilize the output of the red and green fiber lasers. The results of the noise suppression are shown in Figure 5.25. The output power was measured by a fast photodiode with a bandwidth of 15 MHz. The data acquisition system consisted of a fast 16-bit D/A converter card of type NI 6115 from National Instruments with a sampling rate of 10 MS/s. The output power of the red laser with open stabilization loop shows a clear amplitude noise. When the loop was closed, the laser signal showed smaller amplitude fluctuations. However, this improvement was obtained at the cost of lower output power. The plot on the right-hand side presents the noise spectrum of the green laser. This spectrum was obtained by applying a Fourier transform to the output signal. It indicates a relaxation peak at a frequency around 300 kHz. After closing the feedback loop, the amplitude of the noise was suppressed, and the maximum of the relaxation oscillation is shifted to a value around 200 kHz. This shift results from the reduction of the mean pump power when the pump modulation is applied.

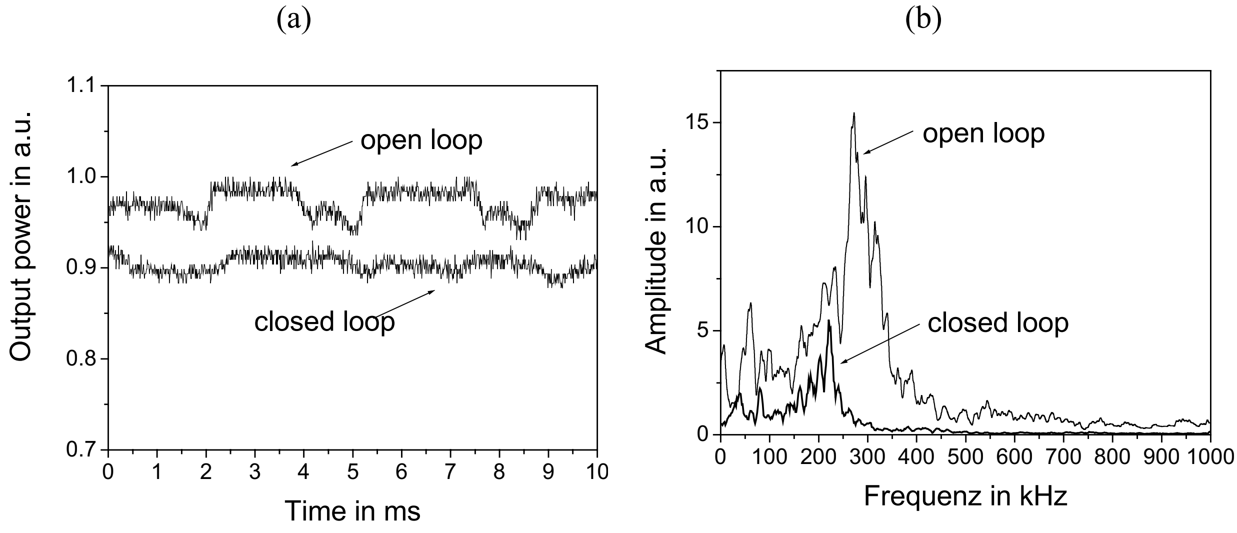

Figure 5.25: Influence of a noise eater system on: (a) the output power of the red laser, (b) the noise spectrum of the green laser

The results presented show an improvement of the noise level, but this improvement is not very large. In order to obtain a reasonably smooth output, the delay time between the signal derived from the photodiode and the change in transmission of the amplitude modulator has to be short compared to the duration of an individual spike. However, an AOM in the setup causes some delay time. This results from the limited speed of an acoustic wave in the crystal. Additionally, the avalanche pumping scheme is quite complicated, and a simple reduction of the pump power does not instantly cause a decreasing population of the upper level. All these features limit the effect of the noise suppression.

5.3.4 Long-term stability

Besides the short-term fluctuation, a long-term drift in the output power is also present, generally arising from e.g. thermal misalignment in the laser cavity and from degradation of mirrors and other optical components, including the active medium itself. One important problem of blue fiber lasers is the photo-induced degradation of the fiber. This effect, called photo-darkening, is commonly known from thulium-doped fiber lasers operating in the 480 nm region [139, 140]. During laser operation, a multiple-photon upconversion process causes ultraviolet emission which leads to creating color centers in the fiber. These color centers lead to high optical attenuation in the blue and green spectral range resulting in an increased laser threshold and a reduced efficiency of the laser process [35]. We tested the long-term stability of a red, a green and a blue laser. The results are presented in Figure 5.26.

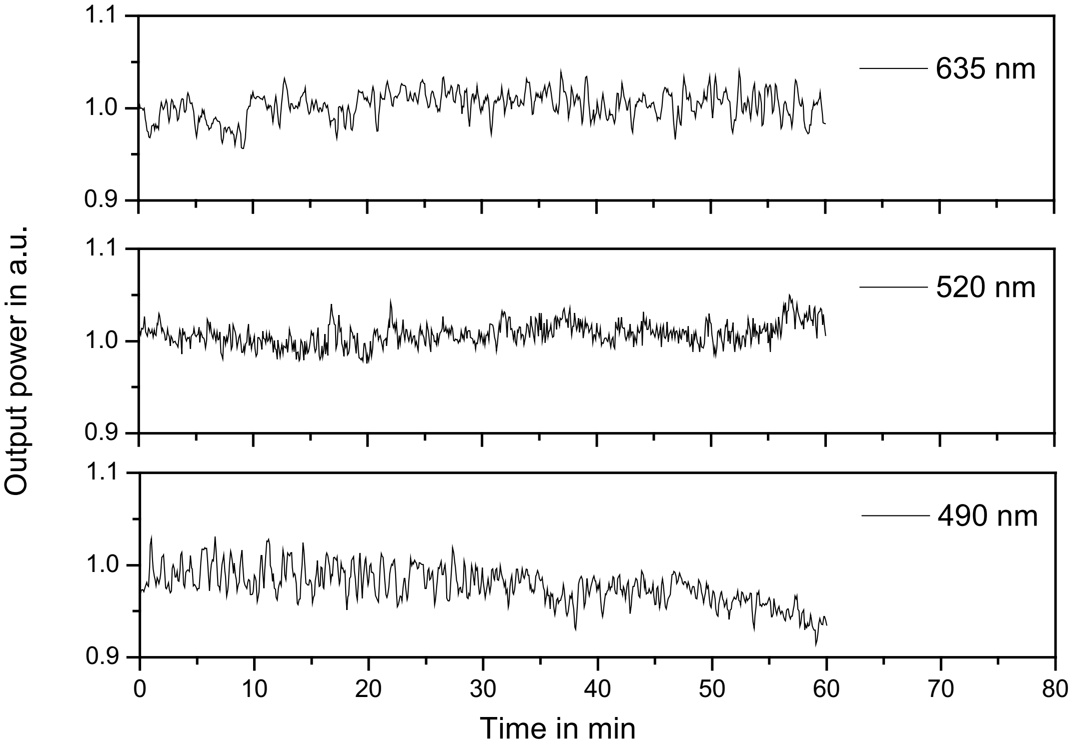

Figure 5.26: Long-term stability of a red, a green and a blue laser during one hour

The output power of each laser was measured over a period of one hour. No significant decrease of the output power was observed during this measurement. Only for the blue laser, we can see a slight drop of the output power at the end of the measurement, but it may have been caused by misalignment of the laser setup. Also, other research groups reported no photo-degradation for a Pr^{3+}/Yb^{3+} ZBLAN fiber lasers [35, 108].

6 All-fiber laser with red emission

The Fabry-Perot type of fiber laser described in the last chapter has a number of disadvantages. It must be pumped by focusing the pump radiation on the fiber end face through a mirror consisting of dielectric thin film coatings on a substrate. The mirror has to be placed between the lens and the fiber, which makes low loss fiber coupling difficult. Additionally, if pumped with a high power laser, thermal damage at the mirrors might occur. Therefore, we examine in this section an alternative approach using configurations in which bulk mirrors are not required. These all-fiber lasers make use of directional couplers; therefore, we will concentrate at first on the fabrication and the parameters of such components.

6.1 Fused fiber couplers

Directional couplers are the optical fiber equivalent to a beam splitter. They have found widespread application in fiber amplifiers and lasers because of their natural fiber form, and they show low losses. There are different methods for fabricating fiber couplers, but fused couplers are most commonly used. The couplers used in this work were made using a system FCI-7011 from NTT-AT. The fabrication process of the coupler is as follows. First, fibers are prepared by removing the coating material in the region of the fiber that will form the coupler and by cleaning the bare fiber. Then, two uncoated fibers are fixed between two motorised linear translation stages and held in contact with each other as shown in Figure 6.1.

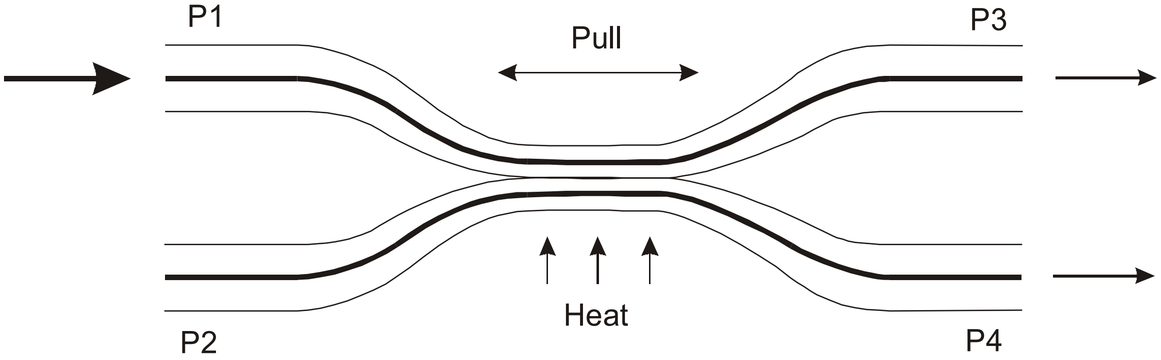

Figure 6.1: Fabrication process of a fused fiber coupler

Fibers are inserted in a hole of an electrical heater and heated homogeneously over a distance of 20 mm. A typical temperature and elongation profile for the coupler production is depicted in Figure 6.2. At the beginning, the heater is set to a temperature of 1600 °C which is above the softening temperature of silica glass. During this time no elongation is made, and the fibers fuse. After some time the stages are moved in opposed directions causing an elongation of the coupling zone. During the elongation, the cross-section of the fused region shrinks. A fused down-taper is formed at one end, and an identical up-taper is formed at the other end. Due to the smaller cross-section of the fused region, pulling speed and temperature must also be decreased in several steps. This assures a uniform oscillation of the coupling ratio during the manufacturing process and allows the reproducible production of couplers even with very long coupling zones. During the fabrication process, a laser source was connected to port 1 of the coupler, and radiation leaving each of the two fiber output ports is continuously measured by optical power meters in order to monitor the coupling ratio and to calculate excess losses. When the required splitting ratio is reached, the heater is withdrawn and the fusion is stopped.

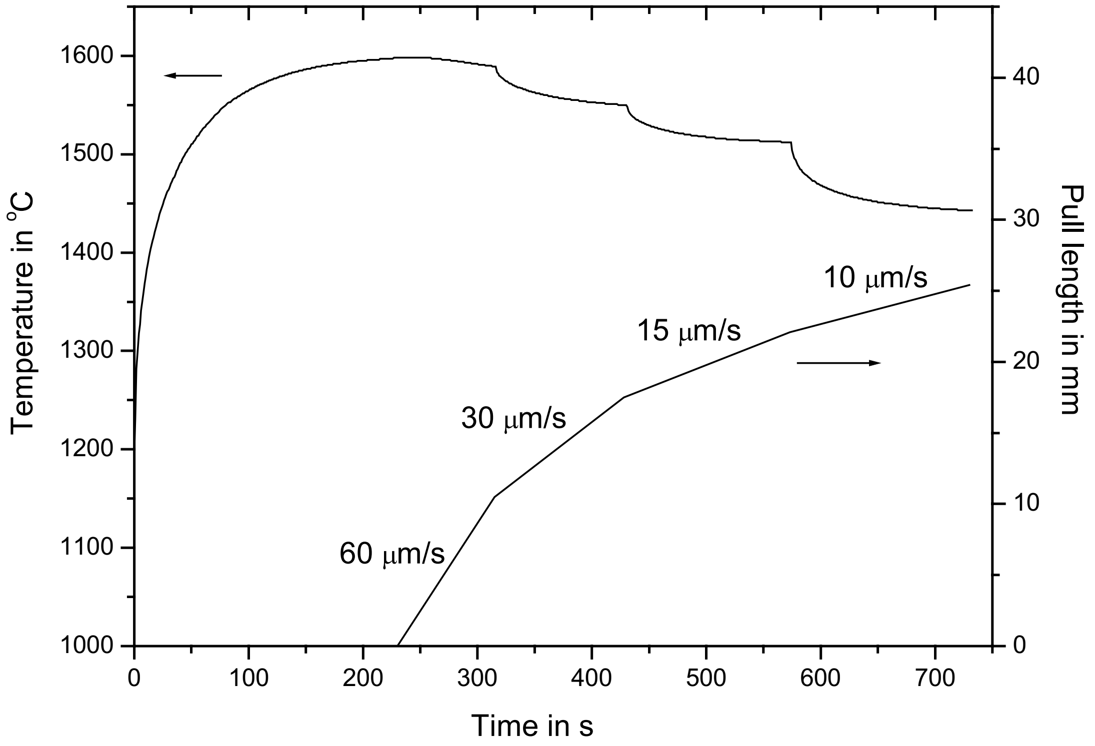

Figure 6.2: Temperature and elongation profile for coupler production

Once the coupler has been made, it is necessary to protect the fragile coupling region from the environment. The coupler is fixed on a glass substrate. Next, the structure is protected using a stainless steel pipe which is then closed from both sides with UV curing adhesives. Care should be taken in this process since the coupling ratio is sensitive to bending and to changes in the refractive index of any material that may by used to encapsulate the coupler.

The optical coupling between the two fibers is caused by the decrease of the distance between the cores and a decrease of the diameters of the core and the cladding. The cross-section profile anywhere along the taper consists of two cores embedded in a finite cladding which is surrounded by air. The amount of interaction, and thus the coupling, is determined by the separation of the fiber cores and the extent to which the fields reach into the cladding. The extent of the field spreading is determined by the normalised frequency V.

For sufficiently large values of V (V>2.405), guidance of the fundamental mode is predominantly by the core-cladding interfaces, and the cladding regions which separate the two cores are more than sufficient to prevent any coupling between the fibers. Therefore, the effect of the cladding-air interface is negligible. However, if due to an elongation the core is very small (V→0), the fundamental mode is essentially guided by the cladding-air interface, and the core-cladding interface has a negligible effect [141]. The fundamental field of one fiber interacts with that of the neighbouring fiber, and power is coupled between the two, as it is schematically shown in Figure 6.1. The transition point in the taper changes from being core-guided to cladding-guided which occurs when a decrease in core radius causes V to be approximately equal to unity [142]. There is a large difference in the refractive indices between the cladding and air. The net effect of this difference is that the field in air is negligibly small [143]. The mode propagation in the taper is continuously changing along the taper. In the down-taper region, the core mode is converted to a cladding mode. Furthermore, in the up-taper this process is reversed, and the fundamental mode is recaptured by the enlarging core. It has been found that if such tapers are made with a very small taper angle, then the field is almost completely recaptured by the core of the original fiber with essentially no losses. This so-called adiabatic criterion is defined by [144]:

$$\left|\frac{dr}{dz}\right| \leq \frac{r(\beta_1 - \beta_2)}{2\pi}, \tag{6.1}$$

where r is the core radius, z the axial coordinate, and β_1 and β_2 are the local propagation constants of the fundamental mode (LP_{01}) and the next possible mode (LP_{02}), respectively. Thus, a taper is approximately adiabatic if the taper angle is small enough everywhere to ensure that there is negligible loss of power from the fundamental mode as it propagates along the length of the taper. On the other hand, if the fiber is strongly tapered, the power of the fundamental mode will be transferred to higher-order modes. As a result, the power propagating in high order modes will not be reconverted to the fundamental mode in the second taper. They continue to propagate as cladding modes which manifests itself as a loss in the fundamental mode. The relationship between the power coming from port 3 compared to the input at port 1 during the elongation process is shown in Figure 6.3. This dependence was measured for a pump wavelength of 845 nm and a signal wavelength of 635 nm. Actually, our pump wavelength was 840 nm, but the laser diode used in the coupler production had a little longer emission wavelength; but this difference is not large. A special fiber of type 630HP from Nufern was used for the coupler production. The core diameter and NA of this fiber were 3.4 µm and 0.13, respectively. The amount of coupling power depends on the length of the coupler. As the coupler length increases, power is coupled back and fourth from one fiber to the other. The length between two coupling minima decreases with increased tapering because of the greater expansion of the fields for lower V values. The patterns for both wavelengths are similar, but coupling occurs at higher wavelengths first, because the mode field diameters for longer wavelengths are larger than those for shorter wavelengths.

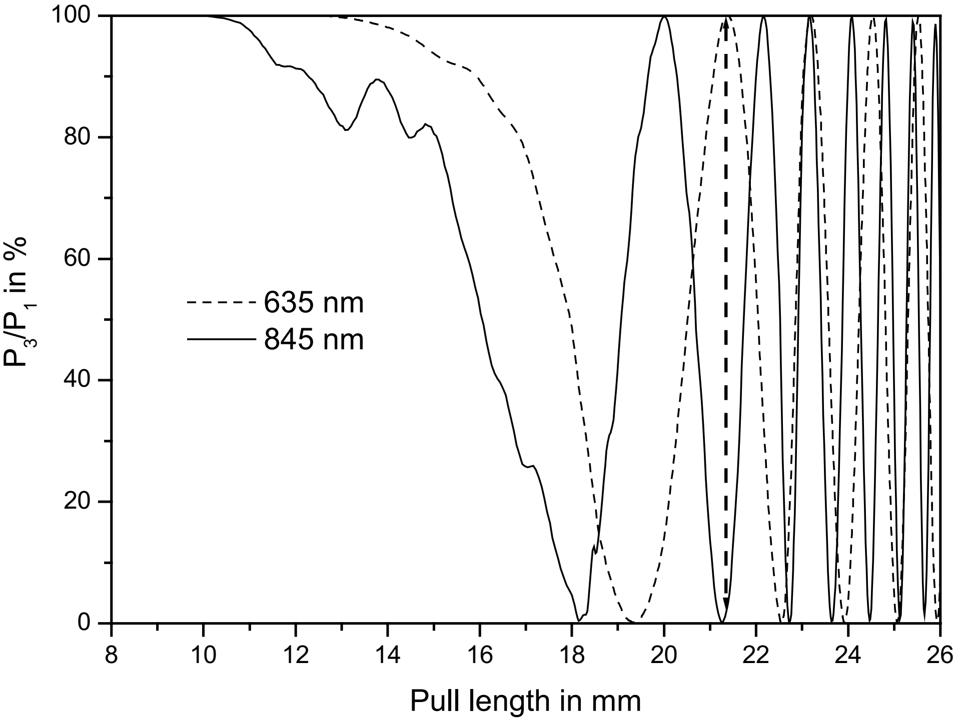

Figure 6.3: Power from port 3 as a function of pull length for two wavelengths

For 845 nm, a beating between higher-order modes at pull length between 10 mm and 16 mm was noticeable. At the beginning of the elongation process, the adiabatic criterion was not reached. Hence, higher-order modes were excited, but the mode beating was negligible due to the pull length of 18 cm. This beating leads to an oscillatory behaviour of the output power which depends on elongation. If the two modes are in phase, the power is concentrated in the centre of the fiber; if they are out of phase, the power is more concentrated near the periphery. The beating phenomenon can be regarded as an exchange of power between the inner and outer regions of the fiber [145]. Usually, the pulling process is stopped just when the coupler achieves a required coupling ratio. Because of this mode beating the coupler was elongated in order to obtain a first minimum at 635nm. When power was increased again, the elongation process was stopped after reaching a required coupling ratio. A longer coupler zone ensures that mode beating does not occur for the pump wavelength.

At a specific pull length, the coupling ratio also depends on the wavelength. This allows fabricating a coupler with a high coupling ratio at one wavelength and a low coupling ratio at another. Such dichroic couplers, known as wavelength division multiplexers (WDM), are of particular importance for a ring laser, where it is necessary to provide different coupling behaviours at the pump and signal wavelengths. The procedure for making such a coupler is to elongate the fiber over a number of cycles of the periodic output variations until the desired high coupling ratio at one wavelength and the low ratio at the other one are reached. These conditions were obtained at a pull length of about 21 mm and are marked by arrows in Figure 6.3.

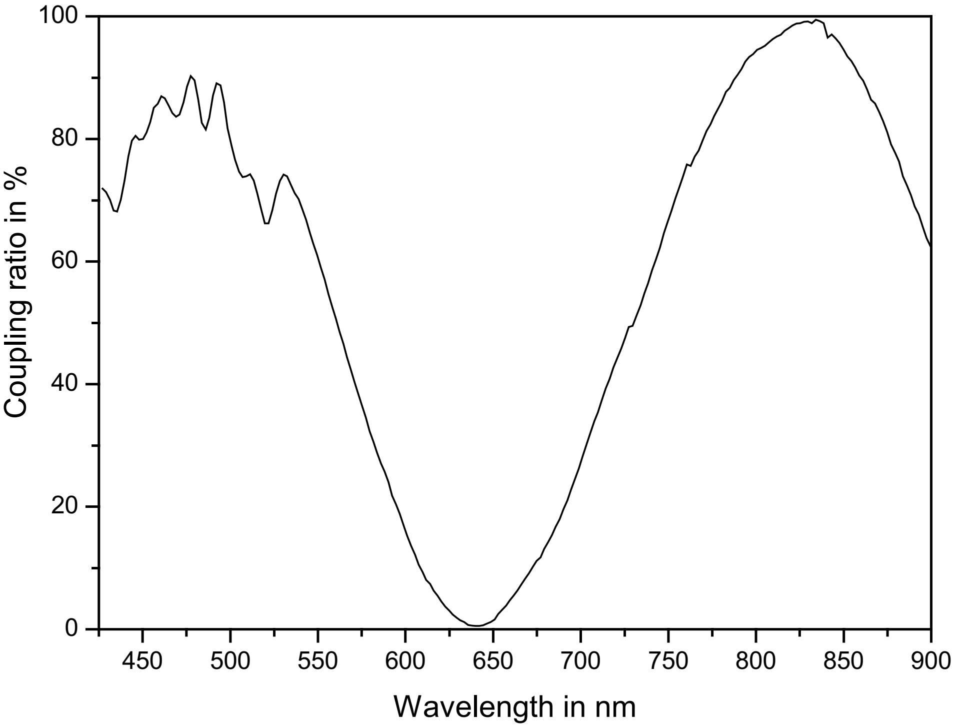

Figure 6.4: Dependence of the coupling ratio on the wavelength for a WDM coupler

The coupling ratio of such a fiber as a function of wavelength is shown in Figure 6.4. The coupling ratio was defined by the relation:

$$CR = \frac{P_4}{P_3 + P_4} , \tag{6.2}$$

where the designation of the ports is consistent with Figure 6.1. The coupling ratio at the signal wavelength reached a minimum; e.g., light at 635 nm launched into port 1 was completely transmitted to port 3, and no power was coupled to port 4. The maximum coupling ratio was obtained at 830 nm, and for a pump wavelength of 840 nm, the coupling ratio was 97 %. The fiber used of type 630HP had a cut-off wavelength at about 570 nm. Therefore, for shorter wavelengths, it guided also higher-order modes. The effects of the higher-order modes on the transmission manifest themselves as additional oscillations at wavelengths shorter than the cut-off wavelength.

6.2 Connecting fluoride and silica fibers

The coupler mentioned in the previous section was manufactured from a silica fiber, but for the active section a fluoride fiber was used. Connecting these different fibers was a serious problem. Because of the completely different compositions and glass matrix structures, the thermal and mechanical properties of silica and fluoride fibers differ significantly. Table 6.1 shows a comparison between the two glasses.

Table 6.1: Thermal and mechanical properties of ZBLAN and SiO_2 glass

Property	ZBLAN	SiO_2	Ref
Melting point (°C)	600	1734	146
Thermal conductivity (W/m°C)	0.628	1.38	12
Thermal expansion (ppm/°C)	17.2 x 10^{-6}	0.55 x 10^{-6}	12
Knoop hardness (kg/mm^2)	225	600	12
Young's modulus (GPa)	58.3	70	12

Weak ionic bonds in fluoride glass cause low mechanical stability and melting temperature. The temperature needed to break the strong covalent bonds in silica glass is much higher. The large difference in melting points between ZBLAN and SiO_2 glasses makes it difficult to apply a conventional thermal fusion spice technology, and, therefore, a mechanical splicing technique was used [47]. A special glue connection between these two types of fibers was developed which yields a stable splice.

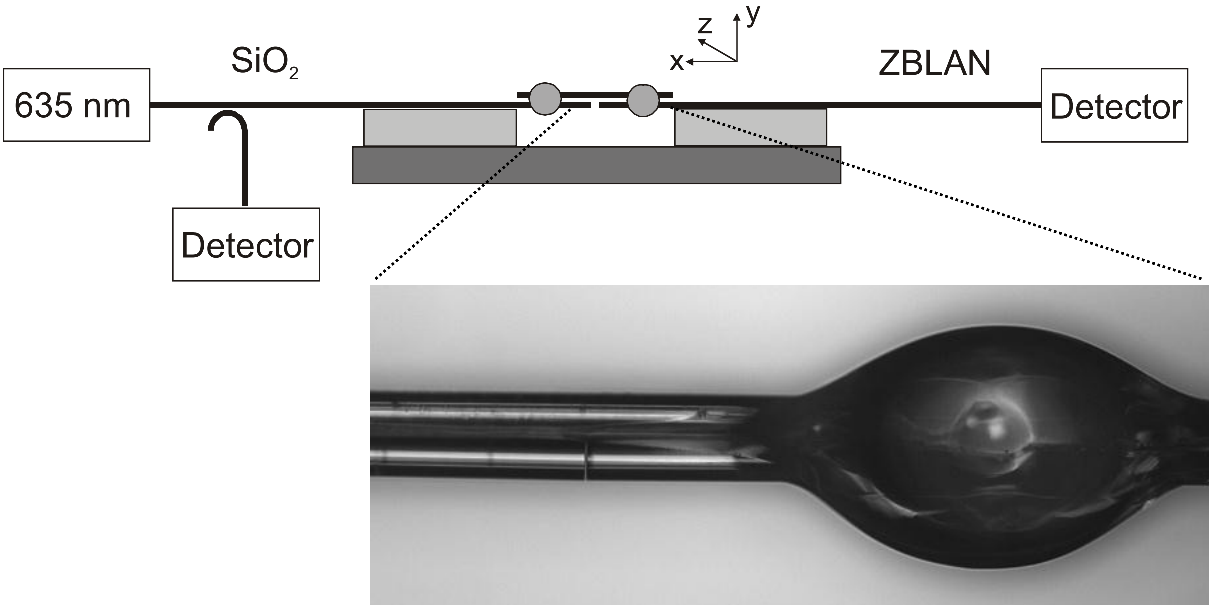

Figure 6.5: Setup used to connect silica and fluoride fibers, and a microphotograph of a glue splice.

The setup used for the glue splicing method is shown in Figure 6.5. The silica fiber was connected to a laser diode emitting at 635 nm. The second fiber end was carefully cut and placed on a plate with a V-groove. The ZBLAN fiber was placed on an XYZ stage equipped with piezoelectric actuators to ensure a precise alignment. This stage allows moving the fiber end in three directions and obtaining an optimum butt coupling between the silica and the fluoride fiber. A detector connected to the ZBLAN fiber made it possible to find this optimum position and to measure the coupling losses. An additional coupler, connected to the signal diode, allowed monitoring the output power from this diode and permitted a precise measurement of the coupling losses. After the optimum butt coupling was achieved, an additional short piece of silica fiber was placed in parallel to both fibers. Afterwards, the silica and the fluoride fiber were fixed to this stabilization fiber by a drop of glue on both sides of the connections.

Using the proper glue is an important point to obtain a reliable glue splice. With short curing times, low curing temperature and low mechanical stress, UV-curable adhesives seem to be the best solution. The adhesive should have an appropriate viscosity. An adhesive with too low viscosity creeps along the fibers, and glue gets between the fiber end faces. As a result, such a connection has large losses. On the other hand, adhesives with too high viscosity bend the fiber when a drop of glue is applied. This leads to misalignment between the fibers. Therefore, two different glues were used. After fiber alignment, a small drop of low viscosity adhesive (NOA 65, Norland Adhesives) was applied, and UV-cured immediately. To improve the mechanical stability of the connection, a drop of high viscosity adhesive (Wave hv Glue, SDI) was applied to cover the first glue. A sphere of glue is shown in the photograph in Figure 6.5. The finished glue splice was packaged in the same way as the couplers. Glue splices were made on both ends of the fluoride fibers, and we produced a module terminated with two silica fibers. This allowed fusing of the module to other components made from silica fibers such as couplers. The glue splice technique that was applied assured a long-term stability at low radiation power in the fiber. The glue splice stability at high power was definitely worse, and a large majority of the glues splices were damaged after several hours of operation in a laser setup.

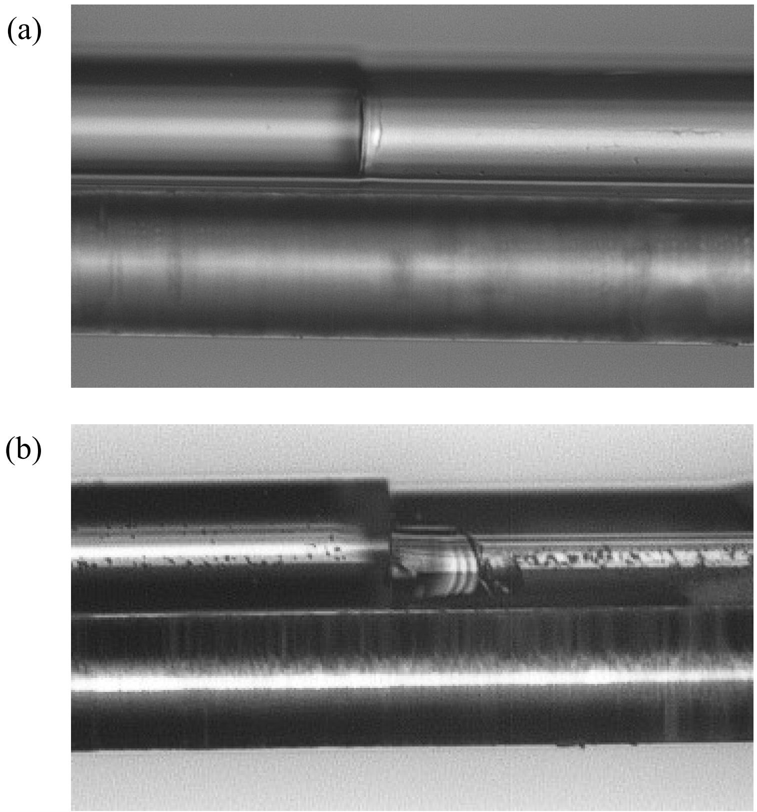

Figure 6.6: Photographs of microscopic inspection of defective splices

In laser systems, the glue splice must transmit high power concentrated in a very small core. This creates considerable thermal effects. The thermal expansion coefficient of fluoride glass is more than 30 times larger than that of silica glass, (see Table 6.1). Additionally, the thermal conductivity of a fluoride fiber is two times smaller. Hence, the temperature increase causes a significant elongation of the fluoride fiber. This in turn leads to deformations of the fluoride fiber, because the glue splice was made without any gap between ZBLAN and SiO_2 fibers. Any substantial change of the pump power causes a permanent change in dimensions of the fluoride fiber. It can lead to misalignment of fiber connections. An inspection of defective splices showed that this was the main reason for the damage.

A photograph of such a splice is shown in Figure 6.6a. We can recognize that the fibers are shifted to each other. Additionally, we see the remainder of some glue or glue solvent on the right fiber which reached an interface between two fiber end faces. Figure 6.6b shows that the elongation can induce a high tension and finally leads to a break in the fluoride fiber. Better results will probably be obtained by allowing a small gap between the fiber ends during the manufacture of the glue splice. Then the fluoride fiber will have some space to adjust its dimensions in response to temperature changes, and additional tensions will not occur.

6.3 Red fiber laser in ring configuration

In contrast to the sensitive free-space Fabry-Perot setup, the fiber laser in ring configuration as presented in Figure 6.7 is inherently stable, because no free-space components are used in the laser resonator.

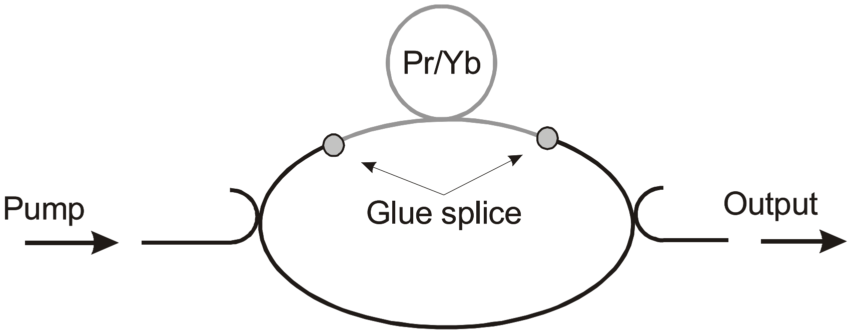

Figure 6.7: Experimental setup of the fiber ring laser

The pump power is coupled into the ring with the aid of a WDM coupler. The spectral characteristic of this coupler was already shown in Figure 6.4. Ninety-seven percent of the pump power at 840 nm is coupled into the ring. The remaining power is coupled to another port which is used for alignment and monitoring of the pump power from the Ti:Sapphire laser. It is easy to exchange this laser by a pigtailed pump laser diode, which is impossible in the Fabry-Perot setup because of the mirrors at the fiber ends which form the laser resonator. However, a pigtailed single-mode laser diode providing sufficient output power was not available, and, therefore, the Ti:Sapphire laser had to be used. The coupling ratio of the WDM coupler for a signal at 635 nm was 0 % which means that no signal was coupled out from the ring. Unfortunately, the coupler had relatively high transmission losses of 0.7 dB. The active medium of the laser was a piece of fiber C. It was 42 cm long; the parameters of this fiber are collected in Table 5.1. Results from the Fabry-Perot experiment as discussed in chapter 5.2.9 showed that this fiber had the worst efficiency among the fibers considered. The reason for using fiber C lies in the fact that only this fiber has a mode field diameter (MFD) similar to fiber 630HP, used for the coupler production. Differences between the MFDs cause additional connection losses. If a fiber with the mode field diameter radius ω_1 is connected to a fiber with mode field diameter radius ω_2, the connection losses caused by the mismatch between their mode field diameters can be estimated by [147]:

$$\alpha = -10dB\log\left[\left(\frac{2\omega_1\omega_2}{\omega_1^2+\omega_2^2}\right)^2\right]. \tag{6.3}$$

The misalignments due to an offset, a tilt and a gap between the fibers are not taken into account. At 635 nm the losses caused by the difference in the MFDs between fiber 630HP and fiber C amount to 0.3 dB. Using fiber A would cause a loss of 1.6 dB. Therefore, in spite of lower efficiency, fiber C was used. The whole module with two glue splices had losses of about 4 dB. Knowing the fiber losses, we can estimate that each glue splice had approximately 1.5 dB of loss. The laser ring was closed with the help of a second coupler which coupled part of the laser emission out of the ring. Figure 6.8 depicts the characteristic of a fiber laser when 52 % of power was coupled out from the ring. The laser characteristics were measured with a closed ring resonator at first, and then with the loop broken up between the two fiber couplers.

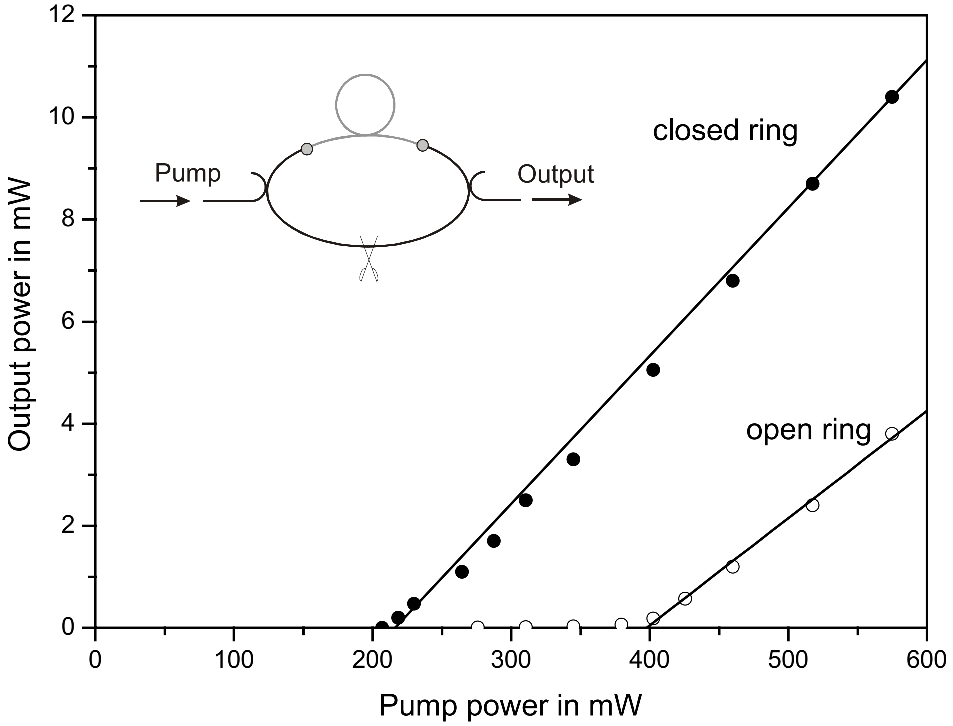

Figure 6.8: Characteristic of fiber laser with closed and opened ring resonator

Reflections from the open fiber ends were minimized by rough fiber end-faces. Due to the fabrication process of the glue splices mentioned, some reflections at fiber connections can be expected and will cause Fabry-Perot resonances between both glue splices. The measurement results indicate a Fabry-Perot threshold of 400 mW, while the threshold of the ring laser setup was only 220 mW. The laser resonator in the latter case, in fact, consists of a combined ring and Fabry-Perot cavity. Using a ring configuration is of advantage, and we obtained 10.4 mW output power by pumping at 575 mW. For comparison, in a Fabry-Perot configuration, only 3.8 mW at the same pump power were measured. The slope efficiency is also larger and amounts to 2.9 % and 2.1 % for closed and open ring, respectively.

Care was taken that there was no air gap between the two fibers when the glue splices were fabricated. However, an air gap in the order of the wavelength cannot be detected with the inspection optics used for glue splice fabrication, and this may lead to reflections. Usually it is not allowed simply to add the reflections from the two interfaces. One must take into account the phase difference which depends on the distance between the interfaces. Therefore, the reflection depends on the length *l* of the air gap. Assuming that the interfaces are perfectly flat and normal to the direction of wave propagation, the reflection factor is given by [81]:

$$R = \frac{\left(n^2 - 1\right)^2 \tan^2(kl)}{4n^2 + \left(n^2 + 1\right)^2 \tan^2(kl)} \tag{6.4}$$

If the gap width is an integer number of half wavelengths in air, there is no reflection. On the other hand, we obtain the maximum reflection of about 15 % of the laser radiation at 635 nm if the gap width is a quarter of a wavelength plus an integer multiple of half the wavelength. When the power transmission through a gap was measured as a function of the length of the gap, the power oscillations were found to be smaller than expected theoretically, and they decreased with increasing width of the gap [81]. Furthermore, the thermal expansion coefficient of the fluoride glass is 17.2 ppm/K in contrast to 0.55 ppm/K in the case of silica glass (compare with Table 6.1). Since the stabilization fiber is a silica fiber, and the distance between the fiber end-faces and the respective glue drop is about 3 mm, the position of the end of the fluoride fiber will change by about 50 nm/K relative to the end of the silica fiber. This means that the reflection of the air gap can be expected to be highly temperature sensitive [148].

Figure 6.9 shows the output power and the threshold power of the ring laser using output couplers with different coupling ratios. The output power was measured at 500 mW of pump power in front of the input fiber. The lowest threshold power of 180 mW was achieved with a 2 % output coupler, but the output power was only 0.4 mW in this case. The maximum output power of 8 mW was reached with a coupling ratio of 52 % at a threshold power of 220 mW. Together with the losses of the fluoride fiber and the glue splices, the total round-trip losses in this case sum up to about 9 dB. Further enlargement of the output coupling ratio caused the threshold power to grew considerably while the output power decreased only slightly. The reason could be a 4 % Fresnel reflection from the fiber end-face which terminated at out-coupling port.

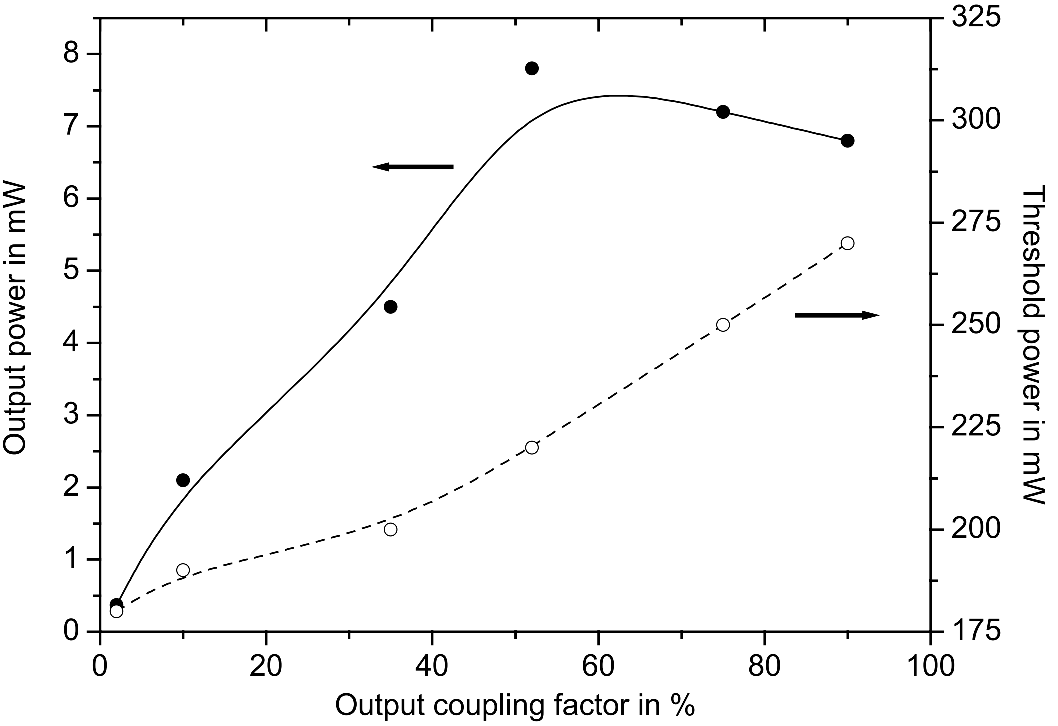

Figure 6.9: Output power and threshold power for different output coupling factors

The larger the out-coupling ratio, the more of the signal is coupled back to the ring, and other Fabry-Perot resonators arise. The coexistence of ring and Fabry-Perot resonators may be the reason that the output power does not decrease significantly as would be expected in a pure ring configuration. Figure 6.10 shows the laser threshold versus round trip losses for the ring laser results from Figure 6.9 together with two Fabry-Perot lasers with the same fiber length. One fiber laser was just using the 4 % Fresnel reflections at both ends of a bare fiber. Together with the fiber losses, this results in 30.2 dB round trip losses. The second Fabry-Perot laser used a high reflector at the pumped end of the fiber and the Fresnel reflection at the other end, which gives a round trip loss of 16.2 dB. To allow for a comparison of both setups, the losses in the pump coupler and the first glue splice have to be taken into account in order to get the pump power entering the doped fiber in the case of the ring laser. Therefore, the threshold power levels are smaller than the values in Figure 6.9. It is likely that the laser resonator in all cases was a combination of a ring and a Fabry-Perot resonator. The Fabry-Perot resonator, consisting of the two glue splices and the doped fiber, should be independent of the output coupler used in the ring resonator. Therefore, its influence should be at minimum in case of minimized ring losses (OC = 2 %) and at maximum in case of large ring losses (OC = 90%). Therefore, Figure 6.10 contains not only the laser threshold powers of the ring laser setup, but also those of two Fabry-Perot fiber lasers with the same fiber length. It is obvious that the data points of the Fabry-Perot lasers and the ring laser with small output coupling are located on a straight line which is included in Figure 6.10, and which reflects the exponential dependence of the laser threshold on the round trip losses in a laser resonator.

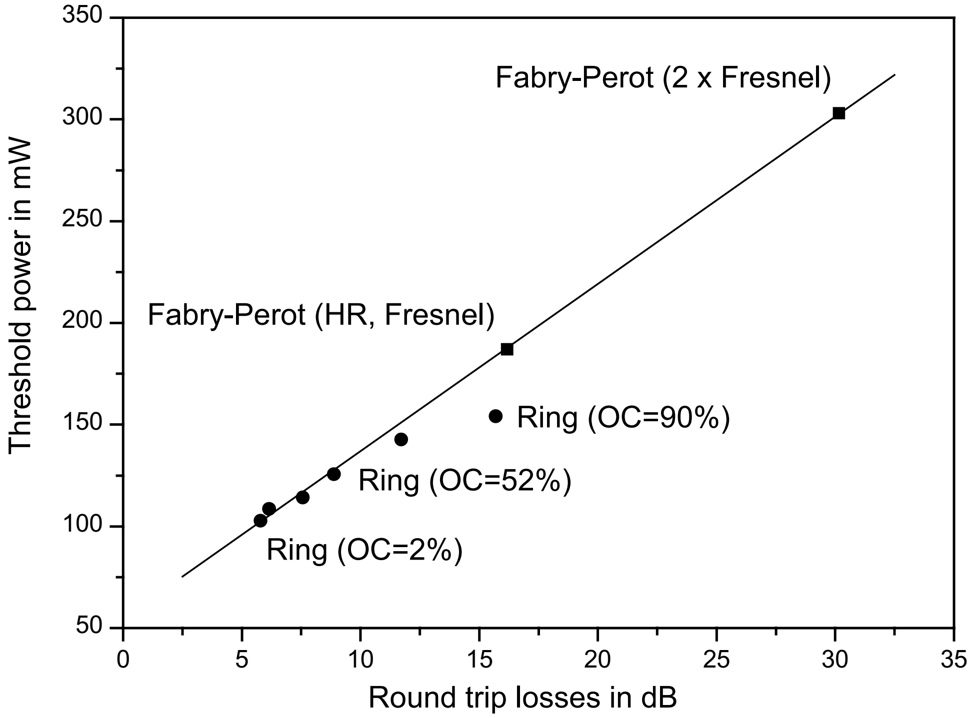

Figure 6.10: Laser threshold versus round trip losses for the ring laser results together with two Fabry-Perot lasers with the same fiber length

Larger output coupling factors, however, lead to discrepancies, especially in case of the maximum value OC = 90 %. The round trip losses in the ring resonator, in this case, are 15.7 dB which is nearly the same as the 16.2 dB for the Fabry-Perot setup with a high reflector. However, the pump power in the doped fiber at the laser threshold was only 154 mW, compared to 187 mW in the Fabry-Perot setup. This is a clear indication that the total round trip losses in the ring resonator setup are, in fact, smaller than just the losses of the fiber ring and reflections from a coupler fiber end.

The ring resonator in this experiment did not contain an isolator. Therefore, the laser radiation travelled in both directions in the fiber loop. It is obvious from Figure 6.11 that the power levels travelling clockwise (output port 4) and anti-clockwise (output port 2) are different, although the measured laser spectrum from both ports was identical. We measured these laser characteristics for two arrangements of glue splice modules. Figure 6.11a shows the results when the pump power initially goes through the splice S1 and then through S2. In contrast, Figure 6.11b was measured after turning around a splice module. Now the pump power goes first through S2 first, and than through S1. The threshold power was found to be independent of the direction of the active fiber and the order of the glue splices. In both cases, the threshold power was approximately 200 mW. This indicates that the attenuation of both glue splices must be the same; otherwise, the threshold power would be larger for the glue splice with higher attenuation carrying the pump radiation. Also, the total output power from both coupler ports shows only a minor dependence on the order of the two glue splices.

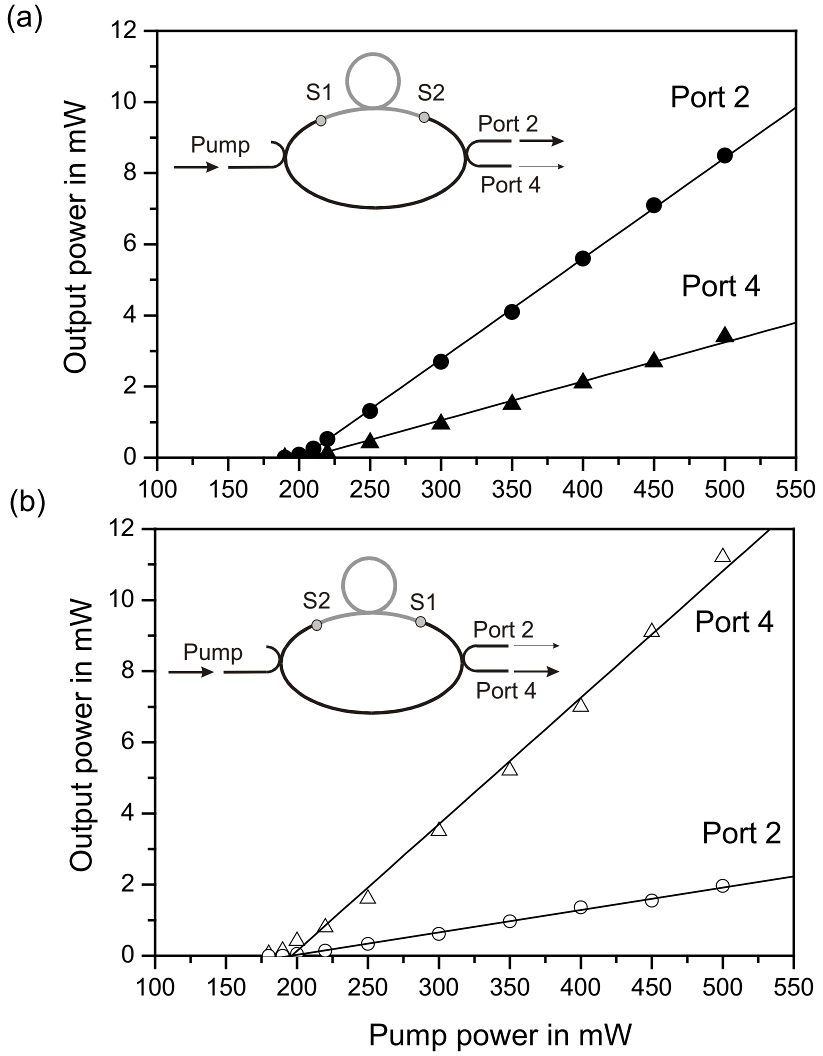

Figure 6.11: Laser emission at both ports of the output coupler versus pump power

At a pump power of 500 mW, we obtained about 12 mW and 13 mW for configurations S1→S2 and S2→S1, respectively. An interesting observation is the asymmetry between the clockwise and the anti-clockwise laser radiation. This is surprising at first, because the ring resonator is symmetric for the laser signal with respect to the travelling direction. Total symmetry, however, is not advantageous for the laser since this situation leads to standing waves and spatial hole burning as in the case of a Fabry-Perot resonator. Therefore, any small asymmetry in the laser radiation will allow gain to avoid the standing wave situation. Such an initial asymmetry may be caused, for example, by different reflections at both glue splices. Analyzing measurements results, we can observe that this ring laser favours the configuration with the laser signal circulating in direction S2→S1. In both cases, the out-coupled signal at a port going in this direction shows a larger output power (Port 2 in Figure 6.11a, and Port 4 in Figure 6.11b). The explanation of this phenomenon could be a larger reflection at splice S2. An estimation of a relative splices reflection is presented in Figure 6.12.

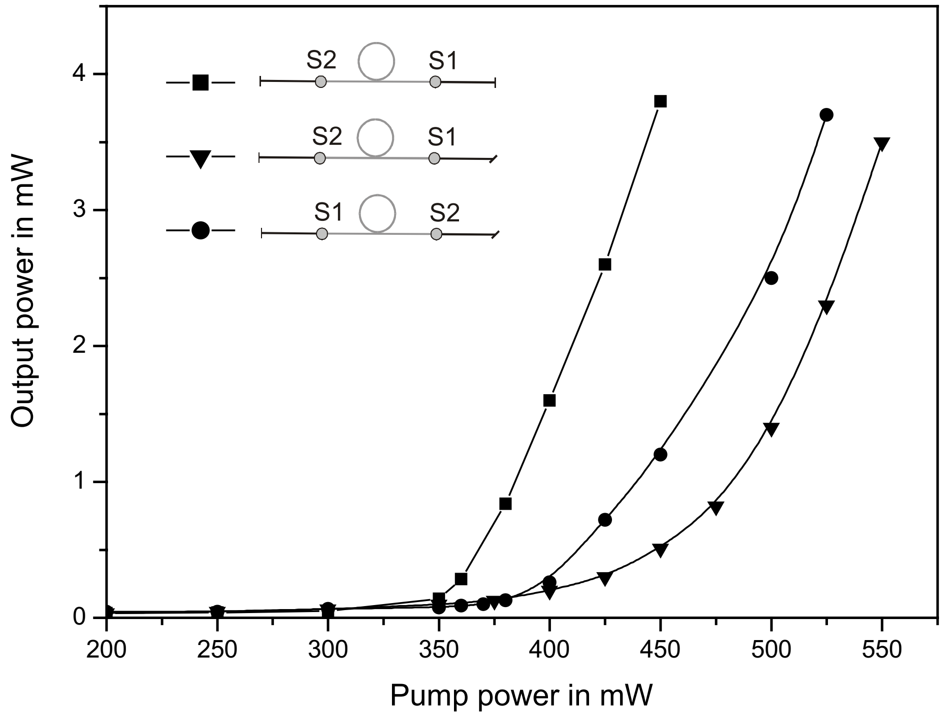

Figure 6.12: Laser characteristic of glue splice module in different configurations

In this experiment, only a glue splice module was taken and pumped. We had several sources of reflection, first, reflections from glue splices, and second, the Fresnel reflections from fiber ends. So, several Fabry-Perot resonators existed. When pumping a splice module, we obtained laser oscillation with a threshold power of about 350 mW. Next, one fiber end was cut at angle of about 8°. This angular end-face reduced the back reflection from the fiber end to a level of only about –55 dB. For comparison with the Fresnel reflection, we had 0.15 dB. The absence of reflections from the fiber end allows us to speak of a kind of superfluorescence source. Therefore, it is difficult to determine a threshold power. But this threshold is definitely larger than without an angular cleaving. Afterwards, the direction of the splice module was changed, and an angular cut was made once again at one fiber end. Comparing the results of both measurements with angular cuts, we see that when splice S2 precedes the angular cut, the threshold power is lower. So we can suppose that it has a larger reflection than splice S1. This assumption was confirmed with a reflection measurement at 635 nm using the Return Loss Measurement Unit AQ7310 from Ando. The reflection from a splice module with splice S2 first and splice S1 next, was 3.2 %. After turning the splice module, we measured a reflection of 2.9 %. The reflection measured originated admittedly from both glue spices, but the reflection from the second splice is strongly damped by the fluoride fiber. The Return Loss Unit was calibrated at 1280 nm, and the sensitivity of the detector at 635 nm was relatively low. Therefore, we have to treat the results as if obtained from relative measurements, showing only which splice has the larger reflection.

Another explanation for asymmetry between clockwise and anti-clockwise laser radiation is a slight asymmetry of the glue splices at the laser wavelength, since the silica fiber at 635 nm is purely single-mode, while the ZBLAN fiber is slightly multi-mode (V=2.7). Therefore, any mode conversion in the active fiber will lead to direction dependent losses at the next glue-splice. Additionally, the core of fiber C was slightly elliptical, so polarisation dependent losses can be expected. Another phenomenon that affects the polarisation of a fiber laser is polarisation dependent gain. This effect stems from the fact that rare earth ions in a glass do not absorb or emit isotropically. Each ion can be thought of as an anisotropic absorber and emitter with a certain spatial orientation. In an amorphous host such as a glass, the ions are randomly oriented. However, the Ti:Sapphire laser used emitted linearly polarised light. Ions oriented roughly parallel to the pump polarisation absorb more strongly than ions oriented roughly perpendicular to it, and they are, thus, excited in larger numbers. Consequently, the gain is higher for a signal polarised parallel to the pump power than for a signal polarised perpendicular to it [10]. The two eigenpolarisations of the fiber are then nearly degenerated and easily coupled by mechanical perturbations. The output polarisation also depends strongly on how the pump is launched into the fiber and the fiber environment, in particular external perturbations (tension, pressure, twist etc.) are of influence.

In order to change the state of polarisation, we applied a polarisation controller (PC) FPC-100 from OZ Optics, in the SiO_2 fiber between the two couplers. The controller works by applying pressure with an adjustable clamp. The pressure on the fiber causes a birefringence within the fiber core, causing the fiber to act as a fractional wave plate. Varying the pressure varies the delay between the fast and slow polarisation components [149]. The clamp was rotatable, allowing one to change the direction in which the stress was applied. This allowed getting any output polarisation.

The opened circle in Figure 6.13 shows the measured output power from both ports when pressure was applied. In the ring, the polarisation is changing along the fiber. For a fiber laser with a stable polarisation state, the polarisation at any given point in the cavity must be the same after one round-trip of the cavity. Applying the PC we can control the state of polarisation in the ring, hence obtaining the maximum output power. At the beginning, the PC was aligned to obtain the maximum output power from port 4. However, the output power increase at port 4 caused simultaneously a decrease of the output power from port 2. Therefore, the position of the PC was aligned to obtain the maximum output power from port 2. The optimum position was found when the clamp was rotated by 90°, and in this case, the output power was doubled. Similarly as before, the optimisation of the output power from port 2 caused the output power from port 4 to decrease. These results suggest that laser emission which travels clockwise (output port 4) and anti-clockwise (output port 2) has two different states of polarisation. Because the core is slightly elliptical, one state of polarisation is amplified more strongly, and this leads to a larger output power.

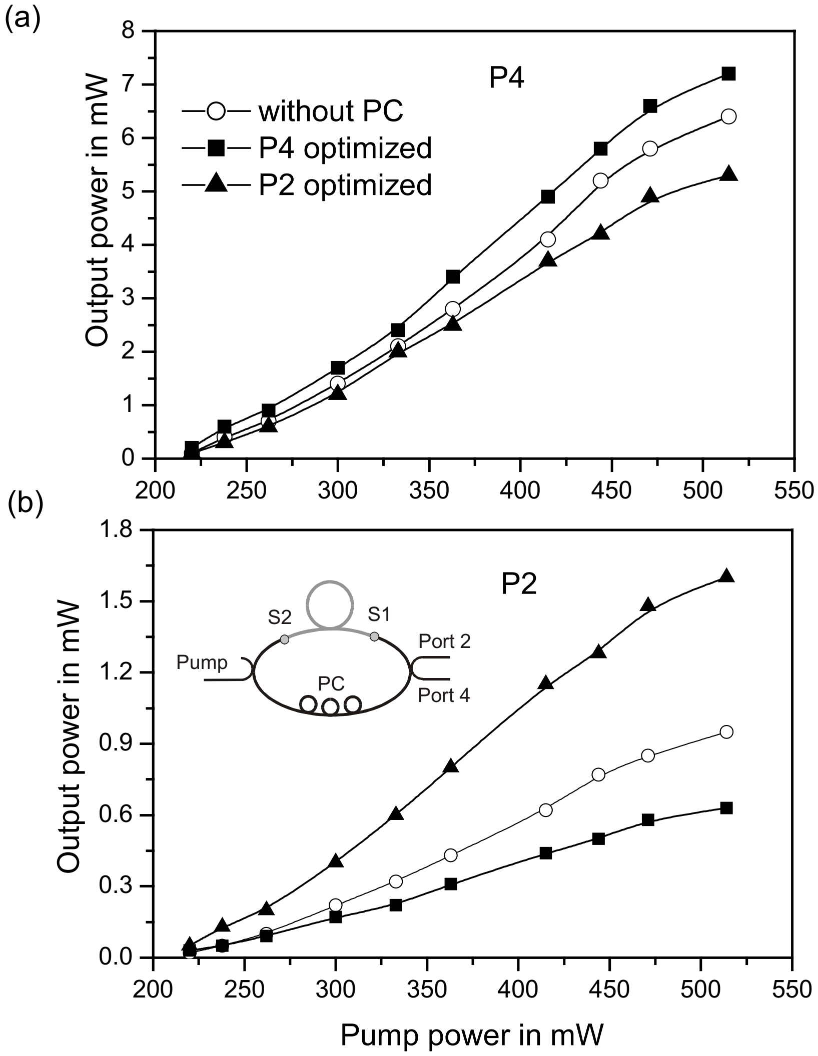

Figure 6.13: Influence of a polarisation controller on the power output from (a) P4 and (b) P2

The presented ring laser configuration has a number of advantages compared to the usual Fabry-Perot setup. The ring laser setup is completely fiber integrated without free-space components. Therefore, it is inherently stable without an alignment procedure. The Ti:Sapphire laser used here could easily be exchanged by a pigtailed pump laser diode. In this case, the whole fiber laser setup would be very compact and transportable. However, a pigtailed single mode diode laser providing sufficient output power was not available until recently. Commercial free-space pump laser diodes around 835 nm offer a maximum of about 200 mW of output power, and this power is only enough to reach the threshold power. The slope efficiency of the presented ring configuration is 3 % which is rather low compared to other red lasers presented in chapter 5.2.2. The main reasons are the large round-trip losses due to the attenuation of the active fiber, the glue splice connections and insertion losses of the fiber couplers. Maximum output power was found for 9 dB optical gain, but 6 dB were lost and only 3 dB were coupled out. Minimising the attenuation losses would allow coupling out the full round-trip loss of 9 dB which would increase the output power by a factor of four.

6.4 Thermally diffused expanded core (TEC) technique

As already shown in chapter 5.2.9, increasing the numerical aperture of the active fiber from 0.16 to 0.25 not only reduced the threshold power significantly, but also increased the slope efficiency. However, using a high-NA fiber causes large connection losses between the active fiber and a fiber used for coupler production. This problem could be solved be using a special high-NA silica fiber and the TEC splice technique, as it is sketched in Figure 6.14

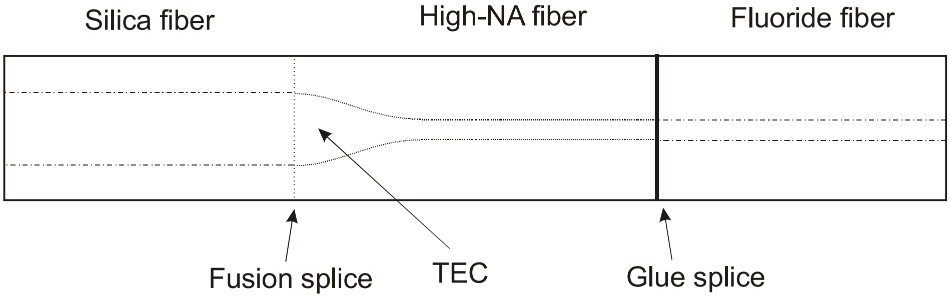

Figure 6.14: Proposal for a connection between fluoride and silica fiber

In order to reduce the splice loss, a high-NA fluoride fiber has to be connected with a high-NA silica fiber with a matching mode field diameter. Then the high-NA silica fiber should be fusion spliced to a fiber used for the coupler production (630HP), using a thermally diffused expanded core (TEC) technique. This method enables the dopant material in the fiber to diffuse by heat treatment. Due to the diffusion of dopant materials, the core diameter gradually increases, and the mode field diameter of the propagating light is also expanded. The formation of the TEC splice will be shown for the case of splicing a standard single mode fiber with a special fiber HP980. The core diameter of the standard fiber is 8µm, but the core diameter of the HP980 fiber is only 4µm. Without the TEC technique, the splice losses are 1.4 dB, but using this technique we were able to modify the core profile and to reduce the splice losses to 0.3 dB. In the practical use of TEC technique, the fibers are heated repeatedly to a high temperature for a short period of time. Figure 6.15 shows changes of the output power during arc impulses. At the start, fibers were spliced using the parameters for a standard fiber corresponding to point 0. Afterwards, arc impulses with a length of 1s were applied. The output power was measured after each impulse. As it can be seen, at the beginning the power increases, reaches a maximum, and than decreases. With heat treatment, the doped material of the core diffuses in the cladding, and the diffusion speed depends on the temperature and the dopant concentration in the core. The diffusion speed of the modification elements in HP980 is higher than in the standard fiber. As the arc impulses continue, the mismatch in core size becomes smaller and smaller, finally core sizes are comparable, and the minimum splice loss is achieved. If the heat treatment is applied for a longer time, the diffusion process continues, and again, differences in core sizes appear and the splice loss increases [150]. Obviously, there is some optimum heating time which guarantees minimum splice losses.

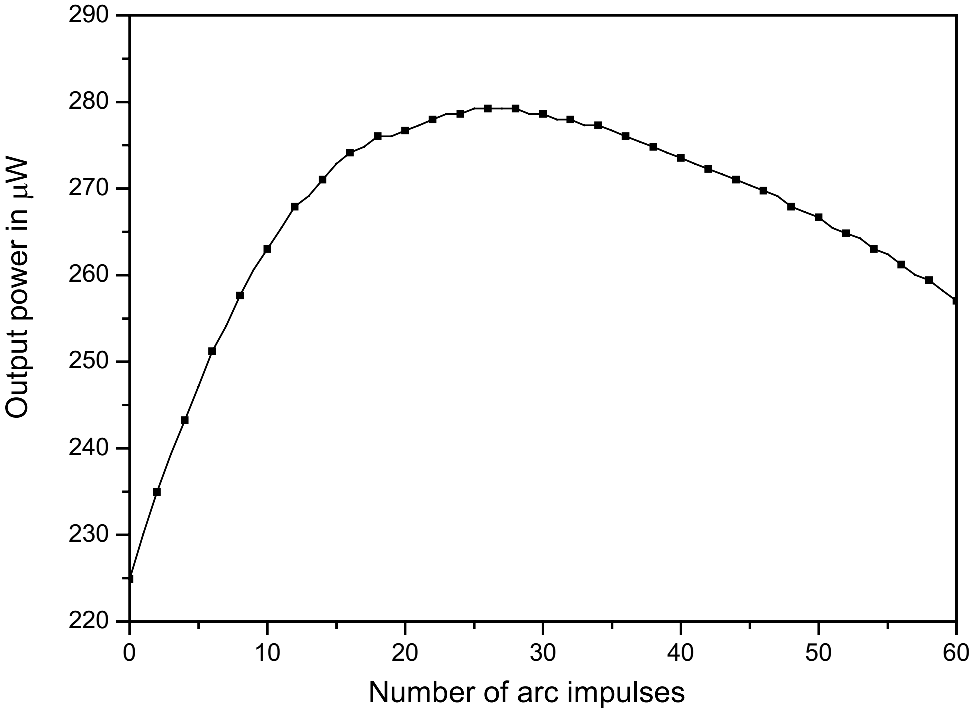

Figure 6.15: Output power versus the number of arc pulses

Applying a TEC splice between a standard fiber and high-NA fiber, we managed to reduce the splice losses from 3.4 dB to only 0.4 dB. Use of the TEC technique will surely enable us also produce a low loss splice between a high-NA fiber and a 630HP fiber. In the future, this will allow us to make a glue splice between a silica and a high NA fluoride fiber with low losses. Using this splice module should allow achieving larger output and higher laser efficiency.

6.5 Red laser with a fiber Bragg grating

The reflection bandwidth provided by standard laser mirrors is often almost as broad as the rare earth fluorescence spectrum. If such reflectors are used, large numbers of longitudinal oscillator modes contribute to the laser output signal. Some form of bandwidth restriction, therefore, must be used to prevent most of these modes from oscillating when single wavelength operation is needed. For this task, a fiber grating can be used in which the grating takes the form of a periodic modulation of the refractive index imposed into the core, a so-called Bragg reflector. Because a distributed Bragg reflector can have a very narrow reflection bandwidth (<0.5 nm), they have been used to great advantage for narrowing the linewidth of fiber lasers.

A fiber grating may be manufactured by exposing a length of the core to a nearly sinusoidal varying intensity of UV light. This variation is created by side illumination of the fiber. The fiber is exposed to the interference pattern of two laser beams or to that created by a laser beam traversing a phase mask. This UV light intensity exposure then imposes a periodic index along the length of the fiber core by creating a corresponding periodic concentration of glass defects [5]. The mechanism of the UV-induced refractive index change is not completely understood but is associated with the colour centres in glassy material. The origin of the photosensitivity lies predominantly with defects associated with oxygen deficiencies in the chemical structure of the fiber. The induced refractive index change to photo-ionisation of a GeO defect is associated with a strong absorption band at 242 nm, and the subsequent trapping of the electron so released. The resultant colour centres are responsible for changes in the UV absorption spectrum of the glass and the refractive index change. There is also evidence that structural rearrangement of the glass matrix, possibly densification, is also correlated with the refractive index increase [151]. It has been found that the diffusion of hydrogen into the fiber substantially increases the refractive index change. The UV-induced refractive index change exceeds 10^{-2} for highly germanium-doped silica fibers after hydrogen loading [7]. The refractive index variation depends on the intensity of the exposing beams and the length of exposure. The UV-written grating has a great advantage because of its low insertion losses, ease of fabrication and high reflectivity at the Bragg wavelength.

Light incident on each of the individual grating layers is partially transmitted and partially reflected. The amplitude of the reflected light from the Bragg reflector is a superposition of all the complex amplitude components that represent the individual layers. The Bragg condition is satisfied when all the points on the grating ruling reflect in phase. The reflectivity of the device is then a maximum. The grating reflects light of Bragg wavelength λ_B, given by [152]:

$$\lambda_B = 2n_{eff}\Lambda, \tag{6.5}$$

where n_{eff} is the effective refractive index of the core mode, and Λ is the grating period.

Figure 6.16a shows the experimental setup applied for making a fiber grating. A second harmonic argon-ion laser emitting at 244 nm was used as a UV-light source. This CW laser had an output power maximum of 300 mW.

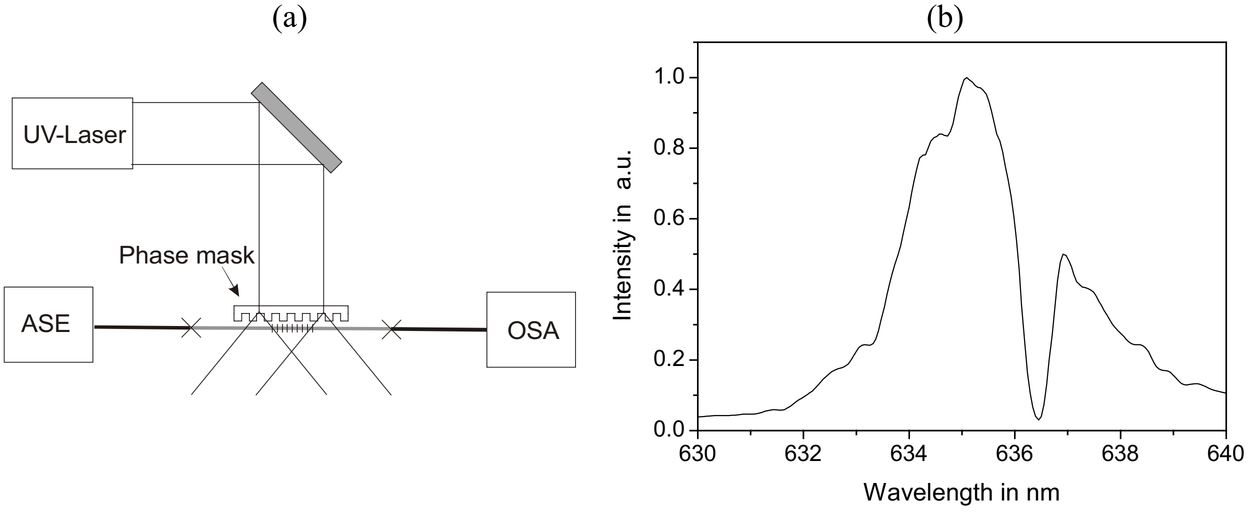

Figure 6.16: (a) Experimental setup for producing a fiber Bragg grating, (b) monitoring of the ASE-source spectrum

The beam was focused in one dimension only by means of a cylindrical lens, and the phase mask was used to produce a periodic pattern in the fiber. The phase mask is made from a flat slab of silica glass which is transparent to ultraviolet light. On one of the flat surfaces, a one-dimensional periodic surface relief structure is etched using photolithographic techniques. The shape of the periodic pattern approximated a square wave in profile. The optical fiber is placed almost in contact with the corrugation of the phase. Ultraviolet light which is incident normal to the phase mask passes through and is diffracted by the periodic corrugations of the phase mask. Normally, most of the diffracted light is contained in the 0, +1, and –1 diffracted orders. However, the phase mask is designed to suppress the diffraction into the zero-order. In practice, the amount of light in the zero-order can be reduced to less than 5 % with approximately 40 % of the total light intensity divided equally in the ±1 orders [152]. The two ±1 diffracted order beams interfere to produce a periodic pattern that photo-imprints a corresponding grating in the optical fiber. The interference pattern periodically modifies the refractive index of the glass in the core of the fiber, gradually building up a Bragg grating.

An ASE source and an optical spectrum analyser were used to allow precise control of the grating properties during inscription. The self-made ASE source consists of a piece of Pr^{3+}/Yb^{3+} fluoride fiber connected to a WDM coupler using a glue splice. This coupler launched the pump power into a fiber and simultaneously coupled out the resulting backward fluorescence. The ASE source was then connected with a photosensitive fiber after hydrogen loading. An observation of the shape of the fluorescence changes allows for control of the grating fabrication process. Figure 6.16b shows the transmission spectrum of the ASE source in the red range after crossing a fiber grating.

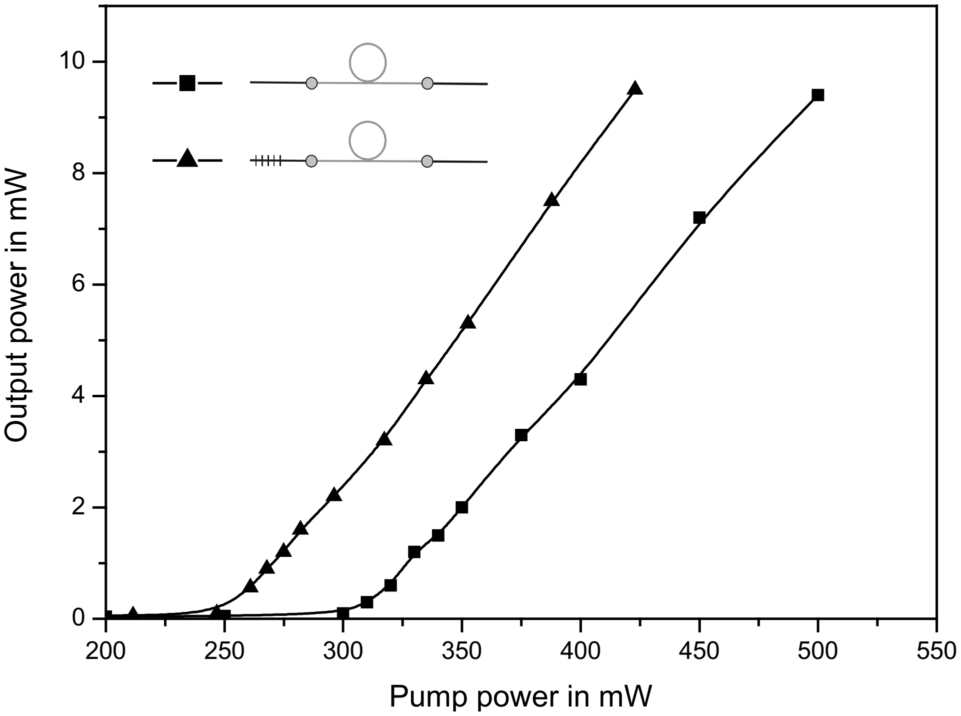

Figure 6.17: Characteristics of a fiber laser with and without Bragg grating

We can easily recognise a hole in the spectrum resulting from a reflection from the grating. Unfortunately, the maximum emission occurs not at the maximum of the fluorescence emission but at 636.5 nm. However, this grating had almost 100 % reflection and a reflection bandwidth of about 0.5 nm. The grating was next used in a fiber laser setup, and the influence of the Bragg grating is presented in Figure 6.17. At first, only a splice module was used without any external mirrors. As already discussed in chapter 6.3, we have a 4 % Fresnel reflection from both fiber end-faces of the splice module. The glue also showed some reflections. This reflection was high enough to get a laser oscillation, but we obtained a relatively high threshold power of 307 nm, and the slope efficiency was 4.9 %.

Next, we spliced a high-reflection fiber grating as an input mirror, and the output reflection was 4 % like before. Since the fiber grating that was used caused some losses of pump power, the laser characteristic was recalculated to take these losses into account. The use of a fiber grating resulted in the threshold power decreasing to 255 mW, and the slope efficiency also slightly increasing to 5.5 %. The influence of the Bragg grating is noticeable not only in the laser characteristic, but especially when we examined the spectrum of these two lasers. The results of these measurements are presented in Figure 6.18.

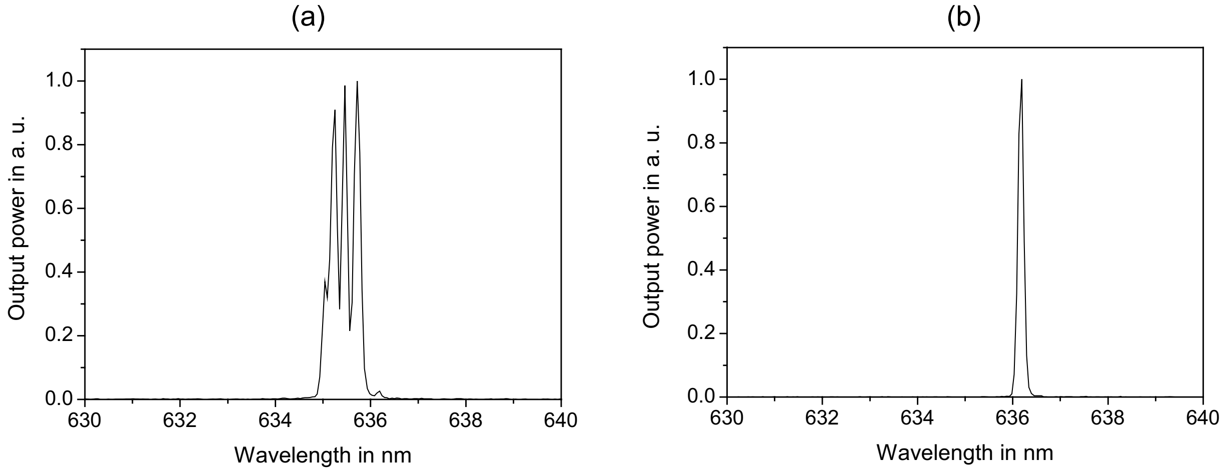

Figure 6.18: Laser spectrum of (a) only a splice module, and (b) after applying a fiber grating

Using only a splice module, we had a small and non-selective reflection. Therefore, we had a mixture of a superfluorescence and a laser emission. We can see many longitudinal modes around 635.5 nm. The output spectrum was unstable because of a strong competition between the modes. However, when a fiber grating was applied as an input mirror, the spectrum was stable, and we measured only one longitudinal mode, in spite of the output mirror showing a Fresnel reflection as before. A full-width at half-maximum (FWHM) of this laser was only about 0.2 nm. The laser emission was shifted to longer wavelengths because the maximum of the fiber grating reflections was also shifted (see Figure 6.16b). For the wavelength reflected, the fluorescence intensity was lower; and therefore, we had also lower gain for this wavelength. We can expect that with the application of a fiber grating which has a reflection peak at a maximum fluorescence emission we will get a better laser characteristic. Using a second grating with optimum reflection will surely produce even better results.

6.6 Fiber laser based on loop mirrors

It is obvious from the discussion above that there are a number of disadvantages in the construction of a fiber laser by butting two mirrors directly against the fiber ends. In this section, we will examine an alternative approach in which directional couplers are used to act as fiber loop mirrors. In this way, all-fiber lasers can be realised, in which bulk mirrors are not required. A fiber loop reflector is depicted in Figure 6.19a.

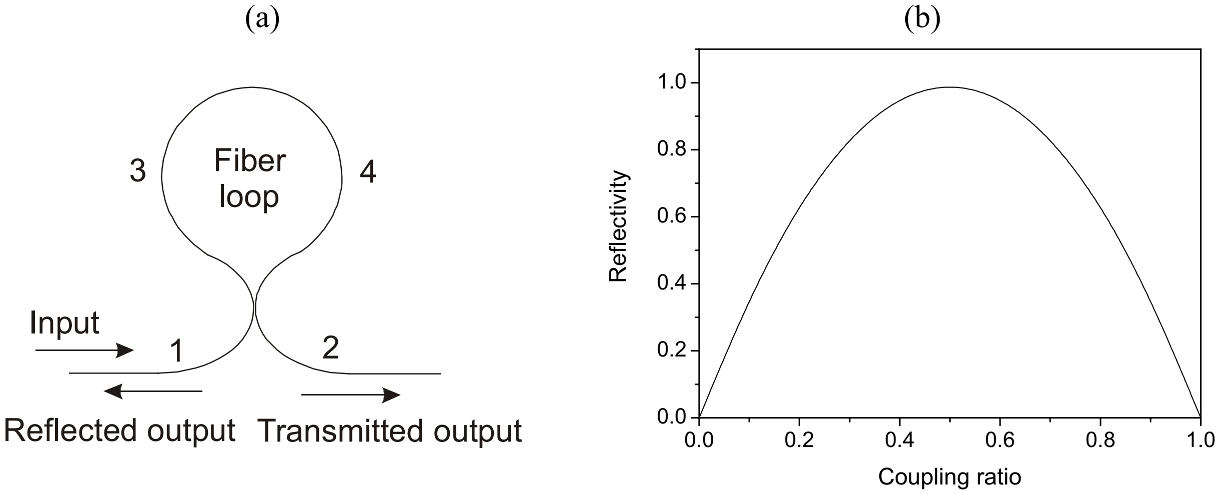

Figure 6.19: (a) Schematic of a fiber loop mirror, (b) reflectivity versus coupling ratio

A fiber loop mirror consists of a loop of optical fiber formed between the output ports of a fiber directional coupler. Light entering the loop via input port 1 can exit either via the other end or, as a backward propagating output, via the input end. There are transmitted and reflected light paths, and there is a clockwise and an anticlockwise pathway round the loop. The loop mirror is a non-resonant interferometer, and its performance must, therefore, be explained by a coherent superposition of fields. The optical path lengths of the two oppositely propagating waves are identical. After making their transit around the loop, the clockwise and anticlockwise components coherently recombine at the coupler. Assume that light travels towards the coupler in port 1 and that the coupler splits half of the power into port 3 and half into port 4. Fifty percent of the input light, consequently, travels clockwise around the loop and fifty percent travels anticlockwise. Light coupled across the waveguide suffers a $\pi/2$ phase lag with respect to light travelling straight through. As a result, the transmitted intensity in port 2 is the sum of a clockwise field of arbitrary phase ϕ and an anticlockwise field of relative phase ϕ - π, both of equal amplitude. As both are of equal intensity, the resultant transmitted intensity is zero, and by conservation of energy, all input is reflected back along the input port 1 [153, 154]. Of course, this is the ideal case and ignores effects such as excess loss, fiber birefringence, etc., that would appear in a real device.

However, the dependence on the coupling ratio K is of greatest interest. The power reflection coefficient of a loop reflector as a function of the coupling ratio K is given by [8]:

$$R = 4K(1-K)\,. \tag{6.6}$$

The coupler and the fiber are assumed to have negligible losses. Variation of reflected power with respect to splicing ratio is presented in Figure 6.19b and shows a parabolic variation with respect to the coupling ratio. It can be seen that the reflection is zero when the coupling ratio is either zero or unit. The reflection is unit when the coupling ratio is 0.5. When two loops are jointed together in series, a resonator is formed.

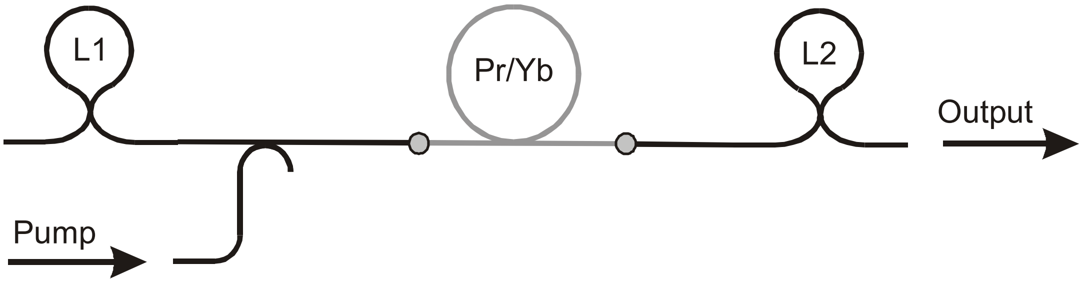

Figure 6.20: All-fiber laser made from two-loops mirrors

An all-fiber laser setup is shown in Figure 6.20. In the centre of this setup a splice module was placed, and loop mirrors were spliced to both silica fibers which terminated this module. If we want to pump through the loop mirrors, the coupler on the left must be designed to be a loop that transmits the pump radiation and reflects the lasing radiation. It means that this coupler should have a 50 % coupling ratio at 635 nm, and 0 % or 100 % at 840 nm. Unfortunately, we did not have such a coupler. Therefore, the laser setup was pumped using the same WDM coupler as in the ring laser arrangement. A characteristic of this coupler is shown in Figure 6.4. The coupling ratio at 635 nm and 840 nm were 0 % and 97 %, respectively. The coupler with a coupling ratio of 52 % at 635 nm was used as the input loop mirror L1, which corresponds to a reflection of almost 100 % of the laser signal. The coupler on the right should be designed to provide high reflection for the pump and an appropriate reflection at the lasing wavelengths in order to achieve maximum lasing output power. For this experiment, a coupler with a coupling ratio of 89 % at 635 nm was chosen. A loop mirror based on this coupler had a reflectivity of 39 % and 48 % at 635 nm and 840 nm, respectively. Particular stages of the laser loop formation are presented in Figure 6.20. The squares mark the results of a measurement when only a splice module with a WDM coupler was used without any loop mirrors. In spite of the lack of external mirrors, Fresnel reflections from the fiber end faces and glue splices were sufficient to excite laser oscillations. The laser had a high threshold power of 365 mW and a slope efficiency of 1.6 %. Splicing of an input loop mirror with a reflection of nearly 100 % at 635 nm led to a clear improvement of laser properties.

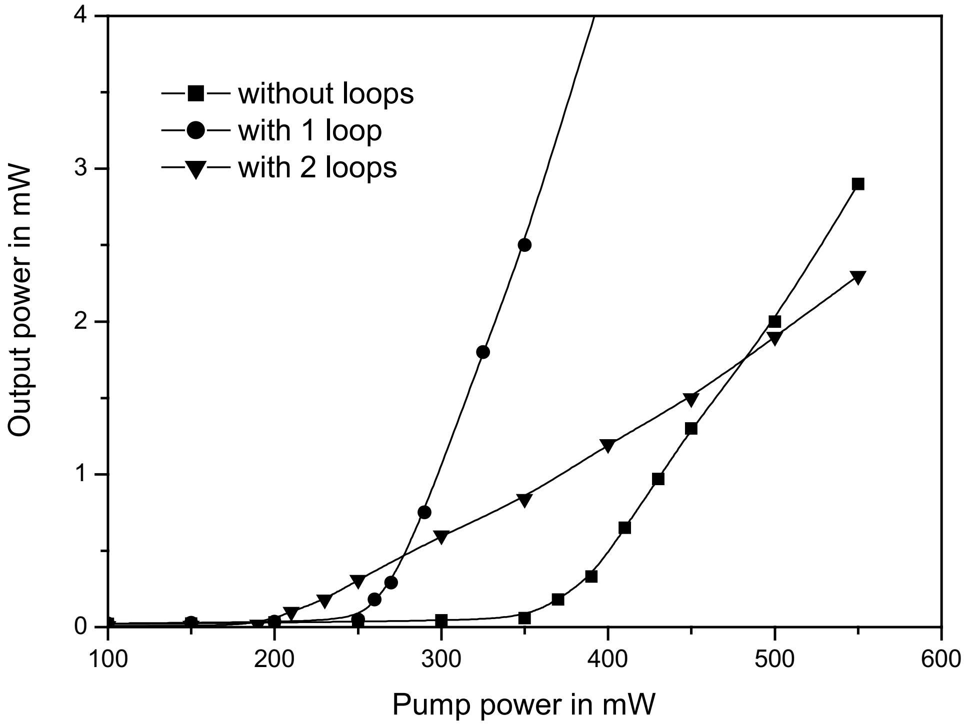

Figure 6.20: Laser characteristics before and after applying loop mirrors

The threshold power diminished to 264 mW, and the slope efficiency doubled. Pumping with 550 mW, we obtained 9.7 mW of output power (not visible in the graph); without this input mirror, we measured 2.9 mW at the same pump power. Adding an output mirror with a reflection of 39 % at 635 nm caused, admittedly, the threshold power to decrease to 209 mW, but also the slope efficiency and the maximum output power were also lower.

Loop mirrors can replace dialectical mirrors, and their reflectivity is governed by the splitting ratio of the coupler. For a typical loop mirror, the reflection peak is fairly broad, several tens of nanometers. This is similar to a bulk mirror, and so the performance of fiber lasers constructed with these devices is similar to those using standard mirrors. The criteria that are used in the design of the optimum reflection by the output loop are the same as those required in selecting the appropriate reflectivity when a bulk mirror is used.

7 Tunable fiber laser

The main reason why rare earth doped fibers are attractive compared to bulk crystals, is their broad fluorescence range which arises from the interaction of the rare earth dopant with the crystal fields of the glass fiber host. We can take advantage of the broad fluorescence profile of rare earth ions in vitreous hosts by introducing a wavelength selective reflector in the cavity of a fiber laser which can in some way be tuned. Lasing only takes place in the narrow band of wavelengths over which there is a suitably high reflectivity. In this chapter, we will discuss the possibility of using a Pr^{3+}/Yb^{3+} fiber in a tunable laser setup, and we will start with a description of tunable reflectors based on a diffraction grating.

7.1 External grating reflectors

In a tunable laser setup, the output mirror is replaced by a reflection or a diffraction grating. It consists of a large number of regularly spaced grooves on a substrate. If a beam of light is incident on a grating, each groove generates a diffracted wavelet. For each wavelength component in the incident beam, the constructive interference of the diffracted components from each groove occurs at a unique set of discrete directions called the diffraction orders of the grating. Diffraction gratings in an external cavity combine the function of a filter and an external mirror. In extended cavities, the light from the grating must be reflected back in the gain medium. Two common geometries for diffraction gratings in external cavity lasers are the Littrow and the Littman configurations.

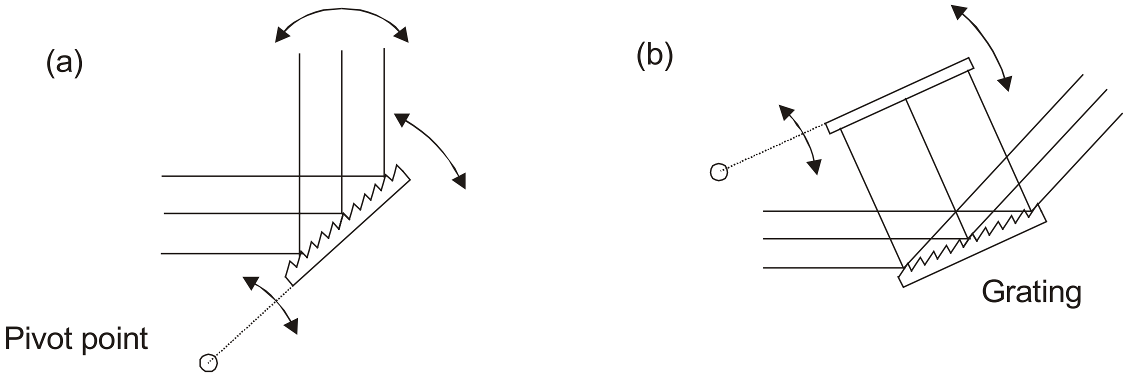

Figure 7.1: Diffraction grating in (a) Littrow, (b) Littman configuration

Figure 7.1a schematically shows a Littrow configuration. The radiation emitted from an active medium hits a holographic grating. The light diffracted in the first order is reflected back into the laser setup, while the light diffracted in the 0th order is coupled out. The grating is installed on a movable arm, and by rotating the grating around the pivot point, we can change the wavelength reflected back into the laser which then might start oscillations. The pivot point has to be precisely calculated to obtain a continuous mode-hop free wavelength tuning. The angle of the diffraction grating must be changed synchronously with the length of the external cavity to preserve the number of cavity modes. A second concept is the Littman configuration presented in Figure 7.1b. Again the output beam from the laser is directed onto the grating. The first diffraction order of the grating hits a mirror and is reflected back onto the grating, and the first order beam is again coupled back into the laser. Wavelength tuning is achieved by tilting the mirror. Littrow and Littman configurations have different characteristics which make them suitable for different types of applications. The Littrow configuration is very easy to align and cost effective. The main drawback is a change of the output beam direction during the wavelength scans which excludes it from some applications. A beam correction mirror that is parallel to the diffraction grating plane can be applied, but tilting the grating still leads to a parallel shift of the output beam. If the beam has to remain stable in position, for example because the laser light has to be coupled into the fiber, the Littman resonator is preferable, because de-tuning is received with tuning the mirror and not the grating, and the beam position does not change. However, the Littrow system shows lower output power than the Littman system, even when using identical laser systems [155]. Because only the first order beam is coupled to the tuning mirror of the laser, the 0th order beam is coupled out of the laser and is lost.

7.2 Orange-red tunable fiber laser

Due to its simplicity and ease to alignment, we used the Littrow configuration in our experiments. The setup applied to tune a Pr^{3+}/Yb^{3+} fiber laser in an orange-red range is shown in Figure 7.2.

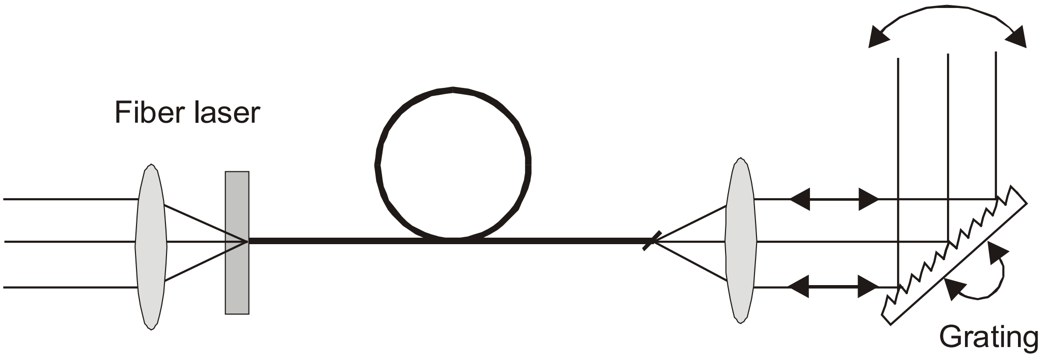

Figure 7.2: Fiber laser operating with a Littrow grating

The setup is very similar to the one used in the Fabry-Perot experiments. The input mirror had a high reflectivity in the range of 600 nm to 690 nm, and it was transparent for the pump wavelength. Instead of an output mirror, we used a grating in the Littrow configuration. In order to avoid a Fresnel reflection from the fiber end, the fiber was cut with an angle to the axis. The fluorescence from fiber A was collimated by a lens with a focal length of 11 mm. This aspherical lens was designed for 633 nm and had an appropriate antireflection coating. We used a diffraction grating with 1200 lines/mm, a blaze wavelength of 500 nm, and a blaze angle of 17°.

In a Littrow configuration, the wavelength is given by the equation:

$$\lambda = 2a \sin\theta , \tag{7.1}$$

where a is the groove spacing, and θ is the angle of incidence (and diffraction) on the grating. Varying the angle of incidence on the grating defines the laser wavelength. The zero-order diffracted beam from the grating was used as the output beam, and the first-order diffracted beam was coupled back into the cavity. The grating was placed on a goniometer, which allows to rotating and tilting the grating in order to obtain an optimum back-coupling in the fiber. We obtained a laser emission if the fluorescence from the fiber was either focused or collimated on the grating. A comparison of laser characteristics for both cases is presented in Figure 7.3.

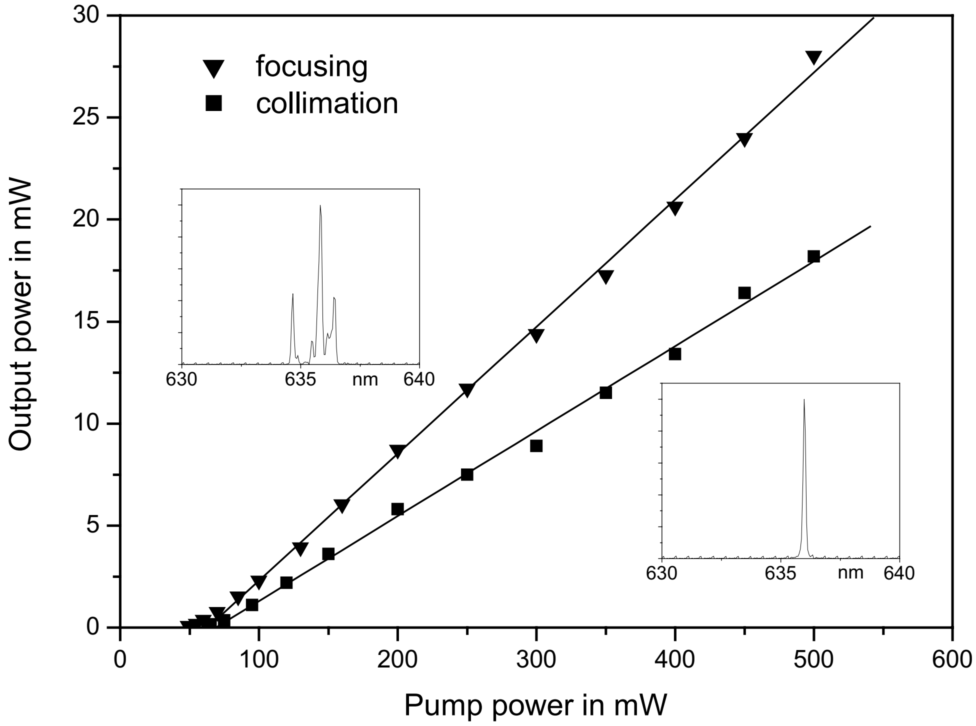

Figure 7.3: Laser characteristics for a focused and a collimated beam on a grating

The grating was aligned for obtaining maximum output power from the laser. The fiber length was 31 cm. If a beam was focused on the grating, we obtained a small pump threshold of 63 mW, and we measured an output power of 27 mW when pumped at 500 mW. The slope efficiency was 6.2 %. On the other hand, if the beam was collimated on the grating, the threshold power was slightly larger and the slope efficiency was 4.2 %. Pumped at 500 mW, we obtained 18 mW of output power. Figure 7.3 shows spectra for both setups. The collimated setup shows lower efficiency, but its laser spectrum was stable, and we can see only one mode. For a focused setup, the laser spectrum had many modes, and the tunability of this system was lower than in the case of the collimated beam. These results could by explained by a different resolution of both systems.

The wavelength resolution for the Littrow mounted grating is given by [156]:

$$\Delta\lambda = \frac{\lambda^2}{2\pi\omega\tan\theta}, \tag{7.2}$$

where ω is the radius of the beam incident on the grating. If the emission from a fiber was collimated on the grating, the beam radius was around 2 mm. This lead to a resolution of about 0.01 nm. But if we focused the beam with the help of an 11 mm lens, the calculated incident beam radius was only 1.1 µm. Then the wavelength resolution was around 145 nm. In this case, a grating worked as a broadband mirror, and the wavelength selection was limited. The resolution can, therefore, be optimised by maximising the free space beam diameter. For this reason in further experiments, only a collimated system was used. As already mentioned, the grating provides a narrow bandwidth feedback with a resolution of 0.01 nm which corresponds to a bandwidth of about 7.5 GHz. This is much larger than the longitudinal mode spacing of the fiber laser cavity which was around 250 MHz. This means that the fiber laser was oscillating on dozens of longitudinal cavity modes. Therefore, we could obtain mode-hop free tuning even when rotating the grating around an axis through its surface. However, a precise calculation of the pivot point is very important in tunable semiconductor lasers. For these lasers, the longitudinal mode spacing is about 100 GHz, and the angle of the diffraction grating must be changed synchronously with the length of the external cavity in order to preserve the number of cavity modes [157].

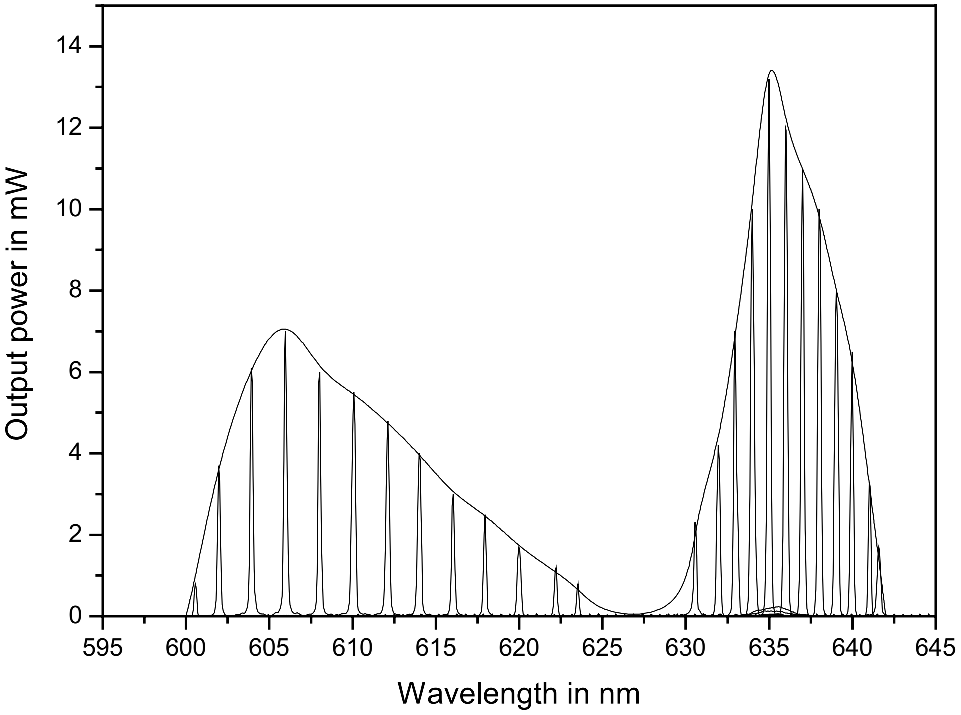

Figure 7.4: Tunable operation of a fiber laser in the orange-red spectral range

The tunability range of a fiber laser was measured with a Spectrometer of type HR4000 from Ocean Optics which had a resolution of 0.1 nm. The tuning curve in the orange-red spectral range is shown in Figure 7.4. All these spectra were measured by pumping a fiber 29 cm long with 300 mW of pump power. After each wavelength change, the grating position was realigned for maximum output power. Tunable operation was observed for the orange laser from 600.6 nm to 623.5 nm and for the red range from 630.6 nm to 641.7 nm. The tunability was a slightly larger than that reported in [21, 28, 33]. In each emission window, we observed continuous tunability of the laser in only one spectral mode with an estimated FWHM of approximately 0.2 nm.

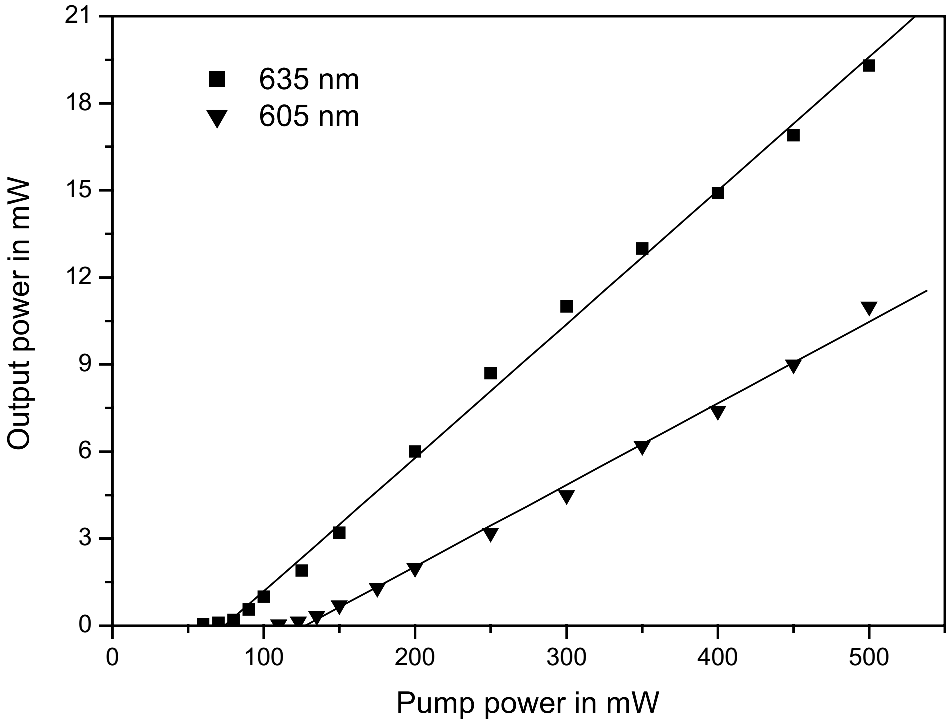

Figure 7.5: Laser characteristics at their optimum emission wavelengths

The red laser had a higher output power compared to the orange one as it is shown in Figure 7.5. We measured these characteristics at conditions which assured maximum output power in each emission window. The threshold powers of the red and the orange laser were 74 mW and 127 mW, respectively. Pumped at 500 mW, we obtained 19 mW of output power from the red laser, and 11 mW from the orange laser. As we see, the red laser was more effective, and the slope efficiency for the red and orange lasers was 4.6 % and 2.8%, respectively.

We measured the laser characteristics only at one fiber length, and this parameter has to be optimised. It should be possible to find a fiber length at which both wavelengths have a similar threshold. Factors that also determine the maximum output power are the losses introduced by the collimating lens and the grating. Lens losses were minimised by using a design that was both aberration corrected and antireflection coated at the lasing wavelength.

Grating-associated losses result from irregularities in the rulings and imperfections on the grating surface. Another important factor is polarisation. If the first diffraction order is used, the grating does not reflect light polarised orthogonally to the grating lines. In order to maximise the reflectivity from the grating, it is usually necessary to use a polarisation controller. In our case, it was impossible, because we had to deal with a fragile fluoride fiber.

7.3 Superfluorescence source

Superfluorescence can be observed as a result of single-pass amplification of spontaneous photons without an optical resonator. The excited ions produce a spontaneous emission, some of which is captured by the fiber core in both the forward direction (co-travelling with the pump) and the backward direction (against the pump). The gain that can be easily achieved in an active single mode fiber is in the order of 30-40 dB. The forward and backward spontaneous photons are amplified as they travel along the fiber and produce amplified spontaneous emission (ASE) with an intensity which saturated the gain. The output power is, therefore, comparable to that which would arise if the fiber had feedback mirrors to form a laser resonator. This ASE operation is sometimes referred to as mirror-less lasing. Because it does not involve an optical resonator, the emitted signals are free of the longitudinal mode structure typical of resonant fiber lasers. Also, unlike most laser sources, the output signal can exhibit a broad optical spectrum, even at high power level.

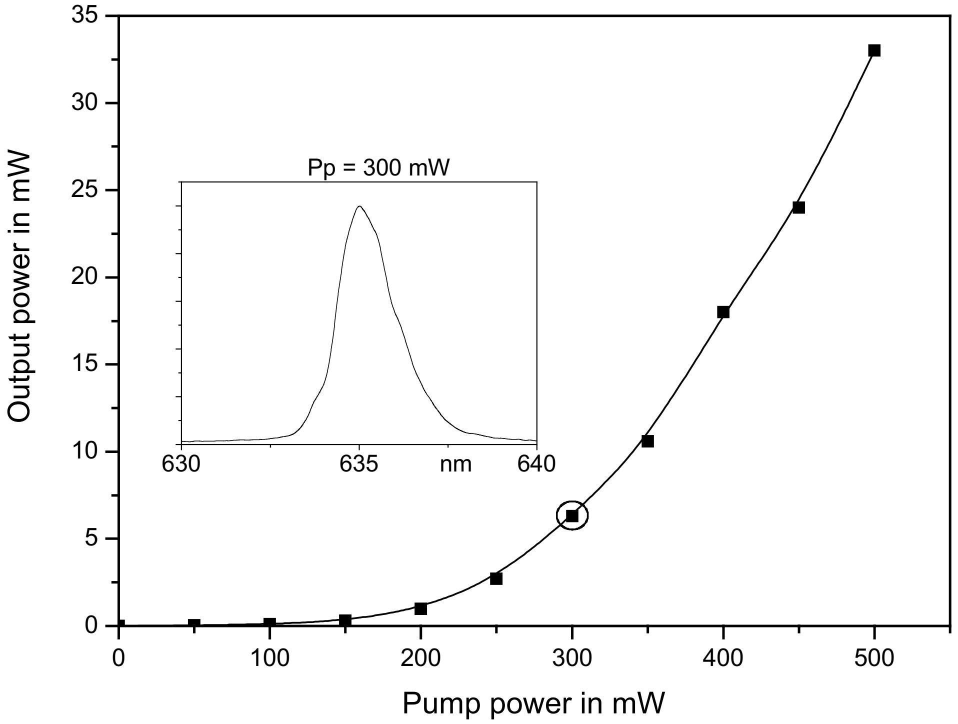

Figure 7.6: Output power as a function of pump power

To build-up a superfluorescece source, we used the same experimental setup as for the tunable laser; only the diffraction grating was eliminated. In our system, an input mirror was used; therefore, we can speak of a double pass configuration. The signal emitted towards the pump was reflected and emitted in the forward direction after two passes through the gain medium. Double pass configurations produce higher power levels than single pass configurations because the effective gain length is doubled. The output fiber end was cleaved with an angle of about 8° to eliminate feedback from the fiber ends, which might otherwise cause the formation of longitudinal cavity modes and reduce the emission bandwidth. The measurement on a silica fiber showed that the reflection from the fiber end-face cut at 8° amounts to only –55 dB [47].

Figure 7.6 shows the output characteristic for a superfluorescence source. For low pump power, the output consisted mostly of spontaneous emission, and the growth was linear at a low rate. As the pump power reached 100 mW, the output became mostly amplified spontaneous emission and increased exponentially without a threshold as normally defined for laser oscillation. With increasing pump power, the slope efficiency became steeper and then the system was operating in the saturated regime. Using a straight line fitting in this regime, we found a slope efficiency of 14.6 %. We measured an output power of 33 mW at 500 mW of pump power. Figure 7.6 also contains the spectrum of the superfluorescence source pumped at 300 mW. For this condition, the FWHM was 1.8 nm. The output bandwidth is one of the important parameters of a superfluorescence light source. Figure 7.7 shows the 3 dB-bandwidth versus the pump power and also the spectra measured at 100 mW and 500 mW.

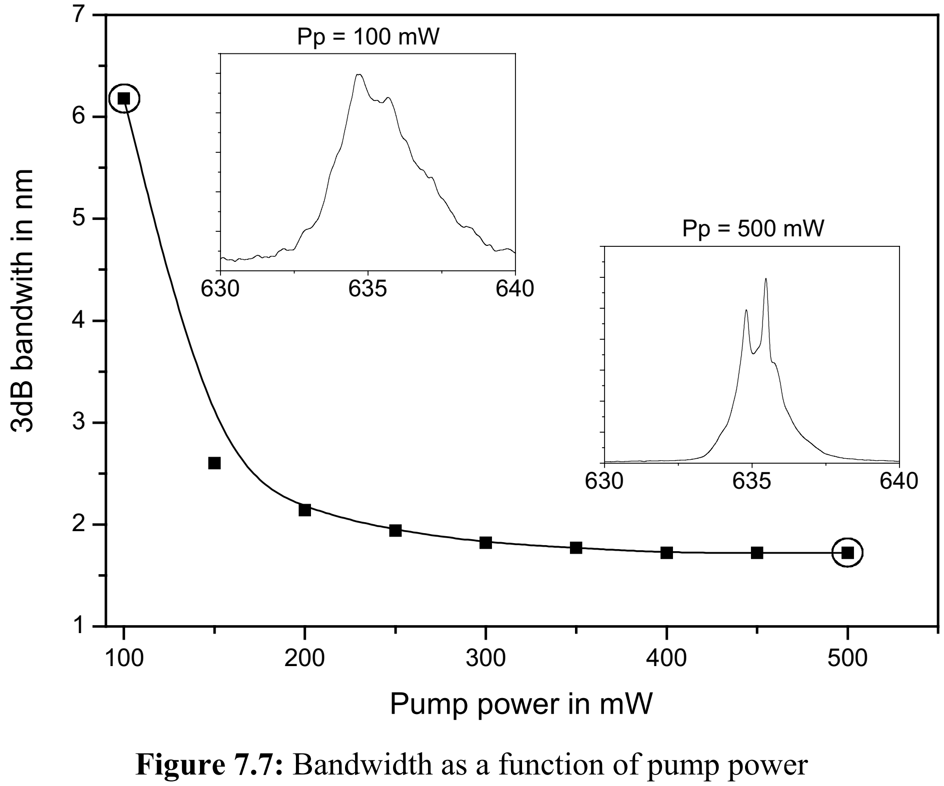

Figure 7.7: Bandwidth as a function of pump power

As the pump power increased, the linewidth narrowed sharply from 6.2 nm to 1.7 nm when reaching the saturation level. Spontaneous emission is preferentially amplified at the peak of the gain curve, causing the spectrum to narrow as the gain is increased. The linewidth remained at ~1.7 nm with continuing increase of pump power. This indicates the inhomogeneous broadening characteristic of the doped fiber. A homogeneously broadened transition would continue to narrow because the peak wavelength consumes all the gain [128]. Of course, most laser transitions exhibit broadening mechanisms of both types. At high pump power, the superfluorescence is driven to lasing even with proper fiber cleaves. This can be seen at the spectrum obtained by pumping with 500 mW. The necessary feedback is provided by Rayleigh scattering within the fiber itself, which constitutes a distributed reflector [158].

The attraction of the superfluorescent emission is that it is spatially coherent but has a broadband emission, and thus, a very short coherence length. A fiber-based superfluorescence light source is a promising broadband light source in fiber sensor applications, in particular fiber gyroscopes, and in some signal-processing fiber systems as low temporal coherence source [159].

Conclusions

The goal of this work was to develop and investigate fiber lasers emitting in the visible spectral range. We concentrated on the improvement of lasers based on Pr^{3+}/Yb^{3+}-doped fiber. Blue, green, orange and red fiber lasers in different configurations were presented.

We started with spectroscopic measurements in which Pr^{3+}-doped ZBLAN and IBZP glass samples were investigated. Comparing the position of absorption peaks in both kinds of glasses, no significant differences were noticeable. However, the emission properties of Pr^{3+}-doped fluoride glasses are dependent on the glass composition.

The knowledge gained from spectroscopic measurements was useful to construct fiber lasers based on the Fabry-Perot configuration. This setup allowed us to obtain lasers emitting at 490 nm, 520 nm, and 635 nm. The greatest efficiency was found for a red laser with 20 mW of output power at a pump power of 500 mW. At the same pump power, the green and blue lasers had an output power of 9.3 mW and 4.8 mW, respectively. During this work, optimization of the laser parameters of the red laser was performed. We found that the optimum pump wavelength is approximately 840 nm, and pump wavelength changes of ± 10 nm cause only a small intensity deviation. The influence of mirror reflectivity and the fiber length was also investigated. Another focus of the measurements was the laser output stability. The red laser exhibited a very low noise level, but the output power from the blue laser was very unstable with strong self-pulsing behavior. For the red and green laser, we applied a noise controlling opto-electronic feedback loop, and we observed some reduction in the noise level. We also tested the long-term stability of our lasers over a period of one hour, and no significant decrease of the output power was observed.

There are a number of disadvantages of the Fabry-Perot setup; therefore, we examined alternative approaches for all-fiber laser configurations. We constructed a red ring laser in which bulk mirrors are not required. This setup used directional couplers; therefore, some part of this work was dedicated to the manufacturing of these components. Another important component of the ring laser was glue splice which enabled us to connect silica and fluoride fibers. The optimum performance of the red ring laser was measured with an output coupling of 52 %, and we obtained 8 mW output power at 500 mW pump power. Another way to construct an all-fiber laser setup is fiber loop mirror. A laser with these components was also investigated. Because of the broad fluorescence width of the Pr^{3+} ions, fiber lasers operate in many longitudinal modes. Fiber Bragg gratings have a very narrow reflection bandwidth, and they have been used for narrowing the linewidth of the fiber laser. When a fiber grating was applied, we observed only one longitudinal mode, and the full-width at half-maximum of this laser was only 0.2 nm.

We took advantage of the broad fluorescence profile of rare earth ions by introducing a tunable wavelength selective reflector into the cavity of the fiber laser. In a Littrow configuration, we were able to obtain a tunable orange-red fiber laser with tunability from 600.6 nm to 623.5 nm and from 630.6 nm to 641.7 nm. We also constructed a superfluorescence source emitting 33 mW output power at 500 mW pump power, and the linewidth of this source was 1.7 nm.

References

[1] J. Wilson, J. F. B. Hawkes: *Optoelectronics: An introduction*, Prentice Hall, New York, 1989.

[2] W. Koechner: *Solid-State Laser Engineering*, Springer, Berlin, 1996.

[3] J. F. Ready: *Industrial Applications of Lasers*, Acad. Press, San Diego, 1997.

[4] B. E. A. Saleh, M. C. Teich: *Fundamentals of Photonics*, Wiley, New York, 1991.

[5] P. C. Becker, N. A. Olsson, L. R. Simpson: *Erbium-Doped Fiber Amplifiers, Fundaments and Technology*, Academic Press, London, 1999.

[6] S. T. Davey, P. W. France: *Rare-earth doped fluorozirconate glasses for fiber devices*, Br. Telecom. Technol. J., vol. 7, no. 1, pp. 58-68, 1989.

[7] S. Sudo (ed.): *Optical Fiber Amplifiers: Materials, Devices, and Applications*, Artech House, Boston, 1997.

[8] P. Urquhart: *Review of rare earth doped fibre lasers and amplifiers*, IEE Proc., vol. 135, no. 6, pp. 385-407, 1988.

[9] P. W. France (ed.): *Optical Fibre Lasers and Amplifiers*, Blackie, Glasgow, 1991.

[10] M. J. F. Digonet (ed.): *Rare-Earth-Doped Fiber Lasers and Amplifiers*, Marcel Dekker, Inc. New York, 2001.

[11] M. J. Weber: *Science and technology of laser glass*, J. Non-Cryst. Solids, vol. 123, pp. 208-222, 1990.

[12] P. W. France et al.: *Fluoride Glass Optical Fibres*, Blackie, Glasgow, 1990.

[13] J. L. Adam, J. Lucas: *Fluoride glasses for laser application*, Ann. Chim. Fr., vol. 20, no. 5, pp. 261-272, 1995.

[14] Y. Miyajima, T. Komukai, T. Sugawa, T. Yamamoto: *Rare earth-doped fluoride fiber amplifiers and fiber lasers*, Opt. Fiber Technol., vol. 1, no. 1, pp. 35-47, 1995.

[15] M. Monerie: *Status of fluoride fiber lasers*, Proc. SPIE, vol. 1581, pp. 2-13, 1992.

[16] F. Auzel: *Upconversion processes in coupled ion systems*, J. Lumin., vol. 45, pp. 341-345, 1990.

[17] M. F. Joubert: *Photon avalanche upconversion in rare earth laser materials*, Opt. Mater., vol. 11, no. 2-3, pp. 181-203, 1999.

[18] F. E. Auzel: *Materials and device using double-pumped phosphors with energy transfer*, Proc. IEEE, vol. 61, no. 6, pp. 758-786, 1973.

[19] P. Goldner, F. Pelle: *Photon avalanche fluorescence and lasers*, Opt. Mater., vol. 5, no. 4, pp. 239-249, 1996.

[20] W. Lenth, R. M. MacFarlane: *Upconversion lasers*, Opt. Photon. News, vol. 3, no. 3, pp. 8-15, 1992.

[21] J. Y. Allain, M. Monerie, H. Poignant: *Tunable cw lasing around 610, 635, 695, 715, 885 and 910 nm in praseodymium-doped fluorozirconate fibre*, Electron. Lett., vol. 27, no. 2, pp. 189-191, 1991.

[22] J. L. Adam, W. A. Sibley: *Optical transitions of* Pr^{3+} *ions in fluorozirconate glass*, J. Non-Cryst. Solids, vol. 76, pp. 267-279, 1985.

[23] R. M. Percival, M. W. Phillips, D. C. Hanna, A. C. Tropper: *Characterization of spontaneous and stimulated emission from praseodymium* (Pr^{3+}) *ions doped into a silica-based monomode optical fiber*, IEEE J. Quantum. Electron., vol. QE-25, no.10, pp. 2119-2123, 1989.

[24] Y. Zhao, S. Fleming: *Theory of* Pr^{3+}*-doped fluoride fiber upconversion lasers*, IEEE J. Quantum. Electron., vol. 33, no. 6, pp. 905-915, 1997.

[25] R. G. Smart et al.: *CW room temperature upconversion lasing at blue, green and red wavelengths in infrared-pumped* Pr^{3+}*-doped fluoride fibre*, Electron. Lett., vol. 27, no. 14, pp. 1307-1309, 1991.

[26] Y. Zhao: *An analytical model for* Pr^{3+}*-doped fluoride fibre upconversion laser*, Opt. Commun., vol. 13, no. 1-6, pp. 470-478, 1997.

[27] R. S. Quimby, B. Zheng: *New excited-state absorption measurement technique and application to* Pr^{3+} *doped fluorozirconate glass*, Appl. Phys. Lett., vol. 60, no. 9, pp. 1055-1057, 1992.

[28] R. G. Smart et al: *CW room temperature operation of praseodymium-doped fluorozirconate glass fibre lasers in the blue-green, green and red spectral regions*, Opt. Commun., vol. 86, no. 3-4, pp. 337-340, 1991.

[29] J. Y. Allain, M. Monerie, H. Poignant, T. Georges: *High-efficiency ytterbium-doped fluoride fibre laser*, J. Non-Cryst. Solids, vol. 161, pp. 270-273, 1993.

[30] M. C. Brierley et al.: *Visible fibre lasers*, Br. Telecom. Technol. J., vol. 11, no. 2, pp. 128-136, 1993.

[31] J. Y. Allain, M. Monerie, H. Poignant: *Energy transfer in* Pr^{3+}/Yb^{3+}*-doped fluorozirconate fibres*, Electron. Lett., vol. 27, no. 12, pp. 1012-1014, 1991.

[32] D. Piehler, D. Craven, N. Kwong, H. Zarem: *Laser-diode-pumped red and green up-conversion fibre lasers*, Electron. Lett., vol. 29, no. 21, pp. 1857-1858, 1993.

[33] P. Xie, T. R. Gosnell: *Room-temperature upconversion fiber laser tunable in the red, orange, green, and blue spectral regions*, Opt. Lett., vol. 20, no. 9, pp. 1014-1016, 1995.

[34] J. Y. Allain, M. Monerie, H. Poignant: *Red upconversion Yb-sensitised Pr fluoride fibre laser pumped in 0.8* μm *region*, Electron. Lett., vol. 27, no. 13, pp. 1156-1157, 1991.

[35] H. Zellmer, P. Riedel, A. Tunnermann: *Visible upconversion lasers in praseodymium-ytterbium-doped fibers*, Appl. Phys. B, vol. 69, no. 5-6, pp. 417-421, 1999.

[36] G. Huber, E. Heumann, T. Sandrock, K. Petermann: *Up-conversion processes in laser crystals*, J. Lumin., vol. 72-74 , pp. 1-3, 1997.

[37] T. Sandrock, H. Scheife, E. Heumann, G. Huber: *High-power continuous-wave upconversion fiber laser at room temperature*, Opt. Lett., vol. 22, no. 11, pp. 808-810, 1997.

[38] T. R. Gosnell: *Avalanche assisted upconversion in Pr^{3+}/Yb^{3+}-doped ZBLAN glass*, Electron. Lett., vol. 33, no. 5, pp. 411-413, 1997.

[39] W. L. Barnes, R. I. Laming, E. J. Tarbox, P. R. Morkel: *Absorption and emission cross section of Er^{3+} doped silica fibers*, IEEE J. Quantum. Electron., vol. 27, no. 4, pp. 1004-1010, 1991.

[40] R. Caspary: *Applied Rare-Earth Spectroscopy for Fiber Laser Optimisation*, Doctoral dissertation, Gemeinsame Fakultät für Maschinenbau und Elektrotechnik der Technische Universität Braunschweig, 2001.

[41] D. E. McCumber: *Theory of photon-terminated optical masters*, Phys. Rev., vol. 134, no. 2A, pp. A299-A306, 1964.

[42] W. J. Miniscalco, R. S. Quimby: *General procedure for the analysis of Er^{3+} cross sections*, Opt. Lett., vol. 16, no. 4, pp. 258-260, 1991.

[43] B. R. Judd: *Optical absorption intensities of rare-earth ions*, Phys. Rev., vol. 127, no. 3, pp. 750-761, 1962.

[44] G. S. Ofelt: *Intensities of crystal spectra of rare-earth ions*, J. Chem. Phys., vol. 37, no. 3, pp. 511-520, 1962.

[45] R. S. Quimby, W. J. Miniscalco: *Modified Judd-Ofelt technique and application to optical transitions in Pr^{3+}-doped glass*, J. Appl. Phys., vol. 75, no. 1, pp. 613-615, 1994.

[46] J. A. Medeiros Neto, D. W. Hewak, H. Tate: *Application of a modified Judd-Ofelt theory to praseodymium- doped fluoride glasses*, J. Non-Cryst. Solids, vol. 183, no. 1-2, pp. 201-207, 1995.

[47] M. M. Kożak: *Development of Thulium-Doped Fluoride Fiber Amplifiers*, Doctoral dissertation, Fakultät für Elektrotechnik und Informationstechnik der Technische Universität Braunschweig, 2005.

[48] P. Goldner, F. Auzel: *Application of standard and modified Judd-Ofelt theories to a praseodymium-doped fluorozirconate glass*, J. Appl. Phys., vol. 79, no. 10, pp. 7972-7977, 1996.

[49] A. A. Kornienko, A. A. Kaminskii, E. B. Dunina: *Dependence of the line strength of f-f transitions on the manifold energy*, Phys. Status Solidi B, vol. 157, no. 1, pp. 267-273, 1990.

[50] A. Akella, E. A. Downing, L. Hesselink: *New fluoroindate glass compositions*, J. Non-Cryst. Solids, vol. 213&214, pp. 1-5, 1997.

[51] R. Rolli et al.: *Yellow-to-blue frequency upconversion in* Pr^{3+}*-doped aluminium fluoride glasses*, J. Non-Cryst. Solids, vol. 280, pp. 269-276, 2001.

[52] L. Wetenkamp: *Charakteririsierung von laseraktiv dotierten Schwermetallfluorid-Gläsern und Faserlasern (engl. Characterization of Laser-Actively Doped Heavy-metal Fluoride Glasess and Fiber Lasers)*, Doctoral dissertation, Gemeinsame Fakultät für Maschinenbau und Elektrotechnik der Technische Universität Braunschweig, 1991.

[53] J. McDougall, D. B. Hollis, M. J. P. Payne: *Spectroscopic properties of* Er^{3+} *in ZBLAN fluoride glass*, Phys. Chem. Glasses, vol. 37, no. 6, pp. 256-257, 1996.

[54] I. D. Aggarwal (ed.): *Fluoride Glass Fiber Optics,* Academic Press, Boston, 1991.

[55] W. Lozano, et al.: *Upconversion of infrared-to-visible light in* Pr^{3+}*-*Yb^{3+} *codoped fluoroindate glass*, Opt. Commun., vol. 153, no. 4-6, pp. 271-274, 1998.

[56] W. Seeber, E. A. Downing, L. Hesselink, M. M. Fejer, D. Ehrt: Pr^{3+}*-doped fluoride glasses*, J. Non-Cryst. Solids, vol. 189, no. 3, pp. 218-226, 1995.

[57] E. Meneses-Pacheco, C. B. de Araujo, Y. Messaddeq: *Energy transfer between* Pr^{3+} *ions in a fluoroindate glass*, J. Non-Cryst. Solids, vol. 226, no. 3, pp. 265-272, 1998.

[58] D. Metzdorf: *Organische Mehrschicht-Photolumineszenz-Bauelemente mit Miktoresonatoren (engl. Organic multi-layer photoluminescence devices with micro cavities*), Studienarbeit, Institut für Hochfrequenztechnik, Technische Universität Braunschweig, 1997.

[59] G. Amaranath, et al.: *Spectroscopic properties of* Pr^{3+}*-doped multicomponent fluoride glasses*, Mat. Res. Bull., vol. 25, pp. 1317-1323, 1990.

[60] H. Hu, F. Lin, G. Yi, B. Guo, C. Qi: *The spectroscopic and fluorescent properties of* Pr^{3+}*-doped fluoride glass*, Conference on Halide Glasses '94.

[61] M. Eyal, E. Greenberg, R. Reisfeld, N. Spector: *Spectroscopy of praseodymium(III) in zirconium fluoride glass*, Chem. Phys. Lett., vol. 117, no. 2, pp. 108-114, 1985.

[62] A. Bjarklev: *Optical Fiber Amplifiers: Design and System Applications*, Artech House, Boston, 1993.

[63] F. Tisco (ed.): *Fiber Optic, Communications Handbook*, Tab Books, 1990.

[64] P. Görrn: *Spektroskopie von* Cr^{3+}*-dotierten Gläsern und Glasfasern (engl. Spectroscopy of* Cr^{3+}*-doped glasses and fibers)*, Studienarbeit, Institut für Hochfrequenztechnik, Technische Universität Braunschweig, 2003.

[65] R. Alcala, R. Cases: *Optical properties of Pr^{3+} circle plus ions in fluoride glasses*, Advan. Mater., vol. 7, no. 2, pp. 190-193, 1995.

[66] B. P. Petreski, P. M. Farrell, S. F. Collins: *Cross-relaxation in praseodymium-doped fluorozirconate glass*, Opt. Commun., vol. 132, no. 1-2, pp. 89-93, 1996.

[67] M. Braglia et al.: *Local structure of Pr^{3+} in fluorozirconate glasses*, J. Non-Cryst. Solids, vol. 257, pp. 83-88, 1999.

[68] T. Sun, Z. Y. Zhang, K. T. V. Grattan, A. W. Palmer: *Temperature dependence of the fluorescence lifetime in Pr^{3+}: ZBLAN glass for fiber optic thermometry*, Rev. Sci. Instr., vol. 68, no. 9, pp. 3447-3451, 1997.

[69] A. B. Arauzo, R. Cases, R. Alcala: *Optical absorption, photoluminescence and cross relaxation of Pr3+ ions in some fluoride glasses*, Phys. Chem. Glasses., vol. 35, no. 5, pp. 202-206, 1994.

[70] T. B. Nguyen, S. Trpkovski, P. M. Farrell, G. W. Baxter, S. F: Collins: *Dependence of the fluorescence lifetime on dopant concentration and temperature in praseodymium-doped fluoride glass*, Opt. Commun., vol. 186, no. 4-6, pp. 277-281, 2000.

[71] H. Kiriyama et al.: *Temperature dependence of emission cross-section of Yb:glass*, Jpn. J. Appl. Phys., vol. 36, no. 9A/B, pp. L1165-L1167, 1997.

[72] Y. B. Hou, Y. B. Li, X. B. Chen, G. Y. Zhang, Y. Wang,: *Temperature dependence of upconversion luminescence from Pr^{3+} and Yb^{3+} codoped ZBLAN glass pumped by 960 nm laser diode*, J. Non-Cryst. Solids, vol. 260, no. 1-2, pp. 54-58, 1999.

[73] S. Sengar, S. J. Dhoble, D. S. Raghuvanshi, B. P. Chandra: *Temperature dependence of anti-stokes luminescence in ZBLAN:Pr^{3+}*, I. J. Pure & Appl. Phys., vol. 41, no. 7, pp. 575-577, 2003.

[74] Y. Ohishi, T. Kanamori, T. Nishi, S. Takahashi: *A high gain, high output saturation power Pr^{3+}-doped fluoride fiber amplifier operating at 1.3 µm*, IEEE Photon. Technol. Lett., vol. 3, no. 8, pp. 715-717, 1991.

[75] A. Remillieux, et al.: *Upconversion mechanisms of a praseodymium-doped fluoride fibre amplifier*, J. Phys.-D-Appl. Phys., vol. 29, no. 4, pp. 963-974, 1996.

[76] Y. Ohishi, T. Kanamori, T. Nishi, S. Takahashi, E. Snitzer: *Gain characteristics of Pr^{3+}-Yb^{3+} codoped fluoride fiber for 1.3µm amplification*, IEEE Photon. Technol. Lett., vol. 3, no. 11, pp. 990-992, 1991.

[77] Y. Ohishi, et al.: *Laser diode pumped Pr^{3+}-doped and Pr^{3+}-Yb^{3+}-codoped fluoride fibre amplifiers operating at 1.3µm*, Electron. Lett., vol. 27, no. 22, pp. 1995-1996, 1991.

[78] P. Xie, T. R. Gosnell: *Efficient sensitisation of praesodymium 1.31 µm fluorescence by optically pumped ytterbium ions in ZBLAN glass*, Electron. Lett., vol. 31, no. 3, pp. 191-192, 1995.

[79] J. C. Zhong et al.: *Thermal and optical properties of* Pr^{3+}/Yb^{3+}*-codoped ZBLAPN glasses*, J. Non-Cryst. Solids, vol. 257, pp. 304-309, 1999.

[80] D. Marcuse: *Principles of Optical Fiber Measurements*, Academic Press, New York, 1981.

[81] E. G. Neumann: *Single-Mode Fibers: Fundamentals*, Springer, Berlin, 1998.

[82] D. Marcuse: *Loss analysis of single-mode fiber splices*, Bell System Tech. J., vol. 56, no. 5, pp. 703-718, 1976.

[83] G. P. Agrawal: *Fiber-Optic Communication Systems*, Wiley-Interscience, New York, 2002.

[84] P. Riedel, R. Urschel, T. Fehn, M. Ledig: *Upconversion fiber lasers - applications in industry and medicine*, Glass Sci. Tech., vol. 76, no. C2, pp. 97-102, 2003.

[85] R. H. Jarman: *Novel optical fiber lasers*, Curr. Op. in Solid State &Mat. Sci., vol. 1, no. 2, pp. 199-203, 1996.

[86] D. S. Funk, J. G. Eden: *Glass fiber lasers in the ultraviolet and visible*, IEEE J. Sel. Top. Quant. Electron., vol. 1, no. 3, pp. 784-791, 1995.

[87] W. A. Gambling: *Optical fibres, lasers, and amplifiers*, Endeavour, vol. 16, no. 1, pp. 17-22, 1992.

[88] J. Nilsson, et al.: *High power fiber lasers*, Optical Fiber Communications Conference Technical Digest, Anaheim, USA, vol. 2, pp. 3-5, 2005.

[89] G. Tohmon, J. Ohya, T. Uno: *Fluoride-based fiber lasers: prospects for the future*, Proc. SPIE, vol. 3416, pp. 144-149, 1998.

[90] M. Poulain, G. Maze: *Vitreous materials for red green blue fiber lasers*, Glass Sci. Tech., vol. 76, no. C2, pp. 47-52, 2003.

[91] A. Pfeil: *Blue fiber laser for the bioanalytic efficient light sources as a replacement for Ar-ionlaser*, www.unique-mode.de.

[92] C. J. Koester, E. Snitzer: *Amplification in a fiber laser*, Appl. Opt., vol. 3, no. 10, pp. 1182-1186, 1964.

[93] D. S. Funk, J. W. Carlson, J. G. Eden: *Ultraviolet (381 nm), room temperature laser in neodymium- doped fluorozirconate fibre*, Electron. Lett., vol. 30, no. 22, pp. 1859-1860, 1994.

[94] D. S. Funk, J. W. Carlson, J. G. Eden: *Room-temperature fluorozirconate glass fiber laser in the violet (412 nm)*, Opt. Lett., vol. 20, no. 13, pp. 1474-1476, 1995.

[95] J. Y. Allain, M. Monerie, H. Poignant: *Blue upconversion fluorozirconate fibre laser*, Electron. Lett., vol. 26, no. 3, pp. 166-168, 1990.

[96] S. G. Grubb, K. W. Bennett, R. S. Cannon, W. F. Humer: *CW room-temperature blue upconversion fibre laser*, Electron. Lett., vol. 28, no. 13, pp. 1243-1244, 1992.

[97] T. J. Whitley, et al.: *Upconversion pumped green lasing in erbium doped fluorozirconate fibre*, Electron. Lett., vol. 27, no. 20, pp. 1785-1786, 1991.

[98] D. S. Funk, S. B. Stevens, S. S. Wu, J. G. Eden: *Tuning, temporal, and spectral characteristics of the green (λ=0.549 µm), holmium-doped fluorozirconate glass fiber laser*, IEEE J. Quantum Electron., vol. 32, no. 4, pp. 638-645, 1996.

[99] D. C. Hanna: *Recent developments in visible light sources*, Phil. Trans. R. Soc. London A, vol. 354, no. 1708, pp. 779-791, 1996.

[100] H. M. Pask, A. C. Tropper, D. C. Hanna: *A Pr^{3+}-doped ZBLAN fibre upconversion laser pumped by an Yb^{3+}- doped silica fibre laser*, Opt. Commun., vol. 134, no. 1-6, pp. 139-144, 1997.

[101] R. Diehl (ed.): *High-Power Diode Lasers: Fundamentals, Technology, Applications*, Springer, Berin, 2000.

[102] H. Zellmer, P. Riedel, M. Kempe, A. Tünnermann: *High-power diode pumped upconversion fiber laser in red and green spectral range*, Electron. Lett., vol. 38, no. 21, pp. 1250-1251, 2002.

[103] D. M. Baney, G. Rankin, K. W. Chang: *Simultaneous blue and green upconversion lasing in a laser- diode-pumped Pr^{3+}/Yb^{3+} doped fluoride fiber laser*, Appl. Phys. Lett., vol. 69, no. 12, pp. 1662-1664, 1996.

[104] S. Salewski: *Mehrfarbig emitierende, diodenerregte Aufkonversions-Laser auf Basis Pr,Yb-dotierter Fluoridglasfasern (eng. Multi-Color Emitting, Laser Diode Pumped Upconversion Lasers Based on Pr/Yb-Doped Fluoride Fibers),* Doctoral dissertation, Fachbereich Physik der Universität Hamburg, 2005.

[105] D. M. Costantini, et al.: *Actively mode-locked visible upconversion fiber laser*, Opt. Lett., vol. 25, no. 19, pp. 1445-1447, 2000.

[106] B. P. Petreski, P. M. Farrell, S. F. Collins: *Optical amplification on the $^3P_0 \rightarrow {}^3F_2$ transition in praseodymium-doped fluorozirconate fiber*, Fiber & Integr. Opt., vol. 18, no. 1, pp. 21-32, 1999.

[107] H. Scheife: *Faseroptischer Verstärker in Selten-Erd-dotiertem Fluorideglas für den sichtbaren Spektralbeich (eng. The Fiber Optic Amplifier in a Rare Earth-Doped Fluoride Glass for a Visible Spectral Range)*, Doctoral dissertation, Fachbereich Physik der Universität Hamburg, 2001.

[108] A. C. Tropper, et al.: *Analysis of blue and red laser performance of the infrared-pumped praseodymium-doped fluoride fiber laser*, J. Opt. Soc. Amer. B, vol. 11, no. 5, pp. 886-893, 1994.

[109] Y. Zhao, S. Poole: *Efficient blue Pr^{3+}-doped fluoride fibre upconversion laser*, Electron. Lett., vol. 30, no. 12, pp. 967-968, 1994.

[110] Y. X. Zhao, S. Fleming, S. Poole: *22 mW blue output power from a Pr^{3+} fluoride fibre upconversion laser*, Opt. Commun., vol. 114, no. 3-4, pp. 285-288, 1995.

[111] Y. X. Zhao: *Pr^{3+} upconversion laser performance improvement by use of pump scavenging*, Opt. Lett., vol. 20, no. 6, pp. 566-568, 1995.

[112] D. M. Baney, L. Yang, J. Ratcliff, K. W. Chang: *Red and orange Pr^{3+}/Yb^{3+} doped ZBLAN fibre upconversion*, Electron. Lett., vol. 31, no. 21, pp. 1842-1843, 1995.

[113] Y. Zhao, S. Fleming: *All-solid state and all-fibre blue upconversion laser*, Electron. Lett., vol. 32, no. 13, pp. 1199-1200, 1996.

[114] D. M. Baney, G. Rankin, K. W. Chang: *Blue Pr^{3+}-doped ZBLAN fiber upconversion laser*, Opt. Lett., vol. 21, no. 17, pp. 1372-1374, 1996.

[115] Y. Zhao, S. Fleming: *Analysis of the effect of numerical aperture on Pr:ZBLAN upconversion fiber lasers*, Opt. Lett., vol. 23, no. 5, pp. 373-375, 1998.

[116] H. Zellmer, K. Plamann, G. Huber, H. Scheife, A. Tünnermann: *Visible double-clad upconversion fibre laser*, Electron. Lett., vol. 34, no. 6, pp. 565-567, 1998.

[117] M. Zeller, H. G. Limberger, T. Lasser: *Tunable Pr^{3+}-Yb^{3+}-doped all-fiber upconversion laser*, IEEE Photon. Technol. Lett., vol. 15, no. 2, pp. 194-196, 2003.

[118] R. W. Waynant, M. N. Ediger: *Electro-Optics Handbook*, McGraw-Hill, New York, 2000.

[119] S. Nakamura, S. F. Chichibu (ed.): *Introduction to Nitride Semiconductor Blue Laser and Light Emitting Diodes*, Taylor&Francis, London, 2000.

[120] G. B. Stringfellow, M. G. Craford, (ed.): *High Brightness Light Emitting Diodes*, Academic Press, San Diego, 1997.

[121] N. M. Johnson, A. V. Nurmikko, S. P. DenBaars: *Blue diode lasers*, Physics. Today, vol. 53, no. 10, pp. 31-36, 2000.

[122] J. Hecht: *Understanding lasers*, IEEE Press, New York, 1994.

[123] G. Huber, T. Kellner, H. M. Kretschmann, T. Sandrock, H. Scheife: *Compact diode pumped cw solid-state lasers in the visible spectral region*, Opt. Mater., vol. 11, no. 2-3, pp. 205-216, 1999.

[124] P. Urquhart: *Device aspects of fiber lasers and amplifiers*, Proc. SPIE, vol. 1171, pp. 27-42, 1990.

[125] P. Peterson, M. P. Sharma: *Back-reflection pumping versus contradirectional pumping in upconversion solid state lasers*, Opt. Commun., vol. 146, no. 1-6, pp. 189-195, 1998.

[126] C. D. Davis: *Laser and Electro-Optics: Fundamentals and Engineering*, Cambridge Univ. Press, 1996.

[127] O. Svelto: *Principles of Lasers*, Plenum Press, New York, 1998.

[128] M. J. F. Digonnet (ed.): *Rare Earth Doped Fiber Lasers and Amplifiers*, Dekker, New York, 1993.

[129] D. Marcuse, J. Stone: *Coupling efficiency of front surface and multilayer mirrors as fiber-end reflectors*, J. Lightwave Technol. vol. LT-4, no. 4, pp. 377-381, 1986.

[130] V. Gaebler, H. J. Eichler: *Blue upconversion ZBLAN-fiber laser*, Proc. Int. Conf. on Lasers, Albuquerque, 2000, pp. 511-516.

[131] P.J. Suni, et al.: *Lasing characteristics of ytterbium, thulium and other rare-earth doped silica based fibers*, Proc. SPIE, vol. 1171, pp. 244-260, 1989.

[132] Yariv: *Optical Electronics*, Rinehart &Wilson, New York, 1985.

[133] F. Sanchez, B. Meziane, T. Chartier, G. Stephan, P. L. Francois: *Output-coupling optimization of Nd-doped fiber lasers*, Appl. Opt., vol. 34, no. 33, pp. 7674-7679, 1995.

[134] B. Pedersen, W. J. Miniscalco, R. S. Quimby: *Optimization of* Pr^{3+}*- ZBLAN fiber amplifiers*, IEEE Photon. Technol. Lett. vol. 4, no. 5, pp. 446-448, 1992.

[135] A. E. Siegman: *Lasers*, University Science Books, Mill Valley, 1986.

[136] D. C. Hanna, R. G. Smart, P .J. Suni, A. I. Ferguson, M. W. Phillips: *Measurement of fibre laser losses via relaxation oscillations*, Opt. Com., vol. 68, no. 2, pp. 128-132, 1988.

[137] P. R. Morkel, M. C. Farries, D. N. Payne: *Losses in fibre laser cavities*, Electron. Lett., vol. 24, no. 2, pp. 92-93, 1988.

[138] H. Zellmer, P. Riedel, A. Tuennermann, I. Freitag, P. Rottengatter: *Noise suppression of a blue upconversion fiber laser*, Conference on Lasers and Electro-Optics, Nice, France, pp. CThE43, 2000.

[139] R. Paschotta, N. Moore, W. A. Clarkson, A. C. Tropper, D. C. Hanna: *230 mW of blue light from a thulium-doped upconversion fiber laser*, J. Sel. Top. Quant. Electron., vol. 3, no. 4, pp. 1100-1102, 1995.

[140] A. Chandonnet, P. Laperle, S. LaRochelle, R, Vallee: *Photodegradation of fluoride glass blue fiber laser*, Proc. SPIE, vol. 2998, pp. 70-81, 1997.

[141] C. M. Ragdale, M. H. Slonecker, J. C.Williams: *Review of fused single-mode coupler technology*, Proc. SPIE, vol. 479, pp. 2-8, 1984.

[142] D. T. Cassidy, D. C. Johnson, K. O. Hill: *Wavelength-dependent transmission of monomode optical fiber tapers*, Appl. Opt., vol. 24, no. 7, pp. 945-950, 1985.

[143] J. D. Love, W. M. Henry, W. J. Stewart, R. J. Black, S. Lacroix, F. Gonthier: *Tapered single-mode fibers and devices*, IEE Proc., vol. 138, no. 5, pp. 343-364, 1991.

[144] T. A. Birks, Y. W. Li: *The shape of fiber tapers*, J. Lightwave. Technol., vol. 10, no. 4, pp. 432-438, 1992.

[145] F. Gonthier, et al.: *Investigation of power oscillations along tapered monomode fibers*, Appl. Opt., vol. 26, no.3, pp. 444-449, 1987.

[146] J. S. Sanghera, I. D. Aggarwal: *Infrared Fiber Optics*, CRC Press, Boca Raton, 1998.

[147] M. Kihara, M. Matsumoto, T. Haibara, S. Tomita: *Characteristics of thermally expanded core fiber*, J. Lightwave. Technol. vol., 14, no. 10, pp. 2209-2214, 1996.

[148] T. P. Baraniecki, R. Caspary, W. Kowalski: *All-fiber red fiber laser in ring configuration*, Appl. Phys. B., vol. 83, pp. 17-20, 2006.

[149] www.ozoptics.com

[150] W. Zheng, O. Hulten, R. Rylander: *Erbium-doped fiber splicing and splice loss estimation*, J. Lightwave. Technol., vol. 12, no. 3, pp. 430-435, 1994.

[151] I. Bennion, J. A. R.; Williams, L. Zhang, K. Sugden, N. J. Doran: *UV-written in-fiber Bragg gratings*, Opt. Quant Electron., vol. 28, no. 2, pp. 93-135, 1996.

[152] K. O. Hill, G. Meltz: *Fiber Bragg grating technology fundamentals and overview*, J. Lightwave. Technol., vol. 15, no. 8, pp.1263-1276, 1997.

[153] D. B. Mortimore: *Fiber loop reflectors*, J. Lightwave. Technol., vol. 6, no. 7, pp. 1217-1224, 1988.

[154] P. Urquhart: *Fiber lasers with loop reflectors*, Appl. Opt., vol. 28, no. 17, pp. 3759-3767, 1989.

[155] L. Hidebrandt, R. Knispel, S. Stry, J. R. Sacher, F. Schael: *Antireflection-coated blue GaN laser diodes in an external cavity and doppler-free indium absorption spectroscopy*, Appl. Opt., vol. 42, no. 12, pp. 1-9, 2003.

[156] F. J. Duarte: *Tunable Lasers Handbook*, Academic Press, San Diego, 1995.

[157] W. T. Trutna, L. F. Stokes: *Continuously tuned external cavity semiconductor laser*, J. Lightwave. Technol., vol. 11, no. 8, pp. 1279-1286, 1993.

[158] Y. Shi, O. Poulsen: *High-power broadband singlemode Pr^{3+}-doped fiber superfluorescence light source*, Electron. Lett., vol. 29, no. 22, pp. 1945-1946, 1993.

[159] M. J. F. Digonnet: *Theory of superfluorecent fiber lasers*, J. Lightwave. Technol., vol. LT-4, no. 11, pp. 1631-1639, 1986.

Appendix A

Table A.1: Summary of the characteristics of visible Pr^{3+}-doped ZBLAN fiber lasers

λ_p nm	λ_p nm	P_{th} nm	P_o mW	P_p mW	η %	l cm	d μm	NA	Pr/Yb %	Ref
491	835/1010	200/280	1	n.a.	n.a.	120	4.6	0.15	0.056/-	25
491	476.5	150	6	450	2	80	4.6	n.a.	0.056/-	28
491	835/1017	65/40	9	65/100	13	85	3	0.21	0.05/-	109
491	835/1017	42/40	22	42/250	7.5	78	2.8	0.24	0.05/-	110
491	835/1017	21/35	3	21/90	5	65	2.8	0.24	0.05/-	111
491	860	60	4	200	3	26	3	0.3	0.3/2	33
491	840	260	6.5	38	5.7	200	3.3	0.2	0.048/-	100
491	850	140	165	1600	12.1	30	3.5	0.16	0.3/2	35
492	835/1017	28/30	1.2	28/45	8.5	68.5	n.a	0.39	0.1/-	113
492	856	85	0.7	350	n.a.	170	1.7	0.39	0.1/1	103
492	835/1017	45/40	30	45/200	n.a.	80	1.7	0.39	0.1/-	26
492	835/1017	28/40	16	28/170	n.a.	80	1.7	0.39	0.1/-	24
492	835/1017	50/20	14	50/120	14	75	1.7	0.39	0.1/-	115
492	831/1017	29/24	1	50/54	1	48	1.7	0.39	0.1/-	114
520	835/1010	160/160	1	n.a.	n.a.	120	4.6	0.15	0.056/-	25
520	476.5	200	2	500	n.a.	100	4.6	n.a.	0.056/-	28
520	860	21	20	200	12.4	42	3	0.3	0.3/2	33
520	840	180	18	380	8.5	500	3.3	0.2	0.048/-	100
520	840	n.a.	100	3000	n.a.	300	5/25	0.15/0.35	0.3/2	116
520	850	4600	320	6500	17	50	35	0.3	0.3/2	102
521	833/1016	138/36	0.7	138/80	1.6	n.a.	4	n.a.	0.2/0.4	32
602	860	~120	0.2	~150	n.a.	98	1.7	0.39	0.3/1	112
603	840	190	55	500	19	30	3.5	0.2	0.3/2	117
605	476.5	150	150	800	21.5	100	4.6	n.a.	0.056/-	28
605	835/1010	150/1000	30	1000/1000	7	120	4.6	0.15	0.056/-	25
610	476.5	370	20	780	n.a.	60	12	n.a.	0.12/-	21
615	860	29	44	430	11.5	60	3	0.3	0.3/2	33
635	476.5	270	100	780	20	60	12	n.a.	0.12/-	21
635	849	125	25	350	10	75	5.7	0.17	0.1/2	34
635	835/1010	700/250	185	700/2000	9.6	1000	4.6	0.15	0.056/-	25
635	476.5	200	250	800	42	100	4.6	n.a.	0.056/-	28
635	833/1016	112/9	6	112/80	8.7	n.a.	4	n.a.	0.2/0.4	32
635	860	42	300	760	52	60	3	0.3	0.3/2	33
635	860	69	3.9	150	1	110	1.7	0.39	0.3/1	112
635	860	202	1020	5510	19	51	5	0.2	0.3/2	37
635	840	120	54	380	23	550	3.3	0.2	0.048/-	100
635	840	700	440	3000	17	300	5/25	0.15/0.35	0.3/2	116
635	838	50	3	500	n.a.	40	3.5	0.16	0.3/2	105
635	850	2000	2060	6500	45	100	35	0.3	0.3/2	102
635	840	57	100	800	n.a.	30	3.5	0.2	0.3/2	117

η - slope efficiency, l - fiber length, d - core diameter

Appendix B

Below photos of fiber lasers emitting at different wavelengths are presented. In each picture the laser spectrum below threshold power is shown in the upper right corner.

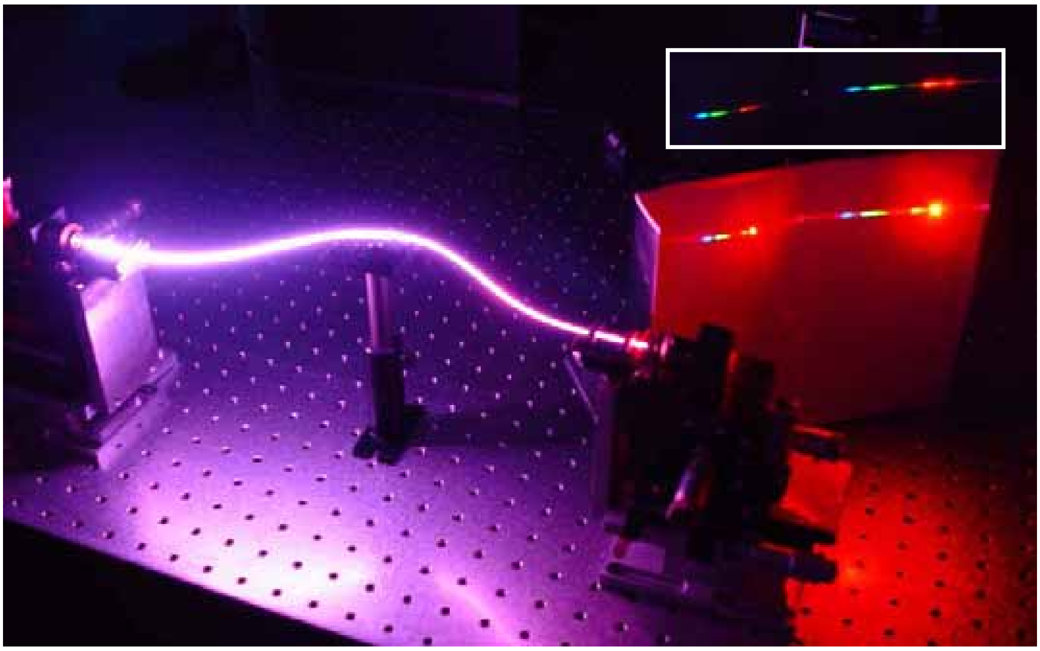

Figure B.1: Red fiber laser without external mirrors (only with Fresnel reflectors)

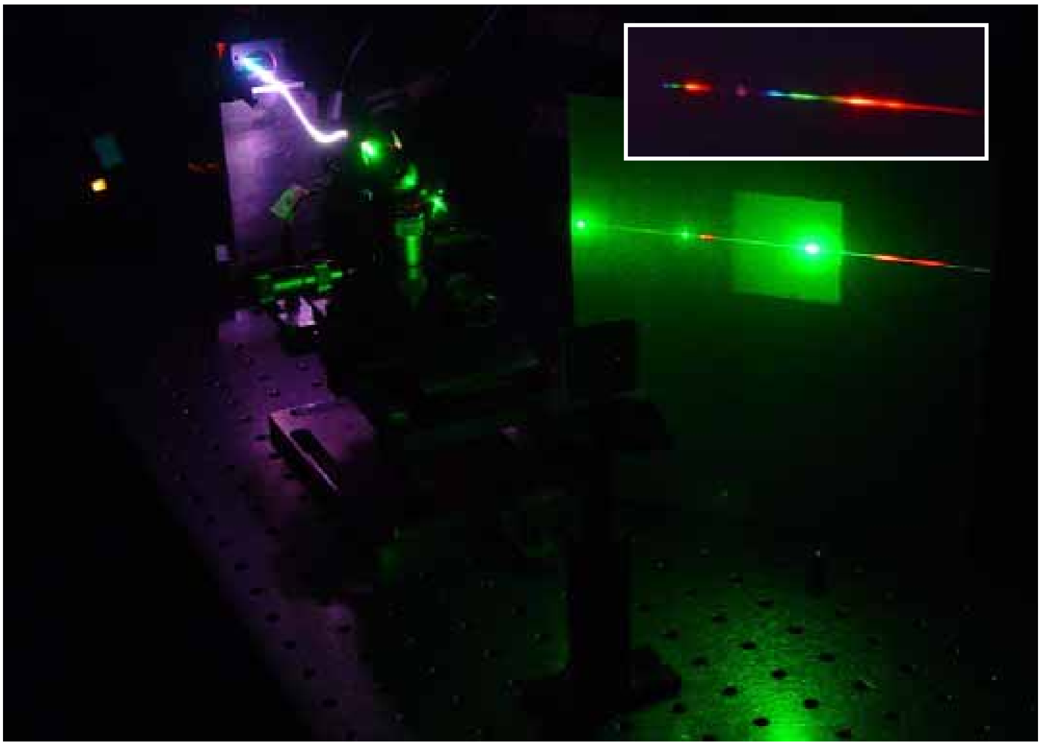

Figure B.2: Fiber laser emitting green light

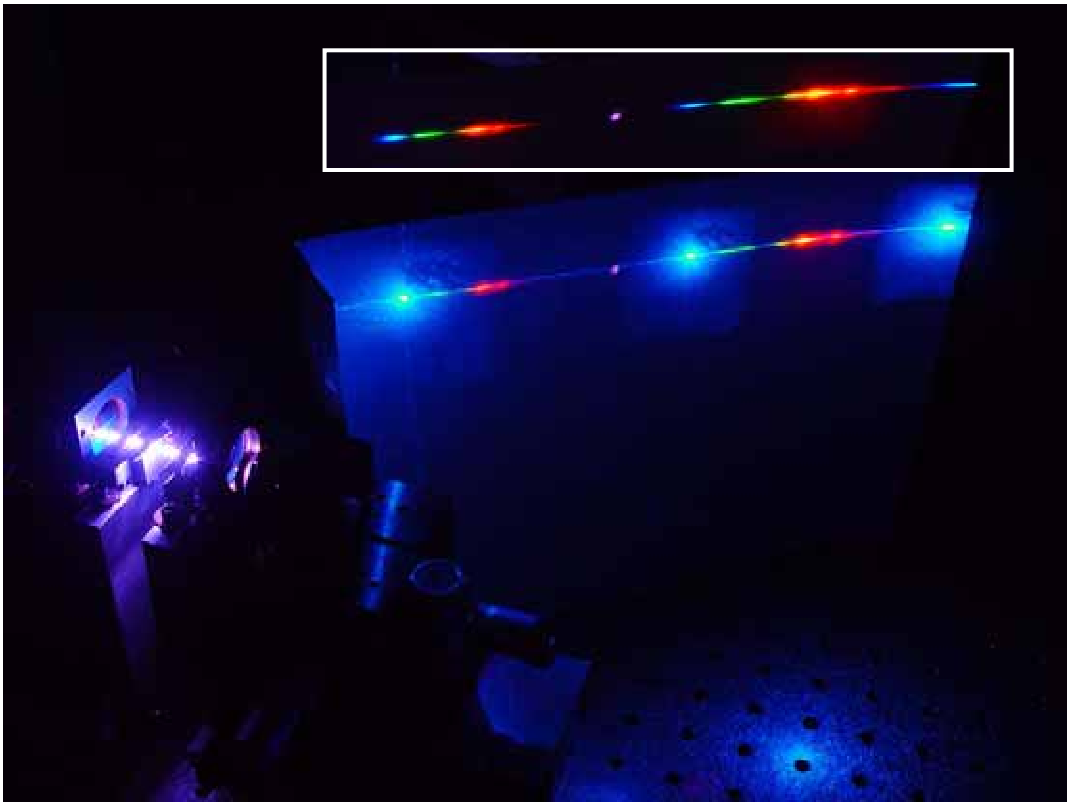

Figure B.3: Blue emission from the fiber laser

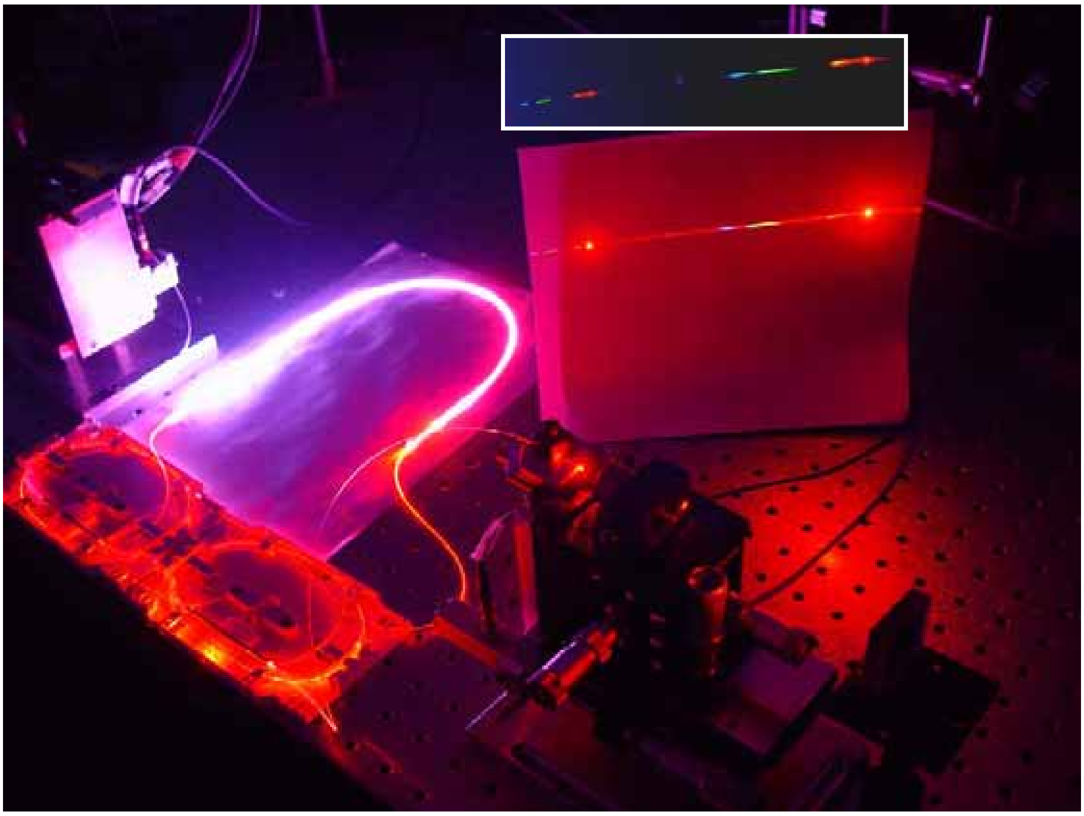

Figure B.4: Red fiber laser in ring configuration